

Data Analysis for Continuous Gravitational Waves

Deepest All-Sky Surveys

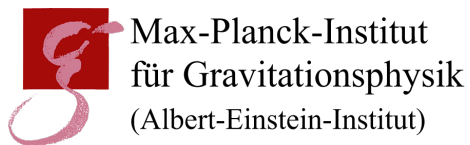
Von der Fakultät für Mathematik und Physik
der Gottfried Wilhelm Leibniz Universität Hannover
zur Erlangung des Grades

Doktor der Naturwissenschaften
– Dr. rer. nat. –

genehmigte Dissertation
von

M. Sc. Holger Johannes Pletsch
geboren am 16. August 1982 in Saarburg

2009



Referent:	Prof. Bruce Allen
Korreferent:	Prof. Bernard F. Schutz
Tag der Promotion:	04.11.2009

Abstract

Direct detection of gravitational waves would not only validate Einstein's theory of General Relativity but also constitute an important new astronomical tool. Continuous gravitational-wave (CW) signals are expected for instance from rapidly rotating neutron stars. Most such stars are estimated to be electromagnetically invisible, but might be detected and studied via gravitational waves.

This dissertation is concerned with the development, study and application of data-analysis techniques to detect CW signals from previously unknown sources through all-sky surveys over broadest possible ranges of putative source frequencies and frequency time-derivatives.

An all-sky CW search is presented using 510 hours of data from the fourth science run (S4) of the Laser Interferometer Gravitational-wave Observatory (LIGO), covering frequencies of 50 to 1500 Hz and linear drifts in frequency. The main computational work of the search is distributed over hundreds of thousands of computers via the public volunteer computing project "Einstein@Home". This enormous computing capacity allows the exploration of a wide parameter space, despite of using comparably long coherent integration times of 30 hours, subdividing the 510 hours of data into 17 segments. To enhance the sensitivity of the search, in a post-processing stage the coherent-analysis results from the 17 data segments are combined through a highly efficient coincidence scheme. Moreover, the sensitivity of the search is estimated, along with the fraction of parameter space vetoed because of contamination by instrumental artifacts.

In a further Einstein@Home CW search the previous S4 analysis is extended to use 840 hours of early fifth-science-run (S5) LIGO data, which are examined in 28 coherent segments of 30 hours. The major part of the post-processing is again related to efficiently combining the 28 coherently-analyzed segments. Despite probing a slightly larger parameter space, this analysis achieves 3 times better sensitivity over the antecedent S4 search. Over large parts of parameter space these are the most sensitive continuous gravitational-wave search results to date.

Furthermore, the global parameter-space correlations in the coherent statistic for CW detection are comprehensively studied. The novel insights I have obtained lead to further important applications in CW data analysis. Among these is the construction of a veto method which excludes false candidate events from instrumental noise artifacts.

The improved understanding of the global parameter-space correlations also leads to a new hierarchical semi-coherent method for CW detection. For more than a decade, the problem of how to best form the incoherent combination of coherent search statistics has been addressed in creative, but ad hoc ways. This method removes the arbitrariness from the incoherent step by finding the optimal solution through direct mathematical derivation for the first time. As a result, the technique I have invented shows drastic sensitivity improvements over previously available methods, yielding an increase in the spatial volume probed by more than two orders of magnitude at even lower computational cost. It is therefore a significant step toward the first detection of a prior unknown CW source.

Keywords: Continuous gravitational-wave detection, data analysis, all-sky surveys

Kurzfassung

Der direkte Nachweis von Gravitationswellen wäre nicht nur eine bedeutende Bestätigung von Einsteins allgemeiner Relativitätstheorie, sondern auch der Beginn eines völlig neuen Forschungszweigs der Astronomie. Als Paradebeispiel für astrophysikalische Quellen kontinuierlicher Gravitationswellen (CW) gelten schnell rotierende Neutronensterne. Die Mehrheit solcher Sterne ist möglicherweise elektromagnetisch völlig unsichtbar, Gravitationswellen hingegen ermöglichen deren Entdeckung und Untersuchung.

Die vorliegende Dissertation legt den Schwerpunkt auf die Entwicklung, Optimierung und Anwendung von Techniken zur Detektion kontinuierlicher Gravitationswellen von bislang unbekanntem Quellen. Der Suchparameterraum erstreckt sich dabei über alle Himmelsrichtungen, sowie über eine ausgedehnte Bandbreite möglicher Frequenzen und potentielle zeitliche Frequenzänderungen.

Zu Beginn wird eine Suche nach CW Signalen in 510 Stunden aus den S4 Daten der LIGO Detektoren dargestellt. Diese Suche umfasst Frequenzen von 50 bis 1500 Hz und lineare Frequenzänderungen. Den größten Teil des benötigten Rechenaufwands bewältigt das Projekt "Einstein@Home" unter Beteiligung der Öffentlichkeit. Die immense Rechenleistung von über 100 000 Heimcomputern ermöglicht die Erforschung eines äußerst weiten Parameterraums bei vergleichsweise langen kohärenten Integrationszeiten über 17 Datensegmente zu je 30 Stunden. Zur Steigerung der Suchempfindlichkeit werden die kohärenten Detektionsstatistiken der 17 Segmente mithilfe einer hocheffizienten Koinzidenzanalyse kombiniert. Außerdem wird eine Methode zur Beseitigung stationärer, instrumenteller Rauschartefakte implementiert. Die Empfindlichkeit dieser Suche wird per Monte-Carlo Methodik abgeschätzt.

In einer weiteren Einstein@Home CW Suche wird eine dreifach erhöhte Empfindlichkeit im Vergleich zur vorherigen S4 Datenanalyse erzielt. Diese Analyse verwendet 840 Stunden der LIGO S5 Daten in Form von 28 kohärent analysierten Segmenten zu je 30 Stunden. Im Anschluß daran wird ebenfalls eine effiziente Kombination der kohärenten Detektionsstatistiken dieser Segmente durch Koinzidenzanalyse durchgeführt. Über weite Regionen des abgesuchten Parameterraums sind die hier erzielten Ergebnisse die empfindlichsten, welche jemals in CW Suchen erreicht wurden.

Des Weiteren wird eine umfassende Studie durchgeführt, welche die globalen Parameterkorrelationen in der kohärenten Detektionstatistik für CW Signale untersucht. Aus den dabei gewonnenen, neuartigen Erkenntnissen leiten sich bedeutende Anwendungen für die CW Datenanalyse ab. Eine dieser Anwendungen beinhaltet eine Veto-Methode, die vermeintliche Kandidaten infolge instrumenteller Artefakte eliminiert.

Ferner führt der Erkenntnisgewinn hinsichtlich der globalen Parameterkorrelationen zu einer neuen hierarchischen, semi-kohärenten Methode zur Detektion von CW Quellen. Diese neuartige Technik liefert eine drastische Erhöhung der Sensitivität im Vergleich zu bislang verfügbaren Methoden. Konkret bedeutet das eine Vergrößerung des Beobachtungsvolumens um mehr als zwei Größenordnungen bei sogar niedrigerem Rechenaufwand. Daher begründet dies einen maßgeblichen Fortschritt auf dem Weg zur ersten direkten Detektion kontinuierlicher Gravitationswellen einer zuvor unbekanntem Quelle.

Stichworte: Detektion kontinuierlicher Gravitationswellen, Datenanalyse, Ganzhimmelerfassung

Meinen Eltern gewidmet

Contents

Abstract	i
Kurzfassung	iii
Contents	vii
List of Figures	xi
List of Tables	xiii
1 Synopsis	1
1.1 Preface	1
1.2 Dissertation outline	2
2 Introduction	5
2.1 Gravitational-wave phenomenology in General Relativity	6
2.1.1 Linearized theory of gravitational waves	7
2.1.2 Effect of gravitational waves on free particles	9
2.1.3 Polarization of gravitational waves	11
2.1.4 Generation of gravitational waves	12
2.2 Direct observation of gravitational waves	14
2.2.1 Resonant-mass detectors	15
2.2.2 Laser-interferometric detectors	16
2.3 Gravitational-wave sources searched for with Earth-based detectors	22
2.3.1 Coalescing compact binaries	23
2.3.2 Gravitational-wave burst sources	24
2.3.3 Stochastic gravitational-wave background	25
2.3.4 Continuous gravitational-wave (CW) sources	26
3 Einstein@Home search for CW sources in S4 LIGO data	31
3.1 Overview and context	31
3.2 Data analysis strategy	33
3.3 Data selection and preparation	34
3.4 Data processing	36
3.4.1 BOINC workunit distribution and validation	36
3.4.2 Workunit design and gridding of search parameter space	41

3.4.3	The output of a workunit	44
3.4.4	Total computation time	45
3.5	Post-processing	46
3.5.1	Preparation and selection of candidate events	46
3.5.2	Number of cells in the post-processing coincidence grid	48
3.5.3	False alarm rate and the number of candidate events retained	49
3.5.4	Choice of false alarm probability and detection threshold	50
3.5.5	Shifting candidate-event frequencies to a fixed fiducial time	52
3.5.6	Search for coincident candidate events	53
3.5.7	Output of the coincidence search	59
3.6	Estimated sensitivity	62
3.6.1	Iteration method	62
3.6.2	Population of simulated sources	63
3.6.3	Determination of $2\mathcal{F}$ values for a single simulated source	63
3.6.4	Search sensitivity and estimated errors	64
3.6.5	Comparison with other search and upper-limit methods	66
3.7	Vetoing of instrumental line artifacts	67
3.7.1	Parameter space locations of instrumental lines	68
3.7.2	Fraction of parameter space excluded by the veto	69
3.8	Hardware-injected signals	73
3.8.1	Parameters of hardware injections	74
3.8.2	Duty cycle of hardware injections	76
3.8.3	Results from the hardware injections	76
3.9	Results	79
3.10	Conclusions	90
4	Einstein@Home search for CW sources in early S5 LIGO data	93
4.1	Overview and context	93
4.2	Data selection and preparation	95
4.3	Data processing	99
4.4	Post-processing	101
4.4.1	The post-processing steps	102
4.4.2	Construction of coincidence windows	102
4.4.3	Output of the post-processing	104
4.4.4	False alarm probability and detection threshold	105
4.5	Estimated sensitivity	107
4.6	Results	109
4.6.1	Vetoing Instrumental-noise lines	109
4.6.2	Post-processing results	111
4.7	Comparison with previous searches	115
4.8	Conclusions	117

5	Global correlations in the coherent statistic for CW detection	119
5.1	Overview and context	119
5.2	Coherent detection of continuous gravitational-wave signals	122
5.3	Matched-filtering detection statistic of a simplified signal model	124
5.3.1	The simplified signal model	124
5.3.2	The simplified matched-filtering detection statistic	127
5.4	Global-correlation hypersurfaces in parameter space	128
5.4.1	The global-correlation equations	128
5.4.2	The geometry of the global-correlation equations	130
5.4.3	Visualization of the global-correlation hypersurfaces	131
5.4.4	Validity estimation	136
5.5	Verifying the predictions by the global-correlation equations	140
5.5.1	Comparison of simulated signals with no detector noise	141
5.5.2	Comparison of simulated signals in real detector noise	143
5.6	Vetoing instrumental noise artifacts	150
5.7	Effects of the diurnal spinning motion of the Earth	153
5.8	Conclusions	161
6	New method for CW detection exploiting global correlations	163
6.1	Overview and context	163
6.2	Fully coherent CW matched filtering: \mathcal{F} -statistic	164
6.3	Hierarchical semi-coherent search strategies	165
6.3.1	\mathcal{F} -statistic based hierarchical searches	166
6.4	The GCT method	167
6.5	An implementation of the GCT method	169
6.5.1	The coherent stage	169
6.5.2	The incoherent combination stage	170
6.6	GCT versus Hough performance	171
6.6.1	Application to simulated data	171
6.6.2	Results	172
6.7	Conclusions	174
7	Summary and outlook	177
	Appendix	183
A	Search for CW sources in NAUTILUS data	185
A.1	Overview and context	185
A.2	Data analysis methods	186
A.3	Search procedure	190
A.4	Analysis of candidates	191

A.5	Upper limits	195
B	Search for tight binary radio pulsars in Arecibo radio data	199
B.1	Overview and context	199
B.2	Pulsars in circular orbits	200
B.3	Search methodology	201
B.4	Analysis of simulated signals	205
B.5	Current status	205
	References	209
	Acknowledgments	229
	Curriculum Vitae	231
	Publications	233

List of Figures

2.1	Gravitational-wave tidal deformation of a ring of free particles	12
2.2	The LIGO, GEO 600 and VIRGO gravitational-wave detectors	20
3.1	Strain amplitude spectral densities of the S4 LIGO detector data	38
3.2	Schematic overview of the Einstein@Home project	39
3.3	Four typical sky parameter-space search grids	44
3.4	Number of candidate events retained in the post-processing	48
3.5	Importance of the spin-down induced widening of frequency bands	53
3.6	Example sky grid and its projection onto the equatorial plane	58
3.7	Sky coincidence-window model for an exemplary frequency band	60
3.8	Sky coincidence-window model parameters versus frequency band	60
3.9	Estimated sensitivity of the Einstein@Home S4 search	65
3.10	Average fraction of sky excluded by the veto method	73
3.11	Results of the 10 hardware-injected CW signals	78
3.12	Spectrum of post-processing candidates with 7 or more coincidences	80
3.13	Sky-map of post-processing candidates with 7 or more coincidences	81
3.14	Results for a frequency band of pure Gaussian noise	82
3.15	Results for a frequency band containing a hardware injection	83
3.16	Results for a “quiet” frequency band of real instrumental data	84
3.17	Results for a frequency band polluted by instrumental noise	85
3.18	Sky-map of candidates passing the veto with 7 or more coincidences	91
3.19	Conclusion diagram of candidates discriminated by the veto method	92
4.1	Strain amplitude spectral densities of the cleaned input data	97
4.2	Sky coincidence-window model as function of frequency band	104
4.3	False alarm probabilities as function of frequency band	106
4.4	Estimated sensitivity of the Einstein@Home early-S5 search	108
4.5	Sky-maps of post-processing candidates with more than 7 coincidences	112
4.6	Spectrum of post-processing candidates with more than 7 coincidences	113
4.7	Comparison with recent PowerFlux search	116
5.1	Schematic drawing of intersecting global-correlation hypersurfaces	121
5.2	Mismatch contours of the simplified detection statistic	133
5.3	Contours of the global-correlation hypersurfaces	134
5.4	Contours of the global-correlation hypersurfaces (continued)	135

5.5	Estimating the number of relevant global-correlation hypersurfaces	138
5.6	Sky-maps of results from fully coherent 10-h searches	144
5.7	Sky-maps of results from fully coherent 1-day searches	145
5.8	Sky-maps of results from fully coherent 30-h searches	146
5.9	Sky-maps of results from fully coherent 2-day searches	147
5.10	Verification of global-correlation equations for a hardware injection	149
5.11	Global correlations produced by an instrumental-noise line	152
5.12	Phase-mismatch effects of the Earth's spin for the LIGO detectors	156
5.13	Effects of the Earth's spin on the detection statistic, example 1	157
5.14	Effects of the Earth's spin on the detection statistic, example 2	158
5.15	Effects of the Earth's spin on the detection statistic, example 3	159
5.16	Comparison of Earth's spin- and orbital-motion effects	160
6.1	Receiver operating characteristic curves	172
6.2	Probability of detection as function of source strain amplitude	173
7.1	Illustrative comparison of increase in volume of space probed	180
A.1	Amplitude spectrum estimation of the NAUTILUS data	191
A.2	Histogram of the candidate frequencies	192
A.3	Candidates with highest increase in signal-to-noise ratio	193
A.4	Results of the coincidence analysis among candidates	196
A.5	Probability distribution of the candidate $2\mathcal{F}$ -values	198
A.6	Upper limits based on the loudest candidates	198
B.1	Visualizing global correlations in the physical parameters	206
B.2	Analyzing software simulated radio binary pulsar signals	207

List of Tables

3.1	Data segments used in the Einstein@Home S4 search	35
3.2	Instrumental noise lines removed from in the input data	37
3.3	False alarm probabilities in four different 0.5 Hz frequency bands	51
3.4	Fractional volume of the sky excluded by the veto method	71
3.5	Parameters of the hardware-injected CW signals during the S4 run	75
3.6	Time overlap of the Einstein@Home data with the hardware injections	77
3.7	Predicted and measured results for the hardware injection	79
3.8	Post-processing candidates that have 10 or more coincidences	87
3.9	Candidates not excluded by the veto and having 9 or more coincidences	89
4.1	Data segments used in the Einstein@Home early-S5 search	96
4.2	Instrumental-noise lines <i>a priori</i> excluded from the data	98
4.3	Instrumental-noise lines <i>a posteriori</i> excluded from the results	110
4.4	The ten most significant post-processing candidates	114
5.1	Amplitude and phase parameters of the simulated signals	141
5.2	Verification of predictions by the global-correlation equations	142

Synopsis

1.1 Preface

This dissertation is based on four research publications [1, 2, 3, 4], which represent my genuine contribution. Each of these papers have been published in *Physical Review D*, except for [4] which has appeared in *Physical Review Letters*.

Chapter 3 of this dissertation refers to work published in:

- [1] LIGO Scientific Collaboration, “Einstein@Home search for periodic gravitational waves in LIGO S4 data”, *Physical Review D* **79**, 022001, (2009).

Chapter 4 presents material that has appeared in:

- [2] LIGO Scientific Collaboration, “Einstein@Home search for periodic gravitational waves in early S5 LIGO data”, *Physical Review D*, **80**, 042003, (2009).

Chapter 5 is based on the publication:

- [3] H. J. Pletsch, “Parameter-space correlations of the optimal statistic for continuous gravitational-wave detection”, *Physical Review D*, **78**, 102005, (2008).

Chapter 6 discusses work referring to:

- [4] H. J. Pletsch and B. Allen, “Exploiting global correlations to detect continuous gravitational waves”, *Physical Review Letters*, **103**, 181102, (2009).

Further completed and ongoing projects, which I have also made significant direct con-

tributions to, are described in Appendices A and B, based on references [5] and [6], respectively.

All software code developed in the course of this dissertation is released under the GNU General Public License version 2 [7], as part of either LAL, LALApps [8] or the Einstein@Home CVS archive [9]. The many computational tasks in the course of this dissertation have been done on LIGO Scientific Collaboration computational and data storage resources [10], while by far the largest fraction thereof has been carried out on the high-performance Computing Cluster ATLAS [11] at the Albert-Einstein-Institut in Hannover.

1.2 Dissertation outline

The central goal of this dissertation is the development and application of data analysis techniques to detect continuous gravitational waves from previously unknown sources through all-sky surveys, covering broadest possible ranges of the putative source parameter space.

Chapter 2 provides a basic introduction to the research area of gravitational-wave phenomenology. In the context of General Relativity, gravitational waves are briefly discussed in the linearized theory of gravity, along with a condensed description of the most basic properties of gravitational radiation. In addition, gravitational-wave detector technologies are summarized, which are currently in operation on Earth and planned for the future. Furthermore, the different types of anticipated gravitational-wave sources being searched for in data of current Earth-based detectors are compactly overviewed.

Chapter 3 presents an all-sky search for continuous gravitational waves in data from the fourth LIGO science run (S4) using the public distributed volunteer-computing project Einstein@Home [12]. The steps of data selection and preparation are discussed and a detailed description of the data processing follows. The search parameter space is described, followed by a detailed presentation of the different stages involved in the post-processing. An estimate of the search sensitivity is illustrated based on Monte-Carlo sim-

ulations. Furthermore, a veto method is described which has been implemented to discriminate parts of parameter space contaminated by instrumental-noise artifacts. Moreover, the results from analyzing narrow frequency bands containing hardware-injected simulated CW signals for validation purposes are shown and discussed. Finally the complete set of search results is presented and a brief conclusion is given.

Chapter 4 extends the search presented in the previous chapter based on similar methods while analyzing not only a larger volume, but also more sensitive data from LIGO's fifth science run (S5), in addition to using refined search setup. The data selection and preparation are exposed before describing the data processing of the main search work through Einstein@Home. This search deeply probes wide parts of parameter space with unprecedented sensitivity. A detailed discussion elucidates the different aspects of the post-processing methods developed and carried out in this analysis. As part of that, the conducted sensitivity estimation yields an improvement of a factor of about 3 in comparison with the previous analysis of S4 LIGO data described in Chapter 3. Furthermore, the discrimination of instrumental noise artifacts is explained and the final post-processing results are presented, followed by a concluding section.

Chapter 5 presents a comprehensive study of the global parameter-space correlations in the coherent detection statistic for continuous gravitational-wave searches. The experience accreted during the careful analysis of the search and post-processing results (subject to the previous chapters) has taught me much about the underlying parameter-space structure. This in turn has led to the novel insights described in this chapter. To investigate the global correlations in the coherent detection statistic, first simplified statistic is considered. This lays the foundation for obtaining the family of so-called "global-correlation equations", describing the "global maximum structure" of the detection statistic. The solution to each of these equations is a different hypersurface in parameter space, which are further investigated and graphically visualized. In addition, one direct application of these results is derived permitting the construction of a veto method which excludes false candidate events from instrumental noise artifacts. This veto technique is demonstrated using real detector data and has also been applied in the Einstein@Home searches described in Chapters 3 and 4. Finally, a brief discussion on the influence of the Earth's spinning motion to global parameter-space correlations in

comparison to the orbital motion is investigated, followed by a brief conclusion.

Chapter 6 introduces a new semi-coherent technique for detecting continuous gravitational-wave sources. In contrast to previous approaches, this method exploits the improved understanding of the global parameter-space correlations in the coherent detection statistic (as described in Chapter 5), to optimally solve the subsequent incoherent combination step. The advanced understanding of the global correlations yields new coordinates which enable to obtain the first analytical solution for the incoherent-step metric. Furthermore, an explicit implementation of the method is described and demonstrated using simulated data. The results are compared to previously available techniques, showing significant sensitivity improvements, which lead to an increase in the volume of space probed by more than two orders of magnitude at lower computational cost. Finally, a short concluding section outlines the future prospects of this search method.

Chapter 7 gives a brief summary and compares the different search techniques presented in this dissertation in the overall context of search sensitivity. Finally, prospects of ongoing and future work are sketched.

Appendices A and B describe further projects either directly concerning or closely related to continuous gravitational-wave data analysis, and which I have made relevant contributions to as a collaborative participant. In Appendix A, results from an all-sky continuous-wave search of NAUTILUS bar detector data is presented. Thereby, major aspects of the post-processing methods introduced in Chapter 3 have been applied. Appendix B outlines an ongoing effort to search for tight binary radio pulsars in Arecibo telescope data using a subordinate fraction of Einstein@Home's computational resources.

Introduction

Despite almost one century of history, the theory best-explaining gravitation – Einstein’s theory of General Relativity – is comparably less well-tested than other physical theories. The primary reason behind this is the fundamental weakness of the gravitational force. In consequence, the precision measurements required to test the theory were not possible at the time Einstein first published it [13] and even for many years later.

In the theory of General Relativity, gravitation has dynamical degrees of freedom which can be excited by the motion of matter. General Relativity predicts [14, 15], that a changing mass distribution can create perturbations in space-time which propagate away from the source at the speed of light. These freely propagating ripples in space-time are called *gravitational waves*.

Today, effects of the static relativistic gravitation beyond the Newtonian description have been well-studied by means of precision measurements observing the motion of the planets, their satellites and the principal asteroids. Dynamical gravitation has also been tested *indirectly* by detailed observations of the slow, secular decay of the Hulse-Taylor binary pulsar system PSR1913+16 [16, 17, 18]. The recent discovery of the first double pulsar system PSR J0737-3039A,B [19] enables further indirect tests of General Relativity to eventually higher precision [20]. However, the effects of dynamical gravitation (gravitational waves) have so far eluded *direct* observation with a controlled laboratory instrument.

The direct observation of gravitational radiation will provide a new astronomical tool to explore our cosmos. *Gravitational-wave astronomy* is expected to complement observations based on electromagnetic waves. While electromagnetic radiation couples

strongly to charges and thus is easy to measure, it can also be easily scattered or absorbed by matter between us and the emitting source. In contrast, gravitational waves couple very weakly to matter, which makes it harder to detect them, but it also means that the source information they carry reaches us substantially unaltered, even from the earliest moments of the universe.

The gravitational-wave spectrum is completely different from the electromagnetic spectrum. Electromagnetic waves are primarily emitted with short wavelength by individual charged particles from small regions, whereas gravitational waves are produced by an entire non-spherical bulk motion of mass, resulting in long wavelengths and immediate information about large-scale regions. In particular, the wavelength of electromagnetic waves is always smaller than the size of the emitter, while the gravitational-wave source is usually larger than the emitted wavelength. This implies that one cannot directly reconstruct a source image from gravitational-wave data. Therefore, gravitational-wave astronomy is much more like audio, “listening to sounds of the universe”.

2.1 Gravitational-wave phenomenology in General Relativity

This section provides an extremely condensed introduction to the gravitational-wave phenomenology in the framework of General Relativity. A more complete discussion may be found in standard textbooks [21, 22, 23, 24] as well as numerous review articles [25, 26, 27, 28, 29]. Henceforth, geometrized units $G = c = 1$ are used, but in places where numerical values are of interest, their SI values are considered to obtain order-of-magnitude estimates.

2.1.1 Linearized theory of gravitational waves

According to Wald [23] General Relativity is summarized as follows. Spacetime is a manifold on which there is defined a metric $g_{\mu\nu}$ of Lorentzian signature $(-, +, +, +)$. The curvature of $g_{\mu\nu}$ is related to the matter distribution in spacetime by Einstein's equation:

$$G_{\mu\nu} \equiv R_{\mu\nu} - \frac{1}{2}g_{\mu\nu}R = 8\pi T_{\mu\nu}, \quad (2.1)$$

where $G_{\mu\nu}$ is the Einstein tensor, $R_{\mu\nu}$ the Ricci tensor (resulting from the Riemann curvature tensor by contraction). The so-called curvature scalar R is the trace of the Ricci tensor, and $T_{\mu\nu}$ represents the stress-energy-momentum tensor.

In a situation, where the gravitational field is weak, spacetime is nearly flat. For example this is the case for a gravitational wave propagating through the interstellar space far away from the source. Correspondingly, the curvature tensor $g_{\mu\nu}$ may be written as a flat Minkowski metric $\eta_{\mu\nu}$, plus a "small" perturbation $h_{\mu\nu}$:

$$g_{\mu\nu} = \eta_{\mu\nu} + h_{\mu\nu}. \quad (2.2)$$

An adequate definition of "smallness" in this context is $|h_{\mu\nu}| \ll 1$, in coordinates where $\eta_{\mu\nu} = \text{diag}(-1, 1, 1, 1)$. This ansatz leads to the formalism of *linearized gravity*, approximating General Relativity in the weak-field situation. In Einstein's equation (2.1), $g_{\mu\nu}$ is substituted by Equation (2.2), and keeping only terms linear in $h_{\mu\nu}$. Thus, the linearized Einstein equation is found to be

$${}^{(1)}G_{\mu\nu} = {}^{(1)}R_{\mu\nu} - \frac{1}{2}\eta_{\mu\nu} {}^{(1)}R = 8\pi T_{\mu\nu}, \quad (2.3)$$

where the linearized Ricci tensor is given by

$${}^{(1)}R_{\mu\nu} = -\frac{1}{2}\partial^\alpha\partial_\alpha\bar{h}_{\mu\nu} + \partial^\alpha\partial_{(\nu}\bar{h}_{\mu)\alpha} - \frac{1}{2}\eta_{\mu\nu}\partial^\alpha\partial^\beta\bar{h}_{\alpha\beta}, \quad (2.4)$$

defining the *trace reverse*, $\bar{h}_{\mu\nu} = h_{\mu\nu} - \frac{1}{2}\eta_{\mu\nu}h$.

The line element ds , which describes the proper distance between nearby points in spacetime whose coordinates separation is infinitesimal dx^μ , is given by

$$ds^2 = g_{\mu\nu} dx^\mu dx^\nu = \eta_{\mu\nu} dx^\mu dx^\nu + h_{\mu\nu} dx^\mu dx^\nu. \quad (2.5)$$

The metric $g_{\mu\nu}$ describes how the proper distance between spacetime points is connected to the choice of coordinate system. Small changes in the coordinate system leave the

proper distance unchanged, one only changes the way of labeling the points. This freedom in the choice of coordinates (called *gauge freedom*) may be used to simplify the expression for the perturbation $h_{\mu\nu}$.

The propagation of gravitational waves is governed by the source-free ($T_{\mu\nu} = 0$), linearized Einstein equation, which becomes a set of second-order, linear differential equations

$$\partial^\alpha \partial_\alpha \bar{h}_{\mu\nu} = 0. \quad (2.6)$$

To seek solutions thereof, the so-called *transverse traceless* (TT) gauge¹, which is always possible for radiative perturbations about Minkowski space. Monochromatic plane waves² is used,

$$\bar{h}_{\mu\nu}^{\text{TT}} = H_{\mu\nu}^{\text{TT}} \exp(i k_\alpha x^\alpha), \quad (2.7)$$

where the amplitude $H_{\mu\nu}^{\text{TT}}$ is some constant tensor field and k_α is the wave vector, solve the source-free linearized Einstein equation if and only if $k^\alpha k_\alpha = 0$, and requiring the TT gauge conditions

$$k^\mu H_{\mu\nu}^{\text{TT}} = 0 \quad (4 \text{ equations}), \quad (2.8)$$

$$H_{0\nu}^{\text{TT}} = 0 \quad (4 \text{ equations}), \quad (2.9)$$

$$H_{\mu\nu}^{\text{TT}} \delta^{\mu\nu} = 0 \quad (1 \text{ equation}). \quad (2.10)$$

On more physical grounds, the three constraints above imply, $h_{\mu\nu}^{\text{TT}}$ is purely transverse, $h_{\mu\nu}^{\text{TT}}$ is purely spatial, and $h_{\mu\nu}^{\text{TT}}$ is tracefree. Thus, in TT gauge $h_{\mu\nu}^{\text{TT}} = \bar{h}_{\mu\nu}^{\text{TT}}$, there is no difference between the metric perturbation $h_{\mu\nu}^{\text{TT}}$ and the gravitational field $\bar{h}_{\mu\nu}^{\text{TT}}$.

The tensor $H_{\mu\nu}^{\text{TT}}$ is symmetric and thus has ten independent components. Thus, fixing the coordinates (by choosing the TT gauge) yields eight conditions on the ten components of $h_{\mu\nu}^{\text{TT}}$ (Equations (2.8) and (2.9) imply both that $H_{\mu 0}^{\text{TT}} k^\mu = 0$). Therefore, this leaves two linearly independent solutions for $H_{\mu\nu}^{\text{TT}}$, which are two dynamical degrees of freedom. These are identified as the two independent polarization states, h_+ and h_\times , of plane gravitational waves. One may orient the spatial axes so that the wave is traveling in the direction $k_\alpha = \omega(1, 0, 0, 1)$. In this chosen frame the components of $H_{\mu\nu}^{\text{TT}}$ in matrix

¹In the following, the superscript TT indicates that the TT gauge has been chosen.

²Here, the distance to the source is always assumed to be large compared to the wavelength; thus the incident gravitational waves are effectively plane.

form are

$$H_{\mu\nu}^{\text{TT}} = \begin{pmatrix} 0 & 0 & 0 & 0 \\ 0 & h_+ & h_\times & 0 \\ 0 & h_\times & -h_+ & 0 \\ 0 & 0 & 0 & 0 \end{pmatrix}. \quad (2.11)$$

Any arbitrary well behaved solution of the vacuum linearized Einstein is a superposition of these plane wave solutions. Thus any gravitational wave has only two independent components h_+ and h_\times , which correspond to the two independent gravitational-wave polarization states.

2.1.2 Effect of gravitational waves on free particles

In General Relativity, the notion of “gravitational force” is replaced by the concept that freely falling particles follow *geodesics* of spacetime. A geodesic of spacetime is defined by a curve whose tangent vector is parallel propagated along itself. A property of geodesics of a derivative operator arising from a metric is that they extremize the length of curves connecting given points (“straightest possible lines”).

For a given spacetime metric and a set of coordinates x^μ , the *geodesic equation* describes the geodesic trajectories by

$$\frac{d^2 x^\mu}{d\tau^2} + \Gamma^\mu_{\sigma\nu} \frac{dx^\sigma}{d\tau} \frac{dx^\nu}{d\tau} = 0, \quad (2.12)$$

where the curve is affinely parameterized by τ and $\Gamma^\mu_{\sigma\nu}$ denotes the affine connection (or Christoffel symbol). The parameter τ is the proper time as measured by an observer who is traveling along the geodesic. Assuming that the test particle’s motion is non-relativistic (much slower than the speed of light) implies $dx^\mu/d\tau \approx (1, 0, 0, 0)$. Thus, Equation (2.12) becomes

$$\frac{d^2 x^\mu}{dt^2} + \Gamma^\mu_{00} = 0. \quad (2.13)$$

with coordinate time $x^0 \equiv t$.

In linearized gravity (cf. Section 2.1.1) the Christoffel symbol is given by

$${}^{(1)}\Gamma^\mu_{\sigma\nu} = \frac{1}{2}\eta^{\mu\lambda}(\partial_\sigma h_{\nu\lambda} + \partial_\nu h_{\sigma\lambda} + \partial_\lambda h_{\sigma\nu}), \quad (2.14)$$

and so the Riemann tensor takes the following gauge-independent form:

$${}^{(1)}R_{\mu\nu\alpha}{}^{\beta} = \frac{1}{2} (\partial_{\nu}\partial_{\alpha}h_{\mu}{}^{\beta} + \partial_{\mu}\partial^{\beta}h_{\nu\alpha} - \partial_{\nu}\partial^{\beta}h_{\mu\alpha} - \partial_{\mu}\partial_{\alpha}h_{\nu}{}^{\beta}). \quad (2.15)$$

Thus, choosing the TT gauge yields ${}^{(1)}\Gamma^{\mu}{}_{00} = 0$. Hence, one finds that $d^2x^{\mu}/dt^2 = 0$. This means that in TT gauge the coordinate location of a slowly moving and freely falling particle is unaffected by the passage of the gravitational wave, because the chosen coordinates effectively move with the wave.

Therefore, to observe the effect of gravitational waves on freely falling test particles, in General Relativity one has to relate gauge-invariant quantities to physical observables [30]. Hence, at least two test particles have to be considered, because the incident gravitational wave causes the *proper distance* between them to oscillate, though leaving the their *coordinate distance* constant.

So consider two freely falling nearby particles are described by neighboring geodesics. If ξ^{μ} denotes the displacement to the infinitesimally nearby geodesic (called the *deviation vector*), then its relative acceleration is related to curvature by the Riemann tensor, leading to the equation of *geodesic deviation*:

$$\frac{d^2\xi^{\mu}}{d\tau^2} = R_{\sigma\lambda\nu}{}^{\mu} \frac{dx^{\sigma}}{d\tau} \frac{dx^{\lambda}}{d\tau} \xi^{\nu}. \quad (2.16)$$

Now consider a situation where the two particles are initially separated by ξ^{μ} and nearly at rest. In this context “at rest” means staying at constant coordinate position, which has itself no invariant geometrical meaning. By looking at their physical separation (proper distance) rather than the coordinate separation the metric has to be invoked. If the distance ξ^{μ} is significantly smaller than a wavelength (long-wavelength approximation), the equation of geodesic deviation may be used.

In linearized gravity, and assuming again the case of slowly moving particles, Equation (2.16) simplifies to

$$\frac{d^2\xi^{\mu}}{dt^2} = {}^{(1)}R_{\nu 00}{}^{\mu} \xi^{\nu}. \quad (2.17)$$

By choosing again the TT gauge, one obtains for the relevant components of the linearized Riemann tensor,

$${}^{(1)}R_{j00k}^{\text{TT}} = \frac{1}{2} \frac{\partial^2}{\partial t^2} h_{jk}^{\text{TT}}. \quad (2.18)$$

Taken together, Equation (2.17) and Equation (2.18) yield

$$\frac{d^2 \xi^j}{dt^2} = \frac{1}{2} \eta^{j\ell} \xi^k \frac{\partial^2 h_{\ell k}^{\text{TT}}}{\partial t^2}, \quad (2.19)$$

This implies for a gravitational wave propagating along the 3-direction, the deviation vector of two particles with initial separation L along the 1-axis, with $\xi^\mu = (0, L, 0, 0)$, obeys

$$\frac{\partial^2 \xi^1}{\partial t^2} = \frac{L}{2} \frac{\partial^2}{\partial t^2} h_+, \quad \frac{\partial^2 \xi^2}{\partial t^2} = \frac{L}{2} \frac{\partial^2}{\partial t^2} h_\times. \quad (2.20)$$

Likewise, two particles separated in the 2-direction, with $\xi^\mu = (0, 0, L, 0)$, follow

$$\frac{\partial^2 \xi^2}{\partial t^2} = \frac{L}{2} \frac{\partial^2}{\partial t^2} h_\times, \quad \frac{\partial^2 \xi^1}{\partial t^2} = -\frac{L}{2} \frac{\partial^2}{\partial t^2} h_+. \quad (2.21)$$

This tidal effect is the basis of all present detectors. Thus, in principle, it is possible to detect gravitational radiation by carefully tracking the separation of the two test masses suspended freely from supports, e.g. by the use of laser beams [31, 32, 33].

2.1.3 Polarization of gravitational waves

The previous section has described the effect to the gravitational wave on the separation between the two test particles: As h_{jk}^{TT} oscillates, the proper distance does, too. Gravitational-wave detectors are designed to be sensitive to these tidal displacements of their components caused by passing gravitational waves.

This effect of altering the proper distance between two free particles depends on the direction of their separation. To illustrate the effect in all directions, consider a circular ring of free test particles in the transverse plane, surrounding another free particle at the center, as illustrated in Figure 2.1. As a plane gravitational wave with “+” polarization ($h_+ \neq 0, h_\times = 0$) passes through, the ring, as measured initially in the proper reference frame of the central particle, is tidally deformed into an ellipsoidal shape of the same area, oscillating back and forth in the way shown in Figure 2.1a. In contrast, the tidal deformation by a wave of “ \times ” polarization ($h_+ = 0, h_\times \neq 0$) is shown in Figure 2.1b. If $h_+ = h_\times \neq 0$, the waves are circularly polarized, and the case $h_+ \neq h_\times \neq 0$ is referred to as elliptical polarization.

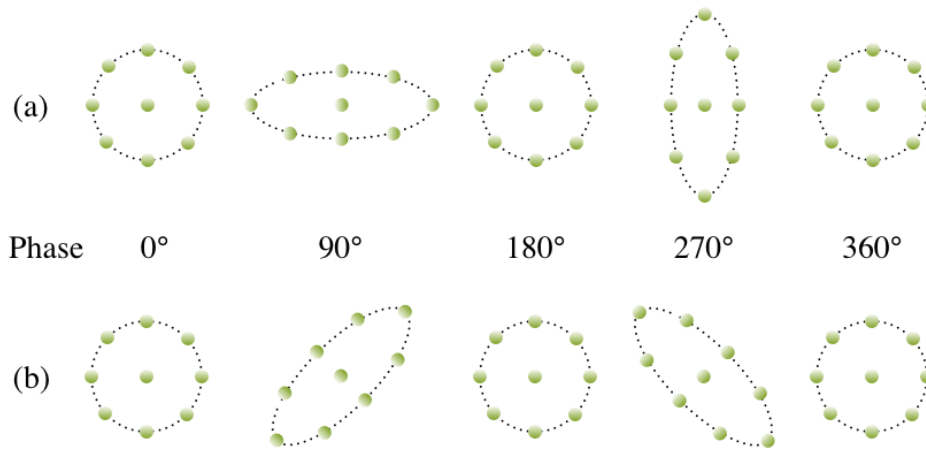


Figure 2.1: Tidal deformation of a circular ring of free particles in the transverse plane of an incident gravitational wave. In case (a), the effect of a gravitational wave with purely “+” polarization ($h_+ \neq 0$, $h_\times = 0$), is shown and in (b) the wave has “ \times ” polarization ($h_+ = 0$, $h_\times \neq 0$). In both cases, the individual snapshots are taken at a step size of 90° in phase.

From Figure 2.1 one can also see, that at any moment of time, a gravitational wave is invariant under rotation of 180° about its direction of propagation. In fact, this symmetry of the waves is related to the spin-2 character of the gravitational field. In general, a classical radiation field of a spin- S particle is invariant under rotation of $360^\circ/S$ about its direction of propagation. For comparison, in the case of electromagnetic waves the analogous angle is 360° , because $S = 1$, being the spin of the photon.

2.1.4 Generation of gravitational waves

In presence of a source the solutions of the linearized Einstein equation can be analyzed in the slow-motion approximation. For any source of size R and velocity v inside the source region, the wavelength λ of the emitted radiation is approximately $2\pi R/v$. The slow-motion condition, $v \ll 1$, then requires that $2\pi R/\lambda \ll 1$, confining the source to a small region surrounding it. This condition is satisfied by all gravitationally bound systems, which are the majority of astrophysical sources. The slow-motion limit allows a multipole expansion, linking orders in the expanded metric with those in the expanded

source terms. At leading order, the gravitational-wave amplitude h_{jk}^{TT} , at distance r (outside the source, $r > R$) is related to the matter distribution of the source according to the “quadrupole formula” [22]:

$$h_{jk}^{\text{TT}}(t, \mathbf{x}) = \frac{2}{r} \frac{d^2}{dt^2} Q_{jk}^{\text{TT}}(t - r), \quad (2.22)$$

where Q_{jk}^{TT} denotes the transverse-traceless part of the quadrupole moment,

$$Q_{jk}^{\text{TT}} = P_{j\ell} Q_{\ell m}^{\text{TT}} P_{mk} - \frac{1}{2} P_{jk} Q_{\ell m}^{\text{TT}} P_{\ell m}, \quad (2.23)$$

$$Q_{jk} = \int d^3x \rho(t, \mathbf{x}) \left(x_j x_k - \frac{1}{3} \delta_{jk} \right), \quad (2.24)$$

$$P_{jk} = \delta_{jk} - \hat{n}_j \hat{n}_k. \quad (2.25)$$

Applying the projection operator P_{jk} to Q_{jk} recovers the TT gauge, transverse to the direction of motion of the wave, whose unit vector is given by $\hat{n}_j = x_j/r$.

Equation (2.22) shows that for spherically symmetric motions no gravitational-wave emission takes place, because in such cases the quadrupole moment is constant. A rapidly rotating neutron star only emits continuous gravitational waves if the star is somewhat deformed from axial symmetry, for example having a small mountain. Possible mechanisms which could support the building of such neutron-star deformations along with other continuous emission mechanisms are discussed in Section 2.3.4.

In electrodynamics, the lowest multipole radiating is an electric dipole moment and there is no monopole radiation because of charge conservation. Analogously, in the gravitational counterpart, there is no radiation from mass monopole, mass dipole and angular momentum due to conservation laws of mass, momentum and angular momentum. The quadrupolar nature of gravitational radiation in fact follows from a general theorem [34] as a property of classical radiation fields whose quantum mechanical particles have zero rest mass and integer spin S . When expanding the radiation field into multipole moments, the lowest non-vanishing order moment is S . For slowly moving sources the lowest non-vanishing multipoles dominate, thus gravitational radiation ($S = 2$) is quadrupolar, and electromagnetic radiation ($S = 1$) is predominantly dipolar.

From Equation (2.22) a rough estimate of the gravitational-wave amplitude from an astrophysical source may be obtained. Components of $d^2/dt^2 Q_{jk}^{\text{TT}}$ have a typical value of $E_{\text{kin}}^{\text{non-symm}}$, corresponding to twice the non spherically-symmetric part of the kinetic

energy inside the source. Restoring G and c in Equation (2.22) yields the scale factor G/c^4 in the right-hand side, thus:

$$h_{jk}^{\text{TT}} \lesssim \frac{2G E_{\text{kin}}^{\text{non-symm}}}{c^4 r}. \quad (2.26)$$

If one sets $E_{\text{kin}}^{\text{non-symm}}$ equal to one solar mass, $E_{\text{kin}}^{\text{non-symm}}/c^2 \approx 1M_{\odot}$ and if one assumes the source location at an inter-galactic distance (e.g. the Virgo cluster, $r \approx 18$ Mpc), the components of h_{jk}^{TT} are bound to values of order $h_{jk}^{\text{TT}} \lesssim 10^{-21}$. While this number represents an upper-limit estimate, most sources will radiate with significantly smaller gravitational-wave amplitudes.

Similarly, one may estimate an upper limit for gravitational-wave frequencies. The Schwarzschild radius $R = 2GM/c^2$ (in SI units) represents a lower boundary on the size R of a gravitational-wave source, because it would otherwise be smaller than the horizon size for its mass. Arguing that a source cannot emit gravitational waves at periods shorter than the light travel time around its circumference $4\pi GM/c^3$ yields a maximum frequency of

$$f \lesssim \frac{c^3}{4\pi GM} \approx 10^4 \text{ Hz} \times \left(\frac{M_{\odot}}{M} \right). \quad (2.27)$$

As will be discussed later, Earth-based gravitational-wave detectors are in principle sensitive to frequencies in the range of $1 - 10^4$ Hz. Lower frequencies are only detectable with spaceborne instruments. Thus, the above relation implies that no system with a mass larger than about $10^4 M_{\odot}$ is capable of generating gravitational quadrupole radiation measurable in the sensitive frequency band of Earth-based detectors.

2.2 Direct observation of gravitational waves

Direct observation of gravitational waves relies on their tidal nature. As described earlier in Section 2.1.2, for detection one has to measure the gravitational tidal force by monitoring the relative acceleration of test masses, or the periodic tidal deformations of extended bodies. A gravitational wave propagating in flat spacetime, generates periodic

perturbations (as illustrated in Figure 2.1), which are described in terms of the Riemann tensor measuring the curvature of spacetime.

In contrast to telescopes for electromagnetic radiation, gravitational-wave detectors are practically omni-directional due to a wide quadrupolar antenna-pattern and they measure a single scalar function of time. Therefore, they are closely analogous to acoustic microphones rather than optical telescopes.

2.2.1 Resonant-mass detectors

If the masses are not in free motion, but connected by a solid piece of matter, the gravitational tidal forces then stress the material. Thus, a solid bar is set into oscillation by these oscillating stresses. When the frequency of the gravitational wave is near the resonant frequency of the bar, the oscillations produced by the wave can be detected. The material used for bar detectors is typically material of high Q -factor (rate at which a vibrating system dissipates energy).

This was the first ground-based detector scheme explored and pioneered by Joseph Weber at the University of Maryland and at the Argonne National Laboratory in the 1960s [35]. He and his colleagues looked for tidal strains in cylindrical aluminum bars (with resonant frequency near 1600 Hz) held at room temperature and well isolated from ground vibrations and acoustic noise in the laboratory [36, 37]. Coincident excitations of his detectors separated by about 10^3 km were reported at a rate of approximately one event per day. Though similar experiments with improved sensitivity carried out thereafter in other laboratories were unable to reproduce his results, which makes it therefore seem unlikely that Weber had observed gravitational-wave signals [25].

Nonetheless, Weber's bar-type detectors have been developed further [38] based on improved bar materials and cryogenic technology. Current resonant-bar detectors include the ALLEGRO detector [39] in Louisiana, USA, the EXPLORER detector [40] in Geneva, Switzerland, the ultra-cryogenic NAUTILUS detector [41] in Frascati, Italy, the AURIGA detector [42] in Padova, Italy, NIOBE at the University of Western Australia in Perth [43] and the spherical prototype called MiniGRAIL [44] in Leiden, Netherlands. However, resonant-mass detectors still have only a narrow detection bandwidth

near their resonant frequency, which is mostly around 900 Hz.

The most important noise sources in bar detectors include thermal noise, sensor noise and quantum noise. Thermal noise is due to Brownian motion of the detector atoms. The sensor noise is related to the transducer employed to convert the bar's mechanical energy into electrical energy. An amplifier increases the signal level to record it. Both of these components introduce additional noise, limiting the sensitivity to frequencies near the resonance frequency. The quantum limiting noise is due to the uncertainty principle. Alternative detector designs using nested cylinders or spheres, or masses designed to sense multiple modes of vibration might help to improve sensitivity [45].

2.2.2 Laser-interferometric detectors

The idea of using a Michelson interferometer, consisting of a 50/50 beam splitter and two end test masses (mirrors), to directly observe gravitational radiation has been discovered by several groups independently [46, 47, 48], leading to the first prototype detector [49, 50].

The laser-interferometric detector design [31, 32, 33] offers very high sensitivities over a wide range of frequencies. It involves test masses that are widely separated and freely suspended as pendulums to isolate against seismic noise and reduce the effects of thermal noise. If the difference in arm length is held such that the light returning from the end test masses destructively interferes at the beamsplitter (the dark fringe" operating point) then nominally no light exits the beamsplitter in the direction of the output photodiode. Gravitational waves incident normal to the interferometer plane will produce differential changes in the distance between the corner and end mirrors. For wavelengths much larger than an interferometer arm, the corresponding changes in the fringes are proportional to the tidal effects of the impinging gravitational wave. Thus, a differential strain $h(t)$ on the two arms is produced and light exits the beamsplitter and produces measurable current at the output photodiode.

2.2.2.1 Detector response to gravitational waves

In the literature, the measured strain $h(t)$ at the detector due to the effect of an incident gravitational wave, is derived in two flavors (for example see [22, 24, 25, 51, 52, 27]). The first one relies on the vanishing proper length along the null geodesic (of the light) separating the ends of each detector arm. The second is based on geodesic deviation to calculate the changing distance between the end mirrors and the beam splitter. Finn [53] has recently pointed out some issues in these “standard” derivation of the interferometric detector response function, which however fortuitously leave the classic results unchanged. As Section 2.1.2 has already introduced the concept of geodesic deviation, hence the second approach to obtain the detector response is briefly summarized in the following.

Although the interferometer arm length L is large (on a few-km scale), it is small compared to the wavelength of the gravitational radiation to be detected [54], $fL \ll 1$ (recall $c = 1$), where f is the gravitational-wave frequency. Therefore, during a single trip of a light ray in one arm, the components of $h_{\mu\nu}$ can be regarded as constant.

The deviation vector ξ^μ connecting the coordinate-fixed worldlines of the beam splitter and the end mirror, which are considered as nearby geodesics, satisfies the geodesic deviation equation (2.16) (cf. Section 2.1.2). The change in the length of ξ^μ is identified as the variations in the light travel time between the beam splitter and the end mirror. Suppose, the beam splitter and the end mirror are at rest relative to each other before the wave arrives, $\xi^j = L^j$, when $h_{\ell k}^{\text{TT}} = 0$. Then integrating Equation (2.19) twice yields

$$\xi^j = L^k \left(\delta_{jk} + \frac{1}{2} h_{jk}^{\text{TT}} \right). \quad (2.28)$$

Note that the gravitational wave acts as a “strain” (usually denoted h) on the detector, producing fractional length changes: $h = 2\delta L/L$, where δL is the distance change between the beamsplitter and the end mirrors. In interferometric gravitational-wave detectors the observable is the difference in phase of the light wavefronts inbound at the beam splitter. The changes in the proper distance calculated above are directly related to the phase shift $\delta\varphi$ accumulated by a photon on a round trip in the interferometer arm when a gravitational wave is present. This phase shift is $\delta\varphi = 4\pi \delta L/\lambda$, where λ is the light wavelength.

The gravitational wave induces antisymmetric length changes of the (usually right-angled) interferometer arms. On the other hand, the laser-light phase noise will enter symmetrically, simply because the same laser state is feed into the arms via the beam splitter. This is the major reason for the L-shaped detector layout.

It is conventional to express the observable in terms of the differential changes of the interferometer arms: The measured scalar strain $h(t)$ due to the effect of a gravitational wave h_{jk}^{TT} is given by

$$\begin{aligned} h(t) &= \frac{1}{2} (e_1^j e_1^k - e_2^j e_2^k) h_{jk}^{\text{TT}} \\ &= F_+(t) h_+(t) + F_\times(t) h_\times(t), \end{aligned} \quad (2.29)$$

where e_1^j and e_2^l represent the spatial unit vectors along the first and the second interferometer arm, respectively. $F_{+,\times}(t) \in [-1, 1]$ are the so-called antenna-pattern functions, which describe the sensitivity of the detector with respect to the $+$ and \times polarization. They depend on the direction to the source, the polarization angle of the wave, and on the detector's orientation. For Earth-based detectors, $F_{+,\times}$ are periodic functions over one sidereal day, due to the spinning motion of the Earth [55].

2.2.2.2 Noise sources

A primary goal of the experimentalists involved in commissioning the laser-interferometric detectors is the reduction of noise. The sensitivity at low frequencies (< 50 Hz) is limited by seismic noise, at intermediate frequencies (50 to 150 Hz) by thermal noise, and at high frequencies (> 150 Hz) by laser shot noise. The most important noise sources for the initial Earth-based interferometric detectors are described in the following.

Seismic noise mostly occurs at low frequencies and decreases with frequency as $1/f^2$. These influences occur also as the Earth is in motion because of seismic and volcanic activities, because of ocean waves hitting the shores, because of the wind, and because of tidal forces involving the moon. Multi-stage pendulums and other isolation systems have been development to reduce the seismic noise [56].

Thermal noise occurs as vibrations of the suspension elements. The magnitude of these motions depends on the temperature. The steel wire suspending the mirror is at room temperature and thermal motion of the particles in the wire produce motion of the

mirror and change the arm length. Thermal noise can also drive the normal modes of the mirrors. By using high- Q material for the suspension elements, one can restrict the thermal-noise oscillations to a small bandwidth. Thermal noise can also be produced when (partly) transmissive components of the interferometer absorb small amounts of light power, which raises their temperature and changes their refraction index (“thermal lensing” effects).

Photon shot noise causes statistical fluctuations of the number of photons in the input beams during the measurement. Using more photons (higher light power) improves the signal error. As will be discussed below, currently employed light-recycling techniques overcome this problem and allow to increase light power to build up in the interferometer arms.

Quantum effects like shot noise also have a conjugate noise. When increasing the laser power to reduce the shot noise, the position sensing precision improves and eventually approaches the Heisenberg principle. Modifying the quantum state of the light, by so-called “squeezing” of the Heisenberg uncertainty ellipse to reduce the effect of this uncertainty on the variable being measured, at the expense of its (unmeasured) conjugate. Recent progress in implementing the squeezing technique have been reported in [57].

Gravity gradient noise is due to changes in the local Newtonian gravitational field on time scales of the measurements. Environmental noise sources, such as seismic waves are accompanied by changes in the gravitational field, and changes in air pressure are accompanied by changes in air density. The gravity-gradient noise spectrum falls steeply with increasing frequency, so for first-generation interferometers this is not a problem, but may limit the performance of advanced detectors.

2.2.2.3 Current detectors

Today, laser-interferometric gravitational-wave detection is pursued with two complementary approaches: space-based and Earth-based detectors. A space-based detector eludes the seismic excitations on Earth and can employ a long arm length of order 10^{10} m. Thus it is most sensitive in the frequency band of about $10^{-4} - 10^{-1}$ Hz. In contrast, an Earth-based detector is limited at low frequencies of a few Hertz by the gravity gradient and seismic noise, the most sensitive frequency range of about $10 - 10^3$ Hz. This thesis



Figure 2.2: Aerial view of the 4-km LIGO detectors located in in Hanford, Washington, USA and in Livingston, Louisiana, USA, the GEO 600 detector in Hannover, Germany, and the 3-km VIRGO detector in Pisa, Italy.

is primarily devoted to the analysis of ground-based detector data, hence the following elaborates on the laser-interferometric detectors on Earth.

All around the globe, a network of interferometer detectors is currently operational. These include the three kilometer-scale instruments of LIGO [58, 54] (two with 4-km and 2-km arm length are located in a common vacuum tube in Hanford, Washington, USA and one of 4-km arm length in Livingston, Louisiana, USA), the 3-km-long VIRGO detector [59, 60] (operated by a French-Italian collaboration) in Pisa, Italy, the GEO 600 detector [61, 62] (operated by a British-German collaboration) in Hannover, Germany and the TAMA 300 detector [63] in Tokyo, Japan.

The optimal arm length is one quarter of the gravitational wavelength (so that the light spends half a period in the arms). For instance, a gravitational wave at 150 Hz has a 2000-km wavelength. But the LIGO interferometers have only arms of 4-km length. The detectors achieve a roughly 100 times longer effective arm length by using Fabry-Perot

cavities. These are formed by the input test masses and end test masses, to store the light longer in the arms. In addition, the power-recycling technique [64] makes use of the fact that the interferometer, when operated at the dark fringe, acts as a compound mirror for the input laser light. By installing a power recycling mirror before the beamsplitter an optical cavity is formed which increases the input laser power by a factor of about 40. This is important because the sensitivity of the detector in the shot-noise-limited regime increases as the square root of the input laser power.

LIGO, VIRGO and TAMA 300 detectors are configured as power-recycled Michelson interferometers with Fabry-Perot arm cavities. The GEO 600 detector does not use Fabry-Perot arm cavities, but instead a combination of folded arms and dual-recycling (power recycling and signal recycling [65]). Due to the better seismic isolation system, the VIRGO instrument has a better low-frequency sensitivity than the LIGO detectors, and an overall sensitivity comparable to the LIGO detectors. Despite the shorter arm length of 600 m of GEO 600, the employed advanced technologies (such as signal recycling) enable to achieve a narrow-band sensitivity comparable to that of the km-scale instruments. TAMA 300 has an arm length of 300 m and was the very first large-scale interferometer in operation. To exclude acoustic disturbances and fluctuations in the local refraction index, the interferometers operate in ultra-high vacuum at pressures below about 10^{-13} bar.

2.2.2.4 Future detectors

There are plans to construct further long-baseline instruments. The AIGO detector is planned to be similar to LIGO and VIRGO, and should be located in Western Australia [66]. This location, being far from the existing detectors, would improve global detector network sensitivity with respect to sky position reconstruction [67] and help determining the polarization of the gravitational-wave observations.

The initial LIGO detectors have recently finished a two-year-long data run during which a full year of triple-coincidence data was collected at design sensitivity. A large period of this run was also coincident with the data runs of GEO 600 and VIRGO. The joint data analysis from this international network of detectors is ongoing. Currently, the two 4-km LIGO detectors (H1 and L1) were taken offline to implement a number of incremental upgrades that, based on knowledge of the noise sources limiting initial

LIGO, will improve their sensitivity by roughly a factor of two. This program is called Enhanced LIGO [68, 69] and data recording is expected to start in July 2009.

In parallel, construction of Advanced LIGO [70], a major upgrade to LIGO, has started. Installation and commissioning of Advanced LIGO hardware at the LIGO sites will begin at the end of the Enhanced LIGO data run in 2011. Once fully commissioned, the Advanced LIGO detectors should be ten times as sensitive as the initial LIGO detectors. Therefore, Advanced LIGO is expected to guarantee gravitational wave detection [71]. Further second-generation interferometric detectors, such as Advanced LIGO, comprise Advanced VIRGO [72] and GEO-HF [73] are also expected to be operational in a few years with significantly improved sensitivity. Another km-scale cryogenic interferometer, called LCGT [74], is also built in Japan.

2.3 Gravitational-wave sources searched for in the data of Earth-based detectors

The idea of setting up a laboratory generator of gravitational waves for direct observations is a rather non-promising one. Following an example given in [24], consider a man-made gravitational-wave generator consisting of two 10^3 kg masses held 10 m apart by a light rigid beam rotating about its center with a frequency of 10 Hz. To estimate the gravitational-wave amplitude based on Equation (2.26), all the motion is considered non-spherical, such that $E_{\text{kin}}^{\text{non-symm}}/c^2$ is approximately 10^8 kg. The source distance r must be at least one wavelength in order to detect the gravitational waves rather than the nearby Newtonian gravity field. The generator emission will be at twice the rotation frequency of 20 Hz as the mass distribution is symmetric about the rotation axis, and the corresponding wavelength will be 1.5×10^7 m. Given these values the gravitational wave amplitude h_{jk}^{TT} is estimated as 10^{-43} , which is about 20 orders of magnitude below the level current ground-based instruments are able to detect. This shows that human scale objects are not promising sources of measurable gravitational radiation.

Candidates bearing good prospects for emission of gravitational waves detectable by

an Earth-based observer can only be massive astrophysical objects. In the following a brief summary is given of the most promising gravitational-wave source for Earth-based detectors. A more extensive source overview may be found in [25].

The analysis efforts of ground-based detector data basically fall into four principal categories based on the different class of gravitational-wave sources one searches for: *coalescing compact binaries*, *gravitational-wave burst sources*, *stochastic gravitational-wave background*, and *continuous gravitational-wave sources*. This thesis is primarily concerned with searches for previously unknown continuous gravitational-wave sources. However, in what follows a brief overview of all types of gravitational-wave signals currently searched for in ground-based detector data is given. Only now technology has reached a stage where the detectors are built with a sensitivity required to observe such interesting sources can be envisaged [75].

2.3.1 Coalescing compact binaries

Compact binaries coalescence (CBC) sources are generated during the final evolution stage of binary systems where the two compact objects merge into one. Several searches for gravitational waves from coalescing compact binary systems have been performed [76, 77, 78, 79, 80, 81, 82, 83] for systems of two neutron stars (BNS), two black holes (BBH), neutron star and black hole (NSBH), and primordial black holes (PBH). The gravitational wave emission from some parts of the life cycle of compact binary systems is relatively well-modeled, and the expected frequencies of some systems are near the most sensitive frequency band of Earth-based interferometric gravitational-wave detectors [84].

CBC sources are expected to emit gravitational radiation in three distinct stages: the inspiral stage, the merger stage, and the ringdown stage. During the inspiral stage, both objects of the binary system are well-separated in space and the system evolves in quasi-circular orbits decaying due radiation reaction. If the orbits are eccentric initially, they are circularized quickly through gravitational-wave emission. In this evolution, the two bodies merge into each other producing a single excited Kerr black hole. In the ring down stage, the excited black hole loses energy via gravitational-wave emission and finally forms a Kerr black hole. In the case of a BNS, a hypermassive neutron star might

be created in the merger stage which eventually will collapse to a black hole [85].

When the binary-system objects spiral inward, their gravitational waves sweep upward in frequency and amplitude. Such a waveform is referred to as a *chirp*. The waveforms at the merger stage can be more complex, depending on the details of the merger, while the signal from the ring down stage can be decomposed as a superposition of exponentially damped modes.

So-called “standard candles” are systems of known intrinsic luminosity. Therefore, their distance can be deduced, so that the apparent luminosity of a particular system is measured. Gravitationally radiating binaries have this property, if one can measure the effects of radiation reaction on their orbits [86, 87]. Analog to the “standard candles” of electromagnetic astronomy, these systems are named “standard sirens”. Any binary (even with ellipticity and extreme mass ratio) encodes its distance in its gravitational wave signal. This also permits to measure the Hubble constant [86] or other cosmological parameters from observing coalescing compact object binaries. However, this becomes of more interest for the space-borne detectors such as LISA, because observations of BBH binaries could yield an independent measurement of the acceleration of the universe [87, 88].

2.3.2 Gravitational-wave burst sources

Gravitational-wave burst sources emit a short-duration transient burst of gravitational radiation. Possible mechanisms to generate such burst events are thought to happen during the non-spherical core-collapse of highly evolved massive stars in a supernova, accretion induced collapse of white dwarfs, and Gamma ray bursts (GRBs). As the physics is largely unknown for these cases, or too complex as yet to allow computation of detailed gravitational waveforms. Thus these sources are generally categorized as “unmodeled burst sources”.

Simulations of gravitational collapse are of current interest in numerical astrophysics [89], because in most cases predictions for the energy and spectral characteristics of the emitted gravitational waves can be made [90, 91, 92, 93]. However, such predictions are still far from the precision needed to build reliable signal template waveforms. Simula-

tions suggest that the gravitational waves from a typical supernova are produced in the frequency range of about 200 to 1000 Hz.

The collapse events are typically accompanied by electromagnetic and neutrino emission so some advantages of triggered searches can be reaped. However, the events often go unnoticed until some point late in the light curve, which makes extrapolation back to the collapse event difficult. Detection of gravitational waves from a supernova event would shed light on these events, as it would provide information from the core impossible to obtain otherwise, even from neutrino observations.

Searches for gravitational burst sources [94, 95, 96, 97, 98, 99, 100, 101, 102, 103, 104, 105] come in two fashions: all-sky searches and externally triggered searches. An all-sky search is carried out over long stretches of data with no prior information. Externally triggered searches use observations, from gamma ray satellites, telescopes or neutrino detectors for example, to drastically reduce the parameter space of the search.

2.3.3 Stochastic gravitational-wave background

Stochastic gravitational waves are a superposition of numerous discrete systems which can be either confusion noise stochastic backgrounds or primordial stochastic backgrounds.

The primordial stochastic backgrounds are relic gravitational waves from the early evolution of the universe [106]. The background radiation from the Big Bang is very weak, but observing it is of great interest because it can shed light on the laws of physics at extremely high energies as it comes nearly unaltered from as early as 10^{-30} s. Whereas photons began free streaming about 10⁵ years after the Big Bang when electrons and protons condensed into atomic hydrogen, the last scattering of gravitational waves occurred about 10^{-25} s after the Big Bang [107].

Alternatively, a number of deterministic signals from astrophysical sources can superpose to generate an apparent stochastic background. This astrophysical stochastic background can be due to a collection of various sources such as rotating neutron stars [108], binary-neutron stars [109], supernovae [110] or low-mass X-ray binaries [111].

In a single detector, random radiation cannot be distinguished from instrumental

noise, at least not for short observation times. But over the course of a year, as the detector changes its orientation, the noise from this background should rise and fall in a systematic way, allowing it to be identified in case the random field is produced by an anisotropically-distributed set of astrophysical sources. A much better analysis strategy is cross-correlation between two or more detectors after accounting for the different antenna patterns [112, 113, 114, 115]. In doing cross-correlation one detector data stream serves as a template for the other. So if the detector data match a correlation larger than expected is obtained. This technique works well as long as the wavelength of the gravitational waves is longer than the separation between the detectors. Otherwise time delays for waves reaching one detector before the other degrade the correlation. Because one detector has as much noise superimposed on its template as the other detector, the sensitivity of this method (amplitude signal-to-noise ratio of the correlated field) increases only with the fourth root of observing time, which is different from matched-filtering that is characterized by the gain in signal-to-noise ratio with the square root of observation time [116, 117].

2.3.4 Continuous gravitational-wave (CW) sources

Continuous gravitational-wave sources are defined by the emission of quasi-monochromatic signals with a slowly varying intrinsic frequency over long periods of time. CW emitters are thought to consist of compact objects, such as neutron stars, in isolated or (more rare) binary systems. However, gravitational radiation from the binary motion is anticipated to come in a lower frequency range where space-based detectors are sensitive, such as the planned LISA mission [118, 119, 120]. Therefore, in the following, CW emission from spinning stars are discussed, because these are expected to produce CW signals in the most sensitive frequency band of Earth-based detectors. But still, a spinning and CW-emitting object can be part of a binary system, in which the binary motion will Doppler-modulate the CW signals.

2.3.4.1 Possible emission mechanisms

Isolated, rapidly rotating compact objects are thought to emit CW signals in the frequency band $10 - 10^3$ Hz of Earth-based detectors via a number of possible emission mechanisms. This Section is based on recent reviews, which may be found in [121, 122, 123, 124, 125]. These include the three classes of (1) non-axisymmetric deformations of the star [126, 127, 128, 129, 130], (2) spin precession of the star [131, 132], and (3) excited oscillation modes in the fluid of the star [126, 133, 134]. In addition, there could also be yet unknown mechanisms which cause CW emission detectable on Earth.

While settling down into its final state, the crust of newborn neutron star solidifies (crystalizes). Thereby, small non-axisymmetric deviations may occur in the neutron star's crust. Although such deformation cannot exist in a perfect fluid star, in a realistic star such deviation may occur due to elastic stresses in the crust or magnetic fields. These non-axisymmetric deformations (or “mountains”) are considered the most plausible source of detectable CW signals. The equatorial ellipticity is often used to measure the deformation expressed in the moments of inertia, $\epsilon = (I_{xx} - I_{yy})/I_{zz}$, and is proportional to the quadrupole moment. This ellipticity is not to be confused with the centrifugal bulge, which is axisymmetric and thus does not lead to gravitational-wave emission. If such a non-axisymmetric star rotates with a frequency f_{rot} , continuous gravitational waves are emitted at a frequency $f = 2f_{\text{rot}}$. Provided that the source is optimally oriented at distance r , the amplitude of the signal at the terrestrial detector for typical values then is (cf. [55])

$$h_0 = \frac{4\pi^2 G}{c^4} \frac{I_{zz} f^2}{r} \epsilon \approx 1.05 \times 10^{-26} \left(\frac{I_{zz}}{10^{38} \text{ kg m}^2} \right) \left(\frac{\epsilon}{10^{-6}} \right) \left(\frac{f}{100 \text{ Hz}} \right)^2 \left(\frac{1 \text{ kpc}}{r} \right), \quad (2.30)$$

where I_{zz} is the star's principal moment of inertia.

The maximum possible amplitude and ellipticity of neutron stars are highly uncertain parameters and depend on the breaking strain of the neutron star crust, which is related to its shear modulus. Estimates are given in [127, 135] and recent simulations [136] suggest more optimistic values of $\epsilon \lesssim 4 \times 10^{-6}$ for a $1.4 M_{\odot}$ and 10 km radius neutron star. Exotic alternatives to standard neutron stars, such as for instance strange-quark stars with solid cores or hybrid stars of with normal neutron stars outside a mixed quark

and baryon matter solid core, are speculated to support considerably larger ellipticities [130] due a higher shear modulus.

Alternatively, hot newly-formed neutron stars, or stars heated up during accretion from a companion could also emit continuous gravitational waves. The flow of accretion, guided by the star’s magnetic field, produces “hot spots” on the surface, which can result in “hills” in hotter areas and the ellipticity might thus build up to maximum value [126]. In addition, the magnetic field itself could also hold the accreted matter in mountains. The accreted material possesses very high electric conductivity, and thus crosses field lines slowly, therefore piling up in mountains larger than supported by elasticity alone [129, 137]. Even for ordinary neutron stars this mechanism could yield ellipticities of a few times 10^{-6} [123].

Apart from ellipticities that are basically supported by crustal shear stresses, different scenarios causing the ellipticity are possible, such as strong internal magnetic fields [128]. The neutron star’s interior magnetic field can have a large toroidal part, resulting from strong differential rotation immediately after the collapse. Then dissipation drives the symmetry axis of the toroidal magnetic field to orient perpendicular to the rotation axis, which maximizes the equatorial ellipticity.

If the star’s symmetry axis does not coincide with the rotation axis, then the star will precess freely. This wobbling of the star defines the wobble angle θ_{wobble} between its rotation and symmetry axis. Large wobble angles will generate CW signals [138, 131, 132] of amplitude

$$h_0 \approx 10^{-27} \left(\frac{\theta_{\text{wobble}}}{0.1 \text{ rad}} \right) \left(\frac{1 \text{ kpc}}{r} \right) \left(\frac{f_{\text{rot}}}{500 \text{ Hz}} \right)^2. \quad (2.31)$$

To first order, free precession generates CW signal at two frequencies with $f = f_{\text{rot}} + f_{\text{prec}}$ and $f = 2f_{\text{rot}}$, where the latter is a consequence of the body’s deviation from axisymmetry and the former one encodes the precessing motion (with $f_{\text{prec}} \ll f_{\text{rot}}$). Although it might be possible that such wobble is sustained longer than thought earlier [139], the CW amplitude is still expected to be too small for detection by first generation of detectors.

The third major class of CW emission mechanisms is related to various non-axisymmetric instabilities of rapidly spinning of neutron stars at their birth or during a phase of accretion, reviewed in [140, 141]. Among these, the so-called r-modes are fluid oscilla-

tions driven by the Coriolis force. These modes may be unstable [142, 143, 141] due to gravitational back reaction, called Chandrasekhar – Friedman – Schutz (CFS) instability. The CFS instability of the r-modes has been proposed as a CW source with frequency $f \approx 4f_{\text{rot}}/3$ from newly-born stars [144] and from fast accreting stars [126, 145]. However, depending on a number of highly uncertain damping-mechanism time scales, the r-modes in nascent neutron stars are not considered a promising candidate for CW detection, as the emission is expected to be of low amplitude and short-lasting (a few months). Better detection prospects of r-modes are expected from accreting neutron stars [146, 147], because emission may be lasting for a few thousand years [148, 140].

2.3.4.2 Surveying the sky for CW sources

Regardless of CW emission, current astrophysical models of stellar evolution suggest that of order 10^9 neutron stars should exist in our Galaxy. Out of those, 10^5 are estimated to be active radio pulsars. But by now only about 1800 radio pulsars have been observed through observation of electromagnetic-wave emission [149]. The reasons for this are related to selection effects, for example the emitted lighthouse-like radio beam is not intersecting our visual line or the emission is too faint. In fact, surveys of enhanced sensitivity will increase the number of detected pulsars.

All-sky surveys for CW signals have the potential to reveal entirely new neutron-star populations [29, 150]. The large population of neutron stars in the Galaxy, of which most are electromagnetically invisible, might be detected and studied via gravitational waves.

The distribution of observable CW amplitudes from neutron stars is thought to be limited by the fact that strong CW emission causes the star to spin down fast and to move out of the detector’s observation band quickly. In [124] a strong argument is given stating the maximum expected amplitude of a CW signal that one could hope to detect at the Earth is bounded by $h_0 \lesssim 4 \times 10^{-24}$, independent of the deformation and rotation frequency of the objects. The argument is due to Blandford in [25] and is based on energetics and statistics, considering a uniform distribution of neutron stars and assuming that each neutron star “spins down” once. The argument has been recently revisited [151] in a more general framework, testing Blandford’s argument via evolution simulations based on a realistic model of our Galaxy. These results give less optimistic

estimates, reducing the strongest expected CW-signal amplitude by a factor of about 3 for 10^{-6} ellipticity stars.

Searches for continuous gravitational-wave signals from compact objects are conventionally classified as *targeted* (known source location and phase evolution), *directed* (known source location), or *all-sky* (no prior source information).

An interesting class of targeted sources are radio pulsars, because their rotation can be monitored leading to a very good guess of the emitted gravitational waveform to look for. In addition, their locations are known to high precision. Thus, electromagnetic observations strongly reduce the possible gravitational-wave parameter space, allowing very sensitive and computationally feasible searches. In turn, observational upper limits from targeted searches [122, 152, 153, 154, 155] place constraints on the neutron star physics. An example of a directed search is found in [156], where only the source sky position is known and a wide range of possible frequency evolutions is examined.

The main focus of this thesis is the analysis-technique development and application of all-sky (or wide-parameter-space) surveys. In this type of search no source parameters, such as sky position or spin evolution, are known a priori. Due to the weakness of the expected CW signals as mentioned earlier, their detection requires long integration times. However, the longer the integration time, the more increases the effective survey volume and so the size of the parameter space to be probed becomes extremely large. Hence, the number of signal templates necessary for a reasonable resolution suffers a rapid increase with longer integration times and thus data analysis is severely limited by computational resources. Therefore, blind searches [157, 158, 1, 159, 2] are a computationally intensive problem, and require highly efficient analysis techniques [55, 160, 161, 162, 163, 164, 165, 4], such as will be presented in this dissertation.

Once continuous gravitational waves from a neutron star are confirmed, further follow-up studies, using longer data sets with refined template grids, are needed to measure for instance the source's distance from astrometric timing effects. A distance measurement would allow to determine the star's quadrupolar deformation or ellipticity, which in turn would shed some light on the star's interior composition. However, distance measurements at the 10% error level will require next-generation detectors [166], such as Advanced LIGO.

Einstein@Home search for CW sources in S4 LIGO data

Appeared in Physical Review D 79, 022001, (2009)

3.1 Overview and context

As discussed in Section 2.2.2, during the past decade, advances in lasers, optics and control systems have enabled construction of a new generation of gravitational-wave detectors [32] that offer the first realistic promise of a direct detection. The Laser Interferometer Gravitational-wave Observatory (LIGO) [58, 54] is currently the most sensitive of these instruments. In this Chapter, the results of the Einstein@Home search for continuous gravitational-wave (CW) sources in the data from the fourth LIGO science run (S4) are presented. The configuration of the LIGO detectors during the S4 run is described in a separate instrumental paper [167].

Other CW searches of the S4 data with methods different from the ones presented here have also been carried out [154, 158]. Searches for other signal types (burst, inspiral, stochastic background) have been done [102, 168, 169, 115, 114, 113] with this data set, too. The results of these searches are all upper bounds, with no detections reported.

This search looks for continuous gravitational waves which are almost monochromatic signals of duration much longer than the observation time. As described in Section 2.3.4, these signals have a well-defined frequency on short time-scales, which can vary slowly over longer times. These types of waves are expected, for example, from spinning neutron stars with non-axisymmetric deformations. If the system is isolated, then it loses angular momentum due to the radiation. The spinning motion slows down, and the gravitational-wave frequency decreases. Gravitational acceleration towards a large nearby mass distribution can also produce such a frequency drift (of either sign). Many possible emission mechanisms could lead to the emission of such waves by spinning neutron stars, for further details see Section 2.3.4 and Refs. [126, 127, 128, 129, 130, 133, 134, 131, 132].

Using 510 hours of data from the LIGO S4 run, the present search probes a wide parameter space of possible sources. The search is for CW sources in the frequency range from 50 to 1500 Hz, with a linear frequency drift \dot{f} , measured at the solar system barycenter (SSB), in the range $-f/\tau < \dot{f} < 0.1 f/\tau$, where the minimum spin-down age τ was 1000 years for signals below 300 Hz and 10 000 years above 300 Hz. The main computational work of the search has been distributed over approximately 100 000 computers volunteered by the general public. This large computing power allowed the use of a relatively long coherent integration time of 30 h, despite the large parameter space searched. A Monte-Carlo based sensitivity estimation shows that in the 100 to 200 Hz band, more than 90% of sources with dimensionless gravitational-wave strain amplitude greater than 10^{-23} would have been detected.

This Chapter is organized as follows. Section 3.2 briefly reviews the CW signal detection strategies. Sections 3.3 and 3.4 describe the overall construction of the search, including the data set preparation, regions of parameter space searched, and the choices of thresholds and sensitivities. Section 3.5 describes the post-processing pipeline. The level of sensitivity of the search is estimated in Section 3.6. Section 3.7 describes the vetoing of instrumental line artifacts and the fraction of parameter space that was therefore excluded. Section 3.8 describes the end-to-end validation of the search and the post-processing pipeline, which was done by injecting simulated CW signals into the detector hardware. Section 3.9 describes the final results of the search, followed by a short conclusion.

3.2 Data analysis strategy

If there were no acceleration between the LIGO detectors and the CW sources, then it would be possible to search for CW signals using only “standard” computing resources, such as a high-end workstation or a small computing cluster. In this case the analysis technique would be simple: compute the Fast Fourier Transform (FFT) [170, 171] of the original time-series data, and search along the frequency axis for peaks in the power spectrum. Time-domain resampling or similar techniques could be used to compensate for the effects of a linear-in-time frequency drift.

However, this simple analysis is not possible because of the terrestrial location of the LIGO detectors: signals that are purely sinusoidal at the source are Doppler-modulated by the Earth’s motion and thus are no longer sinusoidal at the detector. The Earth’s rotation about its axis modulates the signal frequency at the detector by approximately one part in 10^6 , with a period of one sidereal day. In addition, the Earth’s orbit about the Sun modulates the signal frequency at the detector by approximately one part in 10^4 , with a period of one year. These two modulations, whose exact form depends upon the precise sky location of the source, greatly complicate the data analysis when searching for unknown sources. The search becomes even more complicated if the CW-emitter is part of a binary star system, since the orbital motion of the binary system introduces additional modulations into the waveform.

The “brute force” approach to the data analysis problem would employ matched filtering [116, 117], convolving all available data with a family of template waveforms corresponding to all possible putative sources. The resulting search statistic is called the \mathcal{F} -statistic and was first described in a seminal paper of Jaranowski, Królak, and Schutz [55]. But even for isolated neutron stars (i.e. which are not in binary systems) the parameter space of possible sources is four-dimensional, with two parameters required to describe the source sky position using standard astronomical equatorial coordinates α (right ascension) and δ (declination), and additional coordinates (f, \dot{f}) denoting the intrinsic frequency and frequency drift. To achieve the maximum possible sensitivity, the template waveforms must match the source waveforms to within a fraction of a cycle over the entire observation time (with current detectors this is months or years). So one

must choose a very closely spaced grid of templates in this four-dimensional parameter space, and the computational cost exceeds all available computing resources on the planet [55, 172]. Thus the direct approach is not possible in practice.

More efficient and sensitive methods for this type of search have been studied for more than a decade and are under development [173, 174, 160, 4]. Here, the frequency-domain method described in [122, 124] is used to calculate the \mathcal{F} -statistic. In order to maximize the possible integration time, and hence achieve a more sensitive coherent search, the computation was distributed among approximately 10^5 computers belonging to $\sim 5 \times 10^4$ volunteers in ~ 200 countries. This distributed computation project, called Einstein@Home [12], follows the model of a number of other well-known volunteer distributed computing projects such as SETI@home [175] and Folding@home [176].

3.3 Data selection and preparation

The data for the S4 run was collected between February 22, 2005 and March 23, 2005. The data analyzed consisted of 300 h of data from the LIGO Hanford 4-km (H1) detector and 210 h of data from the LIGO Livingston 4-km (L1) detector.

The search method used here (explained in detail in Section 3.4) consists of computing a coherent \mathcal{F} -statistic over data segments of 30 h each, and combining these results via an incoherent coincidence scheme. However, the 30-hour segments have time-gaps, and the number of templates needed for the coherent \mathcal{F} -statistic step grows rapidly as the gaps get longer. For this reason, the start and end times of the data segments were selected based on the criteria that the gaps totaled no more than 10 h: each data segment contains 30 h of science-mode data and lies within a total time span of less than 40 h. Here and in the following the term “segment” is always used to refer to one of these time stretches of data, each of which contains exactly $T_{\text{obs}} = 30$ h of data. The total time spanned by the data in segment j is written $T_{\text{span},j}$; $30 \text{ h} < T_{\text{span},j} < 40 \text{ h}$.

The data segments consist of *uninterrupted* blocks of 1800 s of *contiguous* science-mode data. This is for technical reasons: the \mathcal{F} -statistic code uses Short Fourier Trans-

Table 3.1: Segments of S4 data used in this search, in order of decreasing sensitivity at 141.3 Hz for H1 and at 135.3 Hz for L1. The columns are the data segment index j , the GPS start time t_j , the GPS end time t_j^{end} , and the time spanned $T_{\text{span},j} = t_j^{\text{end}} - t_j$.

j	Detector	t_j [s]	t_j^{end} [s]	$T_{\text{span},j}$ [s]
1	H1	794461805	794583354	121549
2	H1	794718394	794840728	122334
3	H1	795149016	795285470	136454
4	H1	793555944	793685616	129672
5	H1	795493128	795626713	133585
6	H1	793936862	794078332	141470
7	H1	794885406	795015166	129760
8	H1	794244737	794378322	133585
9	H1	794585154	794714794	129640
10	H1	793766877	793910817	143940
11	L1	795553209	795678679	125470
12	L1	795115986	795246307	130321
13	L1	795408715	795545555	136840
14	L1	794625269	794762685	137416
15	L1	794053883	794197272	143389
16	L1	794206397	794328337	121940
17	L1	794875424	795016053	140629

forms (SFTs) over $T_{\text{SFT}} = 1800$ s as input data, (this data format is described in [177]). To produce these SFTs, the data is first calibrated in the time domain using the method described in [178, 179]. Then the data is windowed in 1800 s intervals using a Tukey window with a characteristic turn-on/turn-off time of 500 ms, followed by an FFT.

Applying the above constraints to the S4 data set yielded a total of $N_{\text{seg}} = 17$ data segments (10 from H1, 7 from L1), labeled by $j = 1, \dots, 17$. The global positioning system (GPS) start time of segment j is denoted t_j , and these values are listed in Table 3.1.

The maximum Doppler modulation (from the Earth's motion about the Sun) is about one part in 10^4 . Over the length of S4, and in the parameter range considered, the frequency changes due to intrinsic spin-down are smaller still. This means that the CW signals searched for here always stays within a narrow frequency band, drifting no more than about ± 0.15 Hz from some fiducial frequency. For this reason the input data, span-

ning the frequency range of 50 to 1500 Hz, is partitioned in the frequency domain into 5800 “slices” of 0.5 Hz plus wings of 0.175 Hz on either side. The size of one such input data slice is 7 368 000 bytes for H1 (containing 600 SFTs from 10 segments) and 5 157 600 bytes for L1 (containing 420 SFTs from 7 segments).

The detector data contains dozens of narrow-band spectral lines whose origin is instrumental, for example the harmonics of the 60 Hz mains frequency, and violin modes of the mirror suspensions in the range from 342 – 350 Hz (H1) and 335 – 355 Hz (L1). To simplify later analysis, line features that are known to be instrumental artifacts are removed (“cleaned”) from the data by replacing the frequency-domain data bins with computer-generated random Gaussian values. The frequencies of these lines are shown in Table 3.2. The cleaning algorithm uses a moving-in-frequency median of the power in individual frequency bins to determine the instrumental noise floor. To prevent bias at the boundaries of the cleaned regions, the mean of the random values to replace the line features interpolates linearly between the noise floor at either side of the line feature. The median noise strain amplitude spectra of the final cleaned H1 and L1 data sets are shown in Figure 3.1.

3.4 Data processing

Figure 3.2 is a schematic flow-diagram of the Einstein@Home data processing which is described in this Section and in the following Section on post-processing. It shows what parts of the analysis were done by project participants, what parts were done on project servers, and the relationships between these.

3.4.1 BOINC workunit distribution and validation

The computational work of the search is partitioned into 6 731 410 workunits (separate computing tasks) and processed using the Berkeley Open Infrastructure for Network Computing (BOINC) [180, 181, 182]. Because the work is done on computers that are

Table 3.2: Instrumental lines replaced with Gaussian noise in the input data. The three columns show the frequency of the fundamental harmonic f_{Line} , the number of harmonics N , and the bandwidth Δf_{Line} removed on either side of the central frequency (total bandwidth removed per harmonic is $2\Delta f_{\text{Line}}$). In total 77.285556 Hz of H1 data (139114 Fourier bins) and 142.137778 Hz of L1 data (255848 Fourier bins) have been excluded ab initio from the frequency range $50 \text{ Hz} \leq f \leq 1500 \text{ Hz}$. If $\Delta f_{\text{Line}} = 0$ then the line-cleaning algorithm replaces a single Fourier bin with the average of bins on either side. The spacing between Fourier bins is $1/1800 \text{ Hz}$.

H1			L1		
$f_{\text{Line}}[\text{Hz}]$	N	$\Delta f_{\text{Line}}[\text{Hz}]$	$f_{\text{Line}}[\text{Hz}]$	N	$\Delta f_{\text{Line}}[\text{Hz}]$
1.0	1451	0.0006	1.0	1451	0.0006
60.0	1	3.0	36.8728	39	0.8
60.0	25	1.0	54.7	1	0.0
346.0	1	4.0	60.0	25	1.0
392.365	1	0.01	345.0	1	10.0
393.1	1	0.0	396.7	1	0.0
393.835	1	0.01	686.5	1	1.0
688.5	1	2.0	688.83	1	0.5
694.75	1	1.25	693.7	1	0.7
973.3	1	0.0	1029.5	1	0.25
1030.55	1	0.1	1031.0	1	0.5
1032.18	1	0.04	1033.6	1	0.2
1032.58	1	0.1	1041.0	1	1.0
1033.7	1	0.1	1151.5	1	0.0
1033.855	1	0.05	1372.925	1	0.075
1034.6	1	0.4	1374.7	1	0.1
1042.5	1	1.5	1375.2	1	0.1
1143.5672	1	0.2	1378.39	1	0.1
1144.3	1	0.0	1387.4	1	0.05
1145.0328	1	0.2	1388.5	1	0.5
1373.75	1	0.1			
1374.44	1	0.1			
1377.14	1	0.1			
1378.75	1	0.1			
1379.52	1	0.1			
1389.06	1	0.06			
1389.82	1	0.07			
1391.5	1	0.5			

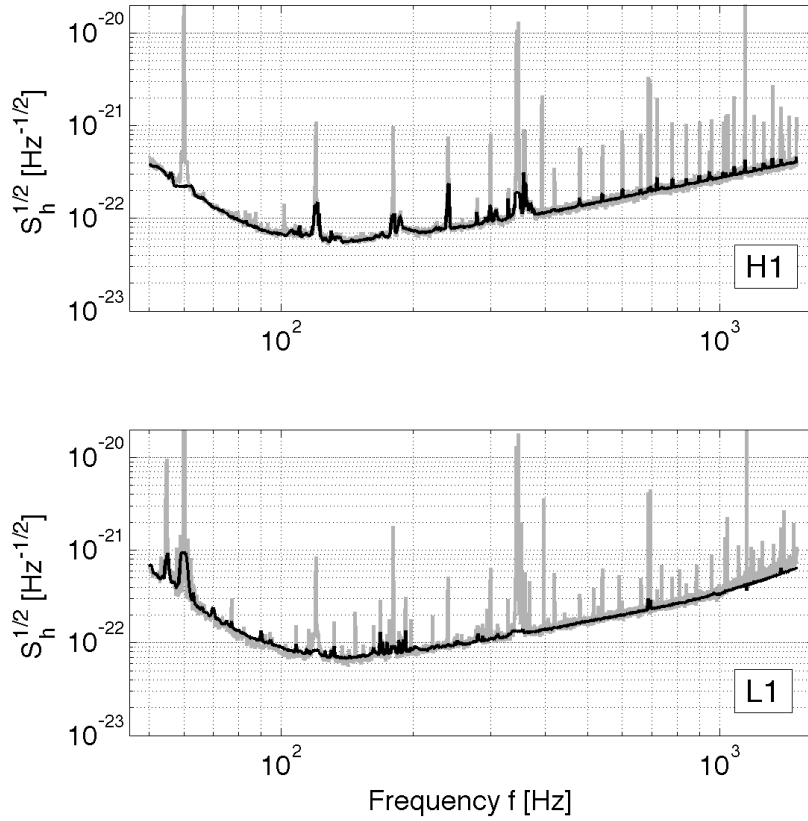


Figure 3.1: Strain amplitude spectral densities $\sqrt{S_h(f)}$ of the S4 data from the LIGO detectors H1 (top) and L1 (bottom). The gray curves are medians of the *entire uncleaned* LIGO S4 science-mode data set with a frequency resolution of 0.125 Hz. The black curves show the *cleaned* S4 data used in this analysis with a frequency resolution of 0.5 Hz. The top (bottom) plot is the mean of the 10 H1 (7 L1) 30-hour data segments used in this Einstein@Home analysis.

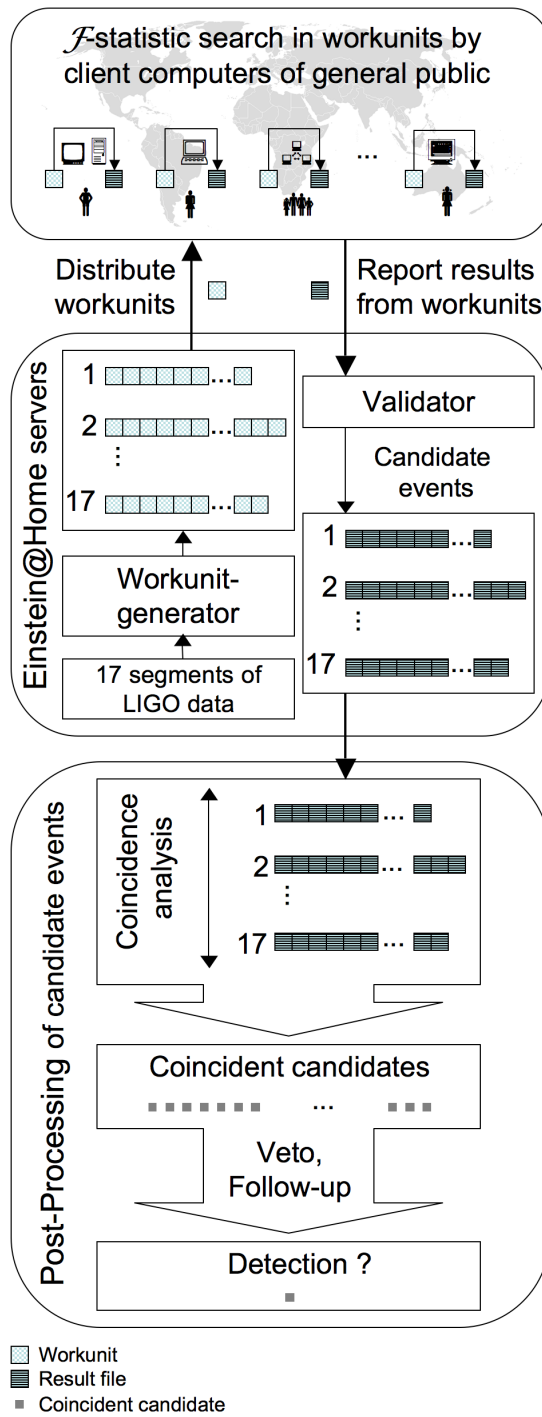


Figure 3.2: Schematic overview of the Einstein@Home data-processing and subsequent post-processing.

not owned or controlled by our scientific collaboration or institutions, any individual result could be wrong. Error sources include defective hardware (such as over-clocked memory), defective software (erroneous system libraries), and malicious users (faking correct results). To identify and eliminate such errors, BOINC was configured so that each workunit is done independently by computers owned by at least three different volunteers.

The most common types of errors (lack of disk space, corrupted or missing input files, inconsistent internal state, etc.) are detected during program execution. If an error is detected during run-time, the program reports to the Einstein@Home server that the workunit was *unsuccessful*, and BOINC generates another instance of the workunit, to be sent to another volunteer's computer. This behavior is repeated as necessary until three successful results have been obtained.

The three successful results obtained for each workunit are then compared by an automatic validator, which rejects results that do not agree closely. The validation process is more complicated than simple byte-by-byte comparison of output files, because Einstein@Home supports multiple computing platforms (Windows, GNU/Linux, Mac OS X on Intel and PPC, FreeBSD, and Solaris) and differences in CPU hardware, compiler instruction ordering, and floating-point libraries mean that correct and valid result files may exhibit small numerical differences. The automatic validation takes place in two steps.

The output files have a fixed five-column format and contain 13 000 candidate events, with one line per candidate event, as described in Section 3.4.3. The first validation step checks that the file syntax is correct and that each value is within the allowed range for that column. This detects most file corruption.

Then the validator does comparison of all possible pairs of result files. For a given pair of result files, the validator checks that corresponding candidate events lie on the same template grid-point and have \mathcal{F} -statistic values that agree to within 1%. Since each file contains the 13 000 events with the largest values of the \mathcal{F} -statistic, numerical fluctuations in determining the value of \mathcal{F} can lead to slightly different lists being returned on different platforms. Hence the validator tolerates unpaired candidate events if they lie within 1% of the smallest value on the list.

A workunit is validated once it has three results that agree with one another to within

these tolerances. If the three results do not pass this validation step, the Einstein@Home server generates more instances of this workunit until three *valid* results have been obtained. For the search described here, a “post-mortem” analysis of the computation shows that the probability of a successful but invalid result is small (0.36%), and the errors which make a successful result invalid are typically unique and irreproducible. Hence we estimate that it is highly improbable that even a single incorrect result has been marked as “valid” by the automatic validator.

3.4.2 Workunit design and gridding of search parameter space

The different workunits cover (search) different parts of parameter space. A key design goal of these workunits is that they should have roughly equal computational run times, of the order of ~ 8 h, and that the computational effort to carry out the entire search should last about 0.5 to 1 years. Another key design goal is that each workunit uses only a small re-usable subset of the total data set. These allow Einstein@Home volunteers to do useful computations on the one-day time-scale, and minimizes the download burden on their internet connections and on the Einstein@Home data servers.

Each workunit uses only one segment of data over a narrow frequency-range, but covers the whole sky and the full range of frequency-derivatives \dot{f} at that frequency. Therefore, the entire search is divided into computational units over different data segments and frequency-bands. In the following it will be useful to label the workunits by three indices (j, k, ℓ) , where $j = 1, \dots, 17$ denotes the data segment, $k = 1, \dots, 2900$ labels the 0.5 Hz band covered by the input data file, and $\ell = 1, \dots, M(j, k)$ enumerates individual workunits associated with data segment j and frequency band k . Note that each workunit uses a frequency band that is *smaller* than the 0.5 Hz covered by the input data files, i.e. $M(j, k) \geq 1$.

3.4.2.1 Search parameter-space grid

The parameter space is gridded in such a way that no point has a “squared-distance” from its nearest grid point that exceeds a certain “maximal mismatch”. The distance is defined by a metric on parameter space, first introduced in [173, 174]. The squared

distance is the fractional loss of squared signal-to-noise ratio (SNR^2) due to waveform mismatch between the putative signal and the template. The search grid was constructed based on the projected metric on the subspace orthogonal to the frequency direction ∂_f with $\dot{f} = 0$. For any given workunit, the parameter-space grid is a Cartesian product of uniformly-spaced steps df in frequency, uniformly-spaced steps $d\dot{f}$ in frequency derivative, and a two-dimensional sky grid, which has non-uniform spacings determined by the projected metric. For frequencies in the range $[50, 290)$ Hz, the maximal mismatch was chosen as $m = 0.2$ (corresponding to a maximal loss in SNR^2 of 20%), while in the range $[300, 1500)$ Hz, the maximal mismatch was $m = 0.5$. Due to a bug in the script generating the sky grids, the range $[290, 300)$ Hz, was covered by frequency and spin-down steps corresponding to $m = 0.2$, whereas the sky grids were constructed for $m = 0.5$. The distribution of actual mismatches in this frequency range will therefore be somewhat in between those of the low-frequency and high-frequency workunits.

It can be shown [183] that these relatively large mismatches give near-optimal sensitivity for a coherent search at fixed CPU power. Choosing finer grid spacings (i.e. a smaller mismatch) would require searching more grid-points, thus reducing the maximal possible coherent integration time. A coarser search grid would allow longer integrations but at a larger average loss in SNR. Because of these two competing tendencies, the sensitivity as a function of mismatch m has a maximum in the range $m \sim 0.25 - 0.7$, depending on the choice of false-dismissal rate from the grid mismatch. Full details of the parameter-space grid and workunit construction are given in [183]; a short summary follows.

3.4.2.2 Search grid in frequency and frequency-derivative

The step-size in frequency was determined using the metric-based expression

$$df_j = \frac{2\sqrt{3m}}{\pi T_{\text{span},j}}, \quad (3.1)$$

so the frequency-spacing depends on $T_{\text{span},j}$ of the data segment j . For the low-frequency workunits ($f < 300$ Hz), this results in frequency steps in the range $df_j \in [3.43, 4.06] \mu\text{Hz}$, while for high-frequency workunits $df_j \in [5.42, 6.41] \mu\text{Hz}$.

The range of frequency-derivatives \dot{f} searched is defined in terms of the ‘‘spin-down age’’ $\tau \equiv -f/\dot{f}$, namely $\tau \geq 1000$ years for low-frequency and $\tau \geq 10\,000$ years for

high-frequency workunits. Neutron stars younger than the limited range of this search probably would have left a highly visible (Sedov phase) supernova remnant or a pulsar wind nebula. Thus our search for unknown neutron stars targeted older objects, which also resulted in less computational cost. The search also covers a small “spin-up” range, so the actual ranges searched are $\dot{f} \in [-f/\tau, 0.1f/\tau]$. In \dot{f} the grid points are spaced according to

$$d\dot{f}_j = \frac{12\sqrt{5m}}{\pi T_{\text{span},j}^2}, \quad (3.2)$$

resulting in resolutions $d\dot{f}_j \in [1.84, 2.59] \times 10^{-10}$ Hz/s for low-frequency workunits, and $d\dot{f}_j \in [2.91, 4.09] \times 10^{-10}$ Hz/s for high-frequency workunits, depending on the duration $T_{\text{span},j}$ of different segments j .

3.4.2.3 Search grid in the sky parameters

The resolution of the search grid in the sky-directions depends both on the start-time t_j and duration $T_{\text{span},j}$ of the segment, as well as on the frequency. The number of grid points on the sky scales as $\propto f^2$, and approximately as $\propto T_{\text{span},j}^{2.4}$ for the range of $T_{\text{span},j} \sim 30 - 40$ h used in this search. Contrary to the simple uniform spacings in f and \dot{f} , the sky grids are computed beforehand and shipped together with the workunits. In order to simplify the construction of workunits and limit the amount of different input-files to be sent, the sky grids are fixed over a frequency range of 10 Hz, but differ for each data segment j . The sky grids are computed at the higher end of each 10 Hz band, so they are slightly “over-covering” the sky instead of being too coarse. The search covers a frequency range of 1450 Hz, and so there are 145 different sky grids for each segment. To illustrate this, four of these sky grids are shown in Figure 3.3 (using the Hammer-Aitoff sky projection [184]) corresponding to two different data segments at two distinct frequency bands.

To ensure that each workunit takes a similar amount of CPU time, the total number of template grid points of each workunit is chosen to be *approximately* constant for all workunits. However, in practice, this number can vary by up to a factor of 2 due to discretization effects. The number of points in the sky grids grows with frequency as f^2 and the number of points in the spin-down grid grows linearly with f . Thus, to keep the number of templates (and therefore the CPU time) approximately constant, the

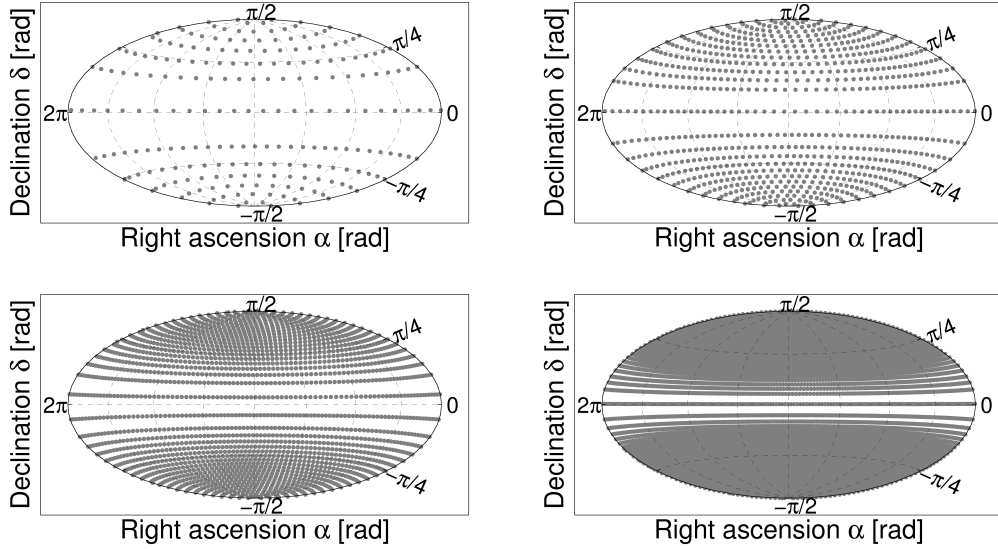


Figure 3.3: Four different sky grids in Hammer-Aitoff projection. The top row is for frequency $f = 60$ Hz and the bottom row is for $f = 310$ Hz. The left column shows data segment $j = 1$ (from H1) with a spanned time of $T_{\text{span},1} = 33.8$ h, while the right column shows data segment $j = 15$ (from L1) with a spanned time of $T_{\text{span},15} = 39.8$ h. The grid points are spaced more closely for a longer spanned time, and for a higher frequency.

frequency range covered by each workunit decreases as f^{-3} . Hence for fixed j , $M(j, k)$ is roughly proportional to k^3 .

3.4.3 The output of a workunit

The result from completing one workunit on an Einstein@Home host computer is a ZIP-compressed ASCII text file containing the 13 000 candidate events with the largest values of the \mathcal{F} -statistic found over the parameter-space grid points analyzed by that workunit. Each line of the output file contains five columns: frequency (Hz), right ascension angle (radians), declination angle (radians), spin-down-rate (Hz/s) and $2\mathcal{F}$ (dimensionless). The frequency is the frequency at the SSB at the instant of the first data point in the corresponding data segment.

The number 13 000 was decided in advance, when the workunits were first launched

on the Einstein@Home project, which was about one year before the post-processing pipeline was developed. The network bandwidth required to retain more than 13 000 candidates per workunit, and the storage space required to preserve them, would have exceeded the capacity of the Einstein@Home server and its internet connection. For frequency-band and data segment combinations with small numbers of workunits, for example the $j = 1$ data set from 301.0 to 301.5 Hz, almost all of the 13 000 candidate events are later used in the post-processing pipeline. However (as can be seen later in Figure 3.4) for most frequency-bands the post-processing pipeline only needed and used a fraction of the events that were returned.

Returning the “loudest” 13 000 candidate events effectively corresponds to a floating threshold on the value of the \mathcal{F} -statistic. This avoids large lists of candidate events being produced in regions of parameter space containing non-Gaussian noise, such as instrumental artifacts that were not removed a priori from the input data.

3.4.4 Total computation time

The analysis of the entire 1450 Hz band computed $2\mathcal{F}$ values for 63 627 287 767 483 distinct points in the four-dimensional parameter space. The bulk of this processing was carried out on the Einstein@Home project between December 24, 2005 and June 30, 2006, and used approximately 4×10^{11} CPU-seconds, or 13 000 CPU-years. In any given week, about 60 000 host machines were active. Thus, a typical host machine contributed about 40% of its potential CPU cycles to the project.

3.5 Post-processing

As shown previously in Figure 3.2, after result files are returned to the Einstein@Home servers by project participants, further post-processing is carried out on those servers and on dedicated computing clusters. The goal of this post-processing pipeline is to identify consistent candidate events that appear in many of the 17 different data segments.

Here, a consistent (coincident) set of “candidate events” is called a “candidate”. Candidate events from different data segments are considered coincident if they cluster closely together in the four-dimensional parameter space. A clustering method using a grid of “coincidence cells” will reliably detect strong CW signals, which would produce candidate events with closely-matched parameters.

The post-processing pipeline operates in 0.5 Hz-wide frequency-bands, and can be summarized in three steps. In *step one*, the coincident false alarm probability is fixed. In *step two*, the frequency values of candidate events are shifted to the same fiducial time. In *step three*, a grid of cells is constructed in the four-dimensional parameter space, and each candidate event is assigned to a particular cell. In the following the details involved in each step are described.

3.5.1 Preparation and selection of candidate events

In the *first step* the individual result files are prepared for the later analysis by uncompressing them and keeping only a subset of the candidate events: from the (j, k, ℓ) 'th workunit only the $\mathcal{E}(j, k, \ell)$ candidate events with the largest values of $2\mathcal{F}$ are retained.

The number of these candidate events is chosen a priori to obtain a pre-determined fixed false alarm probability. The false alarms should be approximately uniformly distributed among the workunits, since each workunit examines a similar number of independent grid points in parameter space. The number of candidate events is chosen so that in a 0.5 Hz-wide frequency-band the probability that one or more coincidence cells after doing the clustering (in step three) has $C_{\max} = 7$ or more coincidences is $P_F = 0.001$. Thus, in the analysis of 2900 such frequency bands, in random noise one would expect to find only about three candidates with seven or more coincidences. (As explained later

in Section 3.5.6.1, this overall probability for the entire search is somewhat increased because the coincidence cell grids are also shifted by half their width in 16 possible combinations).

In terms of the notation introduced in the previous section, the number of candidate events kept from the (j, k, ℓ) 'th workunit takes the form

$$\mathcal{E}(j, k, \ell) = \frac{\mathcal{E}_{\text{seg}}(k)}{M(j, k)}, \quad (3.3)$$

where $\mathcal{E}_{\text{seg}}(k)$ is shown in Figure 3.4. Because the individual workunits are constructed to use approximately the same amount of CPU time, each workunit examines approximately the same number of templates in parameter space, so the same number of candidate events are retained from all workunits which have the same input data file and data segment. This implies that the number of candidate events that are kept per data segment j and per frequency band is independent of the data segment j :

$$\sum_{\ell=1}^{M(j,k)} \mathcal{E}(j, k, \ell) = \mathcal{E}_{\text{seg}}(k). \quad (3.4)$$

Since the sky grids are fixed in 10 Hz intervals, $\mathcal{E}_{\text{seg}}(k)$ takes the same value for all values of k in the range of $20p + 1, \dots, 20(p + 1)$ where p labels the sky grids by an integer in the range $p \in 0, \dots, 144$.

It is illustrative to look at a specific case. For example consider the 0.5 Hz band covering $[301.0, 301.5)$ Hz, this band is labeled by $k = 503$. As is shown in Figure 3.4, in this band the post-processing pipeline retains $\mathcal{E}_{\text{seg}}(k = 503) = 24\,960$ candidate events from each of the 17 different 30-hour data segments. The 30-hour data segment from H1 with the *shortest* time span ($j = 1$) has approximately 4.3×10^8 templates divided among just $M(j = 1, k = 503) = 2$ workunits, so 12 480 candidate events are retained from each of these workunits. The 30-hour data segment from L1 with the *longest* time span ($j = 15$) has approximately 1.7×10^9 templates divided among $M(j = 15, k = 503) = 7$ workunits, so 3 565 candidate events are retained from each of these workunits. In the later stage of the post-processing, this ensures that each of the different data segments contributes equally to the probability of generating false alarms in the coincidence step.

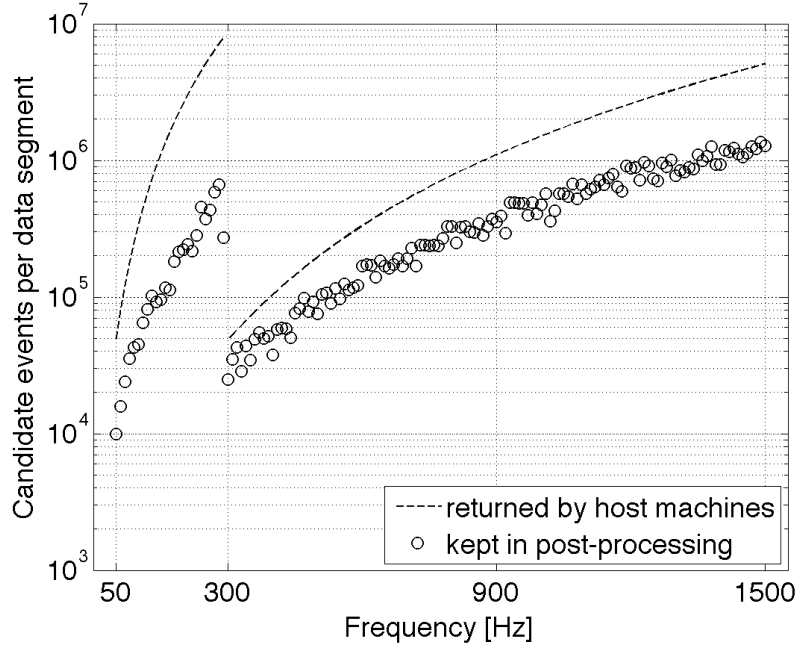


Figure 3.4: The circles show the number of candidate events $\mathcal{E}_{\text{seg}}(k)$ retained per data segment and per 0.5 Hz frequency band in the post-processing in each 10 Hz band. The dashed curve represents the number of candidate events which are returned from volunteering hosts participating in Einstein@Home. The strange location of the point at 290 Hz is explained in Section 3.4.2.1.

3.5.2 Number of cells in the post-processing coincidence grid

It is important to calculate the number of coincidence cells in the coincidence grid. Together with the desired false alarm probability, this determines the number of candidate events to retain in the post-processing pipeline.

The number of coincidence cells $N_{\text{cell}}(k)$ contained in each 0.5 Hz frequency band k (while doing the clustering in step three) is determined by the sizes of the cells. This is given by

$$N_{\text{cell}}(k) = \left(\frac{0.5 \text{ Hz}}{\Delta f} \right) \left(\frac{1.1 f}{\tau \Delta \dot{f}} \right) \int_{-\pi/2}^{\pi/2} \frac{d\delta}{\Delta \delta(\delta)} \int_0^{2\pi} \frac{d\alpha}{\Delta \alpha(\delta)}, \quad (3.5)$$

where Δf denotes the coincidence cell width in frequency, $\Delta \dot{f}$ denotes the width in spin-down, and $\Delta \alpha(\delta)$ and $\Delta \delta(\delta)$ denote the coincidence cell widths in right ascension and declination (both of which vary with declination δ). The choice of the coincidence

cell sizes will be explained in detail later when step three will be described.

3.5.3 False alarm rate and the number of candidate events retained

The number of candidate events that must be retained is determined by the number of cells in the coincidence grid $N_{\text{cell}}(k)$ and by the desired probability of false alarm P_F for false coincidence of candidate events from \mathcal{C}_{max} or more data segments in each 0.5 Hz band. To relate these quantities, consider the case of random instrumental noise, in which the candidate events are distributed uniformly about the coincidence grid. Concentrate on a single 0.5 Hz band k , and consider the first of the $N_{\text{seg}} = 17$ data segments. A total of $\mathcal{E}_{\text{seg}}(k)$ candidate events must be distributed uniformly among $N_{\text{cell}}(k)$ coincidence cells. Each candidate event falls in a random coincidence cell, independent of the locations of the previous candidate events. The probability that the first candidate event falls in the first coincidence cell is $1/N_{\text{cell}}(k)$, and hence the probability that the first coincidence cell remains empty is $1 - 1/N_{\text{cell}}(k)$. If the remaining $\mathcal{E}_{\text{seg}}(k) - 1$ candidate events fall independently and at random into the coincidence cells, then this generates a binomial distribution, and the probability that the first coincidence cell contains no candidate events is

$$p_k(0) = \left(1 - \frac{1}{N_{\text{cell}}(k)}\right)^{\mathcal{E}_{\text{seg}}(k)}. \quad (3.6)$$

Since the first coincidence cell is equivalent to any other, the probability that the candidate events from the first data segment populate any given coincidence cell with one or more candidate events is thus given by

$$\epsilon(k) = 1 - p_k(0) = 1 - \left(1 - \frac{1}{N_{\text{cell}}(k)}\right)^{\mathcal{E}_{\text{seg}}(k)}. \quad (3.7)$$

In random noise, the candidate events produced by each different data segment are independent, so that the coincidence cells that are “marked” by one or more candidate events are also described by a (different) binomial distribution. Without loss of generality, again consider the first coincidence cell. The probability that it contains candidate events from

n distinct data segments is then given by

$$\binom{N_{\text{seg}}}{n} [\epsilon(k)]^n [1 - \epsilon(k)]^{N_{\text{seg}} - n}, \quad (3.8)$$

where $\binom{a}{b} = \frac{a!}{b!(a-b)!}$ is the binomial coefficient. Thus the probability per coincidence cell of finding C_{max} or more coincidences is given by

$$p_{\text{F}}(k) = \sum_{n=C_{\text{max}}}^{N_{\text{seg}}} \binom{N_{\text{seg}}}{n} [\epsilon(k)]^n [1 - \epsilon(k)]^{N_{\text{seg}} - n}. \quad (3.9)$$

The probability P_{F} that there are C_{max} or more coincidences in one or more of the N_{cell} cells per 0.5 Hz band k is

$$P_{\text{F}}(k) = 1 - [1 - p_{\text{F}}(k)]^{N_{\text{cell}}}. \quad (3.10)$$

If $p_{\text{F}}(k) \ll 1$ and $N_{\text{cell}} p_{\text{F}}(k) \ll 1$ then the false alarm probability P_{F} is approximately

$$P_{\text{F}}(k) \approx N_{\text{cell}} p_{\text{F}}(k). \quad (3.11)$$

For the desired $P_{\text{F}} = 0.1\% = 10^{-3}$ with $C_{\text{max}} = 7$ per 0.5 Hz band k , this equation is solved numerically to find $\mathcal{E}_{\text{seg}}(k)$. The results for $\mathcal{E}_{\text{seg}}(k)$ are shown in Figure 3.4.

3.5.4 Choice of false alarm probability and detection threshold

The goal of this work is to make a *confident detection*, not to set upper limits with the broadest possible coverage band. This is reflected in the choice of the *expected false alarm probability* and the choice of a *detection threshold*.

The detection threshold of 12 events was chosen because, as described in Section 3.8, the hardware injections are only “turned on” for 12 of the 17 data segments. The detection threshold ensures that these simulated signals are properly detected by the post-processing pipeline.

The choice of false alarm probability ($P_{\text{F}} = 0.1\% = 10^{-3}$ per 0.5 Hz band to have coincidences in $C_{\text{max}} = 7$ or more data segments) is a pragmatic choice, which leads to

Table 3.3: False alarm probabilities P_F in four different 0.5 Hz frequency bands labeled by the integer k . The frequency at the lower boundary of the 0.5 Hz band k is denoted by f_k . The number of coincidence cells in the k th half-Hz frequency band is denoted by $N_{\text{cell}}(k)$. The probability of finding 7 or more coincidences ($\mathcal{C} \geq 7$) in randomly-distributed noise is fixed to be 0.1%. The probability of finding 12 or more coincidences (the detection threshold, $\mathcal{C} \geq 12$) in random noise varies over two orders of magnitude, from about 10^{-15} to 10^{-13} . The probability of finding 14 or more coincidences ($\mathcal{C} \geq 14$) in random noise varies from about 10^{-18} to 10^{-21} .

f_k [Hz]	k	$N_{\text{cell}}(k)$	$P_F(\mathcal{C} \geq 7)$	$P_F(\mathcal{C} \geq 12)$	$P_F(\mathcal{C} \geq 14)$
50.0	1	734 500	10^{-3}	1.5×10^{-13}	3.0×10^{-18}
290.0	481	35 198 800	10^{-3}	8.7×10^{-15}	5.7×10^{-20}
301.0	503	2 161 284	10^{-3}	6.7×10^{-14}	9.9×10^{-19}
1499.5	2900	233 345 981	10^{-3}	2.2×10^{-15}	8.4×10^{-21}

an extremely small false alarm rate at the detection threshold. For actual data, the probability of finding 7 or more coincidences in a given 0.5 Hz band can be somewhat larger than the target value of 0.1% because the candidate events are not uniformly distributed over the grid of coincidence cells and because (as described in Section 3.5.6.1) 16 sets of coincidence cells are used for each 0.5 Hz band.

In random noise, the probability of reaching the detection threshold of 12 coincidences depends on the number of cells in the coincidence grid, which is a function of frequency. Some representative numbers are given in Table 3.3; they vary from about 10^{-15} to 10^{-13} depending upon the 0.5 Hz band. The false alarm probabilities decrease very rapidly with increasing coincidence number. For example the probability of finding 14 or more coincidences in random noise varies from about 10^{-18} to 10^{-21} .

One might ask why choosing to specify a uniform false alarm probability, across all frequencies, of 0.1% for $\mathcal{C}_{\text{max}} = 7$, rather than directly specify a much lower false alarm probability at the detection threshold $\mathcal{C} = 12$. This was because we wanted the most significant coincident events due to noise alone to have \mathcal{C} values a few less than our detection threshold, and we wanted *these* candidates to be uniformly distributed over frequency bands. Any detected signals could then be compared against fairly uniform fields of noise candidates in adjacent frequency bands. If a uniform false alarm probabil-

ity had been specified at the $\mathcal{C} = 12$ level, then the expected noise candidates with $\mathcal{C} \sim 7$ would *not* have been uniformly distributed over frequency, due to the differing numbers of coincidence cells in each frequency band.

The choice of detection threshold and false alarm probability sacrifice a small amount of sensitivity compared with a higher values, but ensures that high numbers of coincidences are extremely improbable in random noise. A strong signal (say a factor of 1.5 above the upper curve in Figure 3.9 on Page 65) would be expected to produce 15 or more coincidences in this detection pipeline. With the thresholds that we have adopted, this would stand out very strongly: the probability of having even one such an event appear in coincidence in random noise is about 10^{-22} per 0.5 Hz band.

3.5.5 Shifting candidate-event frequencies to a fixed fiducial time

In the *second step* of the post-processing, the frequency value of each retained candidate event is shifted to the same fiducial time: the GPS start time of the earliest ($j = 4$) data segment, $t_{\text{fiducial}} = t_4 = 793\,555\,944$ s. This shifting is needed because a CW source with non-zero spin-down would produce candidate events with different apparent frequency values in each data segment. This step would shift these candidate events back to the same frequency value:

$$f(t_{\text{fiducial}}) = f(t_j) + [t_{\text{fiducial}} - t_j] \dot{f}, \quad (3.12)$$

where \dot{f} and $f(t_j)$ are the spin-down-rate and frequency of a candidate event reported by the search code in the result file, and t_j is the time-stamp of the first datum in the data segment. At the end of the second step, all candidate events for the 0.5 Hz band are merged into one file.

These candidate events are collected from a frequency interval that is slightly wider than 0.5 Hz. To see why this is necessary, consider a potential source whose frequency in the first data segment ($j = 4$) is at the lower (or upper) boundary of the 0.5 Hz interval. If the source has the minimum (or maximum) allowed value of \dot{f} , then in the *later* data segments it moves into, or is recorded in, the previous (or next) 0.5 Hz band. This effect is most apparent for the last $j = 11$ data segment, as illustrated in Figure 3.5. So in

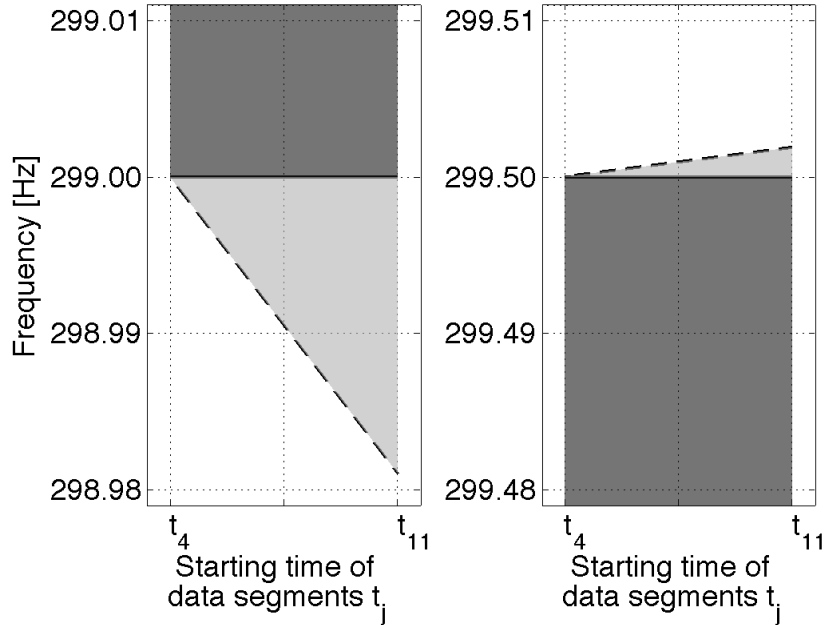


Figure 3.5: Additional “wings” at the boundaries of each 0.5 Hz frequency band must be included in the coincidence analysis stage of the post-processing. This is because spin-down can carry a source below this half-Hz band, and spin-up can carry it above the band. To illustrate this, the frequency band $k = 498$ (covering [299, 299.5) Hz) is (partly) shown by the dark-gray shaded area. The dashed sloped lines show the boundaries of the small additional regions (light gray) in frequency space whose candidate events must also be considered in the post-processing. Because the allowed spin-up range is ten times smaller than the allowed spin-down range, the upper boundary has a slope ten times smaller than the lower boundary.

collecting the candidate events for analysis of a given 0.5 Hz band, the frequency range is enlarged slightly for events coming from later and later data segments, as shown in Figure 3.5.

3.5.6 Search for coincident candidate events

The *third step* and final stage of the post-processing is to search for parameter-space coincidence among the candidate events. If a CW source is present that is strong enough to be confidently detected, then it would produce large \mathcal{F} -statistic values (i.e. candidate

events) in many or all of the 17 data segments. In addition, the values of the frequency at the fiducial time $f(t_{\text{fiducial}})$, sky position (given by right ascension α and declination δ), and spin-down \dot{f} for these candidate events would agree among all data segments (within some coincidence “window” or “cell”).

3.5.6.1 Coincidence search algorithm

To find coincidences, a grid of cells is constructed in four-dimensional parameter space, as described previously. This analysis uses rectangular cells in the coordinates $(f, \dot{f}, \alpha \cos \delta, \delta)$. The dimensions of the cells are adapted to the parameter space search. Each candidate event is assigned to a particular cell. In cases where two or more candidate events from the same data segment j fall into the same cell, only the candidate event having the largest value of $2\mathcal{F}$ is retained in the cell. Then the number of candidate events per cell coming from distinct data segments is counted, to identify cells with more coincidences than would be expected by random chance.

The search for coincident cells containing large numbers of candidate events is done with an efficient code that uses linked-list data structures, $N \log N$ sort algorithms, and $\log N$ bisection search algorithms. To ensure that candidate events located on opposite sides of a cell border are not missed, the entire cell coincidence grid is shifted by half a cell width in all possible $2^4 = 16$ combinations of the four parameter-space dimensions. Hence 16 different coincidence cell grids are used in the analysis.

The cells in the coincidence grid are constructed to be as small as possible to reduce the probability of coincidences due to false alarms. However, since each of the 17 different data segments uses a different parameter space grid, the coincidence cells must be chosen to be large enough that the candidate events from a CW source (which would appear at slightly different points in parameter space in each of the 17 data segments) would still lie in the same coincidence cell.

3.5.6.2 Frequency and spin-down coincidence windows

In frequency, the spacing of the parameter-space grid is largest for the data segment with the smallest value of $T_{\text{span},j}$, which is the first data segment $j = 1$. At first, this would appear to be the correct size Δf for the coincidence cell in the frequency direction.

However since the frequency of a candidate event must be shifted to a fixed fiducial time according to its spin-down value, and since that spin-down value can not be more accurate than the \dot{f} spacing, the size of the coincidence cell must be somewhat larger to accommodate the effects of this discretization error in \dot{f} . The coincidence window in the frequency direction is thus determined by

$$\Delta f = \max_j \left(df_j + \Delta t df_j \right), \quad (3.13)$$

where the maximization over j selects the data segment with the smallest $T_{\text{span},j}$ (which is $j = 1$) and

$$\Delta t = \left| \max_j t_j - \min_j t_j \right| = t_{11} - t_4 = 1\,997\,256 \text{ s} \quad (3.14)$$

is the total time span between the latest and earliest data segments. For safety, e.g. against noise fluctuations that could shift a candidate peak, Δf has been increased by a further 40% below 300 Hz, so that the width of the coincidence cell in frequency is $\Delta f = 0.77 \times 10^{-3}$ Hz, and by 30% above 300 Hz, so that $\Delta f = 1.08 \times 10^{-3}$ Hz.

For the spin-down parameter, the size of the coincidence cell is given by the largest df_j spacing in the parameter space grid, which is also determined by the smallest value of $T_{\text{span},j}$. For safety this is also increased by 40% below 300 Hz giving $\Delta \dot{f} = 3.7 \times 10^{-10}$ Hz s⁻¹, and by 30% above 300 Hz giving $\Delta \dot{f} = 5.18 \times 10^{-10}$ Hz s⁻¹.

3.5.6.3 Coincidence windows in apparent sky position

Determining the optimal size for the coincidence cells in the sky coordinate directions is more difficult. Each of the 17 different data segments uses a different sky grid, as illustrated in Figure 3.3. Ideally the size of the coincidence cells in these sky directions must be just large enough to enclose one parameter space grid point from each of the 17 different sky grids. A practical solution to determine the coincidence cells, which is close to optimal, makes use of an observation concerning the parameter-space metric that first appears in [162].

To understand the properties of the parameter-space metric, first consider the relative orders-of-magnitude of the different frequency modulation effects. The fractional Doppler shift due to the Earth's annual orbital motion about the Sun has magnitude $|\mathbf{v}_{\text{orbital}}|/c = 10^{-4}$ and the fractional Doppler shift due to the detector's daily motion

about the Earth rotation axis has magnitude $|\mathbf{v}_{\text{rotational}}|/c = 10^{-6}$. For the $T_{\text{span}} \approx 40$ h period of a single coherent integration, one can approximate the motion of the Earth's center of mass as motion with constant acceleration (along a parabolic trajectory) rather than as circular motion. The neglected term in the fractional Doppler shift has magnitude $|\ddot{\mathbf{v}}_{\text{orbital}}|T_{\text{span}}^2/2c \approx |\mathbf{v}_{\text{orbital}}||\boldsymbol{\omega}|^2T_{\text{span}}^2/2c \approx 4 \times 10^{-8}$, where $|\boldsymbol{\omega}| = 2\pi/\text{year}$ is the magnitude of the Earth's orbital angular velocity about the sun. This term is a factor of 25 smaller than $|\mathbf{v}_{\text{rotational}}|/c$ and hence can be neglected. With this approximation, the orbital motion of the Earth is simply responsible for an apparent shift in the frequency f and spin-down rate \dot{f} of a source: the effects of the Earth's center of mass motion are degenerate with a shift in frequency and spin-down. So the Earth's orbital motion causes a signal only to shift to a different template in f and \dot{f} ; the Earth's rotation has a period of one sidereal day and can not be modeled by a shift in f or \dot{f} . Note that terms are neglected *only* in determining where to place search grid points in parameter space (because the neglected terms have an insignificant effect on where the grid points are placed). The actual filtering of the data uses "exact" barycentering routines (total timing errors below $3\mu\text{s}$).

The search grid in parameter space is a Cartesian product of a frequency grid, a spin-down grid, and a two-dimensional sky grid. Since the search maximizes the detection statistic over frequency and spin-down, the metric used to place grid points on the sky [183] may be obtained by minimizing the four-dimensional metric over frequency and spin-down and projecting it into the sky directions. As shown in the previous paragraph, this two-dimensional projected sky metric is well-approximated by assuming that the Earth is spinning about its axis but has its center of mass at rest. If the coherent integration period is an integer number of days, then by symmetry the two-dimensional metric on the sky is invariant under rotation about Earth's axis (∂_α is a Killing vector). This is still an approximate symmetry for the search described here, since the coherent integration period and T_{span} are longer than the rotation period (one day).

One can easily find coordinates in which this approximate sky metric (the four-dimensional metric, minimized over frequency and spin-down and projected onto the sky directions) is proportional to $\text{diag}(1, 1)$. These new sky-coordinates are obtained by perpendicular projection of a point on the two-sphere (celestial sphere) vertically down into the unit radius disk that lies in the equatorial plane. If $\hat{\mathbf{n}}$ denotes a unit vector

pointing from the SSB to the source the new coordinates are the components of $\hat{\mathbf{n}}$ in the equatorial plane: $n_x = \cos \delta \cos \alpha$, $n_y = \cos \delta \sin \alpha$. Points which are equally spaced in these coordinates correspond to equal spacing in Doppler shift, since source Doppler shift due to the Earth's rotation is just proportional to the component of the source direction vector in the equatorial plane. It then follows from rotational invariance that (with these approximations) the projected sky metric in these coordinates is proportional to $\text{diag}(1, 1)$ [185]. The effect may be immediately seen in Figure 3.6: the grid of “equally-spaced” points forms a (roughly) uniform square grid on the unit radius disk in the equatorial plane. Computing the Jacobian of the coordinate transformation shows that in the original coordinates (α, δ) the coordinate-space density of grid points should be proportional to $|\cos \delta \sin \delta| = |\sin(2\delta)|$.

This simple behavior of the projected sky metric guides the construction of the coincidence-windows in the sky directions. Define polar coordinates (r, α) on the unit radius disk in the equatorial plane by $r = \cos \delta$. The coordinate boundaries of uniformly distributed coincidence cells containing a single parameter-grid point are then given by $r d\alpha = dr = \text{const}$. When written in terms of the original coordinates this becomes

$$\cos(\delta) d\alpha = |\sin(\delta)| d\delta = \text{const}. \quad (3.15)$$

This is not directly useful, because it is singular as $\delta \rightarrow 0$, but suggests a coincidence window size which varies with declination according to the model

$$\begin{aligned} \Delta\alpha(\delta) &= \Delta\alpha(0)/\cos(\delta) \\ \Delta\delta(\delta) &= \begin{cases} \Delta\delta(0) & \text{if } |\delta| < \delta_c, \\ \Delta\alpha(0)/|\sin(|\delta| - \kappa \Delta\alpha(0))| & \text{if } |\delta| \geq \delta_c. \end{cases} \end{aligned} \quad (3.16)$$

To ensure continuity at $\delta = \delta_c$, the transition point δ_c is defined by the condition $\Delta\alpha(0)/|\sin(|\delta_c| - \kappa \Delta\alpha(0))| = \Delta\delta(0)$. κ is a tuning parameter of order unity, described below. An example of this coincidence window model is shown in Figure 3.7.

For each of the 145 different 10 Hz bands, the window size is determined by the three constants $\Delta\alpha(0)$, $\Delta\delta(0)$ and κ . For each sky grid p these values are directly determined from the sky grids used in the search as follows. For each 10 Hz frequency band the maximum distances between adjacent declination points to either side are calculated for each of the 17 sky grids as a function of declination δ . In this way, 17 different overlaying curves $\Delta_j(\delta)$ (one per data segment) are obtained. These are indicated by the

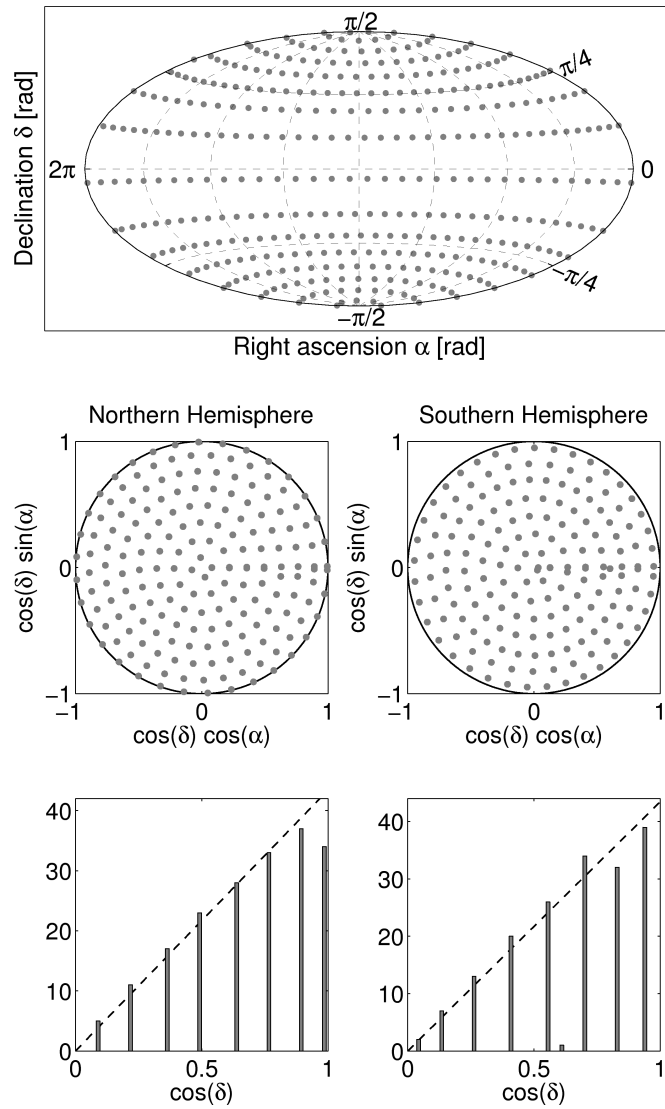


Figure 3.6: Example sky grid and its projection onto the equatorial plane. This sky grid corresponds to the data segment $j = 7$ used in the frequency range from 60 to 70 Hz. The top plot shows a Hammer-Aitoff projection of the sky grid. The middle plots show the projection of the sky-grid points in the northern hemisphere (left column) and in the southern hemisphere (right column) onto the equatorial plane. The bottom plots show histograms of $\cos(\delta)$ and the dashed line represents a linear fit to the distribution showing its uniformity.

circles in Figure 3.7 for a representative 510-520 Hz frequency band as illustration. Then the parameter $\Delta\delta(0)$ is obtained by considering the maximum separation to either side between all neighboring declination grid points *and* between the 17 different sky grids, increased by a 10% safety factor as

$$\Delta\delta(0) = 1.1 \max_{j,\delta} \{\Delta_j(\delta)\} . \quad (3.17)$$

The largest separations near the poles ($1.4 < |\delta| \leq \pi/2$) are then found and increased by a safety factor of 20% to determine the parameter $\Delta\alpha(0)$ via

$$\Delta\alpha(0) = 1.2 \max_{j,\delta} \{\Delta_j(|\delta| > 1.4)\} . \quad (3.18)$$

Finally, the parameter κ was chosen by visually examining diagrams similar to Figure 3.7 for all 145 of the 10 Hz bands. A κ value of 1.5 was found to be sufficient in most cases, while some bands required somewhat higher or lower values. For each triple of sky-coincidence parameters, tests were then performed to check that each sky-cell contained at least one sky-point from each data segment. In Figure 3.7 the complete declination coincidence window model given by Equation (3.16) is represented by the solid black curve.

The three parameters for all sky grids as a function of frequency are shown in Figure 3.8. As stated above, the sky grids are constant for 10 Hz-wide steps in frequency, and so these parameters vary with the same step-size.

3.5.7 Output of the coincidence search

The output of the post-processing pipeline is a list of the most coincident candidates. In each frequency band of coincidence-window width Δf , the coincidence cell containing the largest number of candidate events is found. Thus for each frequency band the pipeline finds the most coincident candidate maximized over the sky and over the spin-down parameter-range. The pipeline outputs the average frequency of the coincidence cell, the average sky position and spin-down of the candidate events, the number of candidate events in the coincidence cell, and the significance of the candidate.

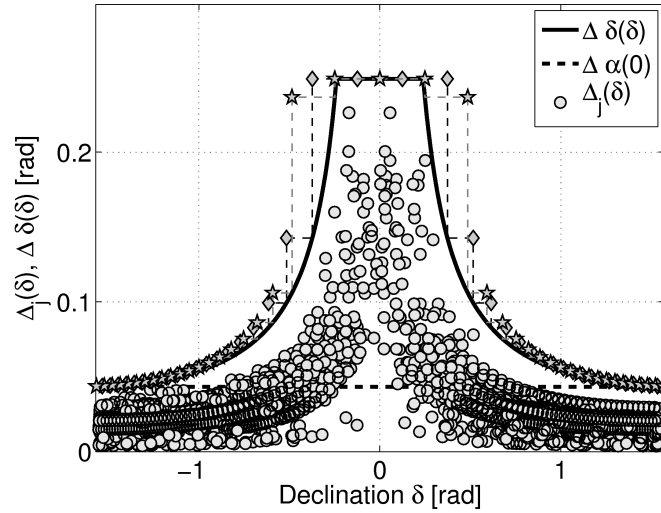


Figure 3.7: The sky coincidence-window model for the frequency band from 510 – 520 Hz. The horizontal axis shows the declination δ in radians. On the vertical axis, the circles labeled $\Delta_j(\delta)$ correspond to the maximum distance in radians to neighboring δ -points on either side. The solid curve shows the declination coincidence-window model $\Delta\delta(\delta)$ with the parameters $\Delta\delta(0) = 0.2489$, $\Delta\alpha(0) = 0.0433$, and $\kappa = 1.5$ used in this frequency band. It lies just above the largest declination separations shown. The stars denote the borders of the declination coincidence cell-grid and the diamonds represent the borders of the shifted declination coincidence cell-grid.

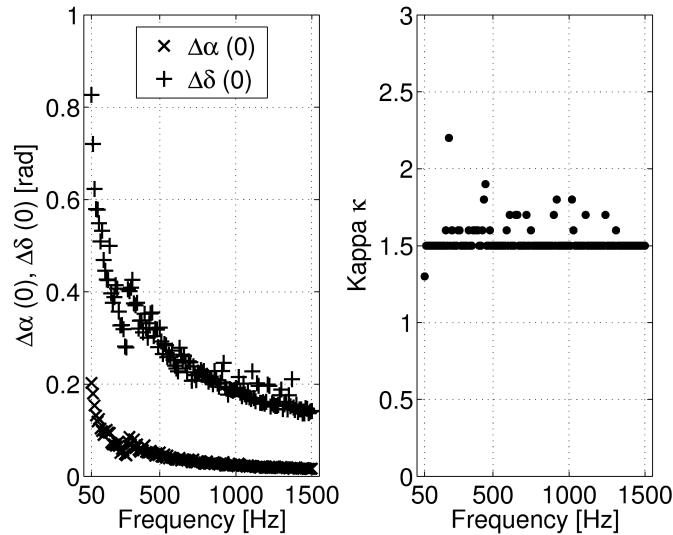


Figure 3.8: The parameters $\Delta\alpha(0)$, $\Delta\delta(0)$ and κ of the sky coincidence-window model as a function of the 10 Hz frequency band.

The “significance” of a candidate was first introduced in [124]. A candidate, consisting of the candidate events $1, \dots, Q$, has significance

$$\mathcal{S}(1, \dots, Q) = \sum_{q=1}^Q (\mathcal{F}_q - \ln(1 + \mathcal{F}_q)) , \quad (3.19)$$

where $Q \leq 17$ is the number of candidate events in the same coincidence cell. To understand the meaning of the significance, consider the case of pure Gaussian noise with no signal present. In this case the values of $2\mathcal{F}$ have a central χ^2 distribution with four degrees of freedom. The corresponding probability density function p_0 of $2\mathcal{F}$ is given by

$$p_0(2\mathcal{F}) = \frac{\mathcal{F}}{2} e^{-\mathcal{F}} . \quad (3.20)$$

The false alarm probability P_0 that $2\mathcal{F}$ exceeds a certain threshold $2\mathcal{F}_0$ when there is no signal present has the form

$$P_0(2\mathcal{F}_0) = (1 + \mathcal{F}_0) e^{-\mathcal{F}_0} . \quad (3.21)$$

The joint false alarm probability of candidate events $1, \dots, Q$ is given by

$$\prod_{q=1}^Q P_0(2\mathcal{F}_q) . \quad (3.22)$$

Therefore, in this analysis candidates are ranked according to

$$1 - \prod_{q=1}^Q P_0(2\mathcal{F}_q) = 1 - e^{-\mathcal{S}} , \quad (3.23)$$

where $\mathcal{S} = \sum_{q=1}^Q -\ln P_0(2\mathcal{F}_q)$ is exactly the significance defined in Equation (3.19). Thus ranking candidates by \mathcal{S} is equivalent to ranking them by false alarm probability: candidates with large positive significance would not be expected to occur in Gaussian random noise. As will be described later in Section 3.9 the significance is used to rank equally coincident candidates within the same narrow frequency-band. In such cases the candidate with the largest significance is considered.

The post-processing pipeline has been validated by internal testing, and review within the LIGO Scientific Collaboration, as well as using simulated CW signals created via so-called “software injections”. In addition, Section 3.8 presents realistic end-to-end testing

of the analysis pipeline using “hardware injections”, where simulated isolated-pulsar signals are physically added into the interferometer control systems to produce instrumental signals that are indistinguishable from those that would be produced by physical sources of gravitational waves.

3.6 Estimated sensitivity

The sensitivity of the search is estimated using Monte-Carlo methods for a population of simulated sources. The goal is to find the strain amplitude h_0 at which 10%, 50%, or 90% of sources uniformly populated over the sky and in their “nuisance parameters” (described below) would be detected. As previously discussed, the false alarm probability (of getting 7 or more coincidences in a 0.5 Hz frequency-band) is of order 10^{-3} . In this analysis, “detectable” means “produces coincident events in 12 or more distinct data segments”. The false alarm probability for obtaining 12 or more coincidences in a 0.5 Hz band is of order 10^{-14} , making it extremely unlikely for candidate events from random noise to show up consistently in 12 or more segments of data. This is therefore an estimate of the signal strength required for high-confidence detection. The pipeline developed for this purpose operates in 0.5 Hz frequency bands and consists of testing a large number of distinct simulated sources (trials) to see if they are detectable. A “trial” denotes a single simulated source which is probed for detection.

3.6.1 Iteration method

For every trial, source parameters are randomly chosen independent of the previous trial, except for the intrinsic amplitude h_0 . For the first trial h_0 is set to a starting value $30\sqrt{S_h/30\text{ h}}$. The rule for varying h_0 depends upon the last N_{last} trials, where $N_{\text{last}}^{10\%} = 100$, $N_{\text{last}}^{50\%} = 20$, and $N_{\text{last}}^{90\%} = 100$. In the past N_{last} trials, if more than 10%, 50%, or 90% of simulated sources have been detected then h_0 is *decreased* by $0.25 h_0/n_{\text{trial}}$ for the following trial, where n_{trial} is an integer in the range $0 \leq n_{\text{trial}} \leq 1000$ that is

incremented with each additional trial. On the other hand, if less than 10%, 50%, 90% of simulated sources have been detected then h_0 is *increased* by $0.25 h_0/n_{\text{trial}}$ for the next trial. This process is followed until h_0 has converged to a stationary range after 1000 trials. Then the median of h_0 is found using the h_0 -values starting from that trial, where the desired detection level has been reached the first time during the N_{last} trials. The following describes the pipeline for a single trial.

3.6.2 Population of simulated sources

For each trial, a random source frequency is chosen from a uniform distribution in a given 0.5 Hz frequency band and a frequency-derivative is drawn from a uniform distribution in the range covered by the Einstein@Home search. A sky position is chosen from a uniform distribution on the celestial sphere, and random values are chosen for the pulsar “nuisance parameters”. These are the inclination parameter $\cos(\iota)$, initial phase ϕ_0 , and polarization angle ψ as defined in [55], and are all drawn from the appropriate uniform distributions.

3.6.3 Determination of $2\mathcal{F}$ values for a single simulated source

The noise floors of the different SFTs are estimated at the source’s frequency intervals using a running median with a window of ± 25 frequency bins. Figure 3.1 showed the average of these for the data segments used from each instrument.

Then for each set of parameters the detection statistic $2\mathcal{F}$ is estimated using a semi-analytic method. From the estimated noise floor at the simulated source’s frequency and given the other source parameters, the expectation value of the \mathcal{F} -statistic is calculated analytically as given in [55]. A random number is then drawn from a non-central χ^2 distribution with four degrees of freedom and with the corresponding mean value.

These random numbers, drawn from the appropriate distribution of $2\mathcal{F}$ values, would be sufficient to determine the sensitivity of the search, if the template grid in parameter space were very closely spaced, so that the template bank always contained at least one waveform that was a very close match to the putative signal. However the grid in

parameter space used in this search is quite “coarse”, corresponding to a mismatch of 20% below 290 Hz and 50% above 300 Hz, so that the $2\mathcal{F}$ value that would be returned by the search might be significantly lower than the value drawn from the distribution above. To account for this effect, the sensitivity prediction considers the mismatch between the parameters of the simulated signals (determined by a random number generator) and the template grid points of the search (fixed as described earlier). For each simulated source, the search grid point that is nearest in the sense of the metric is located. Then, using the parameter-space metric, the mismatch between the simulated signal and the closest search template is computed. This gives the fractional amount by which the $2\mathcal{F}$ value is reduced.

From this ensemble of $2\mathcal{F}$ values, one can determine the number of coincidences that would be produced by each simulated source. As previously described, the post-processing sets an effective lower threshold on the \mathcal{F} -statistic of the retained candidate events. For each simulated source, these thresholds are determined by examining the exact workunits that would have contained the corresponding signal. Then the number of data segments for which the estimated $2\mathcal{F}$ values are above threshold is counted. If the $2\mathcal{F}$ values are above threshold in 12 or more of the 17 data segments, the simulated source is labeled as “detected”, else it is labeled as “undetected”.

3.6.4 Search sensitivity and estimated errors

Shown in Figure 3.9 are the resulting search sensitivity curves as functions of frequency. Each data point on the plot denotes the results of 1000 independent trials. These show the values of h_0 as defined in [55] such that 10%, 50%, and 90% of simulated sources produce 12 or more coincidences in the post-processing pipeline. The dominant sources of error in this sensitivity curve are uncertainties in the magnitudes of the LIGO detector response functions (calibration errors). Details of these frequency-dependent uncertainties may be found in reference [179]. The uncertainties are typically of order 5% (L1) and 8% (H1) in the frequency band from 50 – 1500 Hz, and are always less than 10%. Systematic errors, which arise because of the finite number of Monte-Carlo trials and similar effects, are less than $\pm 2\%$. These can be added in quadrature to the uncertainties given in [179] to obtain frequency-dependent error bounds in the sensitivity

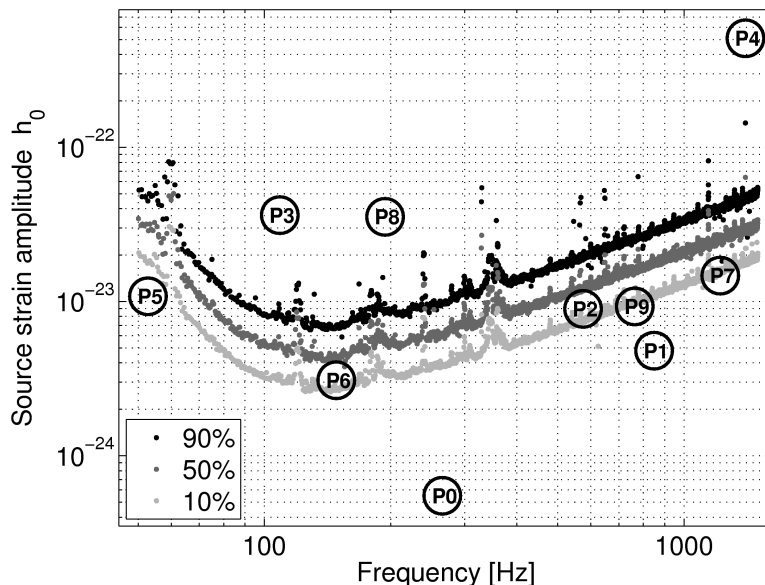


Figure 3.9: Estimated sensitivity of the Einstein@Home search for isolated CW sources in the LIGO S4 data set. The set of three curves shows the source strain amplitudes h_0 at which 10% (bottom), 50% (middle) and 90% (top) of simulated sources would be confidently detected by the Einstein@Home pipeline (appearing in coincidence in 12 or more of the 17 data segments). The centers of the circles labeled P0 to P9 give the strain amplitudes of the S4 hardware injections as listed in Table 3.5. Based on this curve, one would expect that the simulated signals P3, P4 and P8 could be confidently detected, and that P0, P1 and P5 would not be detected.

curve. The resulting error in this sensitivity plot is below 10% at all frequencies.

The behavior of the curves shown in Figure 3.9 essentially reflect the instrument noise given in Figure 3.1. One may fit the curves obtained in Figure 3.9 to the strain noise power spectral density $S_h(f)$ and then describe the three sensitivity curves in Figure 3.9 by

$$h_0^{\mathcal{D}}(f) \approx R_{\mathcal{D}} \sqrt{\frac{S_h(f)}{30 \text{ h}}}, \quad (3.24)$$

where the pre-factors $R_{\mathcal{D}}$ for different detection probabilities levels $\mathcal{D} = 90\%$, 50% , and 10% are well fit below 300 Hz by $R_{90\%} = 31.8$, $R_{50\%} = 20.1$, and $R_{10\%} = 12.6$, above 300 Hz by $R_{90\%} = 33.2$, $R_{50\%} = 21.0$, and $R_{10\%} = 12.9$.

Some other published CW searches were done at 95% detection confidence. For comparison in the next section, the sensitivity of *this* search at that confidence is $R_{95\%} =$

36.2 below 300 Hz and $R_{95\%} = 37.9$ above 300 Hz. The iteration method previously described used $N_{\text{last}}^{95\%} = 200$.

3.6.5 Comparison with other search and upper-limit methods

The methods used here would be expected to yield very high confidence if a strong signal were present. It is interesting to compare the sensitivity of this detection method with the sensitivity of CW upper limits such as that of reference [124]. The sensitivity of the high-confidence detection method used here is well-described by Equation 3.24. The same equation describes the results of the S2 \mathcal{F} -statistic loudest-event upper limit analysis [124], but in that work the 95% detection confidence curve has a pre-factor $R_{95\%} = 29.5$. It is useful to understand the source of this apparent difference in sensitivity (a factor of $37.9/29.5 = 1.28$). There are three main contributors to this difference.

The most significant difference between the two analyses is the spacing of the search grid templates. In this search, the templates are significantly farther apart (worst-case 50% loss of signal-to-noise ratio, or expected $2\mathcal{F}$) than in [124], where the worst-case mismatch was negligible. This effect of employing different mismatches has been studied by running the sensitivity estimation pipeline using simulated sources only at the template grid points, and reduces $R_{95\%}$ in Equation (3.24) by a factor of 1.17.

Another difference between the two analyses is the detection criteria. In this work, detection requires a signal to produce 12 or more coincidences between the 17 different data segments. This corresponds to a false alarm probability (in Gaussian noise) of order 10^{-14} per 0.5 Hz frequency-band. This is different from [124], where simulated signals are compared against the loudest candidate found (largest $2\mathcal{F}$). An equivalent detection criterion for *this* work would be to compare the simulated signals against the loudest candidates (per 0.5 Hz band). These typically had 7 or 8 coincidences, corresponding to a Gaussian noise false alarm probability of order 10^{-3} and 10^{-5} , respectively. To estimate the effect on the sensitivity, the sensitivity estimation pipeline was rerun, but now requiring the signal to exceed the $2\mathcal{F}$ -thresholds in only 7 of the 17 data segments. This reduced $R_{95\%}$ in Equation (3.24) by an additional factor of 1.14.

The least important difference between the two analyses is the effective threshold

on the \mathcal{F} -statistic. As explained in Sections 3.5.1 and 3.5.3, only a subset of candidate events with the largest values of $2\mathcal{F}$ are retained in the post-processing, fixing the false alarm probability. The smallest $2\mathcal{F}$ -value on this list is typically around 28 or slightly higher. In [124] a fixed threshold of $2\mathcal{F} = 20$ has been used. Then, events with a combined significance below $\mathcal{S} = 64.4$ [see Equation (3.19)] were also dropped. While it is difficult to compare these two criteria, they seem to be fairly close.

Taken together, the differences in grid spacing and detection thresholds are responsible for, and explain, the sensitivity difference in the two analyses (a factor of $1.17 \times 1.14 = 1.33 \approx 1.28$).

3.7 Vetoing of instrumental line artifacts

When the instrument data was prepared and cleaned, narrow-band instrumental line features of known origin were removed, as previously described in Section 3.3. However, the data also contained stationary instrumental line features that were not understood, or were poorly understood. These features were *not* removed from the input data for the search. As a consequence, the output from the post-processing pipeline contains instrumental artifacts that in some respects mimic CW signals. But these artifacts tend to cluster in certain regions of parameter space, and in many cases they can be automatically identified and vetoed. In previous incoherent searches for CW sources in LIGO data [158] the S-veto method has been employed, which excludes the regions of parameter space where there is little or no frequency modulation from the Earth's motion, leading to a relatively stationary detected frequency. This cannot directly be applied to a coherent matched-filtering search using the \mathcal{F} -statistic. Thus the method used here will be similar, but arises from a conceptually different approach that is appropriate for an \mathcal{F} -statistic search.

3.7.1 Parameter space locations of instrumental lines

For a coherent observation of 30 h the parameter-space regions where instrumental lines tend to appear in certain regions of parameter space. Chapter 5 shows that these regions are determined by global-correlation hypersurfaces of the \mathcal{F} -statistic in parameter space. The locations of such instrumental-line candidate events are found in Section 5.6 to be described by

$$\dot{f} + \frac{(\boldsymbol{\omega} \times \mathbf{v}_{\text{av}}) \cdot \hat{\mathbf{n}}}{c} f(t_{\text{fiducial}}) = 0, \quad (3.25)$$

where c denotes the speed of light, $\hat{\mathbf{n}}$ is a unit vector pointing to the source's sky-location in the SSB frame and relates to the equatorial coordinates α and δ by $\hat{\mathbf{n}} = (\cos \delta \cos \alpha, \cos \delta \sin \alpha, \sin \delta)$, $\boldsymbol{\omega}$ is the angular velocity vector of the Earth as it orbits around the Sun ($|\boldsymbol{\omega}| \approx 2\pi/\text{year}$) and \mathbf{v}_{av} is the average velocity of the Earth ($|\mathbf{v}_{\text{av}}| \approx 9.9 \times 10^{-5} c$). This equation can also be understood on simple physical grounds. The l.h.s. of Equation (3.25) is the rate of change of detector output frequency, for a source whose SSB frequency and spin-down are f and \dot{f} . An instrumental line, which has fixed detector frequency, mimics such a source when the l.h.s. vanishes.

The potential CW sources whose locations in parameter space are consistent with Equation (3.25) will not produce a modulation pattern that would distinguish them from an instrumental line. As the resolution in parameter space is finite, the post-processing analysis eliminates (vetoes) candidates that satisfy the condition

$$\left| \dot{f} + \frac{(\boldsymbol{\omega} \times \mathbf{v}_{\text{av}}) \cdot \hat{\mathbf{n}}}{c} f(t_{\text{fiducial}}) \right| < \epsilon, \quad (3.26)$$

where the parameter $\epsilon > 0$ accounts for a certain tolerance needed due to the parameter-space gridding. This tolerance-parameter can be understood as

$$\epsilon = \frac{\Delta f}{\Delta T} N_{\text{cell}}, \quad (3.27)$$

where Δf denotes width in frequency (corresponding to the coincidence-cell width in the post-processing) up to which candidate events can be resolved during the characteristic length of time ΔT , and N_{cell} represents the size of the vetoed or rejected region, measured in coincidence cells. In this analysis $\Delta T = 2\,122\,735 \text{ s}$ (≈ 24 days) is the total time interval spanned by the data

$$\Delta T = \left| \max_j t_j^{\text{end}} - \min_j t_j \right| = t_{11}^{\text{end}} - t_4. \quad (3.28)$$

For potential sources that satisfy (3.26), the modulation due to the Earth's motion does not make the signal appear in more than N_{cell} coincidence cells during ΔT .

3.7.2 Fraction of parameter space excluded by the veto

One can visualize and calculate the volume of the region in four-dimensional parameter space that is excluded by this veto. For a given source sky position, Equation (3.26) is linear in f and \dot{f} . Thus, for fixed sky position $\hat{\mathbf{n}}$, the veto condition (3.26) defines two parallel lines in the (f, \dot{f}) -plane. Candidate events that lie in the region between the lines are discarded (vetoed). Candidates that lie outside this region are retained (not vetoed). The locations of these two lines in the (f, \dot{f}) plane depend upon the sky position. The fractional volume excluded by the veto depends upon whether or not (as the source position varies over the sky) the excluded region between the lines lies inside or outside of the boundaries of the search, or intersects it. In this work, for the search region $-f/\tau < \dot{f} < 0.1 f/\tau$ described in the Abstract, the excluded region lies entirely within the parameter space above 300 Hz, but crosses the boundaries below 300 Hz. This is because a wider range of spin-down ages is searched below 300 Hz.

The fractional volume of the region in parameter space excluded by the veto method may be easily calculated. Since the time ΔT is small compared to one year, one may use the following approximation

$$(\boldsymbol{\omega} \times \mathbf{v}_{\text{av}}) \cdot \hat{\mathbf{n}} \approx |\boldsymbol{\omega}| |\mathbf{v}_{\text{av}}| \cos \theta, \quad (3.29)$$

where $\theta \in [0, \pi]$ is the angle between the SSB-to-Earth vector and the source sky position $\hat{\mathbf{n}}$. The veto condition (3.26) may then be rewritten as

$$|\dot{f} + \gamma f \cos \theta| < \epsilon, \quad (3.30)$$

where γ is defined as $\gamma = |\boldsymbol{\omega}| |\mathbf{v}_{\text{av}}|/c$. For fixed values of f and \dot{f} the situation is depicted in Table 3.4. Depending upon the values of $(\pm\epsilon - \dot{f})/\gamma f$, a part of the sky might be excluded by the veto. As shown in the Table, there are six possible cases,

determined by the values of

$$\cos \theta_- = \frac{\epsilon - \dot{f}}{\gamma f} \quad \text{and} \quad (3.31)$$

$$\cos \theta_+ = \frac{-\epsilon - \dot{f}}{\gamma f}. \quad (3.32)$$

For example in the case (labeled case 4 in Table 3.4) where both $\cos \theta_-$ and $\cos \theta_+$ lie in the range $[-1, 1]$ then the excluded region of the sky is an annulus defined by $0 \leq \theta_- < \theta < \theta_+ \leq \pi$, and the excluded solid angle is

$$\Omega_{\text{excluded}} = \int_0^{2\pi} d\phi \int_{\theta_-}^{\theta_+} d\theta \sin \theta \quad (3.33)$$

$$= 2\pi(\cos \theta_- - \cos \theta_+). \quad (3.34)$$

The fraction of sky excluded in this case is then

$$\frac{\Omega_{\text{excluded}}}{4\pi} = (\cos \theta_- - \cos \theta_+)/2 \quad (3.35)$$

$$= \frac{\epsilon}{\gamma f} \quad (3.36)$$

$$= \epsilon \frac{c}{|\boldsymbol{\omega}| |\mathbf{v}_{\text{av}}|} \frac{1}{f}. \quad (3.37)$$

In the other cases listed in Table 3.4 the excluded region of the sky might be a cap about $\theta = 0$ or about $\theta = \pi$ or the null set, or the entire sky.

Table 3.4: For given values of frequency f and spin-down \dot{f} , this shows the fractional volume of the sky excluded by the veto (3.26). There are six possible cases, depending upon the values of $\cos \theta_-$ and $\cos \theta_+$. (There are six rather than nine cases because $\cos \theta_+$ is never greater than $\cos \theta_-$.) For the ranges of f and \dot{f} considered in this work, case 4 applies above 300 Hz. Between 50 Hz and 300 Hz, because of the wider range of \dot{f} considered, the three cases 4, 5 and 6 are found. Values of $\cos \theta$ outside the range $[-1, 1]$ correspond to imaginary (unphysical) values of θ . In such cases the upper and/or lower limits of integration are replaced by $\theta = \pi$ or $\theta = 0$ respectively, as can be seen from the final column of this table.

Case	Range of $\cos \theta_+ = \frac{-\epsilon - \dot{f}}{\gamma f}$	Range of $\cos \theta_- = \frac{\epsilon - \dot{f}}{\gamma f}$	Excluded sky fraction $\Omega_{\text{excluded}}/4\pi$
1	$(-\infty, -1)$	$(-\infty, -1)$	0
2	$(-\infty, -1)$	$[-1, 1]$	$(\cos \theta_- + 1)/2 = (1 + \frac{\epsilon - \dot{f}}{\gamma f})/2$
3	$(-\infty, -1)$	$(1, \infty)$	1
4	$[-1, 1]$	$[-1, 1]$	$(\cos \theta_- - \cos \theta_+)/2 = \epsilon/\gamma f$
5	$[-1, 1]$	$(1, \infty)$	$(1 - \cos \theta_+)/2 = (1 + \frac{\epsilon + \dot{f}}{\gamma f})/2$
6	$(1, \infty)$	$(1, \infty)$	0

In this search, the fraction of the sky excluded for frequencies $f \in [300, 1500)$ Hz has been fixed at the constant fraction $\Omega_{\text{excluded}}/4\pi = 30\%$. This is equivalent to choosing ϵ to be a linear function of frequency

$$\epsilon = 0.3 \frac{|\boldsymbol{\omega}| |\mathbf{v}_{\text{av}}|}{c} f. \quad (3.38)$$

In this search, the fraction of the sky excluded for frequencies $f \in [50, 300)$ Hz has been chosen to depend upon the value of \dot{f} . The instruments allow (e.g. compare with Figure 3.19) the use of a frequency-independent value $\epsilon = 5.4 \times 10^{-10}$ Hz/s which corresponds to $N_{\text{cell}} = 1.5$. Within the region of parameter space which is searched ($-f/\tau < \dot{f} < 0.1 f/\tau$ for $\tau = 1000$ years) cases 4, 5, or 6 from Table 3.4 occur depending of the spin-down value \dot{f} . If

$$\dot{f} > \epsilon - \frac{|\boldsymbol{\omega}| |\mathbf{v}_{\text{av}}| f}{c}, \quad (3.39)$$

then case 4 of Table 3.4 applies, and the fraction of sky excluded is given by

$$\frac{\Omega_{\text{excluded}}}{4\pi} = \epsilon \frac{c}{|\boldsymbol{\omega}| |\mathbf{v}_{\text{av}}| f}. \quad (3.40)$$

This fraction ranges from 52% at 50 Hz to 8.7% at 300 Hz. If \dot{f} is in the interval

$$\dot{f} \in \left[-\epsilon - \frac{|\boldsymbol{\omega}| |\mathbf{v}_{\text{av}}| f}{c}, \epsilon - \frac{|\boldsymbol{\omega}| |\mathbf{v}_{\text{av}}| f}{c} \right], \quad (3.41)$$

then case 5 of Table 3.4 applies, and the fraction of sky excluded is given by

$$\frac{\Omega_{\text{excluded}}}{4\pi} = \frac{1}{2} \left(1 + \frac{\epsilon + \dot{f}}{f |\boldsymbol{\omega}| |\mathbf{v}_{\text{av}}| / c} \right). \quad (3.42)$$

Finally, if

$$\dot{f} < -\epsilon - \frac{|\boldsymbol{\omega}| |\mathbf{v}_{\text{av}}| f}{c}, \quad (3.43)$$

then case 6 applies and none of the sky is excluded by the veto: $\Omega_{\text{excluded}} = 0$. Below 300 Hz, one can compute a uniform average of the excluded sky fraction over the spin-down range considered in this analysis. As shown in Figure 3.10 this gives an excluded sky fraction of 36% at 50 Hz and 6% just below 300 Hz.

The resulting fraction of sky excluded by the veto (uniformly averaged over spin-down) as a function of frequency is shown in Figure 3.10. In this search, the fraction of

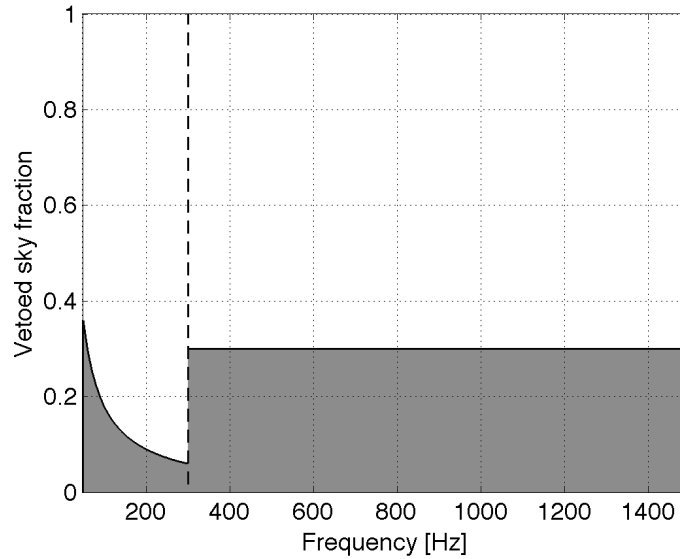


Figure 3.10: The average fraction of sky excluded by the veto method as a function of frequency, uniformly averaged over the searched spin-down range.

the sky excluded for frequencies $f \in [300, 1500)$ Hz has been fixed at the constant fraction 30%. In this search, the fraction of the sky excluded for frequencies $f \in [50, 300)$ Hz has been chosen to depend upon the values of f and \dot{f} , where the uniform average of the excluded sky fraction over the spin-down range considered in this analysis is 36% at 50 Hz and 6% just below 300 Hz. In Section 3.9, Figure 3.19 will present a conclusion diagram illustrating which of the candidates have been vetoed in this search.

3.8 Hardware-injected signals

A good way to test and validate search algorithms and code is to add simulated signals into the detector’s data stream. This can either be done while the experiment is in progress (real-time injections) or after the data has been collected (software injections). If it is done while the experiment is in progress, the simulated signals can either be added into the hardware (into feedback and error-point control signals) or after data acquisition.

At the time that the S4 run was carried out, ten simulated CW signals were injected at the hardware level: using magnetic coil actuators, the interferometer mirrors were physically made to move as if a gravitational wave was present.

3.8.1 Parameters of hardware injections

Table 3.5 shows the parameters of the hardware injections that were carried out at the LIGO detectors during the S4 run, mimicking gravitational-wave signals from ten different isolated pulsars with different frequencies, sky locations, and frequency derivatives. The ten artificial pulsars are denoted Pulsar0 to Pulsar9. At the time of the injections, lack of complete knowledge of the instrument's response function (calibration) meant that the actual hardware injections did not actually have the intended strain amplitudes as given in the Table. The effective strain amplitudes may be computed from correction factors provided in reference [158]. These factors are 1.12 for all simulated pulsars in the H1 detector. In the L1 detector, the correction factor is 1.11 for all simulated pulsars, except for Pulsar1 (1.15) and Pulsar9 (1.18).

Table 3.5: Parameters for hardware-injected CW signals during the S4 run, labeled Pulsar0 to Pulsar9. The parameters are defined at the GPS reference time $t_{\text{ref}} = 793130413$ s in the Solar System Barycenter. These are the frequency $f(t_{\text{ref}})$, the spin-down \dot{f} , the sky position right ascension α and declination δ , the polarization angle ψ , the initial phase Φ_0 , the inclination parameter $\cos \iota$, and the dimensionless strain amplitude h_0 . Because the calibration was only accurately determined after S4 was finished, the H1 strain amplitudes should be multiplied by the correction factor 1.12. The L1 amplitudes should be multiplied by 1.15 for Pulsar1, 1.18 for Pulsar9, and 1.11 for the others.

Name	$f(t_{\text{ref}})$ [Hz]	\dot{f} [Hz s ⁻¹]	α [rad]	δ [rad]	ψ [rad]	Φ_0 [rad]	$\cos \iota$ [rad]	h_0
Pulsar0	265.57693318	-4.15×10^{-12}	1.248817	-0.981180	0.770087	2.66	0.794905	4.93×10^{-25}
Pulsar1	849.07086108	-3.00×10^{-10}	0.652646	-0.514042	0.356036	1.28	0.463799	4.24×10^{-24}
Pulsar2	575.16356732	-1.37×10^{-13}	3.756929	0.060109	-0.221788	4.03	-0.928575	8.04×10^{-24}
Pulsar3	108.85715940	-1.46×10^{-17}	3.113189	-0.583579	0.444280	5.53	-0.080666	3.26×10^{-23}
Pulsar4	1402.11049084	-2.54×10^{-08}	4.886707	-0.217584	-0.647939	4.83	0.277321	4.56×10^{-22}
Pulsar5	52.80832436	-4.03×10^{-18}	5.281831	-1.463269	-0.363953	2.23	0.462937	9.70×10^{-24}
Pulsar6	148.44006451	-6.73×10^{-09}	6.261385	-1.141840	0.470985	0.97	-0.153727	2.77×10^{-24}
Pulsar7	1220.93315655	-1.12×10^{-09}	3.899513	-0.356931	0.512323	5.25	0.756814	1.32×10^{-23}
Pulsar8	193.94977254	-8.65×10^{-09}	6.132905	-0.583263	0.170471	5.89	0.073904	3.18×10^{-23}
Pulsar9	763.8473216499	-1.45×10^{-17}	3.471208	1.321033	-0.008560	1.01	-0.619187	8.13×10^{-24}

3.8.2 Duty cycle of hardware injections

During S4 the hardware injections were not active all of the time. Table 3.6 shows the fractional overlap between the times when the hardware injections were active and the times of the S4 Einstein@home data segments. As can be seen from the table, the hardware injections were only turned on during 12 of the data segments analyzed in this analysis, and for 2 of those 12 data segments, the injections were only turned on for about 20% of the data taking time. In the remaining 10 data segments, the hardware injections were turned on for almost the entire segment. This needs to be taken into account when analyzing the Einstein@Home search results for these injections. Because of this, the maximum possible number of coincidences expected from these simulated signals is 12, even though 17 data segments are searched.

3.8.3 Results from the hardware injections

For each hardware-injected pulsar signal Table 3.7 compares a prediction for the outcome of the Einstein@Home search to the actual results found through the Einstein@Home analysis pipeline. The predicted values given in Table 3.7 are obtained by feeding the sensitivity-estimation pipeline, which was described in Section 3.6, with the parameters of the simulated pulsars and only considering data segments where the hardware injections were active.

As shown in Table 3.7 and consistent with Figure 3.9, the hardware-injected signals Pulsar0, Pulsar1, Pulsar5 and Pulsar6 are too weak to be confidently detected by the search. In contrast, Pulsar2, Pulsar3, Pulsar4 and Pulsar8 are clearly detected. The parameters of Pulsar7 and Pulsar9 are such that in both cases the search pipeline found 7 coincidences, but this is consistent with the level of coincidences that would result from Gaussian noise with no signal present, and so these are not confidently detected.

Figure 3.11 presents the results of the search for all hardware injections. Small subspaces of the search parameter space around the hardware injections are shown, as well as the locations of the artificial signal parameters. The subspaces considered in Figure 3.11 and also for the (measured) results presented in Table 3.7 are constrained to a band of $2 \times 10^{-4} f$ to either side of the injected frequency. This choice of frequency-

Table 3.6: The time overlap between the Einstein@Home data segments and the hardware injections. The hardware injections were only turned on about 2/3 of the time. The columns are data segment index j , detector, the duration of the overlap, and the fractional overlap (obtained by dividing the third column by $30 \text{ h} = 108\,000 \text{ s}$).

j	Detector	Overlapping Duration [s]	Fractional Overlap
1	H1	107201	99.3 %
2	H1	107554	99.6 %
3	H1	107272	99.3 %
4	H1	0	0
5	H1	99799	92.4 %
6	H1	0	0
7	H1	101991	94.4 %
8	H1	21268	19.7 %
9	H1	100773	93.3 %
10	H1	0	0
11	L1	23164	21.5 %
12	L1	106760	98.9 %
13	L1	107294	99.4 %
14	L1	102711	95.1 %
15	L1	0	0
16	L1	0	0
17	L1	98696	91.4 %

bandwidth is motivated by the maximum Doppler shift due to the Earth orbital motion.

The significant sky position offset between the a priori location of the simulated source and the location where the search located the source with respect to the detected signals Pulsar4 and Pulsar8 is explained by the global correlations [3] in parameter space, which are studied in detail in Chapter 5. This arises because for Pulsar4 and Pulsar8, the spin-down range that is searched (region between dashed lines in the far right column) is too small to include the actual spin-down value used in creating the simulated signals. Due to the global parameter-space correlations the offset between the actual and detected spin-down value gives rise to the offset in the sky position. The observed structure of large-coincident events in the sky is consistent with the global-correlation hypersurface description in Chapter 5. This is also why Pulsar4 shows a considerable

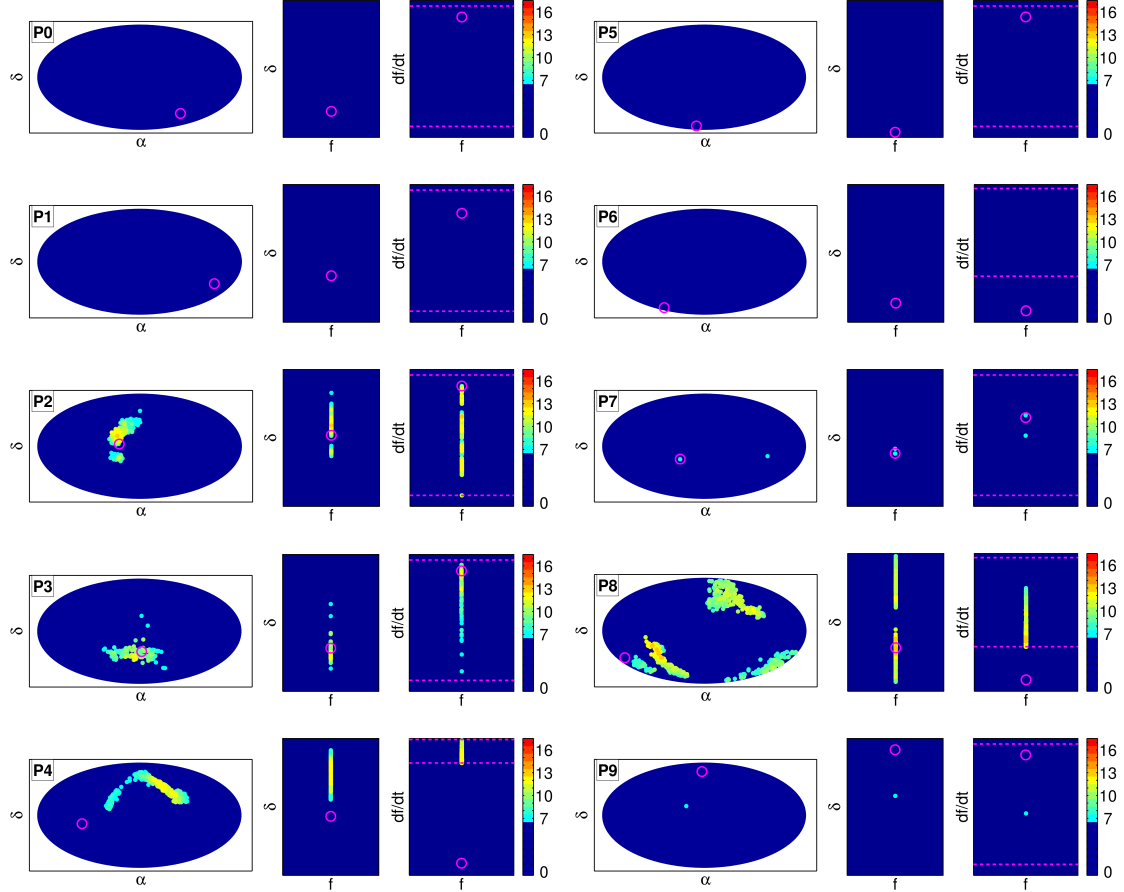


Figure 3.11: Einstein@Home results showing the 10 hardware-injected CW signals labeled P0 to P9. Here, a narrow band of width $2 \times 10^{-4} f$ to either side of each injection's frequency f is considered. The color-bar in each plot indicates the number of coincidences. As shown in the color-scale, only candidates having 7 or more coincidences appear. For each hardware injection a group of three different sub-plots are given representing different projections of the parameter space. The left sub plot is a Hammer-Aitoff projection of the entire sky. The middle sub-plot shows declination δ versus frequency f . The right sub-plot shows spin-down \dot{f} versus frequency f , where the region between the two horizontal magenta dashed lines refers to searched range of spin-downs. The center of a magenta circle represents the location of the injection. P4 and P8 appear at the wrong sky position because their intrinsic spin-downs lie outside the searched range. Table 3.7 shows a comparison with the expectations for these simulated signals.

Table 3.7: The estimated (predicted) and obtained (measured) results for the hardware-injected pulsar signals. For each simulated signal the predicted number of coincidences \mathcal{C} and a predicted value for the significance \mathcal{S} is given, as well as the measured number of coincidences and measured value for the significance from the Einstein@Home search. The measured values are obtained by maximizing over a narrow band of $2 \times 10^{-4} f$ on either side of the injection frequency, the whole sky and the entire spin-down range. As explained in the text, Pulsar4 and Pulsar8 are not expected to have the correct significance. Pulsar0, Pulsar1, Pulsar5 and Pulsar6 are not listed. They are so weak that they produce less than 7 coincidences, consistent with random noise containing no signal.

Name	Predicted \mathcal{C}	Measured \mathcal{C}	Predicted \mathcal{S}	Measured \mathcal{S}
Pulsar2	12	13	263.1	249.3
Pulsar3	12	12	3160.9	2397.5
Pulsar4	12	12	35108.2	1749.6
Pulsar7	6	7	93.2	100.0
Pulsar8	12	13	3692.6	2263.6
Pulsar9	7	7	131.2	98.9

discrepancy between the significance that would have been expected if the search-grid had also covered the a priori parameters, and the significance that was actually observed in the search, as shown in Table 3.7.

3.9 Results

This Section presents the results of the Einstein@Home S4 CW search. Figures 3.12 and 3.13 give a summary of all post-processing results, from 50 to 1500 Hz. In Figure 3.12 the coincidences and significance of all candidates that have 7 or more coincidences are shown as functions of frequency. Figure 3.13 presents the same information as given in Figure 3.12, but projected on the sky, and showing all cells that have more than 7 candidate events.

In Figure 3.13 the number of coincidences is maximized over the entire sky and

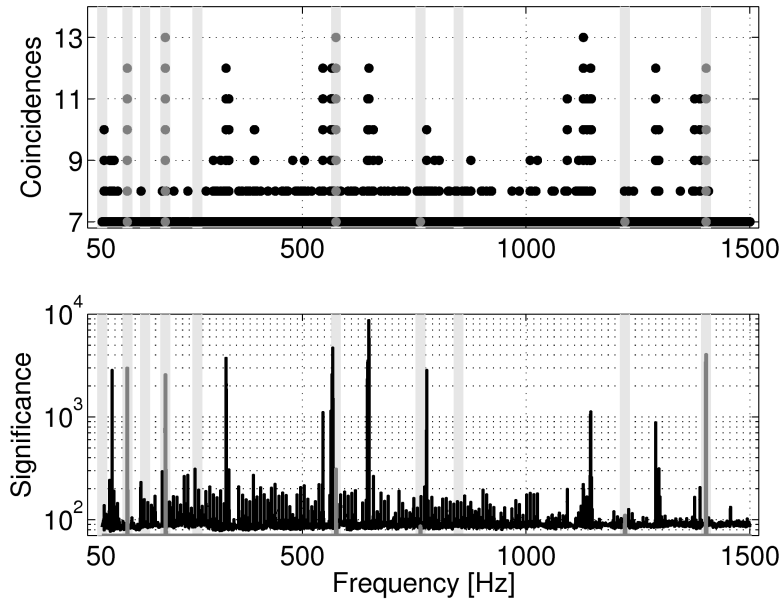


Figure 3.12: Numbers of coincidences of 7 or more (top) and the significance (bottom) of all candidates found in the Einstein@Home post-processing, shown as functions of frequency. The light-gray shaded rectangular regions highlight the S4 hardware injections, listed in Table 3.5. The data points colored in dark-gray show the candidates resulting from the hardware-injected CW signals.

full spin-down range. The color indicates the numbers of coincidences, where the same color-scale has been used in each plot. The maximum possible number of coincidences ranges from a minimum of 0 to a maximum of 17 (the number of data segments analyzed). The meaning of 0 coincidences is that there is no candidate event found, 1 coincidence means a single candidate events is found (which is always coincident with itself).

Illustrative examples of different types of typical post-processing results in four individual 10 Hz bands are shown in Figures 3.14, 3.15, 3.16, and 3.17. Figure 3.14 shows a 10 Hz frequency band containing pure Gaussian noise. Figure 3.15 shows the frequency band of the hardware-injected signal Pulsar2. Figure 3.16 shows a “quiet” 10 Hz band of real instrument data without any “noisy” lines. In contrast to this, Figure 3.17 shows a noisy band which is polluted by instrumental noise artifacts.

Table 3.8 shows all candidates (cells) which have 10 or more coincidences. In cases where a set of candidates is clustered together at slightly different frequencies, Table 3.8

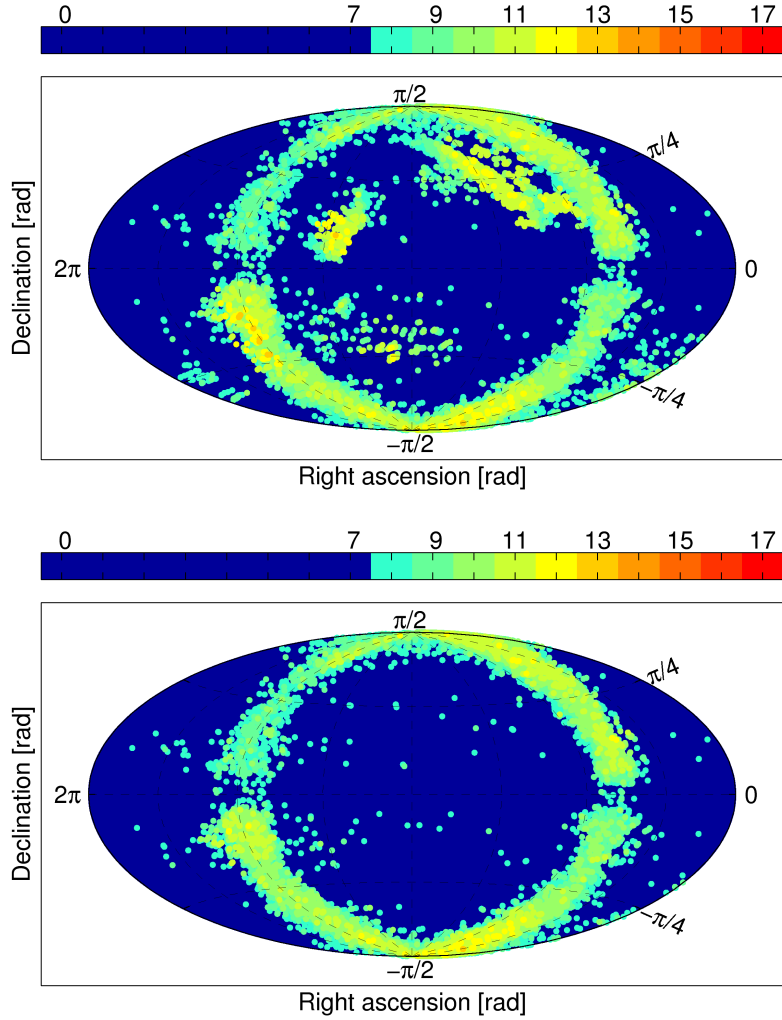


Figure 3.13: All candidates obtained from the post-processing that have more than 7 coincidences, shown in Hammer-Aitoff projections of the sky. The color-bar indicates the number of coincidences of a particular candidate (cell). The upper plot includes the S4 hardware-injected pulsars. In the lower plot, bands of $2 \times 10^{-4} f$ width to either side of the hardware injections' frequencies f have been removed.

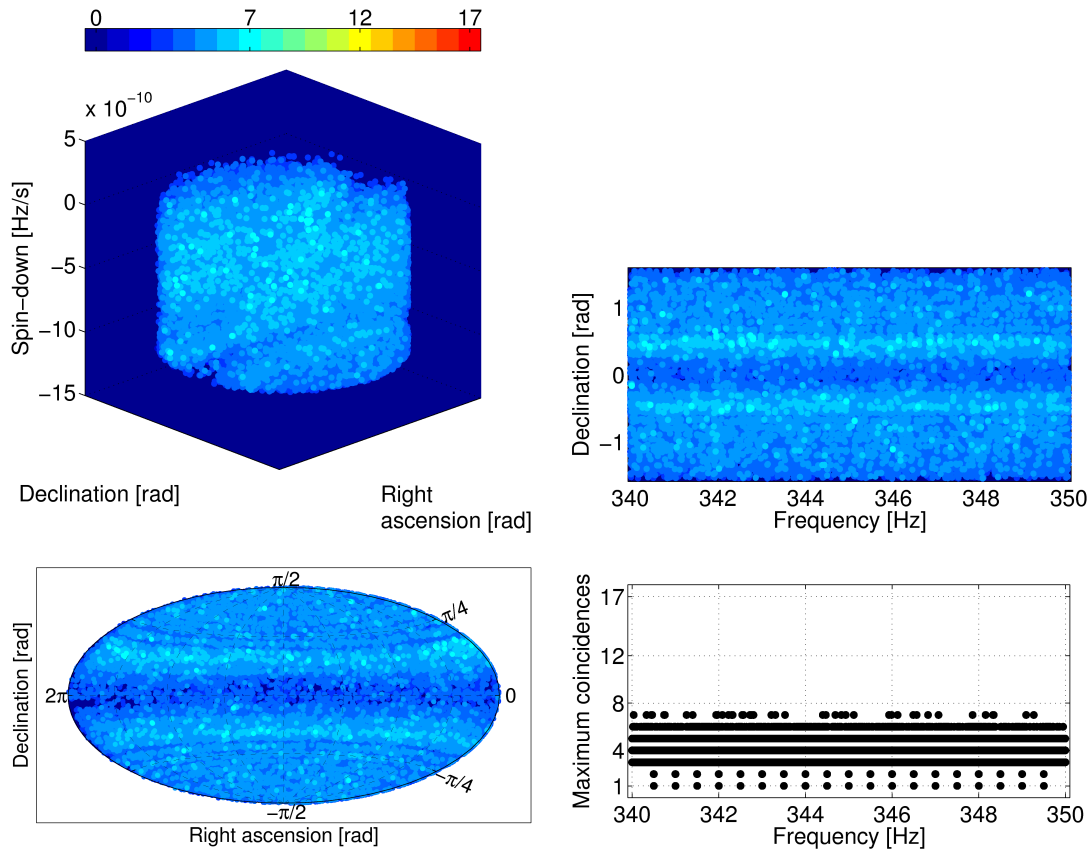


Figure 3.14: Einstein@Home S4 Post-Processing results for the frequency band 340.0–350.0 Hz, which is pure Gaussian noise for L1 and mostly Gaussian noise for H1. This is because in this band the line-cleaning process has replaced all the L1 data and most of the H1 data with computer-generated random numbers (see Table 3.2). From top to bottom, left to right, the different plots show the numbers of coincidences in a 3D map of sky and spin-down, in a 2D plot of declination over frequency, in a 2D Hammer-Aitoff projection of the sky, and in a histogram as a function of frequency.

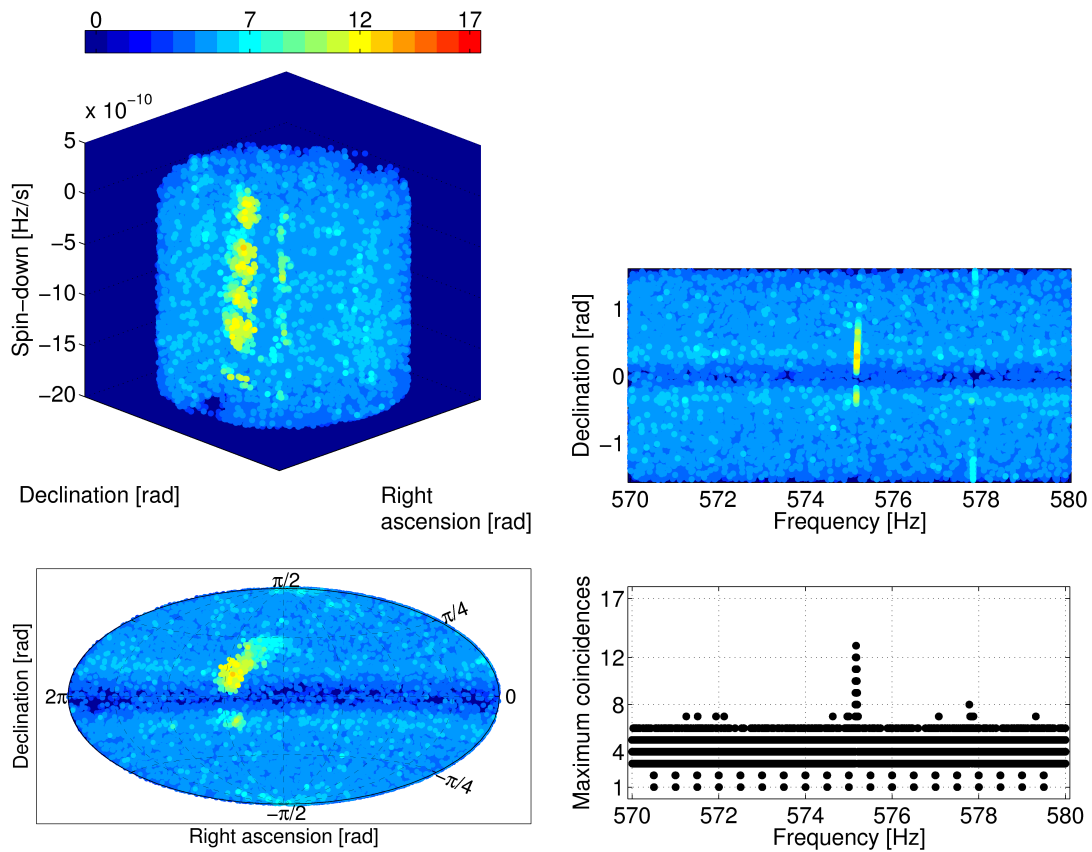


Figure 3.15: Einstein@Home S4 Post-Processing results for the frequency band 570.0–580.0 Hz including a hardware injected CW signal (Pulsar2). From top to bottom, left to right, the different plots show the numbers of coincidences in a 3D map of sky and spin-down, in a 2D plot of declination over frequency, in a 2D Hammer-Aitoff projection of the sky, and in a histogram as a function of frequency.

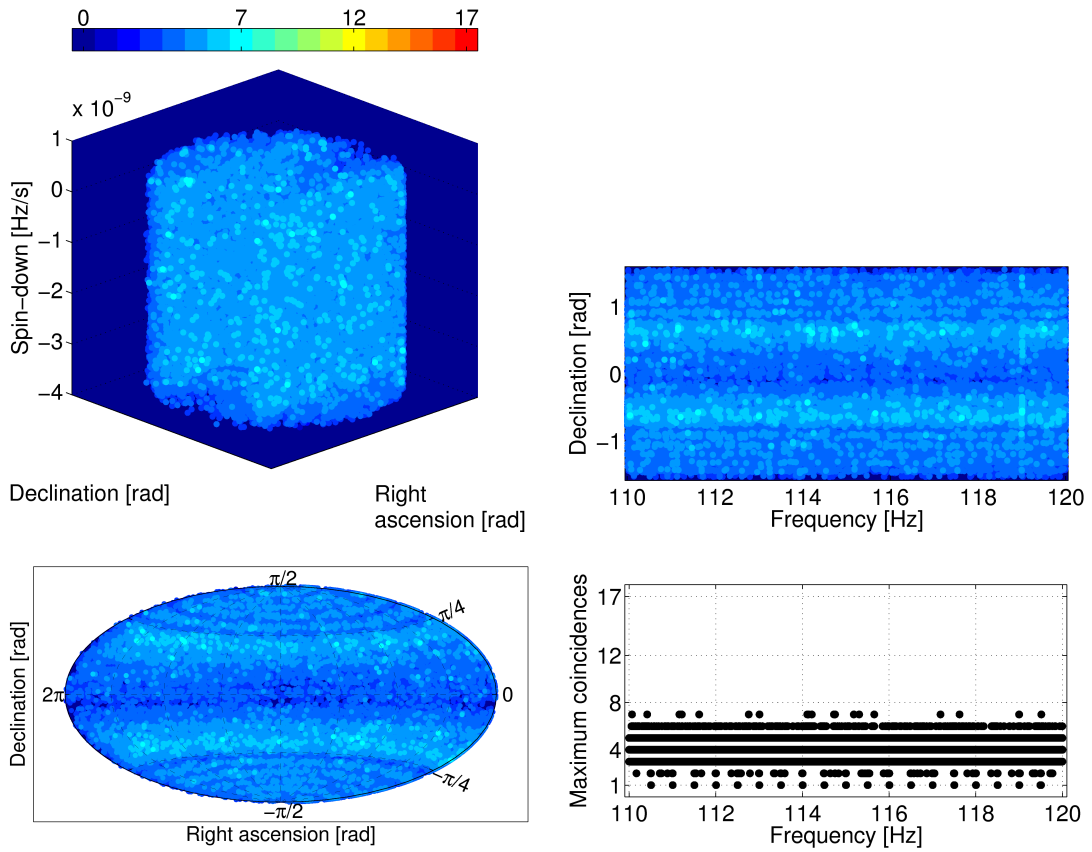


Figure 3.16: Einstein@Home S4 Post-Processing results for a “quiet” frequency band of real instrumental data from 110.0 – 120.0 Hz. From top to bottom, left to right, the different plots show the numbers of coincidences in a 3D map of sky and spin-down, in a 2D plot of declination over frequency, in a 2D Hammer-Aitoff projection of the sky, and in a histogram as a function of frequency.

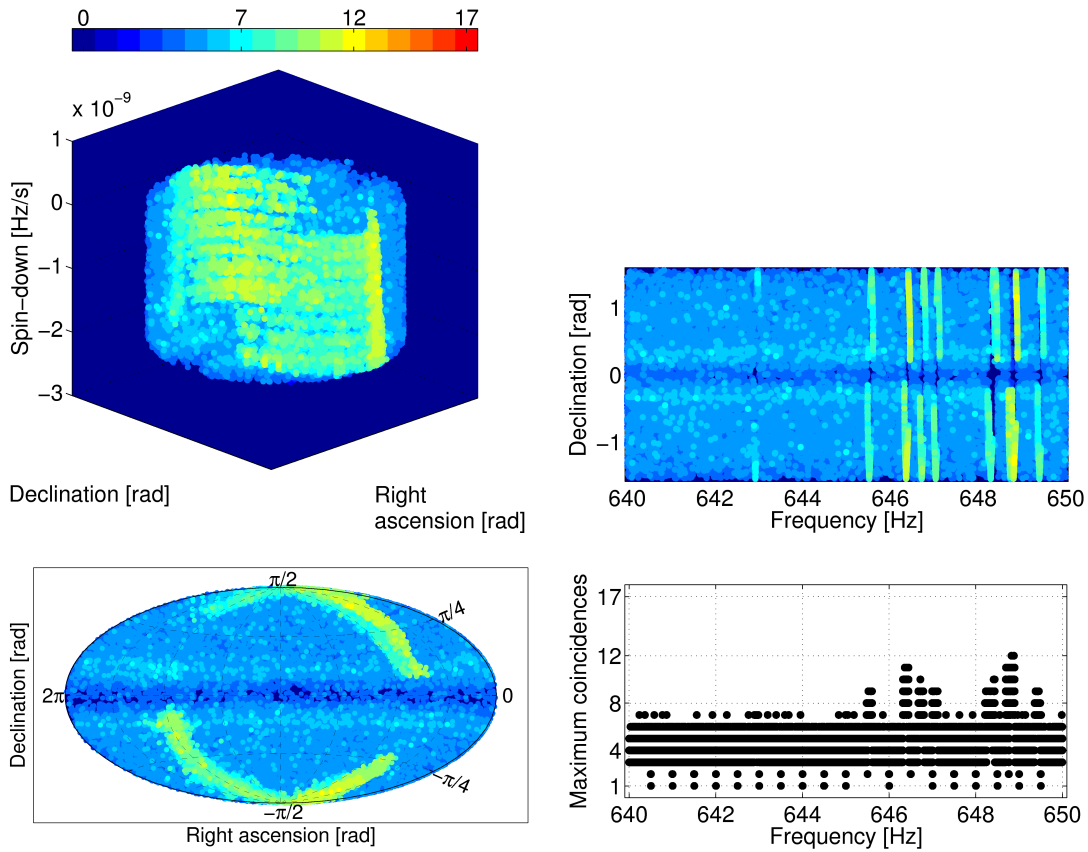


Figure 3.17: Einstein@Home S4 Post-Processing results for a “noisy” frequency band of data polluted by instrumental noise artifacts from 640.0 – 650.0 Hz. These spectral features are resonance modes of the mode cleaner optics suspensions. From top to bottom, left to right, the different plots show the numbers of coincidences in a 3D map of sky and spin-down, in a 2D plot of declination over frequency, in a 2D Hammer-Aitoff projection of the sky, and in a histogram as a function of frequency.

lists the bandwidth in frequency covered by these candidates and shows the parameters of the most coincident candidate. If candidates within these narrow frequency-bands have the same number of coincidences, then the candidate with the largest significance is shown.

Table 3.8: The post-processing candidates that have 10 or more coincidences. The frequency f_{cand} corresponds to the most coincident candidate in the band. The lowest frequency of a candidate in the band is labeled by f_{start} . The difference from the highest frequency is given by Δf_{cand} . The parameters δ_{cand} , α_{cand} , f_{cand} , $C_{\text{cand}} = C_{\text{cand}}^{\text{H1}} + C_{\text{cand}}^{\text{L1}}$ and S_{cand} are for the most significant most coincident candidate within the frequency band, where $C_{\text{cand}}^{\text{H1}}$ and $C_{\text{cand}}^{\text{L1}}$ denote the number of coincidences contributing to C_{cand} from detector H1 and L1, respectively. The column “Information” lists information about the source. The following are understood sources of narrow-band line noise in the instrument: “Demod” are the electronics boards that demodulate the signal at the antisymmetric port of the interferometer, “H1 (or L1) MC 1” is a violin mode resonance of the first mode cleaner mirror, “H1 MC 2/3” are violin mode resonances of the second and third mode cleaner mirrors, “TM violin” are harmonics of the test mass violin modes, “EX +15v” is a fifteen volt power supply at the end station of the X arm, “EM Interference” is electromagnetic interference, “H1 Cal” are side-bands of calibration lines at 393.1 Hz and 1144.3 Hz.

f_{cand} [Hz]	f_{start} [Hz]	Δf_{cand} [Hz]	δ_{cand} [rad]	α_{cand} [rad]	f_{cand} [Hz s ⁻¹]	C_{cand}	$C_{\text{cand}}^{\text{H1}}$	$C_{\text{cand}}^{\text{L1}}$	S_{cand}	Information
193.9276	193.9263	0.040112	-0.583514	4.723595	-5.6001×10^{-09}	13	7	6	2263.6	Pulsar 8
575.1681	575.1562	0.030612	0.285505	3.834511	-5.0913×10^{-10}	13	7	6	249.3	Pulsar 2
1128.1147	1128.0336	0.220321	-1.395918	0.744273	-3.4249×10^{-09}	13	10	3	219.3	H1 MC 2/3
108.8549	108.8522	0.008158	-0.705729	3.361465	-4.4362×10^{-11}	12	9	3	2397.5	Pulsar 3
329.6107	329.5507	0.066447	1.027320	1.336051	-5.7799×10^{-10}	12	10	2	3127.1	Demod
545.9973	545.9929	0.10958	-0.293877	4.849960	-1.5782×10^{-09}	12	10	2	893.3	H1 MC 2/3
566.0868	566.0490	0.105853	-1.367663	0.665233	-1.626×10^{-09}	12	10	2	2340.8	H1 MC 2/3
568.0886	567.9893	0.165769	-1.323532	0.726729	-1.7149×10^{-09}	12	10	2	4137.7	H1 MC 2/3
648.8288	648.6930	0.206223	-1.232868	1.005733	-1.0298×10^{-09}	12	10	2	1870.8	H1 MC 1
1143.9976	1143.9182	0.232221	-1.491264	1.314456	-7.7434×10^{-10}	12	10	2	1028.8	H1 Cal
1144.5198	1144.4533	0.228407	-1.535248	4.497733	-2.5257×10^{-11}	12	10	2	989.8	H1 Cal
1289.6769	1289.5081	0.242915	1.461093	0.266878	-2.0949×10^{-09}	12	10	2	493.7	H1 MC 1
1402.2838	1402.2677	0.063117	1.025583	2.502838	-3.8482×10^{-09}	12	6	6	1749.6	Pulsar 4
329.7593	329.7396	0.066078	-1.536179	4.887048	-5.5375×10^{-10}	11	10	1	3038.3	Demod
335.7735	335.7100	0.065415	0.469606	0.955884	-1.0646×10^{-09}	11	10	1	298.5	EM Interference
545.9232	545.8662	0.063608	-1.060735	1.078303	-8.032×10^{-10}	11	10	1	196.8	H1 MC 2/3
564.1219	564.0096	0.113783	0.386877	1.111355	-1.6868×10^{-09}	11	10	0	1069.3	H1 MC 2/3
646.3758	646.3206	0.127884	-1.281366	0.897933	-1.8931×10^{-09}	11	10	1	3202.7	H1 MC 1
1092.1387	1091.9671	0.217482	-0.523866	1.302500	-6.4347×10^{-11}	11	10	1	196.7	H1 MC 2/3
1136.2217	1136.1460	0.168345	-1.216945	0.935876	-3.4811×10^{-09}	11	10	1	165.6	H1 MC 2/3
1142.8210	1142.7200	0.23173	-1.310037	1.114563	-3.5022×10^{-09}	11	10	1	250.7	H1 Cal
1145.8318	1145.6515	0.231067	1.330065	0.976422	-2.0297×10^{-10}	11	10	1	256.4	H1 Cal
1376.7370	1376.4697	0.271536	0.201677	1.282354	-2.3875×10^{-09}	11	9	2	165.0	TM violin
1388.6402	1388.4070	0.279967	1.176082	0.850794	-2.8907×10^{-09}	11	10	1	200.0	TM violin
56.9966	56.9966		-0.935903	0.150238	-1.5029×10^{-09}	10	8	2	136.7	EM Interference
329.4918	329.4784	0.021358	-1.307440	4.692056	-5.2405×10^{-10}	10	10	0	1137.8	Demod
392.8322	392.8322		-1.210088	1.268596	-1.069×10^{-09}	10	9	1	150.9	H1Cal
393.4060	393.4057	0.000342	0.632053	1.270922	-1.1043×10^{-09}	10	9	1	154.7	H1Cal
646.7224	646.7224	0.002174	-1.446520	0.825633	-1.8813×10^{-09}	10	3	7	2774.4	L1 MC 1
648.4132	648.4132	0.024291	1.319729	1.033730	-1.8479×10^{-09}	10	3	7	5067.5	L1 MC 1
658.6353	658.6353	0.000055	-0.470832	4.762475	-1.6992×10^{-09}	10	3	7	261.4	EX +15v
777.9202	777.8377	0.117087	1.511859	4.010213	-5.6101×10^{-10}	10	3	7	1951.7	EM Interference
1296.4962	1296.4962		-0.993190	4.557370	-1.0022×10^{-09}	10	3	7	247.1	L1 MC 1

Table 3.9 shows the same information *after* the veto method described in Section 3.7 has been applied, for candidates with 9 or more coincidences. There are no candidates that exceed the predefined detection threshold of appearing in 12 or more data segments. (Note that this would be a threshold for initiating a more extensive investigation of the candidate event, not a threshold for announcing a discovery!)

Table 3.9: Post-processing candidates that have 9 or more coincidences and that are not excluded by the veto. The frequency f_{cand} corresponds to the most coincident candidate in the band. The lowest frequency of a candidate in the band is labeled by f_{start} . The difference from the highest frequency is given by Δf_{cand} . The parameters δ_{cand} , α_{cand} , \dot{f}_{cand} , $\mathcal{C}_{\text{cand}} = \mathcal{C}_{\text{cand}}^{\text{H1}} + \mathcal{C}_{\text{cand}}^{\text{L1}}$ and $\mathcal{S}_{\text{cand}}$ are for the most significant most coincident candidate within the frequency band, where $\mathcal{C}_{\text{cand}}^{\text{H1}}$ and $\mathcal{C}_{\text{cand}}^{\text{L1}}$ denote the number of coincidences contributing to $\mathcal{C}_{\text{cand}}$ from detectors H1 and L1, respectively. The column “Information” lists information about the source. The following are understood sources of narrow-band line noise in the instrument: “Demod” are the electronics boards which demodulate the signal at the antisymmetric port of the interferometer, “H1 MC 2/3” are violin mode resonances of the second and third mode cleaner mirrors, “EM Interference” is electromagnetic interference, “H1 Cal” are side-bands of a 1144.3 Hz calibration line. For the single candidate labeled “Unknown” in the last column no instrumental source could be confidently identified, however the 9 coincidences are far below the confident-detection threshold.

f_{cand} [Hz]	f_{start} [Hz]	Δf_{cand} [Hz]	δ_{cand} [rad]	α_{cand} [rad]	\dot{f}_{cand} [Hz s ⁻¹]	$\mathcal{C}_{\text{cand}}$	$\mathcal{C}_{\text{cand}}^{\text{H1}}$	$\mathcal{C}_{\text{cand}}^{\text{L1}}$	$\mathcal{S}_{\text{cand}}$	Information
193.9276	193.9261	0.040646	-0.583514	4.723595	-5.6001×10^{-09}	13	7	6	2263.6	Pulsar 8
575.1681	575.1562	0.039394	0.285505	3.834511	-5.0913×10^{-10}	13	7	6	249.3	Pulsar 2
108.8549	108.8518	0.008506	-0.705729	3.361465	-4.4362×10^{-11}	12	9	3	2397.5	Pulsar 3
1402.2838	1402.2488	0.08678	1.025583	2.502838	-3.8482×10^{-09}	12	6	6	1749.6	Pulsar 4
545.9987	545.9568	0.141563	-0.398855	5.013332	-4.6693×10^{-10}	11	10	1	794.1	H1 MC 2/3
56.9966	56.9963	0.000933	-0.935903	0.150238	-1.5029×10^{-09}	10	8	2	136.7	EM Interference
329.4849	329.4833	0.005843	-0.344739	5.171401	-5.6694×10^{-10}	10	10	0	1024.0	EM Interference
329.6040	329.6040		-0.439100	1.006331	-5.2546×10^{-10}	10	9	1	2625.6	EM Interference
329.7434	329.7413	0.032463	-0.338712	5.025108	-5.6923×10^{-10}	10	9	1	2490.4	EM Interference
567.9984	567.9984	0.051768	-0.353846	5.116972	-1.5532×10^{-09}	10	9	1	409.3	EM Interference
69.6964	69.6964		-1.223613	4.232687	-5.4823×10^{-10}	9	9	0	130.3	EM Interference
317.4207	317.4207		1.389330	2.663214	-8.0338×10^{-10}	9	3	6	157.8	EM Interference
329.5615	329.5615		-1.027976	3.822726	-6.3014×10^{-10}	9	7	2	2176.0	Demod
335.7541	335.7141	0.056927	1.395059	3.271989	-6.362×10^{-10}	9	9	0	259.3	EM Interference
795.4783	795.4783		0.245291	3.211417	-1.4374×10^{-09}	9	7	2	110.7	EM Interference
1092.1564	1092.1564		-0.252089	1.099873	-2.1099×10^{-11}	9	8	1	147.1	H1 MC 2/3
1117.3032	1117.3032		-0.207300	4.051169	-3.3192×10^{-09}	9	4	5	116.1	Unknown
1145.6678	1145.6678		-0.247554	5.067301	-3.1679×10^{-09}	9	6	3	168.7	H1 Cal

Figure 3.18 shows all candidates from the post-processing results that have not been discriminated by the veto introduced in Section 3.7. Figure 3.19 illustrates the fraction of candidates that has been excluded by the veto. Removing fractional bands of $2 \times 10^{-4} f$ around the frequencies f of the S4 hardware injections, the veto discriminates 99.5% of all candidates that have more than 7 coincidences.

3.10 Conclusion

This work has led to the first published scientific results from the Einstein@Home project, which was launched in February 2005. While no credible CW sources were found in this search of LIGO S4 data, the results clearly establish that this type of distributed computing project can carry out a credible and sensitive search for such signals.

A similar search (also with a 30-hour time baseline) has also been completed using 840 h of data from the beginning of the S5 science run. The results from the analysis of this data set are presented in Chapter 4, using methods similar to those employed here.

The post-processing methods introduced here, have also been applied in an all-sky search for CW sources in NAUTILUS bar-detector data, which will be described in the Appendix A. In this analysis, half a year of data over the frequency band of 922.2 to 923.2 Hz, the spindown range of -1.463×10^{-8} to 0 Hz/s and over the entire sky have been searched.

Future Einstein@Home searches overcome some of the sensitivity limitations discussed at the end of Section 3.6 by doing the incoherent step (called “post-processing” here) on the host machines. This allows the use of the closer-to-optimal threshold of $2\mathcal{F} \sim 5$, so those searches are expected to be the most sensitive blind CW searches that will be possible using LIGO data. Results from those searches should become available within the next one to two years, and are expected to offer more than one order of magnitude improvement in strain sensitivity compared with the work presented here.

In the longer term, further increases in sensitivity will result from improvements in the detectors. This year, LIGO has begun its S6 run with an “enhanced” detector con-

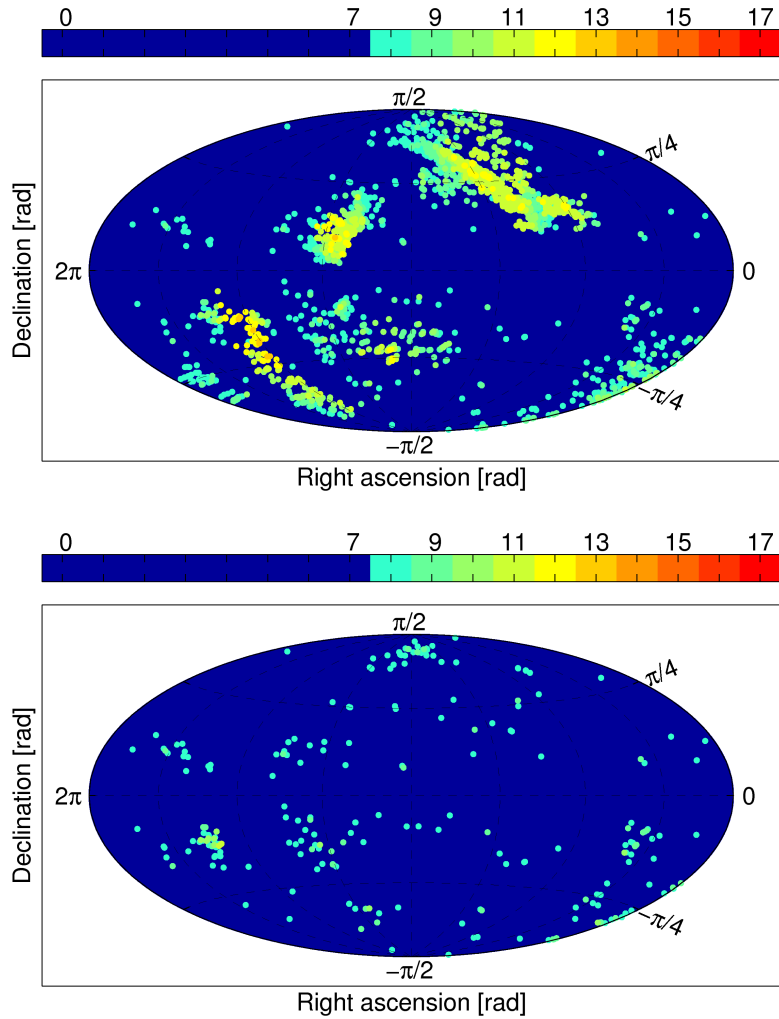


Figure 3.18: Candidates not eliminated by the veto. This shows Hammer-Aitoff sky projections of all candidates obtained from post-processing that had more than 7 coincidences and that passed the veto. The upper plot includes the S4 hardware injections. The lower plot removes bands of $2 \times 10^{-4} f$ width to either side of the hardware injections' frequencies f . In comparison to Figure 3.13, after excluding the hardware injections, the veto rejects 99.5% of all candidates.

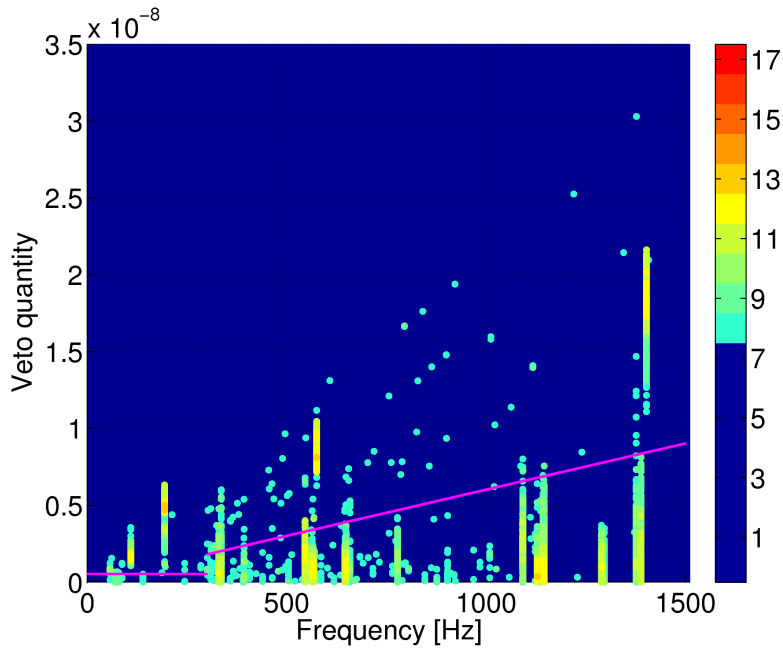


Figure 3.19: Conclusion diagram of candidates discriminated by the veto method. All candidate cells obtained from post-processing that have more than 7 coincidences are shown, where the color-bar indicates the number of coincidences of a particular cell. The vertical axis represents the veto quantity on the left-hand side of (3.26), as a function of frequency. Candidates located below the magenta line are eliminated by the veto. The four accumulations of highly coincident cells above the magenta line are the hardware injected pulsars, which are not eliminated by the veto.

figuration that should improve on S5 sensitivity by at least a factor of two. By 2014, an advanced LIGO detector configuration should give at least another factor of five improvement. By combining these data sets with those from LIGO's international partner projects VIRGO and GEO 600, there is real hope that the first direct CW detection can be made using methods like the ones described here.

Einstein@Home search for CW sources in early S5 LIGO data

Appeared in Physical Review D 80, 042003, (2009)

4.1 Overview and context

The previous Chapter described the results of the Einstein@Home search for continuous gravitational-wave (CW) signals in the data from LIGO's fourth science run (S4) [1]. The work presented in this Chapter extends this search, using more sensitive data in form of 840 hours from 66 days of LIGO's fifth science run (S5), and a refined search configuration.

Because of the weakness of the CW signals buried in the detector noise, the data analysis strategy is critical. A powerful detection method is given by coherent matched-filtering. This means one convolves all available data with a set of template waveforms corresponding to all possible putative sources. The resulting detection statistic has been first derived in [55] and is commonly referred to as the \mathcal{F} -statistic (see Section 5.2 for a more detailed description).

The parameter space to be scanned for putative signals from isolated neutron stars is

four-dimensional, with two parameters required to describe the source sky position using standard astronomical equatorial coordinates α (right ascension) and δ (declination), and additional coordinates (f, \dot{f}) denoting the intrinsic frequency and frequency drift. To achieve the maximum possible sensitivity, the template waveforms must match the source waveforms to within a fraction of a cycle over the entire observation time (months or years for current data samples). So one must choose a very closely spaced grid of templates in this four-dimensional parameter space. This makes the computational cost of the search very high, and therefore limits the search sensitivity [172].

To maximize the possible integration time, and hence achieve a more sensitive search, the computation was distributed via the volunteer computing project Einstein@Home [12]. This large computing power allowed the use of a comparably long coherent integration time of 30 h, despite the enormously large parameter space searched. Thus, the present search method is based on coherent matched-filtering in the form of the \mathcal{F} -statistic over 30-hour-long data segments and subsequent incoherent combination of \mathcal{F} -statistic results via an efficient coincidence strategy.

In this analysis, the data is searched for CW signals with frequencies f in the range from 50 to 1500 Hz, with a linear frequency drift \dot{f} in the range $-f/\tau < \dot{f} < 0.1 f/\tau$, for a minimum spin-down age τ of 1 000 years for signals below 400 Hz and 8 000 years above 400 Hz. Despite probing a slightly larger parameter space in comparison to the antecedent S4 search, this analysis additionally achieves 3 times better sensitivity. In the 125 to 225 Hz band, more than 90% of sources with dimensionless gravitational-wave strain tensor amplitude greater than 3×10^{-24} would have been detected.

The methods used here are further described in Sections 4.2 – 4.4. Estimates of the sensitivity of this search and results are in Sections 4.5 and 4.6, respectively. Previously, other all-sky searches for CW sources using LIGO S4 and S5 data, which combine power from many short coherent segments (30-minute intervals) of data, have been reported by the LIGO Scientific Collaboration [158, 159]. However, this Einstein@Home search explores large regions of parameter space which have not been analyzed previously with LIGO S5 data. The sensitivity of the results here are compared with previous searches in Section 4.7, and conclusions are given in Section 4.8.

4.2 Data selection and preparation

The LIGO S5 data analyzed in the present work was collected between November 19, 2005 and January 24, 2006. The total data set covering frequencies from 50 Hz to 1500 Hz consisted of 660 h of data from the LIGO Hanford 4-km (H1) detector and 180 h of data from the LIGO Livingston 4-km (L1) detector. The configuration of the LIGO detectors during the S5 run is described in [186].

The data preparation method is essentially identical to that of the previous S4 analysis. Therefore only a brief summary of the main aspects is given here; further details are found in Chapter 3 and references therein. The data set has been divided into segments of 30 h each. However, the 30-hour long data segments are not contiguous, but have time gaps. Since the number of templates required increases rapidly with observation span, the 30 h of data for each segment were chosen to lie within a time span of less than 40 h. In what follows, the notion of “segment” will always refer to one of these time stretches, each of which contains exactly $T = 30$ h of data. The total time spanned by a given data segment j is denoted by $T_{\text{span},j}$ and conforms to $30 \text{ h} < T_{\text{span},j} < 40 \text{ h}$.

Given the above constraints, a total of $N_{\text{seg}} = 28$ data segments (22 from H1, 6 from L1) were obtained from the early S5 data considered. These data segments are labeled by $j = 1, \dots, 28$. Table 4.1 lists the GPS start time along with the time span of each segment.

In this analysis, the maximum frequency shift of a signal over the length of any given data segment and parameter-space range examined is dominated by the Doppler modulation due to the Earth’s orbital motion around the solar system barycenter (SSB), while the effects of frequency change resulting from intrinsic spin-down of the source are smaller. The orbital velocity of the Earth is about $v/c \approx 10^{-4}$, hence a signal will always remain in a narrow frequency band smaller than ± 0.15 Hz around a given source frequency. Therefore, for each detector the total frequency range from 50 Hz to 1500 Hz is broken up into 2900 slices, each of 0.5 Hz bandwidth plus overlapping wings of 0.175 Hz on either side.

The detector data contains numerous narrow-band noise artifacts, so-called “lines”, which are of instrumental origin, such as harmonics of the 60 Hz mains frequency. Prior

Table 4.1: Segments of early S5 data used in this search. The columns are the data segment index j , the GPS start time t_j and the time spanned $T_{\text{span},j}$.

j	Detector	t_j [s]	$T_{\text{span},j}$ [s]
1	H1	816397490	140768
2	H1	816778879	134673
3	H1	816993218	134697
4	H1	817127915	137962
5	H1	817768509	142787
6	H1	817945327	143919
7	H1	818099543	139065
8	H1	818270501	143089
9	H1	818552200	134771
10	H1	818721347	138570
11	H1	818864047	134946
12	H1	819337064	143091
13	H1	819486815	120881
14	H1	819607696	116289
15	H1	819758149	136042
16	H1	820482173	143904
17	H1	820628379	138987
18	H1	821214511	126307
19	H1	821340818	126498
20	H1	821630884	141913
21	H1	821835537	138167
22	H1	821973704	142510
23	L1	818812286	130319
24	L1	819253562	140214
25	L1	819393776	126075
26	L1	819547883	138334
27	L1	820015400	121609
28	L1	821291797	140758

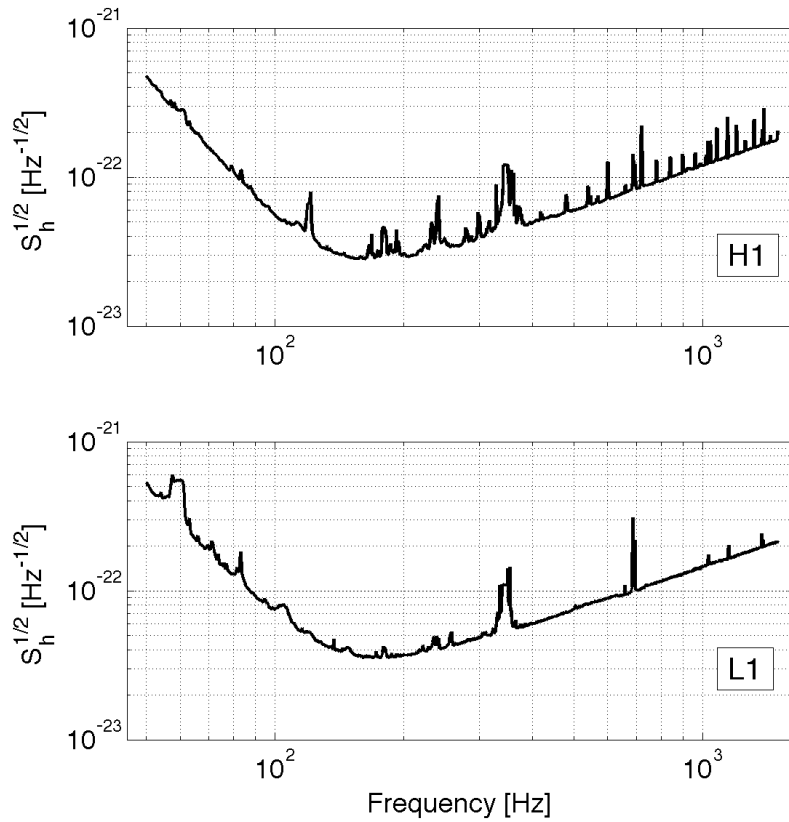


Figure 4.1: Strain amplitude spectral densities $\sqrt{S_h(f)}$ of the cleaned data from the LIGO detectors H1 and L1. The curves in the top (bottom) panel are the harmonic mean of the 22 H1 (6 L1) 30-hour segments of S5 data used this Einstein@Home analysis.

to the analysis, line features of understood origin (at the time before the launch of the search) were removed (“cleaned”) from the data by substitution of the frequency-domain data bins with random Gaussian noise. Table 4.2 shows the frequencies of lines excluded from the data. The harmonic mean noise strain amplitude spectra of the final cleaned H1 and L1 data sets are shown in Figure 4.1.

Table 4.2: Instrumental-noise lines cleaned from H1 and L1 data. The three columns show the central frequency f_{Line} , the bandwidth $\Delta f_{\text{Line}}^{(<)}$ removed below the central frequency and the bandwidth $\Delta f_{\text{Line}}^{(>)}$ removed above the central frequency. Thus the total bandwidth removed per central frequency is $\Delta f_{\text{Line}}^{(<)} + \Delta f_{\text{Line}}^{(>)}$. In addition, at *each harmonic* of the 60 Hz mains frequency, the same bandwidth is also removed. A zero bandwidth indicates that the line-cleaning algorithm replaces in these cases a single Fourier bin with the average of bins on either side. The spacing between Fourier bins is 1/1800 Hz.

H1			L1		
$f_{\text{Line}}[\text{Hz}]$	$\Delta f_{\text{Line}}^{(<)}[\text{Hz}]$	$\Delta f_{\text{Line}}^{(>)}[\text{Hz}]$	$f_{\text{Line}}[\text{Hz}]$	$\Delta f_{\text{Line}}^{(<)}[\text{Hz}]$	$\Delta f_{\text{Line}}^{(>)}[\text{Hz}]$
46.7	0.0	0.0	54.7	0.0	0.0
60.0	1.0	1.0	60.0	1.0	1.0
346.0	4.0	4.0	345.0	5.0	5.0
393.1	0.0	0.0	396.7	0.0	0.0
686.9	0.3	0.3	686.5	1.0	1.0
688.2	0.3	0.3	688.83	0.5	0.5
689.5	0.5	0.6	693.7	0.7	0.7
694.75	1.25	1.25	1029.5	0.25	0.25
1030.55	0.1	0.1	1031	0.5	0.5
1032.18	0.04	0.04	1033.6	0.2	0.2
1032.58	0.1	0.1	1041	1.0	1.0
1033.7	0.1	0.1	1151.5	0.0	0.0
1033.855	0.05	0.05	1372.925	0.075	0.075
1034.6	0.4	0.4	1374.7	0.1	0.1
1041.23	0.1	0.1	1375.2	0.1	0.1
1042.0	0.5	0.2	1378.39	0.1	0.1
1043.4	0.2	0.2	1387.4	0.05	0.05
1144.3	0.0	0.0	1388.5	0.3	0.3
1373.75	0.1	0.1			
1374.44	0.1	0.1			
1377.14	0.1	0.1			
1378.75	0.1	0.1			
1379.52	0.1	0.1			
1389.06	0.06	0.06			
1389.82	0.07	0.07			
1391.5	0.2	0.2			

4.3 Data processing

Chapter 3, describing the previous Einstein@Home search in S4 data, presented in detail the data processing scheme. For the purpose of the present search the same data processing infrastructure is employed. Hence, here only a short summary thereof is given, pointing out the minimal changes applied in setting up the present analysis.

The total computation of the search is broken up into 16 446 454 workunits. Each workunit represents a separate computing task and is processed using the Berkeley Open Infrastructure for Network Computing (BOINC) [180, 181, 182]. To eliminate errors and weed out results that are wrong, each workunit is independently processed by at least two different volunteers. Once two successful results for a workunit are returned back to the Einstein@Home server, they are compared by an automatic validator, which discards results that differ by more than some allowed tolerance. New workunits are generated and run independently again for such cases.

In searching for periodic gravitational-wave signals, each workunit examines a different part of parameter space. A key design goal is that the computational effort to conduct the entire analysis should take about 6 – 7 months. An additional design goal is to minimize the download burden on the Einstein@Home volunteers' internet connections and also on the Einstein@Home data servers. This is accomplished by letting each workunit use only a small re-usable subset of the total data set, so that Einstein@Home volunteers are able to carry out useful computations on a one-day time scale.

Each workunit searches only one data segment over a narrow frequency range, but covering all of the sky and the entire range of frequency derivatives. The workunits are labeled by three indices (j, k, ℓ) , where $j = 1, \dots, 28$ denotes the data segment, $k = 1, \dots, 2900$ labels the 0.5 Hz frequency band and $\ell = 1, \dots, M(j, k)$ enumerates the individual workunits pertinent to data segment j and frequency band k .

In each segment the \mathcal{F} -statistic is evaluated on a grid in parameter space. Each parameter-space grid is constructed such that grid points (templates) are not further apart from their nearest neighbor by more than a certain distance. The distance measure is defined from a metric on parameter space, first introduced in [173, 174], representing the fractional loss of squared signal-to-noise ratio (SNR²) due to waveform mismatch

between the putative signal and the template. For any given workunit, the parameter-space grid is a Cartesian product of uniformly-spaced steps df in frequency, uniformly-spaced steps $d\dot{f}$ in frequency derivative, and a two-dimensional sky grid, which has non-uniform spacings determined by the metric [183, 1].

For frequencies in the range [50, 400) Hz, the maximal allowed mismatch was chosen as $m = 0.15$ (corresponding to a maximal loss in SNR^2 of 15%), while in the range [400, 1500) Hz, the maximal mismatch was $m = 0.4$. It can be shown [183, 1], that these choices of maximal mismatch enable a coherent search of near-optimal sensitivity at fixed computational resources.

The step-size in frequency f obtained from the metric depends on $T_{\text{span},j}$ of the j th data segment: $df_j = 2\sqrt{3m}/(\pi T_{\text{span},j})$. In the low-frequency range this results in frequency spacings in the range $df_j \in [2.97, 3.67] \mu\text{Hz}$, while for high-frequency workunits $df_j \in [4.85, 6.0] \mu\text{Hz}$.

The range of frequency derivatives \dot{f} searched is defined in terms of the “spin-down age” $\tau \equiv -f/\dot{f}$, namely $\tau \geq 1000$ years for low-frequency and $\tau \geq 8000$ years for high-frequency workunits. As in the S4 Einstein@Home search, these ranges were guided by the assumption that a nearby very young neutron star would correspond to a historical supernova, supernova remnant, known pulsar, or pulsar wind nebula. The search also covers a small “spin-up” range, so the actual ranges searched are $\dot{f} \in [-f/\tau, 0.1f/\tau]$. In \dot{f} the grid points are spaced according to $d\dot{f}_j = 12\sqrt{5m}/(\pi T_{\text{span},j}^2)$, resulting in resolutions $d\dot{f}_j \in [1.60, 2.44] \times 10^{-10}$ Hz/s for low-frequency workunits, and $d\dot{f}_j \in [2.61, 3.99] \times 10^{-10}$ Hz/s for high-frequency workunits.

The resolution of the search grid in the sky depends on both the start time t_j and duration $T_{\text{span},j}$ of the segment, as well as on the frequency f . The number of grid points on the sky scales as $\propto f^2$, and approximately as $\propto T_{\text{span},j}^{2.4}$ for the range of $T_{\text{span},j} \sim 30 - 40$ h used in this search. As was done in the previous S4 analysis, to simplify the construction of workunits and limit the number of different input files to be sent, the sky grids are fixed over a frequency range of 10 Hz, but differ for each data segment j . The sky grids are computed at the higher end of each 10 Hz band, so they are slightly “over-covering” the sky at lower frequencies within the band. The search covers in total a frequency band of 1450 Hz, thus there are 145 different sky grids for each data segment.

The output from one workunit in the low (high) frequency range contains the top 1 000 (10 000) candidate events with the largest values of the \mathcal{F} -statistic. In order to balance the load on the Einstein@Home servers, a low-frequency workunit returns a factor of 10 fewer events, because low-frequency workunits require runtimes approximately 10 times shorter than high-frequency workunits. For each candidate event five values are reported: frequency (Hz), right ascension angle (radians), declination angle (radians), frequency derivative (Hz/s) and $2\mathcal{F}$ (dimensionless). The frequency is the frequency at the SSB at the instant of the first data point in the corresponding data segment. Returning only the “loudest” candidate events effectively corresponds to a floating threshold on the value of the \mathcal{F} -statistic. This avoids large lists of candidate events being produced in regions of parameter space containing non-Gaussian noise, such as instrumental artifacts that were not removed *a priori* from the input data because of unknown origin.

4.4 Post-processing

After results for each workunit are returned to the Einstein@Home servers by project volunteers, post-processing is conducted on those servers and on dedicated computing clusters. The post-processing has the goal of finding candidate events that appear in many of the 28 different data segments with consistent parameters.

In this search, the post-processing methods are the same as used for the Einstein@Home S4 search of Chapter 3. Therefore, this Section only summarizes the main steps.

A consistent (coincident) set of “candidate events” is called a “candidate”. Candidate events from different data segments are considered coincident if they cluster closely together in the four-dimensional parameter space. By using a grid of “coincidence cells”, the clustering method can reliably detect strong signals, which would produce candidate events with closely-matched parameters in many of the 28 data segments. The post-processing pipeline operates in 0.5 Hz-wide frequency bands, and performs the following steps described below.

4.4.1 The post-processing steps

A putative source with non-zero spin-down would generate candidate events with different apparent frequency values in each data segment. To account for these effects, the frequencies of the candidate events are shifted back to the same frequency value at fiducial time t_{fiducial} via $f(t_{\text{fiducial}}) = f(t_j) + (t_{\text{fiducial}} - t_j) \dot{f}$, where \dot{f} and $f(t_j)$ are the spin-down rate and frequency of a candidate event reported by the search code in the result file, and t_j is the time-stamp of the first datum in the j th data segment. The fiducial time is chosen to be the GPS start time of the earliest ($j = 1$) data segment, $t_{\text{fiducial}} = t_1 = 816\,397\,490$ s.

A grid of cells is then constructed in the four-dimensional parameter space to find coincidences among the 28 different data segments. The coincidence search algorithm uses rectangular cells in the coordinates $(f, \dot{f}, \alpha \cos \delta, \delta)$. The dimensions of the cells are adapted to the parameter-space search grid (see below). Each candidate event is assigned to a particular cell. In cases where two or more candidate events from the same data segment j fall into the same cell, only the candidate event having the largest value of $2\mathcal{F}$ is retained in the cell. Then the number of candidate events per cell coming from distinct data segments is counted, to identify cells with more coincidences than would be expected by random chance.

To ensure that candidate events located on opposite sides of a cell border are not missed, the entire cell coincidence grid is shifted by half a cell width in all possible $2^4 = 16$ combinations of the four parameter-space dimensions. Hence, 16 different coincidence cell grids are used in the analysis.

4.4.2 Construction of coincidence windows

The coincidence cells are constructed to be as small as possible to reduce the probability of false alarms. However, since each of the 28 different data segments uses a different parameter space grid, the coincidence cells must be chosen to be large enough that the candidate events from a source (which would appear at slightly different points in parameter space in each of the 28 data segments) would still lie in the same coincidence cell.

In the frequency direction, the size Δf for the coincidence cell is given by the largest search grid spacing in f (for the smallest value of $T_{\text{span},j}$) plus the largest possible offset in spin-down: $\Delta f = \max_j (df_j + \Delta t \dot{df}_j)$, where the maximization over j selects the data segment with the smallest $T_{\text{span},j}$ (which is $j = 6$) and $\Delta t = |\max_j t_j - \min_j t_j| = t_{22} - t_1 = 5\,576\,214$ s is the total time span between the latest and earliest data segments. For safety, e.g. against noise fluctuations that could shift a candidate peak, Δf has been increased by a further 30%, so that the width of the coincidence cell in f below 400 Hz is $\Delta f = 1.78$ mHz and $\Delta f = 2.9$ mHz above 400 Hz.

In the frequency-derivative direction, the size of the coincidence cell is given by the largest \dot{df}_j spacing in the parameter space grid, which is also determined by the smallest value of $T_{\text{span},j}$. For safety this is also increased by 30%, so that $\Delta \dot{f} = 3.18 \times 10^{-10}$ Hzs $^{-1}$ below 400 Hz and $\Delta \dot{f} = 5.19 \times 10^{-10}$ Hzs $^{-1}$ above 400 Hz.

In sky position, the size of the coincidence cells is guided by the behavior of the parameter-space metric. As described in Chapter 3, the density of grid points in the sky is approximately proportional to $|\cos(\delta) \sin(\delta)| \propto |\sin(2\delta)|$, and it follows from Section 3.5.6 that $\cos(\delta) d\alpha = |\sin(\delta)| d\delta = \text{const}$. Because of the singularity when $\delta \rightarrow 0$, a useful model for the coincidence window size varying with declination is given by

$$\begin{aligned} \Delta\alpha(\delta) &= \Delta\alpha(0)/\cos(\delta) \\ \Delta\delta(\delta) &= \begin{cases} \Delta\delta(0) & \text{if } |\delta| < \delta_c, \\ \Delta\alpha(0)/|\sin(|\delta| - \kappa \Delta\alpha(0))| & \text{if } |\delta| \geq \delta_c. \end{cases} \end{aligned} \quad (4.1)$$

To ensure continuity at $\delta = \delta_c$, the transition point δ_c is defined by the condition $\Delta\alpha(0)/|\sin(|\delta_c| - \kappa \Delta\alpha(0))| = \Delta\delta(0)$. The tuning parameter κ is chosen based on visual inspection to be $\kappa = 1.5$ in this search. The values of $\Delta\alpha(0)$ and $\Delta\delta(0)$ are directly determined from the sky grids (cf. Section 3.5.6). Figure 4.2 shows these parameters for all sky grids as a function of frequency. As stated above, the sky grids are constant for 10 Hz-wide steps in frequency, and so these parameters vary with the same step-size.

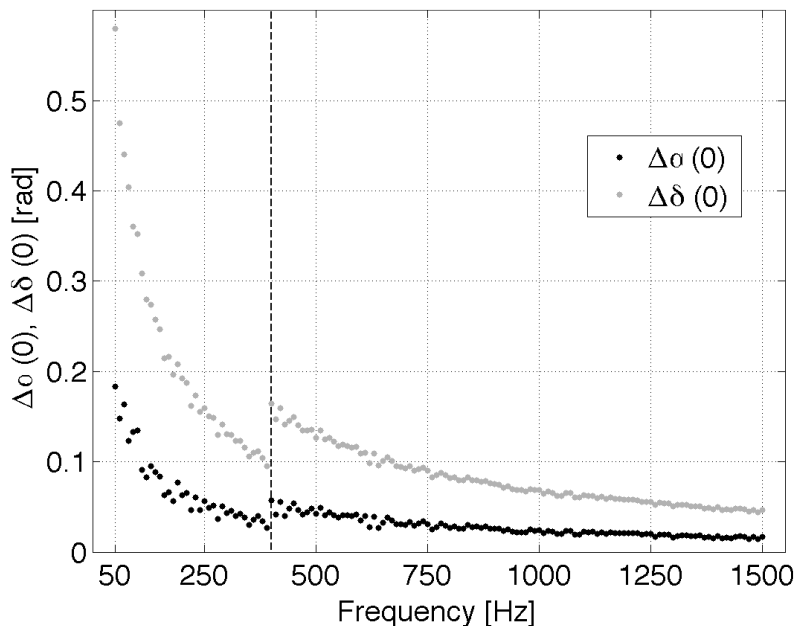


Figure 4.2: The parameters $\Delta\alpha(0)$ and $\Delta\delta(0)$ of the sky coincidence-window model as a function of the 10 Hz frequency band. The vertical dashed line at 400 Hz indicates the separation between the low and high frequency ranges.

4.4.3 Output of the post-processing

The output of the post-processing is a list of the candidates with the greatest number of coincidences. The possible number of coincidences ranges from a minimum of 0 to a maximum of 28 (the number of data segments analyzed). The meaning of \mathcal{C} coincidences is that there are \mathcal{C} candidate events from different data segments within a given coincidence cell. In each frequency band of coincidence-window width Δf , the coincidence cell containing the largest number of candidate events is found. The pipeline outputs the average frequency of the coincidence cell, the average sky position and spin-down of the candidate events, the number of candidate events in the coincidence cell, and the “significance” of the candidate. The significance of a candidate, first introduced in [124] and explained in Section 3.5.7, is defined by

$$\mathcal{S} = \sum_{q=1}^{\mathcal{C}} (\mathcal{F}_q - \ln(1 + \mathcal{F}_q)) , \quad (4.2)$$

where \mathcal{F}_q is the \mathcal{F} -statistic value of the q th candidate event in the same coincidence cell, which harbors a total of \mathcal{C} candidate events.

4.4.4 False alarm probability and detection threshold

The central goal of this search is to make a *confident detection*, not to set upper limits with the broadest possible coverage band. This is reflected in the choice of detection threshold based on the expected false alarm rates. In this search the background level of false alarm candidates is expected at 10 coincidences (out of 28 possible). As a pragmatic choice, the threshold of confident detection is set at 20 coincidences, which is highly improbable to arise from random noise only. These settings will be elucidated in the following.

To calculate the false alarm probabilities, consider the case where $\mathcal{E}_{\text{seg}}(k)$ candidate events per data segment obtained from pure Gaussian noise are distributed uniformly about $N_{\text{cell}}(k)$ independent coincidence cells in a given 0.5 Hz band k . Assuming the candidate events are independent, the probability $p_{\text{F}}(k; \mathcal{C}_{\text{max}})$ per coincidence cell of finding \mathcal{C}_{max} or more candidate events from different data segments has been derived in Section 3.5.3 and is given by the binomial distribution

$$p_{\text{F}}(k; \mathcal{C}_{\text{max}}) = \sum_{n=\mathcal{C}_{\text{max}}}^{N_{\text{seg}}} \binom{N_{\text{seg}}}{n} [\epsilon(k)]^n [1 - \epsilon(k)]^{N_{\text{seg}}-n}, \quad (4.3)$$

where $\epsilon(k)$ denotes the probability of populating any given coincidence cell with one or more candidate events in a given data segment, obtained as

$$\epsilon(k) = 1 - \left(1 - \frac{1}{N_{\text{cell}}(k)}\right)^{\mathcal{E}_{\text{seg}}(k)}. \quad (4.4)$$

Finally, the probability $P_{\text{F}}(k; \mathcal{C}_{\text{max}})$ that there are \mathcal{C}_{max} or more coincidences in *one or more* of the N_{cell} cells per 0.5 Hz band k is

$$P_{\text{F}}(k; \mathcal{C}_{\text{max}}) = 1 - [1 - p_{\text{F}}(k; \mathcal{C}_{\text{max}})]^{N_{\text{cell}}}. \quad (4.5)$$

Figure 4.3 shows the dependence of $P_{\text{F}}(k; \mathcal{C}_{\text{max}})$ on the frequency bands for different values of \mathcal{C}_{max} . One finds that the average false alarm probability of obtaining 10 or more

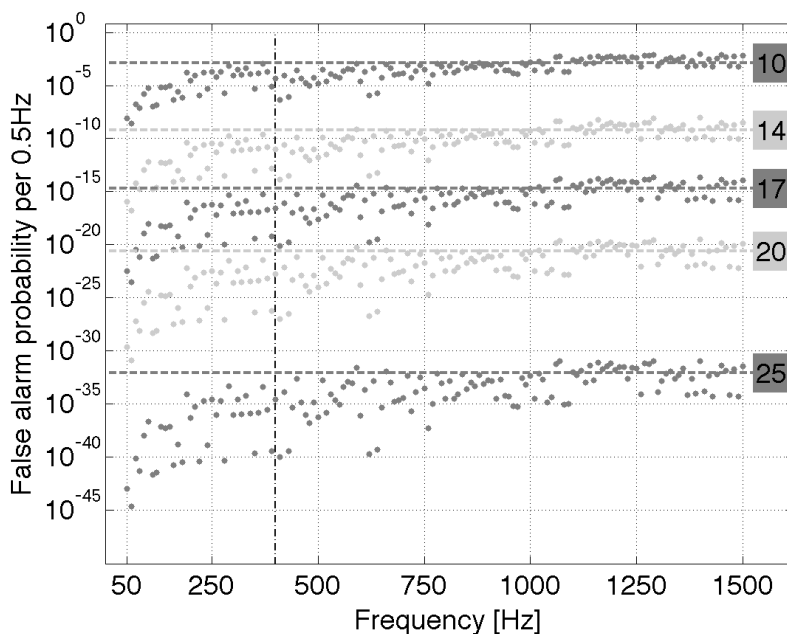


Figure 4.3: False alarm probabilities $P_F(k; C_{\max})$ as a function of frequency band (labeled by k) for different values of $C_{\max} \in \{10, 14, 17, 20, 25\}$. The dashed horizontal lines represent the corresponding average across all frequencies. The vertical dashed line at 400 Hz indicates the separation between the low and high frequency ranges.

coincidences is approximately 10^{-3} . This means, in our analysis of 2900 half-Hz frequency bands, only a few candidates are expected to have 10 or more coincidences. Thus this will be the anticipated background level of coincidences, because from pure random noise one would not expect candidates of *more than* 10 coincidences in this analysis. In contrast, the false alarm probability of reaching the detection threshold of 20 or more coincidences per 0.5 Hz averaged over all frequency bands is about 10^{-21} . Therefore, this choice of detection threshold makes it extremely improbable to be exceeded in case of random noise.

During parts of the LIGO S5 run ten simulated CW signals were injected at the hardware level by modulating the interferometer mirror positions via signals sent to voice actuation coils surrounding magnets glued near the mirror edges. The hardware injections were scheduled with overall duty cycle of about 50% during S5 to minimize potential interference for other gravitational-wave searches. Thus, in only 12 (of the 28) data segments chosen for this search were these hardware injections active more than 90%

of the time. Therefore, the hardware injections are not expected to meet the detection condition defined above, simply because they were inactive during a large fraction of the data used in this analysis. For future science runs improved understanding will allow the hardware injections to be activated permanently.

4.5 Estimated sensitivity

The methods used here would be expected to yield very high confidence if a strong signal were present. To estimate the sensitivity of this detection scheme, Monte-Carlo methods are used to simulate a population of sources. The goal is to find the strain amplitude h_0 at which 10%, 50%, or 90% of sources uniformly populated over the sky and in their “nuisance parameters” would be confidently detected. In this analysis, “detectable” means “produces coincident events in 20 or more distinct data segments”. As discussed above, the false alarm probability for obtaining such a candidate in a given 0.5 Hz band is of order 10^{-21} . This is therefore an estimate of the signal strength required for high-confidence detection. For this purpose, the pipeline developed in Section 3.6 is run here, using the input data of the present analysis. A large number of distinct simulated sources (trials) are tested for detection. A “trial” denotes a single simulated source which is probed for detection.

Figure 4.4 shows the resulting search sensitivity curves as functions of frequency. Each data point on the plot denotes the results of 1 000 independent trials. These show the values of h_0 as defined in [55] such that 10%, 50%, and 90% of simulated sources are confidently detected in the post-processing pipeline.

The dominant sources of error in these sensitivity curves are uncertainties in calibration of the LIGO detector response functions (cf. [159]). The uncertainties range typically from about 8% to 15%, depending on frequency.

The behavior of the curves shown in Figure 4.4 essentially reflects the instrument noise given in Figure 4.1. One may fit the curves obtained in Figure 4.4 to the shape of the harmonic-mean averaged strain noise power spectral density $S_h(f)$. Then the three

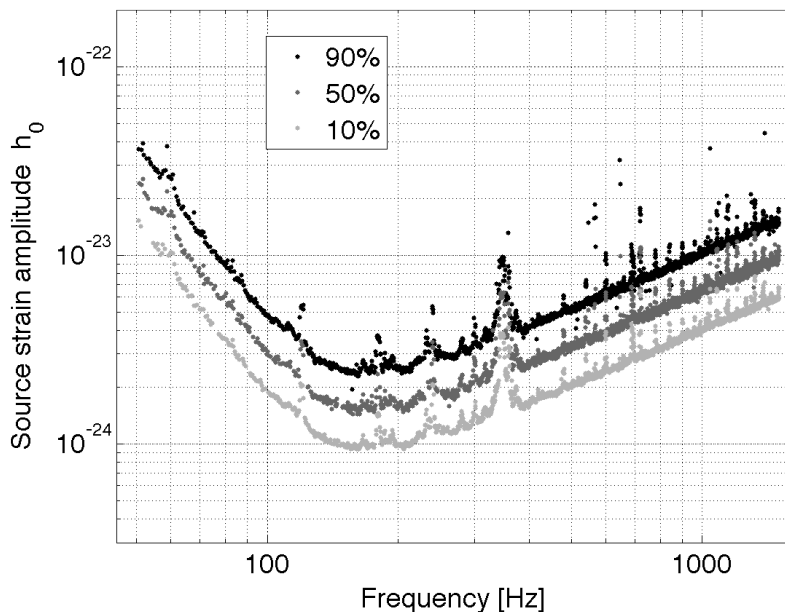


Figure 4.4: Estimated sensitivity of the Einstein@Home search for isolated CW sources in the early LIGO S5 data. The set of three curves shows the source strain amplitudes h_0 at which 10% (bottom), 50% (middle) and 90% (top) of simulated sources would be confidently detected (*i.e.*, would produce at least 20 coincidences out of 28 possible) in this Einstein@Home search.

sensitivity curves in Figure 4.4 are described by

$$h_0^{\mathcal{D}}(f) \approx R_{\mathcal{D}} \sqrt{\frac{S_h(f)}{30 \text{ h}}}, \quad (4.6)$$

where the pre-factors $R_{\mathcal{D}}$ for different detection probabilities levels $\mathcal{D} = 90\%$, 50% , and 10% are well fit below 400 Hz by $R_{90\%} = 29.4$, $R_{50\%} = 18.5$, and $R_{10\%} = 11.6$, and above 400 Hz by $R_{90\%} = 30.3$, $R_{50\%} = 19.0$, and $R_{10\%} = 11.8$.

4.6 Results

4.6.1 Vetoing Instrumental-noise lines

At the time the instrument data was prepared and cleaned, narrow-band instrumental line features of known origin were removed, as previously described in Section 4.2. However, the data also contained stationary instrumental line features that were not understood, or were poorly understood, and thus were not removed *a priori*. After the search had been conducted, at the time the post-processing started, the origin of more stationary noise lines became known. Therefore, these lines, whose origin was tracked down after the search, are excluded (cleaned *a posteriori*) from the results. A list of the polluted frequency bands which have been cleaned *a posteriori* is shown in Table 4.3.

However, noise features still not understood instrumentally at this point were not removed from the results. As a consequence, the output from the post-processing pipeline contains instrumental artifacts that in some respects mimic CW signals. But these artifacts tend to cluster in certain regions of parameter space, and in many cases they can be automatically identified and vetoed as done in previous searches [158, 1]. The method used here is derived in Chapter 5 and a detailed description of its application is found in Section 5.6.

For a coherent observation time baseline of 30 h the parameter-space regions where instrumental lines tend to appear are determined by global-correlation hypersurfaces of the \mathcal{F} -statistic (see Chapter 5). On physical grounds, in these parameter-space regions there is little or no frequency Doppler modulation from the Earth's motion, which can lead to a relatively stationary detected frequency. Thus, according to Section 5.6, the locations of instrumental-noise candidate events are described by

$$\left| \dot{f} + f \frac{\mathbf{v}_j}{c} \cdot \hat{\mathbf{n}} \right| < \epsilon, \quad (4.7)$$

where c denotes the speed of light, $\hat{\mathbf{n}}$ is a unit vector pointing to the source's sky-location in the SSB frame and relates to the equatorial coordinates α and δ by $\hat{\mathbf{n}} = (\cos \delta \cos \alpha, \cos \delta \sin \alpha, \sin \delta)$, \mathbf{v}_j is the orbital velocity of the Earth at the midpoint of the j th data segment ($|\mathbf{v}_j| \approx 10^{-4} c$). The parameter ϵ accounts for a certain tolerance needed due to the parameter-space gridding and can be understood as $\epsilon = \Delta f / N_c \Delta T$,

Table 4.3: Frequencies of instrumental lines that have been excluded *a posteriori* from the post-processed search results. Each column shows the central frequency f_{Line} around which a bandwidth of $\Delta f_{\text{Line}} = f_{\text{Line}} \times 10^{-4}$ has been removed on either side. The cleaned bandwidth corresponds to the maximum possible frequency shift due to the global parameter-space correlations (see Chapter 5). On physical grounds this is related to the maximum possible Doppler shift due to the orbital velocity of the Earth, which is approximately 10^{-4} in units of the speed of light.

$f_{\text{Line}}[\text{Hz}]$	$f_{\text{Line}}[\text{Hz}]$	$f_{\text{Line}}[\text{Hz}]$	$f_{\text{Line}}[\text{Hz}]$
69.75	568.17	1030.55	1292.91
90.0	570.41	1042.19	1294.14
100.0	645.56	1043.33	1297.67
128.0	646.46	1092.01	1298.93
256.0	647.07	1128.28	1317.47
335.0	648.84	1132.22	1377.14
329.0	649.46	1136.23	1388.38
546.01	658.74	1142.87	1390.70
548.38	686.92	1145.29	1391.60
564.14	930.34	1146.59	
566.17	988.19	1291.11	

where Δf denotes width in frequency (corresponding to the coincidence-cell width in the post-processing) up to which candidate events can be resolved during the characteristic length of time ΔT , and N_c represents the size of the vetoed or rejected region, measured in coincidence cells. In this analysis $\Delta T = 5\,718\,724\text{ s}$ (≈ 66 days) is the total time interval spanned by the input data.

Because false alarms are expected at the level of 10 coincidences, candidates that satisfy Equation (4.7) for more than 10 data segments are eliminated (vetoed). The fraction of parameter space excluded by this veto is determined by Monte-Carlo simulations to be about 13%. From Equation (4.7) it follows that for fixed frequency the resulting fraction of sky excluded by the veto (uniformly averaged over spin-down) is greatest at lowest frequencies and decreases approximately as f^{-1} for higher frequencies. Section 3.7.2 presents an example calculation, illustrating the parameter-space volume excluded by

this vetoing method.

4.6.2 Post-processing results

Figures 4.5 and 4.6 summarize all post-processing results from the entire search frequency range of 50 Hz to 1500 Hz, for each frequency coincidence cell maximized over the entire sky and full spin-down range.

In Figure 4.5a all candidates that have 7 or more coincidences are shown in a sky projection. The color scale is used to indicate the number of coincidences. The most prominent feature still apparent forms an annulus of high coincidences in the sky, including the ecliptic poles, a distinctive fingerprint of the Instrumental-noise lines [3]. To obtain the results shown in Figure 4.5b, the set of candidates is cleaned *a posteriori* by removing strong Instrumental-noise lines, whose origin became understood after the search was begun, and excluding the hardware injections. Finally, in Figure 4.5c the parameter-space veto is applied and coincidence cells which contain candidate events from a single detector only are excluded, too.

In Figure 4.6a the coincidences and significance of all candidates that have 7 or more coincidences are shown as a function of frequency. From this set of candidates the hardware injections are excluded, strong Instrumental-noise lines of known origin are removed, the parameter-space veto is applied and finally single-detector candidates are excluded to obtain Figure 4.6b.

As can be seen from Figures 4.5c and 4.6b there are no candidates that exceed the predefined detection threshold of 20 coincidences (which would initiate more a extensive investigation). The largest number of coincidences found is 10, which is at the background level of false alarms expected from random noise only. From these candidates having 10 coincidences, Table 4.4 lists the ten most significant ones.

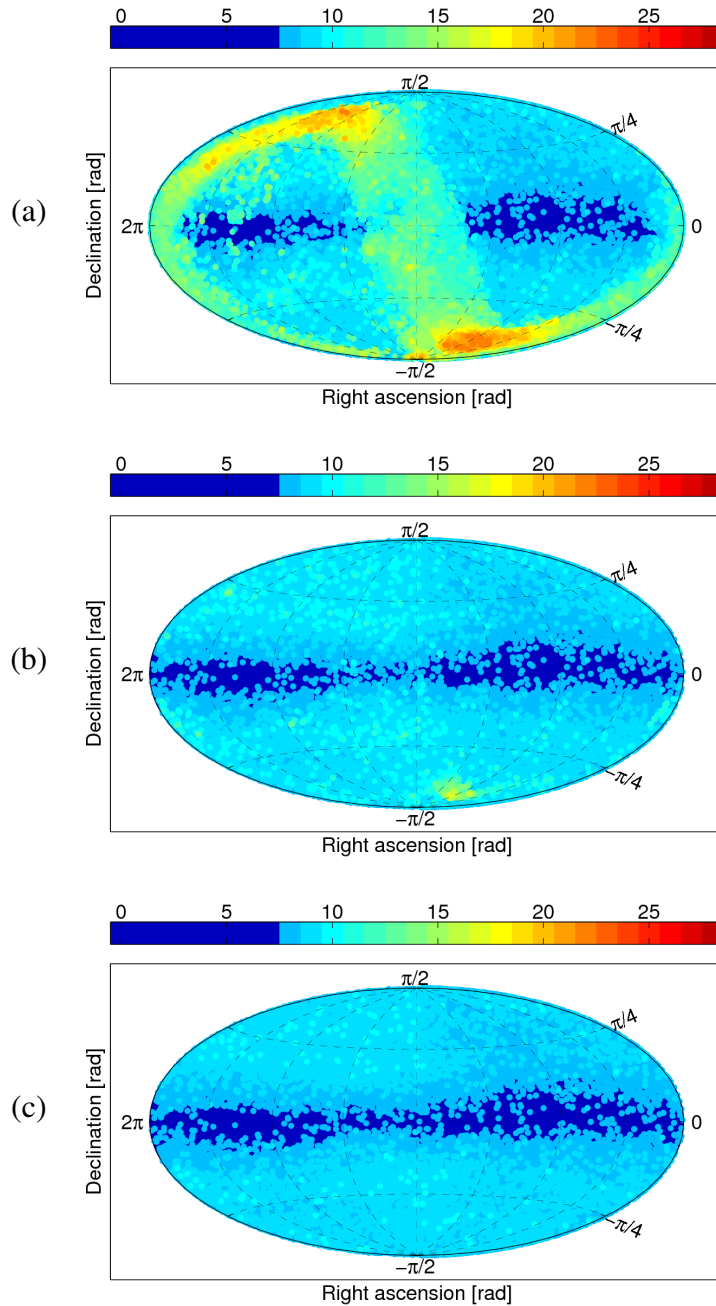


Figure 4.5: Sky maps of post-processing results. Candidates having more than 7 coincidences are shown in Hammer-Aitoff projections of the sky. The color-bar indicates the number of coincidences of a particular candidate (cell). The top plot (a) shows the coincidence analysis results. In (b), *a posteriori* strong lines of known instrumental origin and hardware injections are removed. The bottom plot (c) is obtained by additionally applying the parameter-space veto and excluding single-detector candidates. Note that in every sky map the regions of lower coincidences near the equatorial plane (colored dark blue) are due to the sky-grid construction (cf. Figure 3.3).

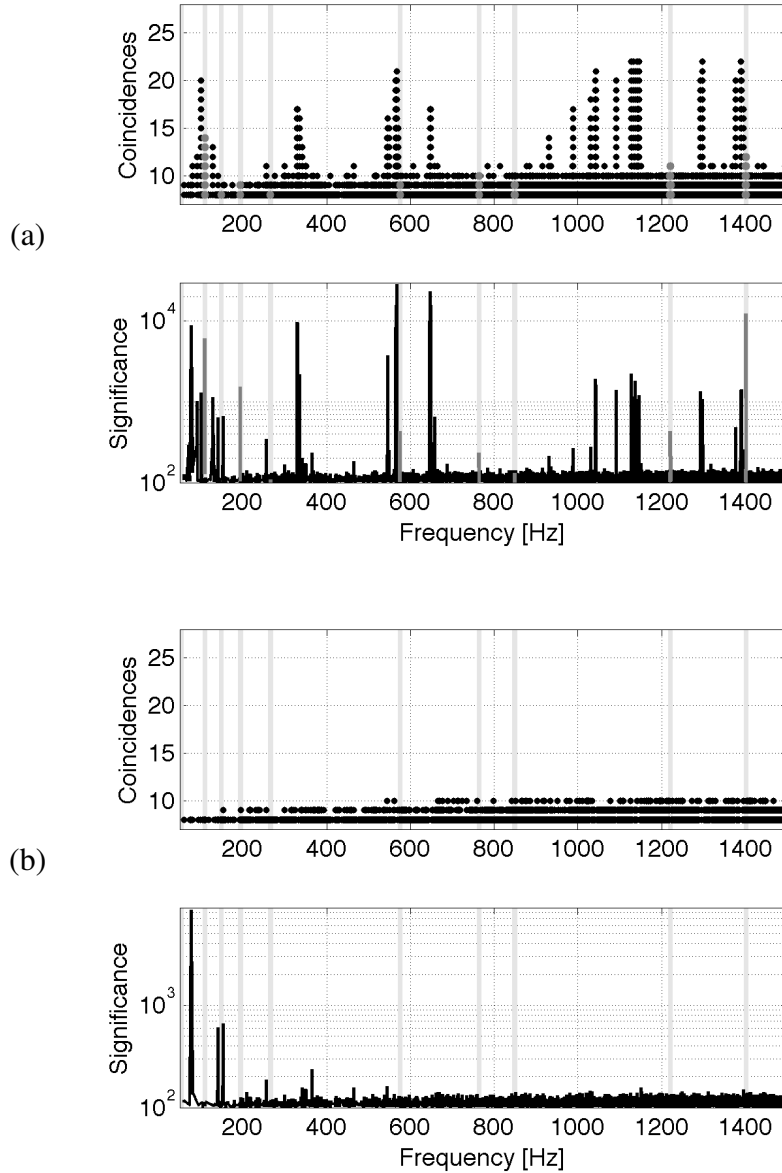


Figure 4.6: The top plot (a) shows the post-processing candidates having more than 7 coincidences as function of frequency. The light-gray shaded rectangular regions highlight the frequency bands of the hardware injections. The dark-gray data points show the candidates resulting from the hardware-injected CW signals. In (b), the final results are shown after exclusion of instrumental lines of known origin and hardware injections, application of parameter-space veto and exclusion of single-detector candidates.

Table 4.4: The ten most significant post-processing candidates that have 10 or more coincidences. The frequency of each candidate f_{cand} refers to the fiducial GPS time $t_{\text{fiducial}} = 816\,397\,490$ s. The parameters δ_{cand} , α_{cand} , \dot{f}_{cand} , $\mathcal{C}_{\text{cand}} = \mathcal{C}_{\text{cand}}^{\text{H1}} + \mathcal{C}_{\text{cand}}^{\text{L1}}$ and $\mathcal{S}_{\text{cand}}$ are for the most-significant, most-coincident candidate with the given frequency of f_{cand} , where $\mathcal{C}_{\text{cand}}^{\text{H1}}$ and $\mathcal{C}_{\text{cand}}^{\text{L1}}$ denote the number of coincidences from detectors H1 and L1, respectively.

f_{cand} [Hz]	δ_{cand} [rad]	α_{cand} [rad]	\dot{f}_{cand} [Hz s ⁻¹]	$\mathcal{C}_{\text{cand}}$	$\mathcal{C}_{\text{cand}}^{\text{H1}}$	$\mathcal{C}_{\text{cand}}^{\text{L1}}$	$\mathcal{S}_{\text{cand}}$	P_{F} per 0.5Hz
543.810438	0.6823	5.9944	-3.24×10^{-10}	10	8	2	160.9	7.2×10^{-5}
1151.534608	1.1330	5.4462	2.11×10^{-11}	10	4	6	154.3	1.4×10^{-3}
1395.351068	-1.1928	2.5980	-3.92×10^{-9}	10	8	2	150.4	7.1×10^{-4}
1249.855062	-1.2380	6.0203	-2.43×10^{-9}	10	8	2	144.2	4.5×10^{-3}
1311.458030	-0.5143	6.1638	-3.32×10^{-9}	10	8	2	142.8	1.7×10^{-3}
1033.967720	0.6002	5.3133	-1.83×10^{-9}	10	8	2	142.7	1.2×10^{-3}
851.799376	1.1071	3.2019	-7.79×10^{-10}	10	8	2	142.1	4.1×10^{-4}
665.944644	-0.4602	2.3638	-1.28×10^{-9}	10	6	4	141.9	1.0×10^{-3}
669.187638	-0.6928	3.0333	-1.58×10^{-9}	10	7	3	141.6	1.0×10^{-3}
1443.831722	0.7046	6.0788	-4.47×10^{-9}	10	7	3	141.5	3.5×10^{-3}

4.7 Comparison with previous searches

The previous Chapter reported on the results of the Einstein@Home search for CW signals in the LIGO S4 data. The present work extends this search analyzing more sensitive LIGO S5 data while using the same methods described in Chapter 3. Therefore, this section elucidates the changes in configuration of the search and post-processing.

First, not only is more sensitive data used here, but also a larger total volume of data is searched compared to Einstein@Home S4 search. The number of 30-hour data segments analyzed increased from 17 to 28.

In addition, the template grids used in each data segment of this search were constructed to be denser, reducing the possible loss of signals due to mismatch in the template waveforms. Compared to the previous search in S4 data, where a maximal mismatch of $m = 0.2$ ($m = 0.5$) was used in the low (high) frequency range, here templates are placed on a grid of higher density using $m = 0.15$ ($m = 0.4$) in the low (high) frequency range.

Moreover, in the high-frequency range a larger range of possible spin-downs is searched. The S4 analysis searched over minimum spin-down ages greater than 10 000 yr for frequencies in the higher range ($f > 300$ Hz), whereas this analysis searches over minimum spin-down ages greater than 8 000 yr for frequencies in the higher range ($f > 400$ Hz). The different partitioning of frequencies into the low and high ranges (split at 300 Hz in S4, split at 400 Hz here) is a consequence of an optimization study reflecting the overall most sensitive search at given computing power.

This search presented here analyzed in total about three times more workunits than in the S4 search. In searching the S4 data, each workunit returned the top 13 000 candidate events, whereas this search is designed to keep only the top 1 000 (10 000) candidate events in the low (high) frequency range. This configuration has the purpose of balancing the load on the Einstein@Home servers, which receive the workunit results. A low-frequency workunit returns a factor of 10 fewer events, because these were designed to last approximately 10 times less than each high-frequency workunit.

Finally, based on the estimates presented in Section 4.5, the present search is overall about a factor of three more sensitive than the previous S4 search. This improvement is

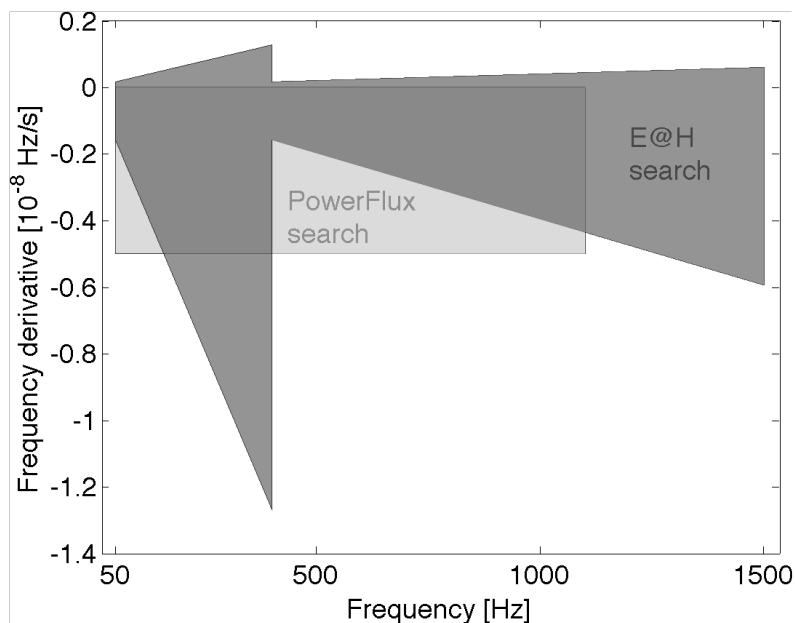


Figure 4.7: Comparison of search parameter spaces in the plane of frequency and frequency derivative. The dark-gray region refers to this Einstein@Home all-sky analysis in early S5 LIGO data. The light-grey area corresponds to the recent all-sky PowerFlux search in early S5 LIGO data.

a consequence of using more sensitive detector data in combination with a finer-spaced template bank.

The methods used here, as well as in the S4 paper, would be expected to give very high confidence if a strong enough signal were present in the data. It is interesting to compare the sensitivity of this detection scheme with the sensitivity of upper limits such as presented recently in [159]. Based on the PowerFlux method [158], that analysis set strain upper limits at the 95% confidence level in the frequency range of 50 – 1100 Hz and the frequency-derivative range of $-5 \times 10^{-9} - 0 \text{ Hz s}^{-1}$ using 7 147 h of early S5 LIGO data, about 8.5 times more data than was used here. Note that this Einstein@Home search explores substantially larger parts of parameter space in frequency and frequency derivative, as shown in Figure 4.7.

The upper-limit worst-case results of [159] for the equatorial sky region are remarkably close to the 90%-detection-level h_0 -values of Figure 4.4. However, these PowerFlux upper limits refer to the most unfavorable polarization and sky position. A population-

based upper limit over all sky locations and polarizations would be lower.

On the other hand, another key difference between the PowerFlux upper limits procedure and the sensitivity estimation carried out here is the detection criteria. In the present work, detection requires a signal to generate 20 or more coincidences among the 28 different data segments. This corresponds to a false alarm probability in Gaussian noise of the order 10^{-21} per 0.5 Hz frequency band. This is different from [159], where simulated signals are compared to the strongest candidates found. Thus, an equivalent detection criterion for this work would be to compare the signals against the strongest candidates in each 0.5 Hz band. These are typically 10 coincidences, which relates to a Gaussian noise false alarm rate of order 10^{-3} . One can estimate the effect on sensitivity by recomputing the sensitivity estimation of Section 4.5, but requiring each signal to produce only 10 coincidences. This reduces the prefactors $R_{\mathcal{D}}$ given above by a factor of 1.24.

Apart from the larger parameter space searched, the present analysis is achieving roughly comparable sensitivity to [159] in spite of searching 8.5 times less data. Much of this effectiveness is due to the increased coherent integration time (30 hours versus 30 minutes), which is only possible due to the great amount of computing power donated by the tens of thousands of Einstein@Home volunteers.

4.8 Conclusion

Using early fifth-science-run LIGO data this Chapter described the results from the Einstein@Home search for unknown CW sources, extending the previous Einstein@Home search in LIGO S4 data presented in Chapter 3. The sensitivity of the present analysis improves upon the previous Einstein@Home S4 search by a factor of about three. Additionally, in large regions of the parameter space probed, this analysis yields the currently most sensitive all-sky search results for CW sources.

No credible periodic gravitational-wave signal was found. Over a 100 Hz-wide band around the detectors' most sensitive frequencies, more than 90% of sources with dimen-

sionless gravitational-wave strain amplitude greater than 3×10^{-24} would have been detected.

While no statistically significant signal was observed in this analysis, the results demonstrate the capability of public distributed computing to accomplish a sensitive CW search for the benefit of future searches.

The sensitivity of the present analysis is essentially limited by the first-stage threshold on \mathcal{F} -statistics forced by the limited data volume which can be returned from the participating clients. The successor Einstein@Home searches currently underway carry out the incoherent combination of \mathcal{F} -statistic results on the client machines (done here in the post-processing once results were sent back), using techniques such as will be presented in Chapter 6. This makes it possible to set a much lower (sensitivity-optimized) first-stage threshold on \mathcal{F} -statistics. Hence, results from the new search promise a significant enhancement in the overall sensitivity for a continuous gravitational-wave detection.

Global correlations in the coherent statistic for CW detection

Appeared in Physical Review D 78, 102005, (2008)

5.1 Overview and context

The emission of continuous gravitational waves (CW) is expected, for instance, from spinning neutron stars with non-axisymmetric deformations, as described in Section 2.3.4. If the system is isolated, it is losing angular momentum through radiation and is slowing down. Therefore the gravitational-wave frequency would be slowly decreasing for this long-lasting type of signal. Such CW sources are among the primary targets of Earth-based, laser-interferometric and resonant-bar detectors.

The terrestrial location of the detectors generates a Doppler modulation of the signal caused by the detector's motion relative to the solar system barycenter (SSB). The observed phase therefore depends on “phase parameters”, which describe the intrinsic frequency evolution and the source's sky location. In addition, there is a time-varying amplitude modulation due to the antenna patterns changing with the Earth's spinning motion. The latter variations depend on the “amplitude parameters”, which are the two polarization amplitudes, and the polarization angle of the gravitational wave.

More than a decade ago, Jaranowski, Królak and Schutz have determined the coherent detection statistic to extract CW signals buried in the detector noise [55]. This data analysis scheme is based on the principle of maximum likelihood detection leading to coherent matched filtering. It was shown, that the amplitude parameters together with the initial-phase parameter can be eliminated by analytically maximizing the detection statistic, such that the search space is just the phase parameters: sky position, frequency and frequency time-derivatives. This detection statistic is commonly referred to as the \mathcal{F} -statistic. For a given sequence of data, wide-band all-sky searches evaluate the \mathcal{F} -statistic over a large number of template-grid points in parameter space. The parameters of the templates for which a predetermined threshold is exceeded are registered as candidate events for potential gravitational-wave signals.

In the *local* parameter-space neighborhood of a given signal one can define a metric [174, 160, 187] from the fractional loss in expected \mathcal{F} -statistic. This fractional loss defines the dimensionless “mismatch” μ . Let \mathbf{p} define a vector of phase parameters for a template. If \mathbf{p}_S denotes the signal’s phase parameters, then the metric $g_{ij}(\mathbf{p}_S)$ is obtained by Taylor-expanding the mismatch at \mathbf{p}_S with respect to the small parameter offsets $\Delta\mathbf{p} \equiv \mathbf{p}_S - \mathbf{p}$ to quadratic order: $\mu = \sum_{ij} g_{ij}(\mathbf{p}_S) \Delta p^i \Delta p^j + \mathcal{O}[(\Delta\mathbf{p})^3]$.

This Chapter presents a comprehensive study of the *global* parameter-space correlations in the coherent detection statistic for continuous gravitational-wave searches. The global parameter-space regions are identified where the detection statistic \mathcal{F} is expected to have large values close to maximal without restriction to the local neighborhood of the signal location. Here, these regions are referred to as the “*global large-value structure*”. To find the global large-value structure of the \mathcal{F} -statistic, a simplified detection statistic \mathcal{F}^* (approximating \mathcal{F}) is considered. The locations in parameter space where \mathcal{F}^* is expected to be maximal are referred to as the “*global maximum structure*”. For increasing parameter offsets from the given signal’s parameters this global maximum structure of \mathcal{F}^* (and therefore also the global large-value structure of \mathcal{F}) is found to become significantly different from the local approximation obtained from the metric.

A previous study [188] examined monochromatic signals in the restricted phase-parameter space of sky location and frequency. It was shown that in an approximate detection statistic, such signals can generate “circles in the sky” while searching a range of template frequencies. The collection of these circles forms a two-dimensional hyper-

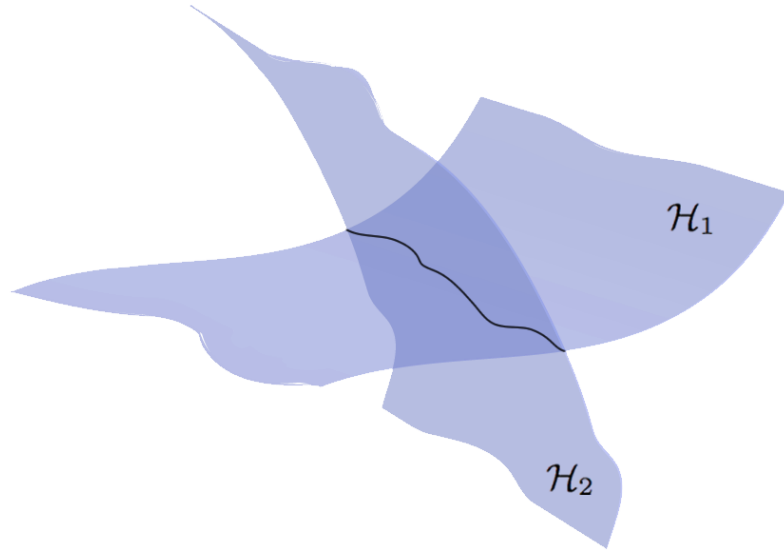


Figure 5.1: Schematic drawing of intersection of two representative global-correlation hypersurfaces \mathcal{H}_1 and \mathcal{H}_2 . The region of intersection, shown by the solid black curve, describes the global maximum structure of the simplified detection statistic \mathcal{F}^* , because the expectation value of \mathcal{F}^* is maximal in these locations. For illustration purposes only two hypersurfaces are shown, whereas in general one might need to consider more hypersurfaces.

surface in the three-dimensional parameter space, described by a single equation. Here, even in this restricted parameter space, this hypersurface is only an approximation of the description of the global maximum structure of the \mathcal{F}^* -statistic to first order in observation time T .

The present work shows that the global maximum structure of the detection statistic \mathcal{F}^* is described by a separate equation for each order of T . The solution to each of these equations is a different hypersurface in parameter space. Therefore, it is this family of *global-correlation hypersurfaces*, which describes the global maximum structure of \mathcal{F}^* : The detection statistic \mathcal{F}^* is expected to be maximal at the intersection of these hypersurfaces. This idea is illustrated schematically in Figure 5.1. The same results also apply when considering the generalization to non-monochromatic signals allowing for an intrinsic frequency evolution of the source.

The global maximum structure of the detection statistic from stationary instrumental-noise artifacts is also described by the global-correlation equations. This permits the

construction of a veto method which excludes false candidate events as will be illustrated, too.

Section 5.2 of this Chapter briefly reviews the matched-filtering method for CW sources. Section 5.3 describes an approximate signal model which leads to the simplified detection statistic allowing the analytical exploration of its global maximum structure. Section 5.4 presents the global-correlation equations of the phase-parameter space and illustrates the geometry of the global-correlation hypersurfaces. In addition, the search-parameter regions are derived for which the approximations used are valid. In Section 5.5 the predictions made by the global-correlation hypersurfaces are compared to a fully coherent \mathcal{F} -statistic search in data sets of software-simulated sources with no detector noise as well as of hardware-injected CW signals in the presence of real detector noise. In Section 5.6 the global large-value of the detection statistic which is caused by stationary instrumental-noise artifacts mimicking astrophysical sources is found to be also well described by the global-correlation equations, and thus a veto method is constructed. Section 5.7 discusses the effects of the Earth's spinning motion in the context of the present topic. Finally a concluding section follows.

5.2 Coherent detection of continuous gravitational-wave signals

In the absence of any signal, the detector output data time series $x(t)$ at detector time t only contains noise $n(t)$, which is assumed to be a zero-mean, stationary and Gaussian random process. If a signal $h(t)$ is present, the noise is assumed to be additive, $x(t) = n(t) + h(t)$. Denote by t_{ssb} the time measured at the solar system barycenter. For a detector at fixed position and orientation, at the SSB the continuous gravitational-wave signal is described by a sinusoid of constant amplitude and a phase given by

$$\Psi(t_{\text{ssb}}) = \Phi_0 + \Phi(t_{\text{ssb}}) = \Phi_0 + 2\pi \sum_{k=0}^{\infty} \frac{f^{(k)}}{(k+1)!} t_{\text{ssb}}^{k+1}, \quad (5.1)$$

where Φ_0 is the initial phase, $f^{(0)} \equiv f$ denotes the frequency, and $f^{(k>0)}$ the k th frequency time-derivative, defining every parameter $f^{(k)}$ at $t = 0$ at the SSB. The integer $s > 0$ denotes the number of frequency time-derivatives to be taken into account, therefore it is set $f^{(k>s)} = 0$. In the case of an isolated rapidly rotating neutron star with non-axisymmetric deformations and negligible proper motion ¹, the waveforms corresponding to the plus (+) and cross (×) polarizations are

$$h_+(t) = A_+ \sin \Psi(t), \quad h_\times(t) = A_\times \cos \Psi(t). \quad (5.2)$$

The Earth's motion with respect to the SSB leads to Doppler effects causing amplitude and phase modulations of the CW signal received at the detector. Define \mathbf{n} as the constant unit vector pointing from the SSB to the source. Neglecting relativistic and higher order corrections, a wavefront arriving at the detector at time t , passes the SSB at time

$$t_{\text{ssb}} = t + \frac{\mathbf{r}(t) \cdot \mathbf{n}}{c}, \quad (5.3)$$

where the vector $\mathbf{r}(t)$ connects from the SSB to the detector, and c is the speed of light.

It is shown in [55] that the resulting phase evolution of the continuous gravitational-wave signal can be reproduced without significant loss in signal-to-noise ratio by the model

$$\Phi(t) = 2\pi \sum_{k=0}^s \left[\frac{f^{(k)} t^{k+1}}{(k+1)!} + \frac{\mathbf{r}(t)}{c} \cdot \mathbf{n} \frac{f^{(k)} t^k}{k!} \right]. \quad (5.4)$$

The received signal is also amplitude modulated by the varying antenna-pattern of the detector due to its motion with the rotation of the Earth. The dimensionless signal response function $h(t)$ of an interferometric detector to a weak plane gravitational wave in the long-wavelength approximation is a linear combination of the form:

$$h(t) = F_+(t) h_+(t) + F_\times(t) h_\times(t), \quad (5.5)$$

where $F_{+,\times}$ are called the antenna-pattern functions, resulting in the amplitude modulations from Earth's spinning motion. They lie in the range $-1 \leq F_{+,\times} \leq 1$, and depend

¹ The effects of the neutron star's proper motion in this context are discussed in [189, 172]. Assuming an extreme case where the star moves with respect to the SSB at 10^3 km/s and its distance to the detector to be at 40 pc, over 120 days of observation, fitting factors (fraction of signal-to-noise ratio when using a filter not perfectly matching to a signal) greater than 99% are obtained. In addition, in this work observation times of order a few days, much less than 120 days, are considered and therefore the proper-motion effects are neglected.

on the orientation of the detector and source, and on the polarization angle ψ of the waves.

The optimal detection statistic [55, 117] in the maximum-likelihood sense is obtained from the likelihood ratio Λ and defines the matched filter

$$\ln \Lambda = \frac{T}{S_h} \left[(x||h) - \frac{1}{2}(h||h) \right], \quad (5.6)$$

where S_h is the one-sided noise strain spectral density which is assumed to be constant over the narrow bandwidth of the signal, and the inner product is defined as

$$(x||y) \equiv \frac{2}{T} \int_{-T/2}^{T/2} x(t) y(t) dt, \quad (5.7)$$

centering the coherent observation-time interval of duration T around $t = 0$. Replacing the amplitude parameters in Equation (5.6) by their values which maximize $\ln \Lambda$, the so-called maximum likelihood (ML) estimators, defines the coherent detection statistic \mathcal{F} as

$$\mathcal{F} \equiv \ln \Lambda_{\text{ML}}. \quad (5.8)$$

5.3 Matched-filtering detection statistic of a simplified signal model

5.3.1 The simplified signal model

The phase of the continuous gravitational-wave signal is expected to change very rapidly at the detector site on the Earth over a characteristic time length of typically less than ten seconds, whereas the amplitude of the signal changes with a period of one sidereal day. As a result [189], the detection of a CW signal requires an accurate model of its phase, because even $1/4$ of a cycle difference between template and signal can lead to a loss in signal-to-noise ratio of 10%. Whereas modeling of its amplitude is less critical. Therefore, the antenna pattern functions $F_{+, \times}$ are assumed to be constant, so

that the signal model (5.5) becomes

$$h(t) = A_1 \cos \Phi(t) + A_2 \sin \Phi(t) , \quad (5.9)$$

where $A_{1,2}$ are defined to be the constant effective amplitudes. The validity of this approximation is investigated using Monte-Carlo simulations in [189].

The vector $\mathbf{r}(t)$ connecting the SSB and the detector can be decomposed into an orbital component $\mathbf{r}_{\text{orb}}(t)$ and a spin component $\mathbf{r}_{\text{spin}}(t)$ as

$$\mathbf{r}(t) = \mathbf{r}_{\text{orb}}(t) + \mathbf{r}_{\text{spin}}(t) , \quad (5.10)$$

where $\mathbf{r}_{\text{orb}}(t)$ represents the vector from the SSB to the Earth's barycenter, and $\mathbf{r}_{\text{spin}}(t)$ is the vector from the Earth's barycenter to the detector. Thus, substituting the decomposition (5.10) into Equation (5.4) one can write separately the orbital component $\phi_{\text{orb}}(t)$ and the spin component $\phi_{\text{spin}}(t)$ in the phase model (5.4) as

$$\Phi(t) = 2\pi \left(\sum_{k=0}^s \frac{f^{(k)}}{(k+1)!} t^{k+1} \right) + \phi_{\text{orb}}(t) + \phi_{\text{spin}}(t), \quad (5.11)$$

where

$$\phi_{\text{orb}}(t) \equiv 2\pi \frac{\mathbf{r}_{\text{orb}}(t) \cdot \mathbf{n}}{c} \left(\sum_{k=0}^s \frac{f^{(k)}}{k!} t^k \right), \quad (5.12)$$

$$\phi_{\text{spin}}(t) \equiv 2\pi \frac{\mathbf{r}_{\text{spin}}(t) \cdot \mathbf{n}}{c} \left(\sum_{k=0}^s \frac{f^{(k)}}{k!} t^k \right). \quad (5.13)$$

The orbital motion of the Earth has a period of one year, so its angular frequency is $\Omega_{\text{orb}} = 2\pi/1 \text{ yr}$. Fully coherent all-sky searches for observation times T much larger than a few days are computationally prohibitive [55, 160]. Thus for computationally feasible coherent searches or coherent stages of hierarchical multistage searches [164, 165] the typical observation time baseline would be of order a few days. Therefore, only observation times T are considered, which are much shorter than one year: $\Omega_{\text{orb}} T \ll 2\pi$. Then the component $\mathbf{r}_{\text{orb}}(t)$ will vary slowly and one may use a Taylor expansion at time t_0 with

$$\mathbf{r}_{\text{orb}}(t) = \sum_{\ell=0}^{\infty} \mathbf{r}_{\text{orb}}^{(\ell)}(t_0) \frac{(t-t_0)^\ell}{\ell!}, \quad (5.14)$$

where $\mathbf{r}_{\text{orb}}^{(\ell)}(t_0)$ denotes the ℓ th derivative with respect to time of $\mathbf{r}_{\text{orb}}(t)$ evaluated at t_0 . Without loss of generality one may choose $t_0 = 0$ as the midpoint of the observation of duration T in the following discussion. Define $\boldsymbol{\xi} \equiv \mathbf{r}_{\text{orb}}(0)/c$ with $\xi \equiv |\boldsymbol{\xi}|$ such that

$$\boldsymbol{\xi}^{(\ell)} = \frac{\mathbf{r}_{\text{orb}}^{(\ell)}(0)}{c} \quad \text{and} \quad \xi^{(\ell)} = \left| \boldsymbol{\xi}^{(\ell)} \right|. \quad (5.15)$$

Together with Equation (5.14) the orbital component of the phase (5.12) can be written as

$$\begin{aligned} \phi_{\text{orb}}(t) &= 2\pi \left(\sum_{k=0}^s f^{(k)} \frac{t^k}{k!} \right) \left(\sum_{\ell=0}^{\infty} \frac{t^\ell}{\ell!} \boldsymbol{\xi}^{(\ell)} \cdot \mathbf{n} \right) \\ &= 2\pi \left[\sum_{k=0}^{\infty} t^k \left(\sum_{\ell=0}^k \frac{f^{(\ell)} \boldsymbol{\xi}^{(k-\ell)} \cdot \mathbf{n}}{\ell! (k-\ell)!} \right) \right]. \end{aligned} \quad (5.16)$$

The spinning motion of the Earth has a period of one sidereal day (1 sd), which translates into an angular frequency of $\Omega_{\text{spin}} = 2\pi/1$ sd. The corresponding average velocity of $v_{\text{spin}}/c \approx 10^{-6}$ is two orders of magnitude smaller than the corresponding orbital velocity, $v_{\text{orb}}/c \approx 10^{-4}$. In what follows, we neglect the contribution of the spin component $\phi_{\text{spin}}(t)$ to the phase (5.11). Section 5.7 will discuss in detail the effects of the spin component $\phi_{\text{spin}}(t)$ in terms of the matched-filtering amplitude.

Using $\phi_{\text{orb}}(t)$ in the form of Equation (5.16), we refer to $\Phi_{\text{orb}}(t)$ as the ‘‘orbital phase model’’:

$$\begin{aligned} \Phi_{\text{orb}}(t) &\equiv 2\pi \left[f \boldsymbol{\xi} \cdot \mathbf{n} + \sum_{k=0}^{\infty} t^{k+1} \left(\frac{f^{(k)}}{(k+1)!} \right. \right. \\ &\quad \left. \left. + \sum_{\ell=0}^{k+1} \frac{f^{(\ell)}}{\ell! (k-\ell+1)!} \boldsymbol{\xi}^{(k-\ell+1)} \cdot \mathbf{n} \right) \right]. \end{aligned} \quad (5.17)$$

By reparameterization the orbital phase model (5.17) can be written as

$$\Phi_{\text{orb}}(t) = \sum_{m=0}^{\infty} u_m t^m, \quad (5.18)$$

where the coefficients u_m of the power series are defined by

$$u_0 \equiv 2\pi f \boldsymbol{\xi} \cdot \mathbf{n}, \quad (5.19a)$$

$$u_1 \equiv 2\pi \left(f + f \boldsymbol{\xi}^{(1)} \cdot \mathbf{n} + f^{(1)} \boldsymbol{\xi} \cdot \mathbf{n} \right), \quad (5.19b)$$

$$u_2 \equiv 2\pi \left(\frac{f^{(1)}}{2} + \frac{f}{2} \boldsymbol{\xi}^{(2)} \cdot \mathbf{n} + f^{(1)} \boldsymbol{\xi}^{(1)} \cdot \mathbf{n} + \frac{f^{(2)}}{2} \boldsymbol{\xi} \cdot \mathbf{n} \right), \quad (5.19c)$$

$$u_3 \equiv 2\pi \left(\frac{f^{(2)}}{6} + \frac{f}{6} \boldsymbol{\xi}^{(3)} \cdot \mathbf{n} + \frac{f^{(1)}}{2} \boldsymbol{\xi}^{(2)} \cdot \mathbf{n} + \frac{f^{(2)}}{2} \boldsymbol{\xi}^{(1)} \cdot \mathbf{n} + \frac{f^{(3)}}{6} \boldsymbol{\xi} \cdot \mathbf{n} \right), \quad (5.19d)$$

so that for arbitrary order of $m > 0$ the coefficient u_m is obtained as

$$u_m \equiv 2\pi \left(\frac{f^{(m-1)}}{m!} + \sum_{\ell=0}^m \frac{f^{(\ell)}}{\ell!(m-\ell)!} \boldsymbol{\xi}^{(m-\ell)} \cdot \mathbf{n} \right). \quad (5.19e)$$

5.3.2 The simplified matched-filtering detection statistic

By analogy to Equation (5.6), we refer to $\ln \Lambda^*$ as the log likelihood function of the simplified CW signal model described in previous Section 5.3.1. Maximization of $\ln \Lambda^*$ with respect to the unknown amplitudes $A_{1,2}$ yields their ML estimators. By substituting the ML estimators back into $\ln \Lambda^*$, the simplified detection statistic \mathcal{F}^* is defined as

$$\mathcal{F}^* \equiv \ln \Lambda_{\text{ML}}^* = \frac{T}{2S_h} |(x||e^{-i\Phi_{\text{orb}}})|^2 = \frac{T}{2S_h} |\mathcal{X}|^2, \quad (5.20)$$

where the detection-statistic amplitude \mathcal{X} has been defined through

$$\mathcal{X} \equiv (x||e^{-i\Phi_{\text{orb}}}), \quad (5.21)$$

using the orbital phase model Φ_{orb} .

For further simplicity consider a data set $x(t)$ which only contains unit-amplitude signal $s(t)$, such that

$$x(t) = \Re[s(t)]. \quad (5.22)$$

Let the phase-parameter vector $\mathbf{p}_S = (\{f_S^{(k)}\}, \mathbf{n}_S)$ define the phase $\Phi_{\text{orb}}^S(t)$ of the signal. Then $s(t)$ can be expressed as

$$s(t) = e^{-i\Phi_{\text{orb}}^S(t)}, \quad (5.23)$$

and one obtains $x(t) = \cos \Phi_{\text{orb}}^{\text{S}}(t)$. The difference in phase $\Delta\Phi_{\text{orb}}(t)$ between the phase $\Phi_{\text{orb}}^{\text{S}}(t)$ of the signal and the phase $\Phi_{\text{orb}}(t)$ of a template $\mathbf{p} = (\{f^{(k)}\}, \mathbf{n})$ is defined by

$$\Delta\Phi_{\text{orb}}(t) \equiv \Phi_{\text{orb}}^{\text{S}}(t) - \Phi_{\text{orb}}(t). \quad (5.24)$$

The maximization of \mathcal{F}^* is equivalent to maximizing $|\mathcal{X}|^2$. Using Equation (5.23) one may rewrite the simplified matched-filtering amplitude \mathcal{X} as

$$\begin{aligned} \mathcal{X} &= \frac{2}{T} \int_{-T/2}^{T/2} x(t) e^{-i\Phi_{\text{orb}}(t)} dt \\ &= \frac{1}{T} \int_{-T/2}^{T/2} e^{i\Delta\Phi_{\text{orb}}(t)} + e^{-i[\Phi_{\text{orb}}^{\text{S}}(t) + \Phi_{\text{orb}}(t)]} dt. \end{aligned} \quad (5.25)$$

Dropping the rapidly oscillating term in Equation (5.25) yields

$$\mathcal{X} \approx \frac{1}{T} \int_{-T/2}^{T/2} e^{i\Delta\Phi_{\text{orb}}(t)} dt. \quad (5.26)$$

Thus, Equation (5.26) shows that $|\mathcal{X}|$ has a global maximum of $|\mathcal{X}| = 1$, if during the observation time interval T the phase difference $\Delta\Phi_{\text{orb}}(t)$ is stationary:

$$\frac{\partial\Delta\Phi_{\text{orb}}(t)}{\partial t} = 0. \quad (5.27)$$

Later, we will demonstrate that for the orbital phase model, unity of $|\mathcal{X}|$ can be obtained *not only* for the case where all individual phase parameters exactly match ($\Delta f^{(k)} \equiv f_{\text{S}}^{(k)} - f^{(k)} = 0$, $\Delta\mathbf{n} \equiv \mathbf{n}_{\text{S}} - \mathbf{n} = \mathbf{0}$) and so $\Delta\Phi_{\text{orb}}(t) = 0$, *but also* for different non-zero offsets ($\Delta f^{(k)} \neq 0$, $\Delta\mathbf{n} \neq \mathbf{0}$) which compensate each other to achieve $\partial\Delta\Phi_{\text{orb}}(t)/\partial t \approx 0$ and thus lead to a value of $|\mathcal{X}|$ close to unity.

5.4 Global-correlation hypersurfaces in parameter space

5.4.1 The global-correlation equations

The central goal of this work is to identify those locations in parameter space where the simplified detection statistic \mathcal{F}^* is maximal, which corresponds to regions where

$|\mathcal{X}|^2$ is one. Consistent with Equations (5.18), (5.19) and (5.24), the differences between the coefficients u_m of the template's phase and the coefficients u_m^S of the signal's phase are defined by

$$\Delta u_m \equiv u_m^S - u_m. \quad (5.28)$$

Thus, Equation (5.24) can be expressed as

$$\Delta \Phi_{\text{orb}}(t) = \sum_{m=0}^{\infty} \Delta u_m t^m, \quad (5.29)$$

and finally one can rewrite Equation (5.25) as

$$\mathcal{X} = \frac{e^{i\Delta u_0}}{T} \int_{-T/2}^{T/2} \exp\left(i \sum_{m=1}^{\infty} \Delta u_m t^m\right) dt. \quad (5.30)$$

It is apparent that $|\mathcal{X}|$ does not depend upon the zero-order term Δu_0 , and therefore the same holds for the detection statistic \mathcal{F}^* . The values of Δu_m for which $|\mathcal{X}|$ attains its maximum of $|\mathcal{X}| = 1$ consistent with (5.27) are obvious from Equation (5.29), namely when

$$\frac{\partial \Delta \Phi_{\text{orb}}(t)}{\partial t} = \sum_{m=0}^{\infty} m \Delta u_m t^{m-1} = 0, \quad (5.31)$$

the following central result is obtained: the family of *global-correlation equations* which describes the global maximum structure of \mathcal{F}^* ,

$$\Delta u_m = 0, \quad (5.32)$$

where $m > 0$, because \mathcal{F}^* is independent of Δu_0 . Because $(1, t, t^2, \dots)$ is a basis of the vector space of real polynomials, the zero vector can only be represented by the trivial linear combination, which is given by Equation (5.32).

Thus, the first global-correlation equation given by $\Delta u_1 = 0$ can be rewritten as

$$f + f \boldsymbol{\xi}^{(1)} \cdot \mathbf{n} + f^{(1)} \boldsymbol{\xi} \cdot \mathbf{n} = K_1, \quad (5.33)$$

where $K_1 \equiv u_1^S/2\pi$ represents a constant defined by the signal's phase parameters. As a side remark, it should be mentioned that Equation (5.33) is a generalization of the first-order global-correlation equation found in [188] to signals with non-zero frequency time-derivatives. But in order to describe qualitatively the global maximum structure of

the simplified detection statistic in parameter space, considering only the first order (as done in [188]) might not be sufficient. As a matter of fact, this is shown in Section 5.4.4 and will be confirmed by analyzing simulated signals later on.

Therefore, continuing to the next order in time, one obtains from the second condition $\Delta u_2 = 0$ the following relation,

$$f^{(1)} + f \boldsymbol{\xi}^{(2)} \cdot \mathbf{n} + 2f^{(1)} \boldsymbol{\xi}^{(1)} \cdot \mathbf{n} + f^{(2)} \boldsymbol{\xi} \cdot \mathbf{n} = K_2, \quad (5.34)$$

where the constant $K_2 \equiv u_2^S/2\pi$ is defined by the signal's phase parameters.

In general, this scheme can be extended to arbitrary order $m > 0$. Thus, the family of global-correlation equations represented by $\Delta u_m = 0$ can be written in the form

$$\frac{f^{(m-1)}}{m!} + \sum_{\ell=0}^m \frac{f^{(\ell)} \boldsymbol{\xi}^{(m-\ell)} \cdot \mathbf{n}}{\ell!(m-\ell)!} = K_m, \quad (5.35)$$

where the signal's phase parameters determine the constant $K_m \equiv u_m^S/2\pi$. In the following the geometry of the solution to the family of equations given by (5.35) will be explored and the *hypersurfaces* they describe in parameter space will be illustrated.

5.4.2 The geometry of the global-correlation equations

Let the space of phase parameters $\mathfrak{p} = (\{f^{(k)}\}, \mathbf{n})$ be a manifold denoted by \mathcal{P} . Previously we defined \mathbf{n} as a unit vector pointing to the source's sky location in the SSB frame of reference. A position on the sky can be determined by two independent coordinates, for example one can use equatorial coordinates of right ascension (RA) and declination, denoted by α and δ , respectively. In these coordinates: $\mathbf{n} = (\cos \delta \cos \alpha, \cos \delta \sin \alpha, \sin \delta)$. Recall that the integer s is related to the number of spin-down parameters considered ($f^{(k>s)} = 0$), thus the phase-parameter space dimensionality is $s + 3$.

By inspection of Equation (5.35), it is obvious that for a given continuous gravitational-wave signal the set of solutions to each global-correlation equation $\Delta u_m = 0$, is a *hypersurface* in the search parameter space \mathcal{P} . Denoting each hypersurface by \mathcal{H}_m one may write

$$\mathcal{H}_m = \{\mathfrak{p} \in \mathcal{P} : \Delta u_m = 0\}, \quad (5.36)$$

given the signal's phase parameters u_m^S . The dimensionality of each hypersurface \mathcal{H}_m is $s + 2$.

Using the parameters u_m of Equation (5.19), we define the vector $\mathbf{u} \equiv (\{u_m\}) = (u_1, u_2, \dots)$ and denote the corresponding parameter-space manifold by \mathcal{U} . Let the vector $\mathbf{u}^S \in \mathcal{U}$ denote the signal's parameters, and define the difference $\Delta\mathbf{u} = \mathbf{u}^S - \mathbf{u} = (\Delta u_1, \Delta u_2, \dots)$. Considering the detection-statistic amplitude $|\mathcal{X}|$ as a function of $\Delta\mathbf{u}$, then this function is extremal with respect to the parameter u_m along the hypersurface \mathcal{H}_m defined by $\Delta u_m = 0$,

$$\left. \frac{\partial |\mathcal{X}(\Delta\mathbf{u})|}{\partial u_m} \right|_{\Delta u_m=0} = 0. \quad (5.37)$$

Obviously, on the intersection of these hypersurfaces \mathcal{H}_m at $\Delta\mathbf{u} = 0$, $|\mathcal{X}|$ is maximum with respect to all the parameters u_m : $\nabla |\mathcal{X}(\Delta\mathbf{u} = 0)| = 0$. Thus, it follows that the simplified detection statistic \mathcal{F}^* is also expected to be maximal at the intersection of these hypersurfaces. Therefore, the global maximum structure is defined by the intersection of the global-correlation hypersurfaces \mathcal{H}_m . This idea has been shown schematically in Figure 5.1. In the absence of noise, all candidate events produced by a given CW signal which follows the simplified model introduced in Section 5.3.1 will be located on the hypersurface \mathcal{H}_1 , described by Equation (5.33). From all candidate events located on \mathcal{H}_1 those will belong to loudest ones (have largest values of \mathcal{F}^*) which are located at the intersection with hypersurface \mathcal{H}_2 , which is described by Equation (5.34). For each higher order m this behavior carries itself forward in the same way.

5.4.3 Visualization of the global-correlation hypersurfaces

As an illustrative example visualization of the geometrical structure formed by the global-correlation hypersurfaces (5.35), we choose the four-dimensional phase-parameter space ($s = 1$). Thus, the four dimensions are sky position (right ascension α and declination δ), the frequency f , and the first spin-down parameter $f^{(1)}$. For demonstration purposes, consider an exemplary continuous gravitational-wave signal with the phase parameters $f_S = 100.0$ Hz, $\alpha_S = 2.0$ rad, $\delta_S = -1.0$ rad and $f_S^{(1)} = -10^{-10}$ Hz/s.

In this illustration, assume that we have a bank of templates available covering the

whole sky, the entire Doppler frequency band ², $f_s \pm f_s \times 10^{-4}$, and for the spin-down value of $f^{(1)} = -10^{-11}$ Hz/s. The attentive reader will notice that the signal's spin-down value is not covered by this template value, but mismatched by an order of magnitude. This choice will demonstrate that due to the parameter-space correlations the signal is still expected to be detected in such a search, producing a detection-statistic maximum-structure which is predicted by the global-correlation equations.

The global-correlation equations only for $m \leq 2$ have to be considered in the present example, because contributions to $|\mathcal{X}|$ in (5.30) from terms beyond second order are negligible, as will be shown later in Section 5.4.4. There, the neglected third-order term in Equation (5.30) is estimated and found to be irrelevant, in the case of the signal investigated here, and for observation times T approximately less than 61 hours.

For the case of $m \leq 2$ the integral (5.30) can be obtained analytically as follows

$$\begin{aligned} \mathcal{X} &\approx \frac{e^{i\Delta u_0}}{T} \int_{-T/2}^{T/2} e^{i(\Delta u_1 t + \Delta u_2 t^2)} dt \\ &= \frac{\sqrt{\pi}}{2T\sqrt{\Delta u_2}} \exp \left[i \left(\Delta u_0 - \frac{\Delta u_1^2}{4\Delta u_2} + \frac{\pi}{4} \right) \right] \\ &\quad \times \left\{ \operatorname{erf} \left[\frac{(\Delta u_1 + \Delta u_2 T)e^{-i\pi/4}}{2\sqrt{\Delta u_2}} \right] - \operatorname{erf} \left[\frac{(\Delta u_1 - \Delta u_2 T)e^{-i\pi/4}}{2\sqrt{\Delta u_2}} \right] \right\}, \end{aligned} \quad (5.38)$$

where the error function $\operatorname{erf}(x)$ is defined by

$$\operatorname{erf}(x) \equiv \frac{2}{\sqrt{\pi}} \int_0^x e^{-t^2} dt. \quad (5.39)$$

Figure 5.2 shows $|\mathcal{X}|$ given by Equation (5.38) as a function of the dimensionless parameters $\Delta u_1 T$ and $\Delta u_2 T^2$. This figure visualizes the fact that when one moves away in parameter space from the global-correlation hypersurfaces at $\Delta u_m = 0$ to increasing non-zero values of Δu_m , the detection-statistic amplitude $|\mathcal{X}|$ decreases rapidly from its maximum of one towards zero, as is shown in Figure 5.2.

As mentioned earlier, the two equations from the family of global-correlation equations (5.35) to be considered for the example signal studied here are:

$$f + f \boldsymbol{\xi}^{(1)} \cdot \mathbf{n} + f^{(1)} \boldsymbol{\xi} \cdot \mathbf{n} = K_1, \quad (5.40a)$$

$$f^{(1)} + f \boldsymbol{\xi}^{(2)} \cdot \mathbf{n} + 2f^{(1)} \boldsymbol{\xi}^{(1)} \cdot \mathbf{n} = K_2, \quad (5.40b)$$

² The maximum Doppler frequency shift due to the Earth motion is given approximately by the maximum Earth's orbital velocity $v_{\text{orb}}/c \approx 10^{-4}$.

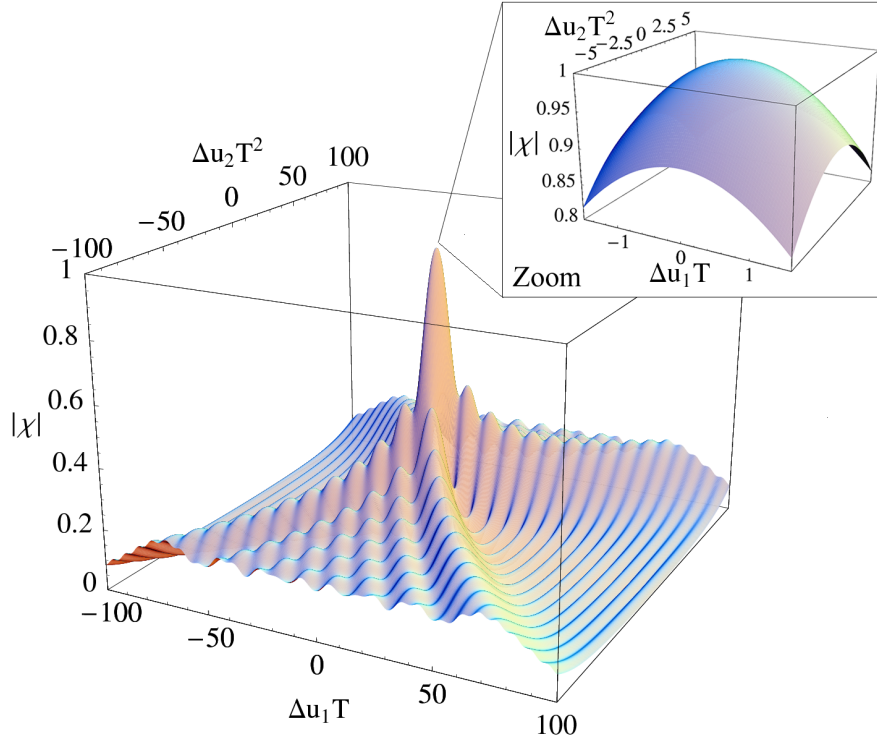


Figure 5.2: Illustration of the simplified detection-statistic amplitude $|\chi|$ for $m \leq 2$, given by Equation (5.38), as a function of the dimensionless parameters $\Delta u_1 T$ and $\Delta u_2 T^2$.

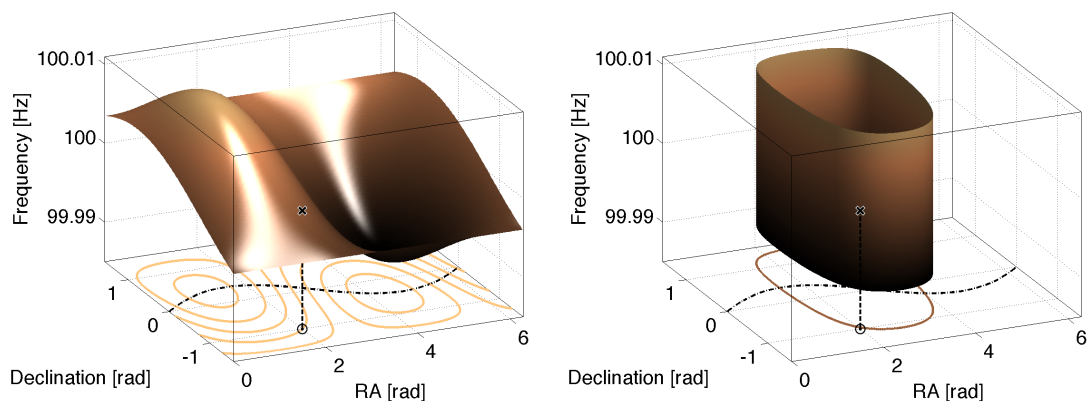
where in this case the constants $K_{1,2}$ are obtained from the signal's phase parameters $(f_s, f_s^{(1)}, \mathbf{n}_s)$ as

$$K_1 = f_s + f_s \boldsymbol{\xi}^{(1)} \cdot \mathbf{n}_s + f_s^{(1)} \boldsymbol{\xi} \cdot \mathbf{n}_s, \quad (5.41a)$$

$$K_2 = f_s^{(1)} + f_s \boldsymbol{\xi}^{(2)} \cdot \mathbf{n}_s + 2f_s^{(1)} \boldsymbol{\xi}^{(1)} \cdot \mathbf{n}_s. \quad (5.41b)$$

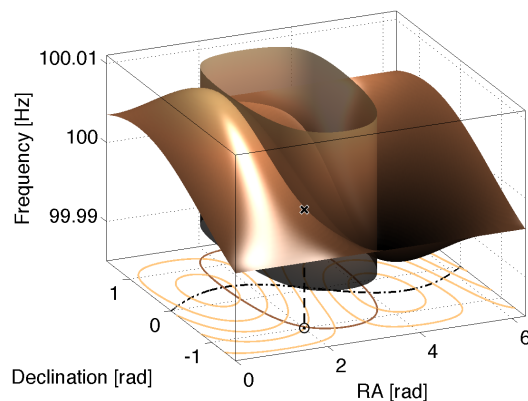
Figure 5.3 presents the visualization of the hypersurfaces \mathcal{H}_1 and \mathcal{H}_2 described by Equations (5.40a) and (5.40b) for the given CW signal. As described in Section 5.4.2, when choosing $s = 1$, then we have $\dim \mathcal{H}_1 = \dim \mathcal{H}_2 = 3$.

In Figure 5.3 the subspace $\{f, \mathbf{n}\}$ is shown at the fixed target spin-down of $f^{(1)} = -10^{-11}$ Hz/s. The hypersurface described by Equation (5.40a) for the fixed $f^{(1)}$ is depicted three-dimensionally in Figure 5.3a. The 3D plot of Figure 5.3b shows the hypersurface defined by Equation (5.40b) for the same signal and same template values.



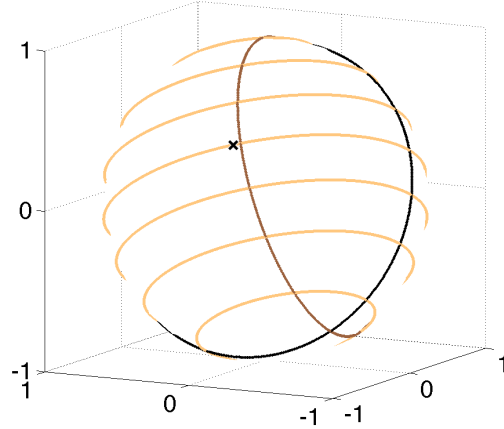
(a) Global-correlation hypersurface \mathcal{H}_1 and contour lines of constant frequency shown in the sky.

(b) Global-correlation hypersurface for \mathcal{H}_2 and contour lines of constant frequency shown in the sky (all close to each other).

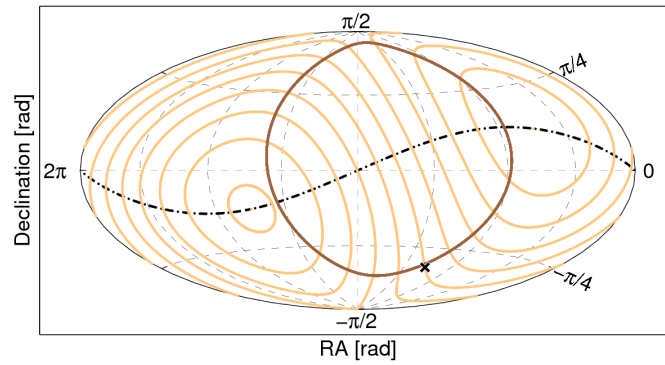


(c) Superposition of global-correlation hypersurfaces $\mathcal{H}_{1,2}$, and their frequency contour lines in the sky.

Figure 5.3: The global-correlation hypersurfaces \mathcal{H}_1 ($\Delta u_1 = 0$) and \mathcal{H}_2 ($\Delta u_2 = 0$) for a given CW signal shown in the three-dimensional subspace $\{f, \mathbf{n}\}$ at the fixed target spin-down of $f^{(1)} = -10^{-11}$ Hz/s. Each plot refers to GPS time 793555944 s. The phase parameters of the signal are $\alpha_S = 2.0$ rad, $\delta_S = -1.0$ rad, $f_S = 100.0$ Hz, $f_S^{(1)} = -10^{-10}$ Hz/s, as indicated by the black cross (black circle) in the subspace $\{f, \mathbf{n}\}$ (in the sky plane). In (c) the superposition of (a) and (b) illustrates the locations of expected maximum detection statistic along the intersection curve of both hypersurfaces. In each plot the light solid contour lines in the sky of constant f (and $f^{(1)}$) are of \mathcal{H}_1 , the dark solid contour lines are the ones of \mathcal{H}_2 . These contours of both hypersurfaces actually describe circles on the three-dimensional sky sphere, see Figure 5.4 for corresponding Hammer-Aitoff sky projections. In the sky subspace of this example, the intersection curve approximately coincides with the contours of \mathcal{H}_2 , and due to the mismatch in spin-down the intersection curve does not pass through the signal's true sky-location. The black dotted-dashed curve represents the ecliptic.



(a) Unit sphere with contour lines (circles) of global-correlation hypersurfaces $\mathcal{H}_{1,2}$.



(b) Hammer-Aitoff sky projection showing the contour lines (circles) of global-correlation hypersurfaces $\mathcal{H}_{1,2}$.

Figure 5.4: (Continuation of Figure 5.3) The global-correlation hypersurfaces \mathcal{H}_1 ($\Delta u_1 = 0$) and \mathcal{H}_2 ($\Delta u_2 = 0$) for a given CW signal shown in the two-dimensional sky subspace at the fixed target spin-down, see Figure 5.3 for further details. In each plot the light solid contour lines in the sky of constant f (and $f^{(1)}$) are of \mathcal{H}_1 , the dark solid contour lines are the ones of \mathcal{H}_2 . These contours of both hypersurfaces, shown in a Hammer-Aitoff projection in (b), actually describe circles on the three-dimensional unit sphere as is visualized by (a). In the sky subspace of this example, the intersection curve approximately coincides with the contours of \mathcal{H}_2 , and due to the mismatch in spin-down the intersection curve does not pass through the signal's true sky-location. The black dotted-dashed curve represents the ecliptic.

Finally, Figure 5.3c combines Figures 5.3a and 5.3b showing both hypersurfaces and illustrating their intersection. Along this intersection curve of both hypersurfaces, $|\mathcal{X}|$ (and so \mathcal{F}^*) is expected to be maximal for the CW signal examined in this example. The contour lines of constant f (and $f^{(1)}$) in the sky of both hypersurfaces are shown on the three-dimensional unit-sphere by Figure 5.4a and in a 2D Hammer-Aitoff projection by Figure 5.4b. Here, in the sky subspace the intersection curve of \mathcal{H}_1 and \mathcal{H}_2 (corresponding to maximal detection statistic) approximately coincides with the contours of \mathcal{H}_2 .

5.4.4 Validity estimation of the global-correlation hypersurface description

This section discusses how many hypersurfaces have to be considered in order to describe the detection-statistic maximum-structure. In other words, the question is investigated, in which region of the search parameter space and at which order m the power series (5.29) can be truncated to approximate the matched-filtering amplitude $|\mathcal{X}|$ better than a certain fractional loss one tolerates.

For a given order m , one can estimate the contributions from the next-order term in the matched-filtering amplitude $|\mathcal{X}|$. As was done earlier in Section 5.4.3, here we consider again the four-dimensional parameter space $\{f, f^{(1)}, \mathbf{n}\}$ of “typical” wide-band all-sky CW searches, with $f \leq 1$ kHz, $|f^{(1)}| < f/\tau_{\min}$, and a minimum spin-down age of $\tau_{\min} = 50$ yrs.

To investigate the contribution from the first-order term in Equation (5.30) to $|\mathcal{X}|$, we compute the following integral ignoring terms in t with order $m > 1$,

$$X_1 \equiv \frac{1}{T} \int_{-T/2}^{T/2} e^{i\Delta u_1 t} dt = \frac{2 \sin(\Delta u_1 T/2)}{\Delta u_1 T}. \quad (5.42)$$

Figure 5.5a shows $|X_1|$ as a function of the dimensionless parameter $\Delta u_1 T$. As already explained earlier, $|X_1|$ attains its global maximum of one, when $\Delta u_1 = 0$, which is the first order global-correlation equation. If one requires for instance $|X_1| \geq 0.9$, using Equation (5.42) this yields the condition $|\Delta u_1| T \leq 1.57$. When expressing Δu_1 in

terms of the original phase parameters using (5.19), one obtains

$$|\Delta u_1| \lesssim 2\pi \left[|\Delta f| (1 + \xi^{(1)}) + 2f_S \xi^{(1)} + |\Delta f^{(1)}| \xi + 2|f_S^{(1)}| \xi \right]. \quad (5.43)$$

But for typical wide-band all-sky CW searches with coherent observation times T of a day or a few days, according to Equation (5.43) $|\Delta u_1| T$ can be considerably larger than 1.57. Therefore, it is clear that the first-order term in Equation (5.30) contributes significantly to the matched-filtering amplitude $|\mathcal{X}|$ and obviously cannot be neglected.

Similarly, we estimate the contribution from the second-order term given that $\Delta u_1 = 0$ and by ignoring terms with $m > 2$ in Equation (5.30). We calculate the corresponding integral denoted by X_2 as

$$\begin{aligned} X_2 &\equiv \frac{1}{T} \int_{-T/2}^{T/2} e^{i\Delta u_2 t^2} dt \\ &= \frac{e^{i\pi/4} \sqrt{\pi}}{\sqrt{\Delta u_2 T^2}} \operatorname{erf} \left[\frac{e^{-i\pi/4}}{2} \sqrt{\Delta u_2 T^2} \right]. \end{aligned} \quad (5.44)$$

In Figure 5.5b, $|X_2|$ is shown as a function of $\Delta u_2 T^2$. Obviously, $|X_2|$ attains the maximum of one at the second order global-correlation hypersurface, which is described by $\Delta u_2 = 0$. One finds that $|X_2| \geq 0.9$ as long as $|\Delta u_2| T^2 \leq 6.11$. Reexpressing Δu_2 in the original phase parameters yields

$$|\Delta u_2| \lesssim 2\pi \left[f_S \xi^{(2)} + |\Delta f^{(1)}| \left(\frac{1}{2} + \xi^{(1)} \right) + 2|f_S^{(1)}| \xi^{(1)} \right]. \quad (5.45)$$

But according to Equation (5.45) for typical wideband all-sky CW searches with coherent observation times T of a day or a few days, $|\Delta u_2| T$ can take values considerably larger than 6.11. Therefore, the second-order term in Equation (5.30) also contributes significantly to the matched-filtering amplitude $|\mathcal{X}|$ and cannot be neglected.

Continuing this scheme to the next order in t , the contribution from the third-order term in Equation (5.30) is considered. Given $\Delta u_1 = 0$ and $\Delta u_2 = 0$, we estimate the

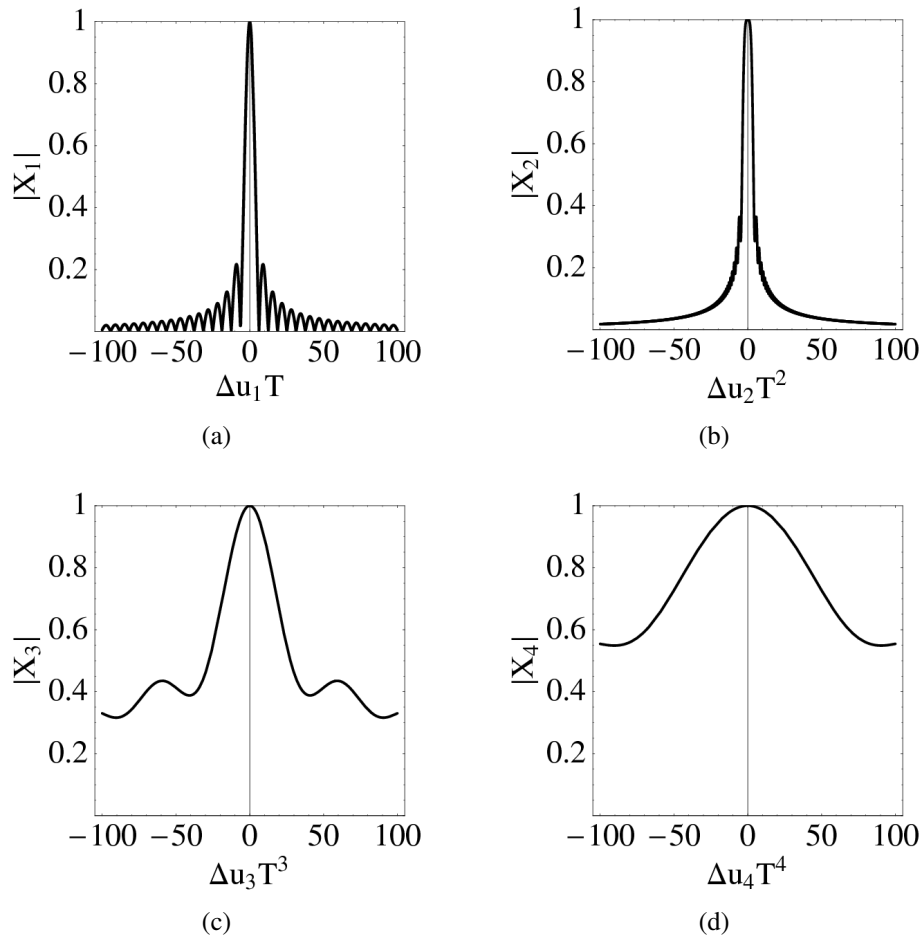


Figure 5.5: Estimating the number of global-correlation hypersurfaces which contribute significantly to the detection statistic. In each plot both axes are dimensionless. For further details the reader is referred to the text.

contribution from the third-order term (with $m = 3$) by evaluating:

$$\begin{aligned} X_3 &\equiv \frac{1}{T} \int_{-T/2}^{T/2} e^{i\Delta u_3 t^3} dt \\ &= \frac{e^{i\pi/6}}{3(\Delta u_3 T^3)^{1/3}} \left[2\Gamma\left(\frac{1}{3}\right) - \Gamma\left(\frac{1}{3}, \frac{i}{8}\Delta u_3 T^3\right) \right. \\ &\quad \left. - \Gamma\left(\frac{1}{3}, -\frac{i}{8}\Delta u_3 T^3\right) \right], \end{aligned} \quad (5.46)$$

where the gamma function $\Gamma(x)$ and the upper incomplete gamma function $\Gamma(a, x)$ are defined by

$$\Gamma(x) \equiv \int_0^\infty t^{x-1} e^{-t} dt, \quad (5.47)$$

$$\Gamma(a, x) \equiv \int_x^\infty t^{a-1} e^{-t} dt. \quad (5.48)$$

As can also be seen from Figure 5.5c, where $\Delta u_3 T^3$ is plotted against $|X_3|$, requiring $|X_3| \geq 0.9$ leads to the condition $|\Delta u_3| T^3 \leq 9.79$. By rewriting Δu_3 using again the original phase parameters according to (5.19), one obtains

$$|\Delta u_3| \lesssim 2\pi \left(\frac{f_S}{3} \xi^{(3)} + |f_S^{(1)}| \xi^{(2)} \right). \quad (5.49)$$

By approximating

$$\xi^{(3)} \approx \Omega_{\text{orb}}^2 \frac{v_{\text{orb}}}{c} \quad \text{and} \quad \xi^{(2)} \approx \Omega_{\text{orb}} \frac{v_{\text{orb}}}{c}, \quad (5.50)$$

a condition is obtained regarding the observation time T for which the contribution to $|\mathcal{X}|$ from the third-order term in Equation (5.30) is negligible:

$$T \lesssim \left[\frac{9.79 c}{2\pi \Omega_{\text{orb}} v_{\text{orb}}} \left(\frac{f_S}{3} \Omega_{\text{orb}} + |f_S^{(1)}| \right)^{-1} \right]^{1/3}. \quad (5.51)$$

In the example presented in Section 5.4.3, a signal is considered with $f_S = 100.0$ Hz and $f_S^{(1)} = 10^{-10}$ Hz/s. In this case, according to Equation (5.51) the third order can be neglected for observation times $T \lesssim 61$ h. For a similar signal and search, but for instance at $f_S = 1000.0$ Hz the third-order term is expected to be non-significant only for observation times $T \lesssim 28$ h.

However, considering cases where the third order in t is non-negligible, an analogous estimation of the contribution from the fourth-order term is necessary. Therefore, we calculate X_4 as

$$\begin{aligned} X_4 &\equiv \frac{1}{T} \int_{-T/2}^{T/2} e^{i\Delta u_4 t^4} dt \\ &= \frac{2}{(-i\Delta u_4 T^4)^{1/4}} \times \left[4\Gamma\left(\frac{5}{4}\right) - \Gamma\left(\frac{1}{4}, -\frac{i}{16}\Delta u_4 T^4\right) \right]. \end{aligned} \quad (5.52)$$

Figure 5.5d shows $|X_4|$ as a function of $\Delta u_4 T^4$. From the condition $|X_4| \geq 0.9$ follows $|\Delta u_4| T^4 \leq 27.78$. Using this, analogously to Equations (5.49) and (5.51), an approximate condition upon T can be found, which in the case of the present example signal yields that $|X_4| \geq 0.9$ for T being approximately less than 10 days. As for the wide-band all-sky CW searches described earlier, coherent observation times are typically only of one day or a few days, this means that in practice contributions from the fourth-order term in Equation (5.30) to $|\mathcal{X}|$ are insignificant in such cases.

5.5 Predictions by the global-correlation equations versus full \mathcal{F} -statistic

In this section the analytical predictions of the global-correlation equations (5.35) based on the simplified detection statistic \mathcal{F}^* are compared to the results of fully coherent searches using the detection statistic \mathcal{F} in different data sets containing artificial CW signals. The computation of the full \mathcal{F} -statistic includes effects of amplitude modulation and involves precise calculation of the detector position with respect to the SSB using an accurate ephemeris model.

Table 5.1: Amplitude and phase parameters introduced in Section 5.3.2 of the two software-simulated continuous gravitational-wave signals.

Signal	A_+	A_\times	ψ [rad]	Φ_0 [rad]
1	1.0	0.5	1.0	2.0
2	1.0	0.0	0.0	0.0

Signal	α_S [rad]	δ_S [rad]	f_S [Hz]	$f_S^{(1)}$ [Hz/s]
1 and 2	2.0	-1.0	100.0	-10^{-10}

5.5.1 Comparison with the \mathcal{F} -statistic for software-simulated signals with no detector noise

Different data sets have been prepared each containing one of two different software-simulated CW signals without noise. A \mathcal{F} -statistic search has been conducted in each data set. The software tools used for data production as well as for data analysis are part of the LSC Algorithm Library Applications [8].

The signal parameters defining the two simulated sources are given in Table 5.1. In both cases the phase parameters are chosen to be identical. These are also the same phase parameters of the signal generating the hypersurfaces illustrated in Figures 5.3 and 5.4. Therefore, solely based on the global-correlation equations one expects the \mathcal{F} -statistic to have a global large-value structure very similar to the one shown by Figures 5.3 and 5.4. To investigate the impact of the antenna pattern functions distinct amplitude parameters have been chosen here, as given by Table 5.1. For every set of simulated data the detector position refers to the LIGO Hanford 4-km (H1) detector, and the time of reference is chosen to be global positioning system GPS time 793555944 s consistent with Figures 5.3 and 5.4.

As listed by Table 5.2, for each data set containing the same signal different searches have been conducted, where the coherent observation time T has been varied between from 10 hours up to 2 sidereal days. In each search consisting of evaluating the \mathcal{F} -statistic on a grid of templates, an isotropic sky grid with equatorial spacing of 0.02 rad,

Table 5.2: Comparison of predictions by the global-correlation equations based the simplified detection statistic \mathcal{F}^* with the fully coherent \mathcal{F} -statistic search results using data sets containing software-simulated continuous gravitational-wave signals. The search labels, listed in the first column, containing the number 1 (number 2) refer to data sets containing only Signal 1 (Signal 2), whereas labels with different letters correspond to different observation times, as can be seen from the second column. From the obtained results the *maximum* relative deviations from the predicted frequencies are specified in the third column.

Search label	Coherent observation time T	Maximum deviation $ f_{\mathcal{F}} - f_{\mathcal{F}^*} /f_{\mathcal{F}^*}$
A1	10 hours	2.5×10^{-6}
B1	1 sidereal day	2.2×10^{-6}
C1	30 hours	2.0×10^{-6}
D1	2 sidereal days	3.2×10^{-6}
A2	10 hours	2.6×10^{-6}
B2	1 sidereal day	2.4×10^{-6}
C2	30 hours	2.3×10^{-6}
D2	2 sidereal days	3.5×10^{-6}

spacings of $1/(2T)$ in the frequency-interval $f \in [99.8, 100.2]$ Hz and a fixed spin-down template of $f^{(1)} = -10^{-11}$ Hz/s have been employed.

First, we compare the results of the searches with the prediction by the global-correlation Equation (5.40a) forming the hypersurface \mathcal{H}_1 , shown in Figure 5.3a. For each sky position and spin-down template-grid point where the \mathcal{F} -statistic search reported a candidate event with frequency $f_{\mathcal{F}}$, one can calculate the relative deviation to the predicted frequency $f_{\mathcal{F}^*}$ obtained from Equation (5.40a) by $|f_{\mathcal{F}} - f_{\mathcal{F}^*}|/f_{\mathcal{F}^*}$. For each search the *maximum* relative deviations between predicted $f_{\mathcal{F}^*}$ and measured $f_{\mathcal{F}}$ over the entire sky (and spin-down) are specified in Table 5.2, and are of order 10^{-6} . The corresponding average relative deviations are typically even one order of magnitude smaller. As in the simplified phase model (5.17) the Earth's spinning component has been neglected, here the observed frequency-deviations are consistent with the fact that the relative corrections to the frequency modulation originating from the Earth's

spinning velocity are of magnitude $v_{\text{spin}}/c \approx 10^{-6}$.

Finally, Figures 5.6, 5.7, 5.8 and 5.9 present the results of each \mathcal{F} -statistic search projected on the sky. As one is only interested in the loudest \mathcal{F} -statistic values, only strong candidate events from the ones reported in the different searches A1,B1,C1 and D1 above a threshold of $2\mathcal{F} \geq 2000$ are shown, and for the searches A2, B2, C2 and D2 a threshold of $2\mathcal{F} \geq 1250$ is set. These thresholds were chosen to reduce the data volume to process and are based the expected global maximum values of $2\mathcal{F}$. These thresholds guarantee that candidate events with \mathcal{F} -statistic values at least larger than $\approx 15\%$ of the global maximum are retained in each search. This thresholding is justified because comparing candidate events with very small detection-statistic values to the global maximum are not of interest in this work.

As shown earlier in Figures 5.3 and 5.4, in the two-dimensional sky projection the intersection curve of hypersurfaces \mathcal{H}_1 and \mathcal{H}_2 approximately coincides with the contours (of constant f and $f^{(1)}$) of \mathcal{H}_2 in the sky. Thus, the dark circle in Figure 5.4b representing the contours of hypersurface \mathcal{H}_2 also describes the predicted global maximum structure of the detection statistic in the sky. In fact, this prediction is actually observed in qualitatively good agreement with the \mathcal{F} -statistic search results shown in Figures 5.6, 5.7, 5.8 and 5.9. One finds that for coherent observation times less than one sidereal day (in searches A1 and A2), the locations of the predicted global maximum structure are only faintly visible in the results, because this feature is still hidden due to the Earth's spin component [see Figures 5.6a and 5.6b]. For coherent observation times beyond one period of the Earth's spinning motion, the results clearly show the locations of large \mathcal{F} -values as predicted [see Figures 5.7a – 5.9b]. As will be discussed later in Section 5.7, the Earth's spinning motion only varies the detection statistic within the global-correlation-equations predicted (and observed) regions.

5.5.2 Comparison with the \mathcal{F} -statistic for a hardware-injected signal in detector noise

For so-called “hardware injections” simulated signals are physically added into the detector control systems to produce instrumental signals that are similar to those that

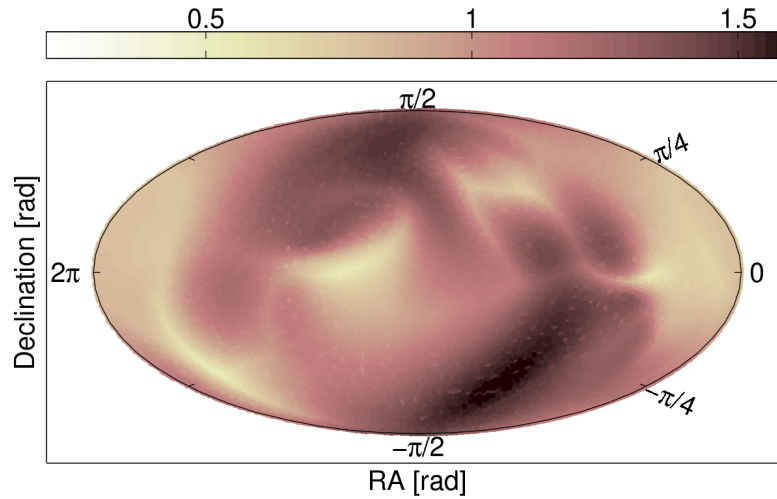
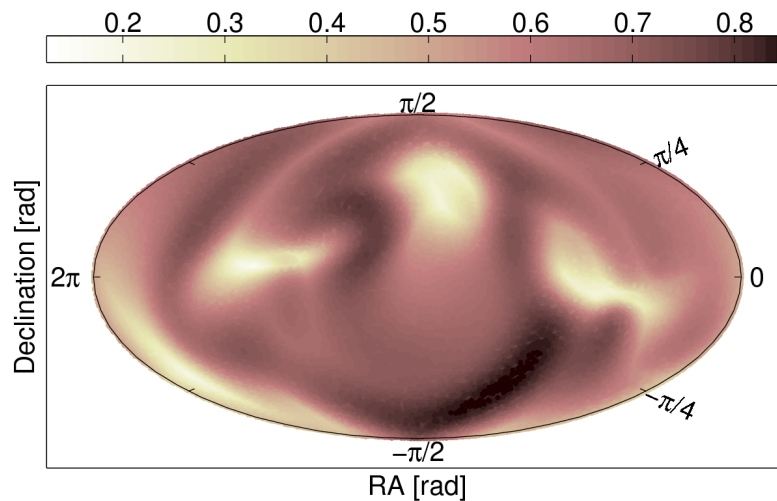
(a) Results of \mathcal{F} -statistic search A1 ($T = 10$ h).(b) Results of \mathcal{F} -statistic search A2 ($T = 10$ h).

Figure 5.6: Hammer-Aitoff sky projections of results from fully coherent \mathcal{F} -statistic searches in the data sets A1 and A2 (both of duration $T = 10$ h), as described in Table 5.2. Each data set contained one of the two software-simulated CW sources defined in Table 5.1, where both signals 1 and 2 have identical phase parameters, but different amplitude parameters. The left (right) plot shows candidate events registered in the search A1 (A2) above a threshold of $2\mathcal{F} \geq 2000$ ($2\mathcal{F} \geq 1250$). The colorbar indicates the values of $2\mathcal{F} \times 10^{-4}$. The corresponding analytical prediction by the global-correlation equations has been illustrated earlier by Figure 5.4b.

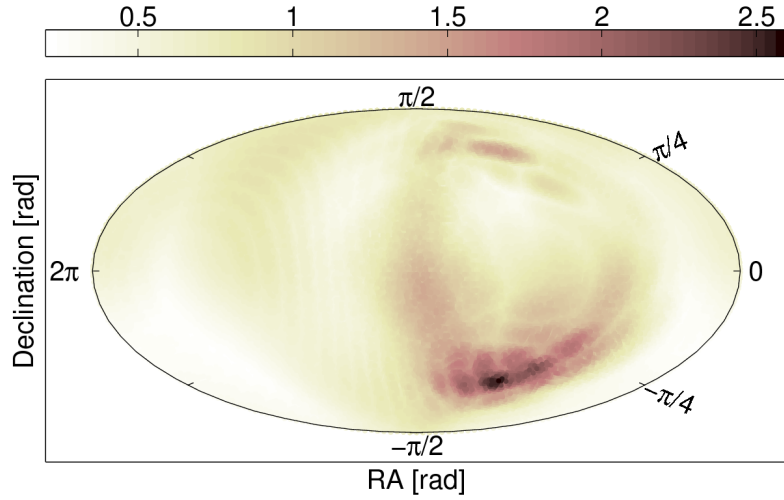
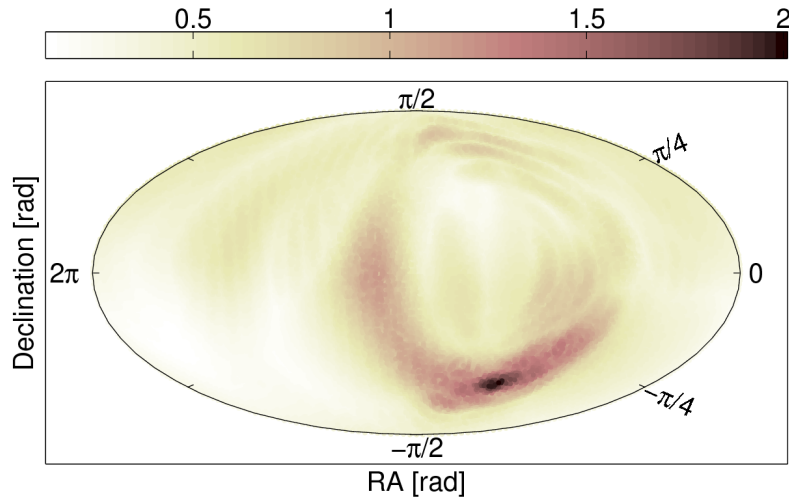
(a) Results of \mathcal{F} -statistic search B1 ($T = 1$ sd).(b) Results of \mathcal{F} -statistic search B2 ($T = 1$ sd).

Figure 5.7: (Continuation of Figure 5.6) Hammer-Aitoff sky projections of results from fully coherent \mathcal{F} -statistic searches in the data sets B1 and B2 (both of duration $T = 1$ sd), as described in Table 5.2. The left (right) plot shows candidate events registered in the search B1 (B2) above a threshold of $2\mathcal{F} \geq 2000$ ($2\mathcal{F} \geq 1250$). The colorbar indicates the values of $2\mathcal{F} \times 10^{-4}$. The corresponding analytical prediction by the global-correlation equations has been illustrated earlier by Figure 5.4b.

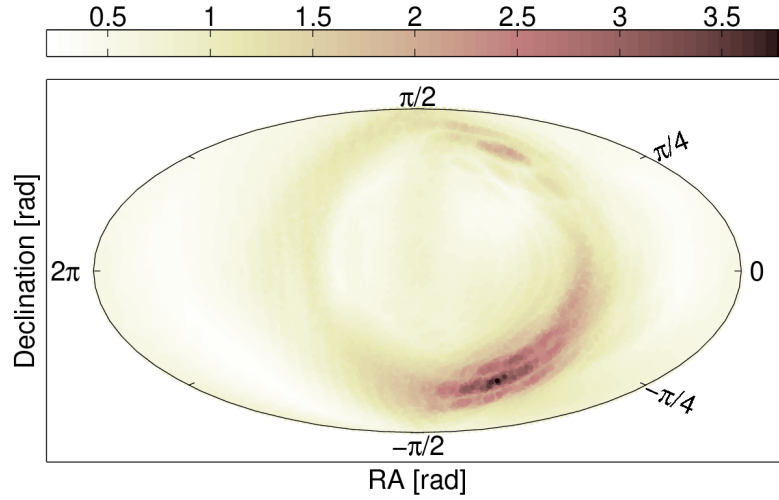
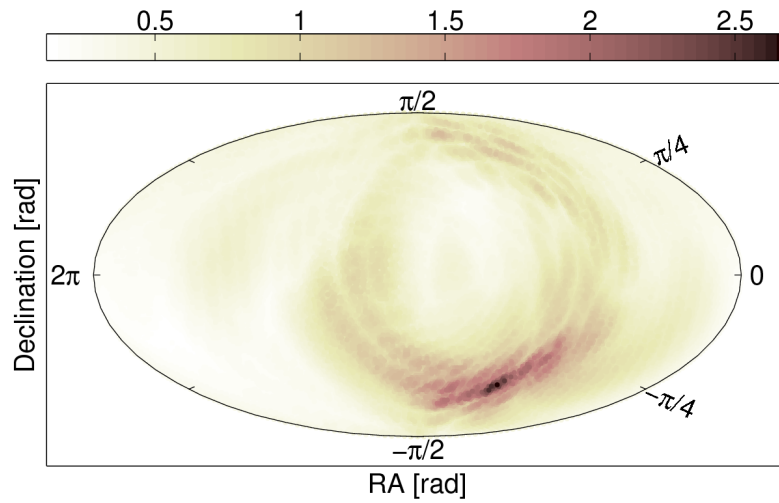
(a) Results of \mathcal{F} -statistic search C1 ($T = 30$ h).(b) Results of \mathcal{F} -statistic search C2 ($T = 30$ h).

Figure 5.8: (Continuation of Figure 5.7) Hammer-Aitoff sky projections of results from fully coherent \mathcal{F} -statistic searches in the data sets C1 and C2 (both of duration $T = 30$ h), as described in Table 5.2. The left (right) plot shows candidate events registered in the search C1 (C2) above a threshold of $2\mathcal{F} \geq 2000$ ($2\mathcal{F} \geq 1250$). The colorbar indicates the values of $2\mathcal{F} \times 10^{-4}$. The corresponding analytical prediction by the global-correlation equations has been illustrated earlier by Figure 5.4b.

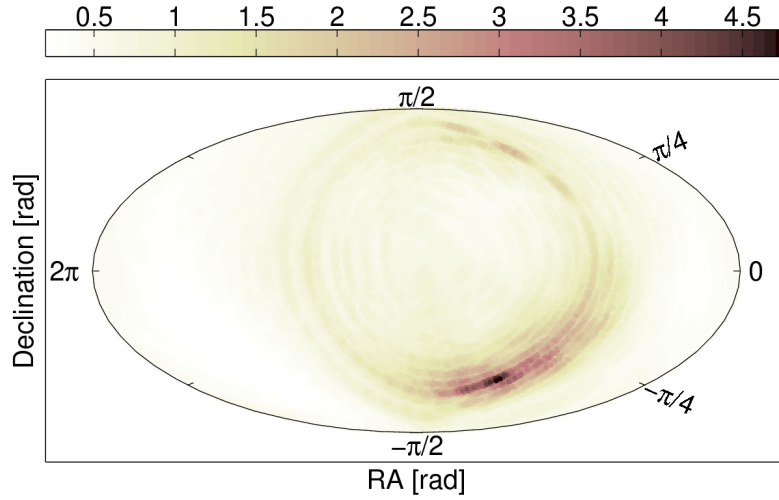
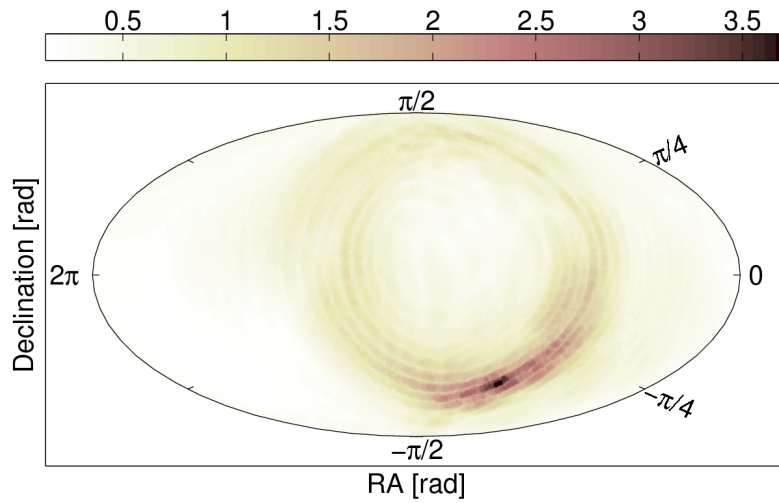
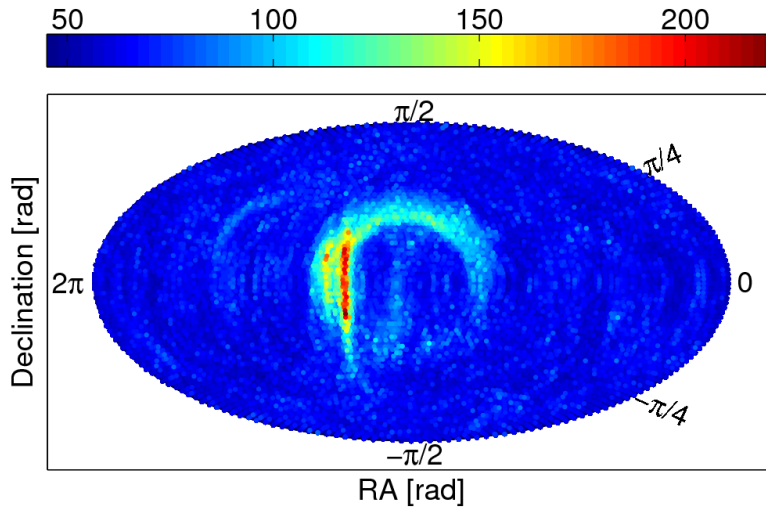
(a) Results of \mathcal{F} -statistic search D1 ($T = 2$ sd).(b) Results of \mathcal{F} -statistic search D2 ($T = 2$ sd).

Figure 5.9: (Continuation of Figure 5.8) Hammer-Aitoff sky projections of results from fully coherent \mathcal{F} -statistic searches in the data sets D1 and D2 (both of duration $T = 2$ sd), as described in Table 5.2. The left (right) plot shows candidate events registered in the search D1 (D2) above a threshold of $2\mathcal{F} \geq 2000$ ($2\mathcal{F} \geq 1250$). The colorbar indicates the values of $2\mathcal{F} \times 10^{-4}$. The corresponding analytical prediction by the global-correlation equations has been illustrated earlier by Figure 5.4b.

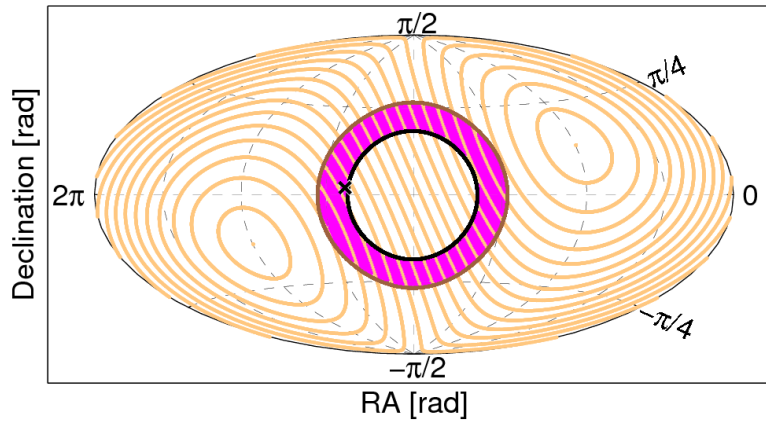
are expected to be produced by astrophysical sources of gravitational waves. Through magnetic coil actuators the interferometer mirrors are made to physically move as if a gravitational wave was present.

Here, we choose 30 hours of data (lying within a time span of less than 38 hours) containing a hardware injection from LIGO's fourth science run (S4) of the LIGO Livingston 4-km (L1) detector. The GPS time of reference is 795408715 s. During this data segment the hardware injection was activated 99.4% of the time. The signal's phase parameters are defined by $\alpha_S = 3.7579$ rad, $\delta_S = 0.0601$ rad, $f_S = 575.163636$ Hz, and $f_S^{(1)} = -1.37 \times 10^{-13}$ Hz/s, at the segment's starting time. The amplitude parameters are $A_+ = 7.48 \times 10^{-24}$, $A_\times = -7.46 \times 10^{-24}$, $\psi = -0.22$ rad and the initial phase is $\Phi_0 = 4.03$ rad. In this segment of data an all-sky \mathcal{F} -statistic search has been carried out in the frequency interval of $f \in [575.048, 575.221]$ Hz, and in the spin-down range $f^{(1)} \in [-1.04 \times 10^{-9}, 1.04 \times 10^{-10}]$ Hz/s. The grid of templates employed spacings of 5.70×10^{-6} Hz in f -direction, separations of 3.23×10^{-10} Hz/s in $f^{(1)}$ -direction, and an isotropic sky grid with equatorial spacing of 0.03 rad.

In Figure 5.10 the results of the actual \mathcal{F} -statistic search are shown and compared to the prediction by the global-correlation hypersurfaces. As the search covers a range of spin-down templates there will be distinct contours of hypersurface \mathcal{H}_2 corresponding to each $f^{(1)}$ -template. Therefore, the structure of maximum detection statistic \mathcal{F}^* is expected to be an annulus in the sky referring to the magenta region in Figure 5.10b. This annulus is framed by the different contour lines of \mathcal{H}_2 which correspond to the minimum (dark-brown colored) and maximum (black colored) value of $f^{(1)}$ searched. Qualitatively, the large-value structure of \mathcal{F} that is visible, is in good agreement with the predicted structure based on the global-correlation hypersurfaces. In Figure 5.10a the \mathcal{F} -statistic results only faintly reproduce the entire predicted structure because of the Earth's spinning motion. Section 5.7 will discuss and explain analytically how the Earth's spinning motion varies the detection statistic within the regions determined by the global-correlation hypersurfaces.



(a) Results of a coherent all-sky \mathcal{F} -statistic search in a data set containing a hardware-injected signal. The colorbar indicates the values of $2\mathcal{F}$.



(b) Prediction of the global maximum structure of the detection-statistic based on the global-correlation hypersurfaces.

Figure 5.10: Comparing the \mathcal{F} -statistic results (a) for a hardware-injected CW signal with the theoretical prediction (b) by the global-correlation equations. Both plots show Hammer-Aitoff projections of the sky. The sky location of the simulated signal is represented by the black cross in (b). The magenta region in (b) represents the predicted structure of maximum detection statistic \mathcal{F}^* and is observed to agree qualitatively well with the actual \mathcal{F} -statistic results (a) from the hardware injection in real detector data.

5.6 Vetoing instrumental noise artifacts

A typical feature of the data from an interferometric gravitational-wave detector are narrow-band noise artifacts, so-called “lines”, which are of instrumental origin. As a consequence, the results of a search for continuous gravitational-wave sources contain instrumental artifacts that in some respects mimic CW signals. But these artifacts tend to cluster in certain regions of parameter space. For the case of *incoherent* searches as reported in [158], candidate events in such parameter-space regions were identified and discriminated. Here, we propose a similar veto method also suitable for *coherent* CW searches, such as those presented in Chapters 3 and 4. Using the global-correlation equations found in this work, the goal is to identify those regions in parameter space where instrumental noise lines can imitate a real signal by producing large detection-statistic values. In such a case these candidate events could automatically be vetoed.

For simplicity, we consider the same four-dimensional parameter space as used in Section 5.4.2 consisting of $\{f, f^{(1)}, \mathbf{n}\}$ and that T has a value, such that third-order contributions to $|\mathcal{X}|$ are insignificant (cf. Section 5.4.4). Thus, the global-correlation equations of relevance are the same as in the example studied in Section 5.4.3. These were given by Equations (5.40a) and (5.40b). It is obvious that the frequency of a stationary instrumental line is independent of the Earth’s position in its orbit around the sun. This decoupling is achieved by setting $\mathbf{n}_S = \mathbf{0}$. For a stationary instrumental line originating from the detector it also holds that $f_S^{(1)} = 0$. In this case the constants $K_{1,2}$ in Equations (5.40a) and (5.40b) simplify to $K_1 = f_S$ and $K_2 = 0$. Thus, the two relevant global-correlation equations are of the following form,

$$f + f \boldsymbol{\xi}^{(1)} \cdot \mathbf{n} + f^{(1)} \boldsymbol{\xi} \cdot \mathbf{n} = f_S, \quad (5.53a)$$

$$f^{(1)} + f \boldsymbol{\xi}^{(2)} \cdot \mathbf{n} + 2f^{(1)} \boldsymbol{\xi}^{(1)} \cdot \mathbf{n} = 0. \quad (5.53b)$$

As stated earlier, for a given $f^{(1)}$, Equation (5.53a) describes a three-dimensional hypersurface in the subspace $\{f, \mathbf{n}\}$. On this hypersurface the detection statistic will attain its maximum along the intersection curve with the hypersurface described by Equation (5.53b). In a projection into the sky subspace this intersection curve approximately coincides with the contours (of constant f and $f^{(1)}$) of hypersurface (5.53b). Therefore

Equation (5.53b) describes the region in the sky for which potential CW signals do not produce a modulation pattern that would distinguish them from an instrumental line.

Using this knowledge one can discriminate (veto) candidate events which satisfy Equation (5.53b). As the resolution in parameter space is finite, the following *veto condition* results:

$$\left| f^{(1)} + f \boldsymbol{\xi}^{(2)} \cdot \mathbf{n} + 2f^{(1)} \boldsymbol{\xi}^{(1)} \cdot \mathbf{n} \right| < \varepsilon, \quad (5.54)$$

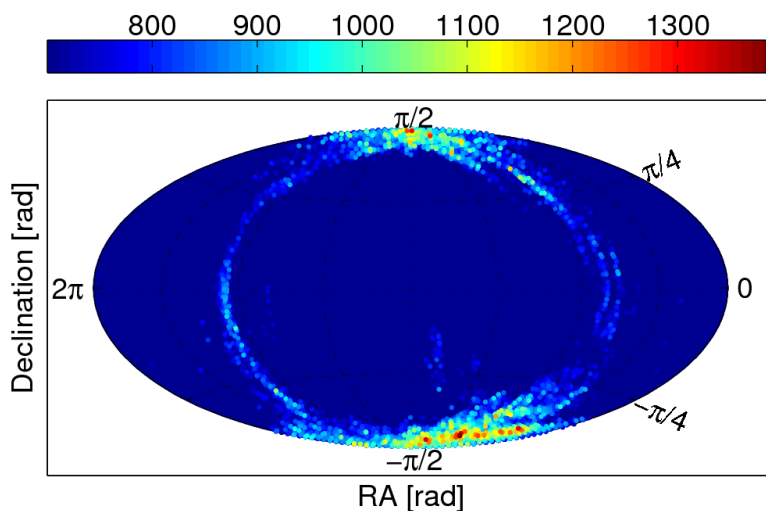
the tolerance-parameter $\varepsilon > 0$ can be understood as

$$\varepsilon = \frac{\Delta f_{\text{cell}}}{\Delta T} N_{\text{cell}}, \quad (5.55)$$

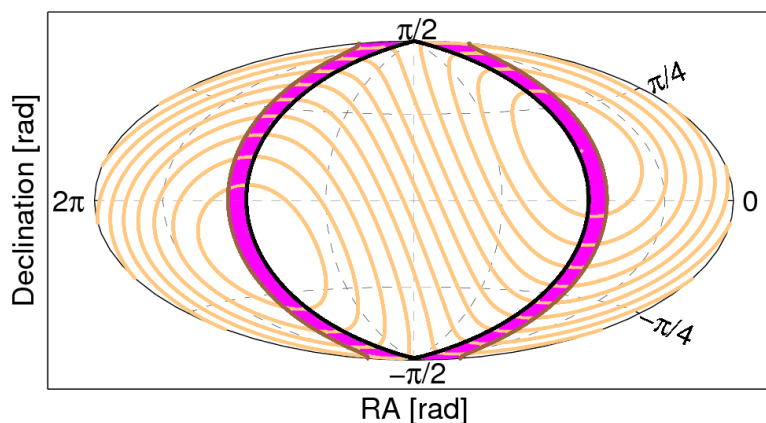
where Δf_{cell} denotes the resolution in the frequency-direction (width of cells), N_{cell} the number of cells one tolerates during a characteristic length of time ΔT .

One can visualize and calculate the volume of the region in four-dimensional parameter space which is excluded by this veto. For a given source sky position, Equation (5.54) is linear in f and $f^{(1)}$. Thus, for fixed sky position \mathbf{n} , the veto condition defines two parallel lines in the $\{f, f^{(1)}\}$ – plane. Candidate events which lie in the region between the lines are discarded (vetoed). Candidate events which lie outside this region are retained (not vetoed). The locations of these two lines in the $\{f, f^{(1)}\}$ – plane depends upon the sky position. The fractional volume excluded by the veto depends upon whether or not (as the source position varies over the sky) the excluded region between the lines lies inside or outside of the boundaries of the search, or intersects it. Alternatively, for a given value of f and $f^{(1)}$, one can calculate the portion of the sky which is excluded by the veto, depending upon the ranges of parameter space searched. The details of such a calculation for a particular search have been in Section 3.7.2.

Figure 5.11 illustrates the veto method for an example noise line. Thereby, Figure 5.11a presents the results of a fully coherent matched-filtering search using the \mathcal{F} -statistic for a 30-hour observation time. The data set analyzed contains a detector-noise line, which is in this case a violin mode resonance of the mode cleaner mirrors of the LIGO Hanford 4-km (H1) detector. In Figure 5.11b, a comparison with the theoretical prediction by the global-correlation equations given by (5.53a) and (5.53b) is made featuring a very good agreement. Thus the veto will be very efficient in excluding the parameter-space regions of largest $2\mathcal{F}$ -values produced by instrumental lines.



(a) Results of a coherent all-sky \mathcal{F} -statistic search in a data set containing an instrumental noise line. The colorbar indicates the values of $2\mathcal{F}$.



(b) Prediction of the global maximum structure of the detection statistic based on the global-correlation hypersurfaces.

Figure 5.11: Comparing the results of a fully coherent matched-filtering search using the \mathcal{F} -statistic (a) with the theoretical prediction (b) by the global-correlation equations for a given instrumental-noise feature mimicking a real CW signal. Both plots show Hammer-Aitoff projections of the sky. The all-sky search was carried out in a 0.5 Hz frequency-band $f \in [568.0, 568.5]$ Hz and for a range of frequency time-derivatives $f^{(1)} \in [-3.63 \times 10^{-9}, 3.63 \times 10^{-10}]$ Hz/s, for an observation time of $T = 30$ h. The GPS time of reference is 795149016 s. The upper plot (a) shows all candidate events reported by the search above a detection-statistic threshold of approximately 50% of the largest $2\mathcal{F}$ -value found. The frequency of the instrumental-noise line present in this data set is a resonance violin mode of the mode cleaner mirrors of the LIGO Hanford 4-km (H1) detector. The magenta region in (b) of maximum expected detection statistic agrees well with the \mathcal{F} -statistic results (a) from the real instrumental line.

Note that this veto excludes only the loudest candidate events (of largest $2\mathcal{F}$), but as shown in Figure 5.11 an instrumental line is capable of contaminating large parts of the sky due to the global correlations (depending on the search parameters). Therefore in some cases it might be necessary to increase the tolerance-parameter ε artificially to account for these effects if necessary. However, in a \mathcal{F} -statistic search one is interested in the strongest candidate events arising from the background level. Thus in eliminating such false instrumental-noise events the veto condition presented is very efficient as these regions are well described. This veto method as presented here have been applied in the Einstein@Home searches described in previous Chapters 3 and 4.

5.7 Effects of the diurnal spinning motion of the Earth

By considering the Earth's spinning motion in the phase model, we here investigate the variation of the detection statistic along the predicted global maximum structure by the global-correlation hypersurfaces. In other words, given the solution $\Delta u_m = 0$, which are the the global-correlation hypersurfaces, we study how the spin component $\phi_{\text{spin}}(t)$ of Equation (5.13) in the phase model (5.4) modulates the detection statistic in the locations consistent with this solution. In order to simplify this discussion, in what follows frequency time-derivatives in the spin component $\phi_{\text{spin}}(t)$ are ignored to obtain

$$\phi_{\text{spin}}(t) \approx 2\pi f \frac{\mathbf{r}_{\text{spin}}(t) \cdot \mathbf{n}}{c}. \quad (5.56)$$

Thus, the phase difference between the spin component of the signal $\phi_{\text{spin}}^{\text{S}}(t)$ and a template $\phi_{\text{spin}}(t)$ is given by

$$\begin{aligned} \Delta\phi_{\text{spin}}(t) &\equiv \phi_{\text{spin}}^{\text{S}}(t) - \phi_{\text{spin}}(t) \\ &= 2\pi \frac{\mathbf{r}_{\text{spin}}(t)}{c} \cdot (\mathbf{n}_{\text{S}}f_{\text{S}} - \mathbf{n}f) \\ &= \frac{\mathbf{r}_{\text{spin}}(t)}{c} \cdot \Delta\mathbf{k}, \end{aligned} \quad (5.57)$$

defining the vector

$$\Delta \mathbf{k} \equiv 2\pi (\mathbf{n}_S f_S - \mathbf{n} f). \quad (5.58)$$

Taking into account $\Delta \phi_{\text{spin}}(t)$ in the detection-statistic amplitude and provided that $\Delta u_m = 0$, one has to compute the following integral

$$X_{\text{spin}} \equiv \frac{1}{T} \int_{-T/2}^{T/2} e^{i\Delta \phi_{\text{spin}}(t)} dt. \quad (5.59)$$

For observation times T relevant to CW searches (of order days), the phase modulation due to the spinning motion of the Earth is oscillatory, because it has a period of one sidereal day $\Omega_{\text{spin}} = 2\pi/1 \text{ sd}$. Therefore, in order to evaluate (5.59) we follow a route previously taken in [190, 188], which makes use of the Jacobi–Anger identity:

$$e^{iz \cos \theta} = \sum_{n=-\infty}^{\infty} i^n J_n(z) e^{in\theta}, \quad (5.60)$$

where $J_n(z)$ is the n -th Bessel function of the first kind. This identity allows to expand exponentials of trigonometric functions in the basis of their harmonics. To employ the Jacobi–Anger expansion we rewrite Equation (5.57) by approximating the diurnal detector motion due to the Earth’s rotation to be circular,

$$\Delta \phi_{\text{spin}}(t) = \frac{R_E}{c} [\Delta k_{\parallel} \sin \lambda + \Delta k_{\perp} \cos \lambda \cos(\phi_0 + \Omega_{\text{spin}} t)], \quad (5.61)$$

where R_E is the radius of the Earth, λ is the latitude of the detector, Δk_{\parallel} is the absolute value of the component of the vector $\Delta \mathbf{k}$ parallel to the rotation axis, Δk_{\perp} is the absolute value of the component of $\Delta \mathbf{k}$ orthogonal to the rotation axis, and ϕ_0 is determined by $\Delta \mathbf{k}$ at $t = 0$. Defining

$$\Delta \phi_{\text{spin},\parallel} \equiv \frac{R_E}{c} \Delta k_{\parallel} \sin \lambda, \quad (5.62)$$

$$\Delta u_{\text{spin}} \equiv \frac{R_E}{c} \Delta k_{\perp} \cos \lambda, \quad (5.63)$$

the Jacobi–Anger identity is applied:

$$e^{i\Delta \phi_{\text{spin}}(t)} = e^{i\Delta \phi_{\text{spin},\parallel}} \sum_{n=-\infty}^{\infty} i^n e^{in\phi_0} J_n(\Delta u_{\text{spin}}) e^{in\Omega_{\text{spin}} t}. \quad (5.64)$$

Substituting this expression into Equation (5.59) and taking the modulus, one obtains

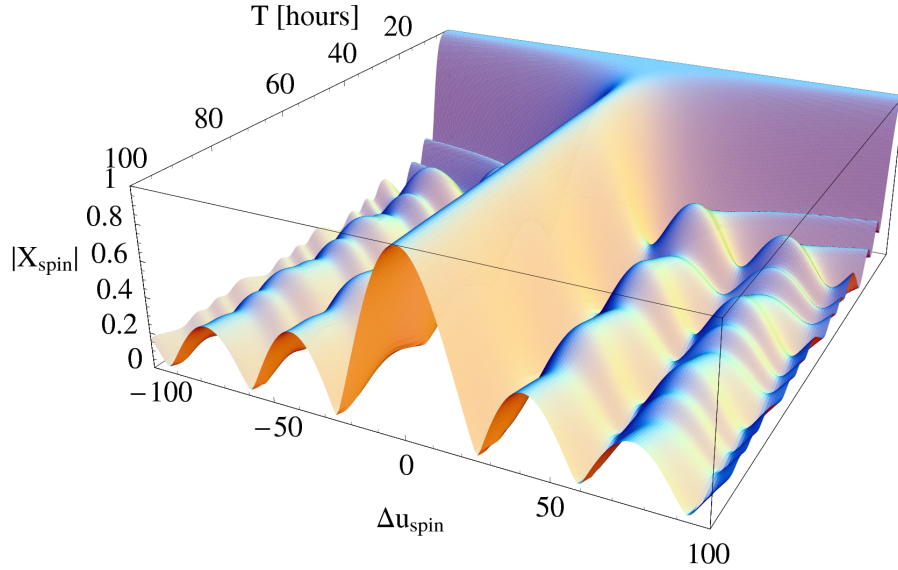
$$|X_{\text{spin}}| = \left| \sum_{n=-\infty}^{\infty} i^n e^{in\phi_0} J_n(\Delta u_{\text{spin}}) \text{sinc} \left(\frac{n\Omega_{\text{spin}}T}{2} \right) \right|. \quad (5.65)$$

Figure 5.12 shows $|X_{\text{spin}}|$ for the two LIGO detectors as a function of T and Δu_{spin} . It is obvious that for the observation time being an integer multiple ℓ of the Earth's spin period, such that $T = 2\pi\ell/\Omega_{\text{spin}}$, Equation (5.65) then simplifies to $|X_{\text{spin}}| = |J_0(\Delta u_{\text{spin}})|$, because only the term corresponding to $n = 0$ does not vanish. By inspection, we find that this is also approximately the case for all observation times of one day or longer, as can be seen from Figure 5.12. Therefore, $|X_{\text{spin}}|$ is approximated for $T \gtrsim 2\pi/\Omega_{\text{spin}}$ (which is also the regime relevant to CW searches) by

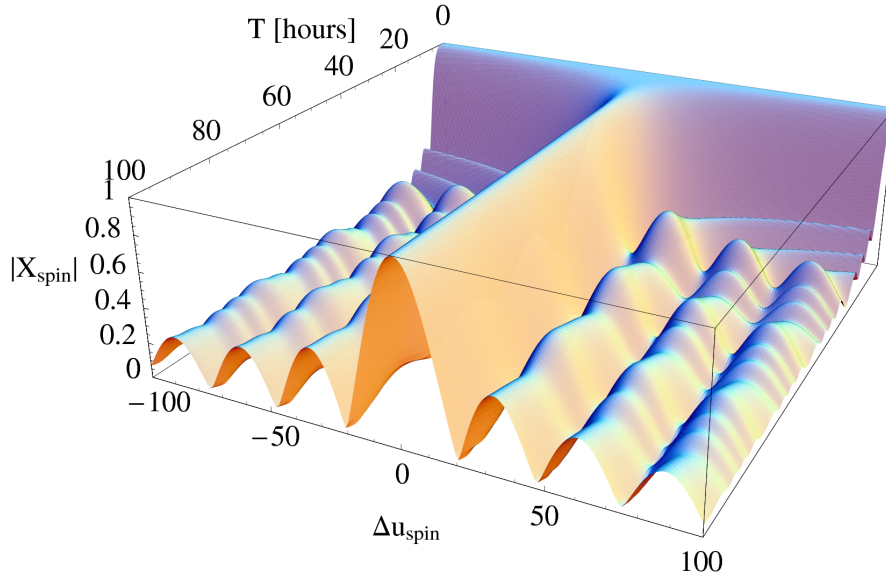
$$|X_{\text{spin}}| \approx |J_0(\Delta u_{\text{spin}})|. \quad (5.66)$$

Figures 5.13, 5.14 and 5.15 illustrate $|J_0(\Delta u_{\text{spin}})|$ over the entire sky for the three different cases studied previously in this Chapter: the software-injected signal, the hardware-injected signal and the instrumental-noise line. Comparing Figure 5.13 with Figures 5.6–5.9, Figure 5.14 with Figure 5.10a, and Figure 5.15 with Figure 5.11a, one finds that the variation of the \mathcal{F} -statistic in the regions determined by the global-correlation hypersurfaces (locations consistent with $\Delta u_m = 0$) can in fact be recovered.

To illustrate better why the Earth's orbital motion determines the regions of largest detection-statistic and the Earth's spinning motion only modulates the detection-statistic within these regions, the examples presented in Figure 5.16 are considered. There, as a basis of comparison to $|X_{\text{spin}}|$ of Equation (5.66) we use $|\mathcal{X}|$ of Equation (5.38) of the orbital phase model for $m \leq 2$. As shown in Section 5.4.4, higher orders of m are insignificant for the example cases considered. Figure 5.16 compares $|\mathcal{X}|$ and $|X_{\text{spin}}|$ as functions of sky position for the given signal phase parameters. In the two diagrams 5.16a and 5.16c, the sky has been sliced along α at constant declination $\delta = \delta_S$, and for fixed values of frequency $f = f_S$ and for simplicity also at zero spin-down offset $f_S^{(1)} = f^{(1)}$. In the plots 5.16b and 5.16d, the sky has been sliced along declination δ at constant right ascension $\alpha = \alpha_S$, and for the remaining template parameters coinciding with the signal's parameters. The essential observation is that $|\mathcal{X}|$ drops off much more rapidly compared to $|X_{\text{spin}}|$. Therefore, $|\mathcal{X}|$ dominantly determines the global maximum structure of the detection statistic, whereas $|X_{\text{spin}}|$ only modulates the detection statistic within these regions where $|\mathcal{X}|$ is maximal.



(a) LIGO Hanford detector



(b) LIGO Livingston detector

Figure 5.12: The simplified detection-statistic amplitude $|X_{\text{spin}}|$ for phase-mismatch only in the spin component of the phase model as a function of observation time T and dimensionless parameter-mismatch Δu_{spin} as defined in Equation (5.63), for the two LIGO detectors. For observation times beyond $T \gtrsim 2\pi/\Omega_{\text{spin}}$, a good approximation of $|X_{\text{spin}}|$ is given by the dominant term $|J_0(\Delta u_{\text{spin}})|$.

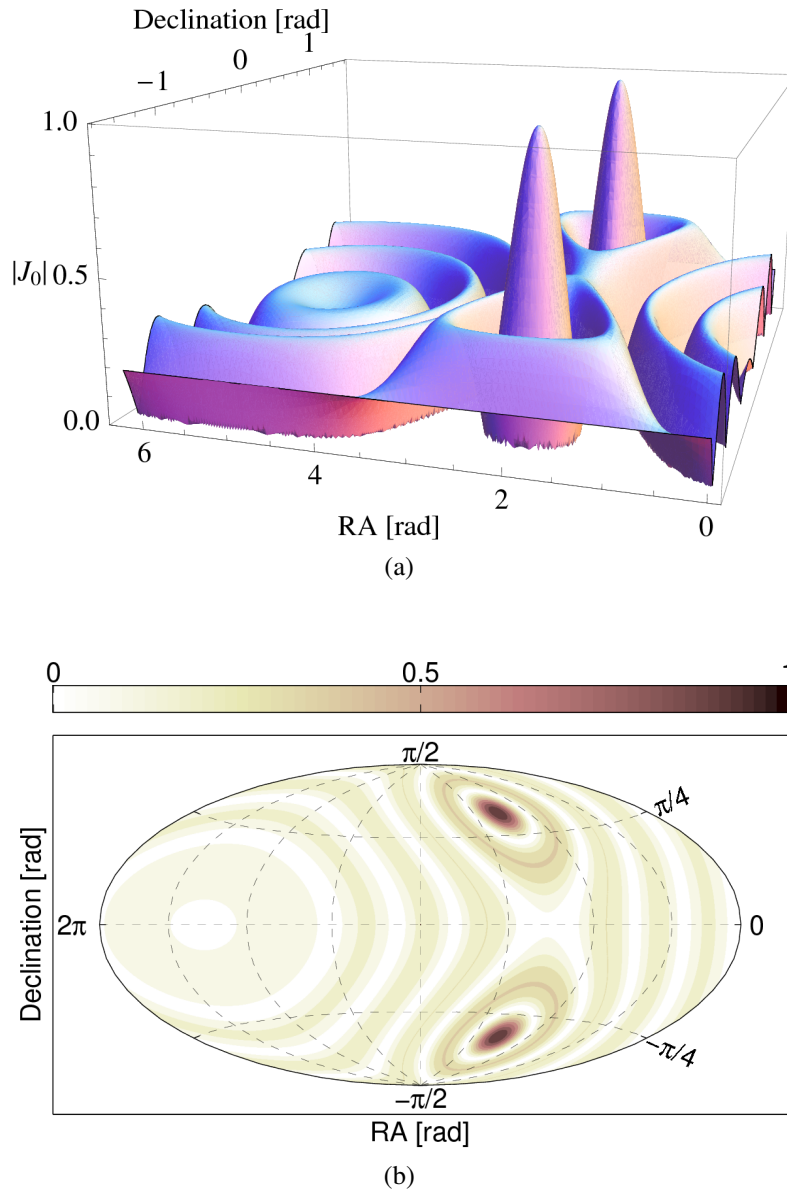


Figure 5.13: Shown is $|X_{\text{spin}}| \approx |J_0(\Delta u_{\text{spin}})|$ over the entire sky using equatorial coordinates of right ascension α and declination δ for the software-simulated signal studied previously in this Chapter [cf. Figures 5.6–5.9]. The top plot shows $|J_0(\Delta u_{\text{spin}})|$ as functions of α and δ . The bottom plot is a two-dimensional Hammer-Aitoff projection of the sky, illustrating the contours of $|J_0(\Delta u_{\text{spin}})|$.

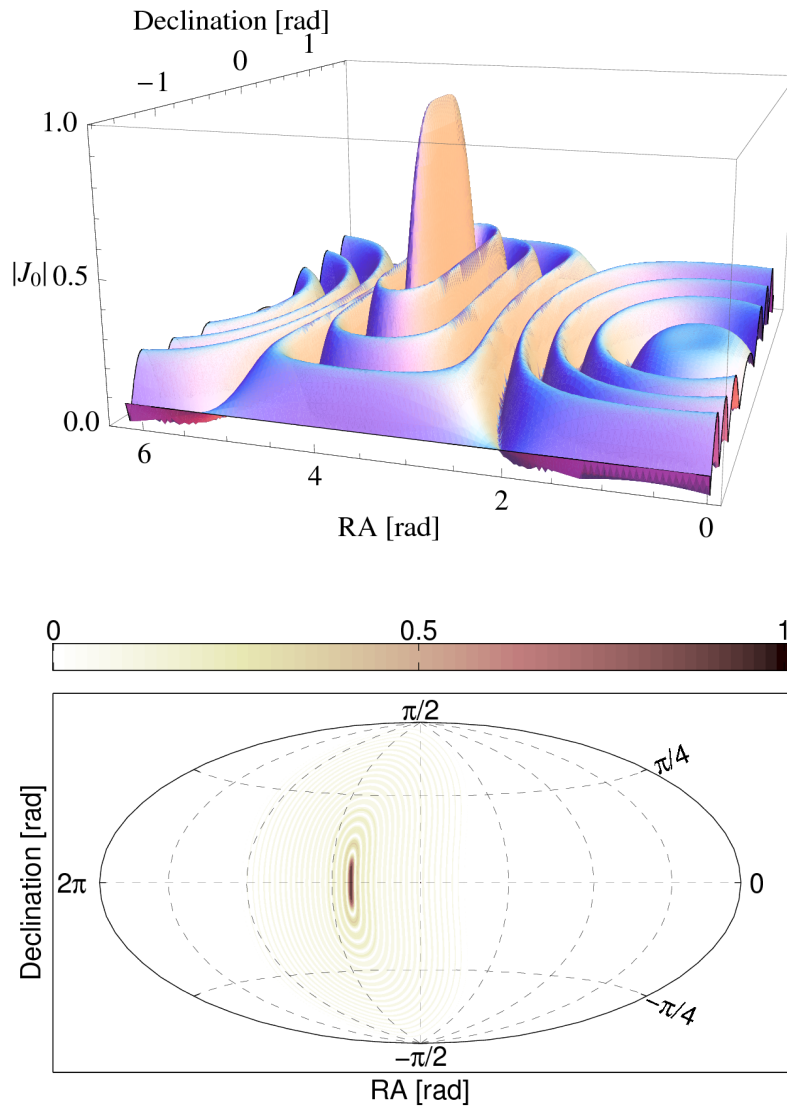


Figure 5.14: Shown is $|X_{\text{spin}}| \approx |J_0(\Delta u_{\text{spin}})|$ over the entire sky using equatorial coordinates of right ascension α and declination δ for the hardware-injected signal studied previously in this Chapter [cf. Figure 5.10a]. The top plot shows $|J_0(\Delta u_{\text{spin}})|$ as functions of α and δ . The bottom plot is a two-dimensional Hammer-Aitoff projection of the sky, illustrating the contours of $|J_0(\Delta u_{\text{spin}})|$.

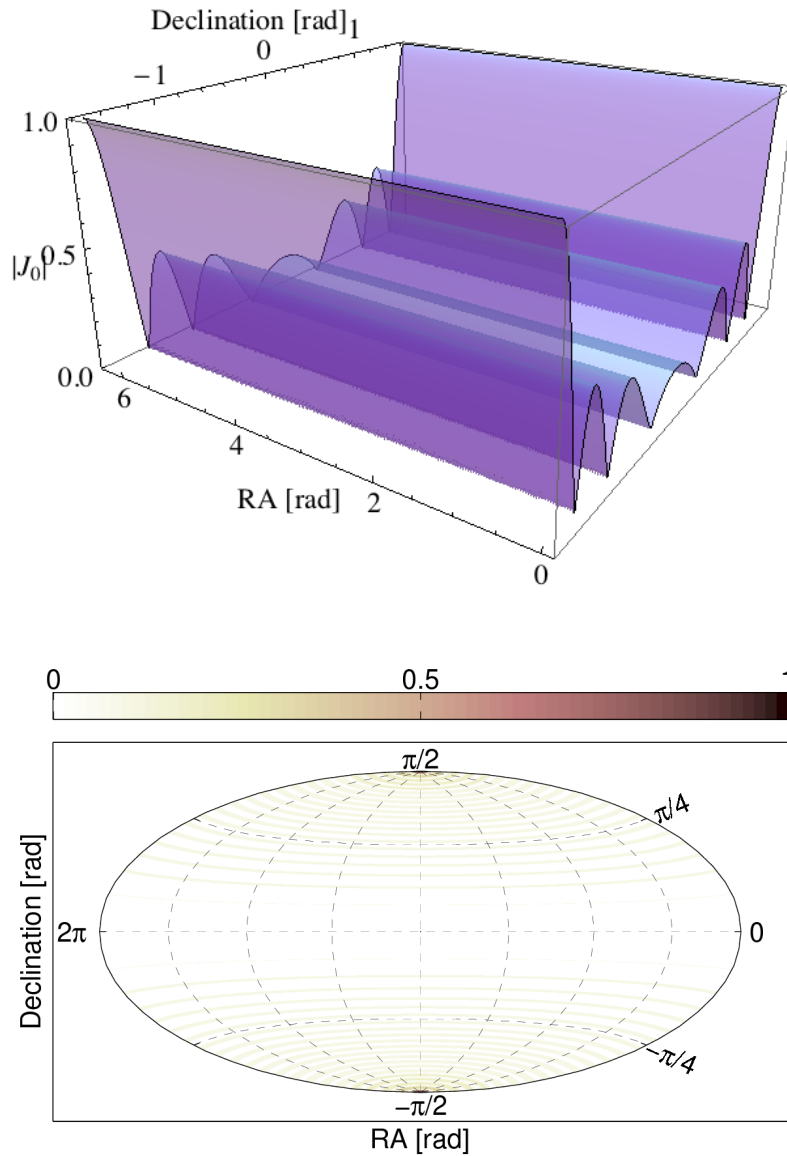


Figure 5.15: Shown is $|X_{\text{spin}}| \approx |J_0(\Delta u_{\text{spin}})|$ over the entire sky using equatorial coordinates of right ascension α and declination δ for the instrumental-noise line studied previously in this Chapter [cf. Figure 5.11a]. The top plot shows $|J_0(\Delta u_{\text{spin}})|$ as functions of α and δ . The bottom plot is a two-dimensional Hammer-Aitoff projection of the sky, illustrating the contours of $|J_0(\Delta u_{\text{spin}})|$.

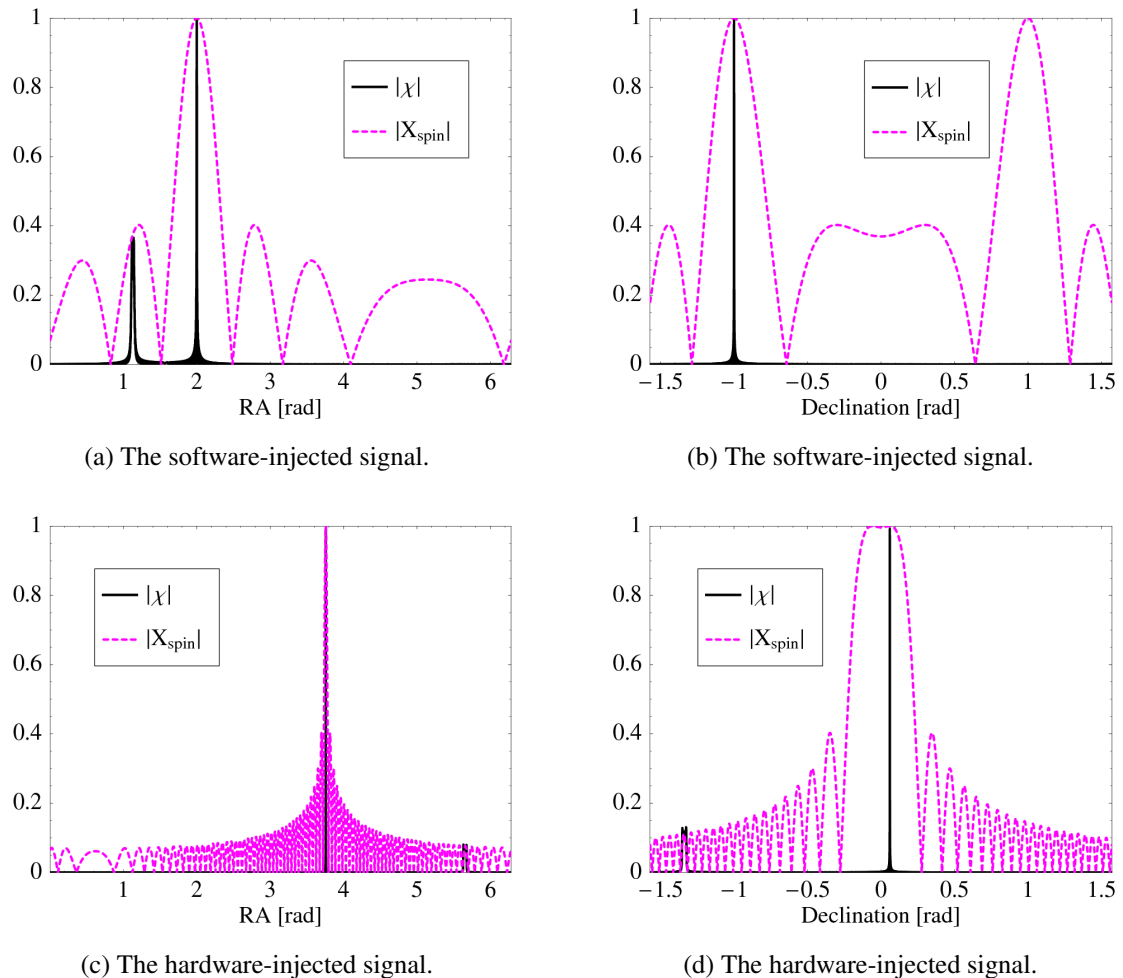


Figure 5.16: Comparison of $|\mathcal{X}|$ (solid curves) computed using $\Phi_{\text{orb}}(t)$ and $|X_{\text{spin}}|$ (dashed curves) calculated using $\phi_{\text{spin}}(t)$ as functions of sky position. In (a) and (b) the signal's phase parameters correspond to the software injection of Section 5.5.1, and (c) and (d) refer to the hardware-injected signal introduced in Section 5.5.2. In (a) and (c), $|\mathcal{X}|$ and $|X_{\text{spin}}|$ are shown as functions of right-ascension (RA) template-value α for the given signal-value α_S , while fixing the remaining template parameters to perfectly match the signal's parameters, $\delta_S = \delta$, $f_S = f$ and $f_S^{(1)} = f^{(1)}$. Whereas in (b) and (d), $|\mathcal{X}|$ and $|X_{\text{spin}}|$ are shown as functions of declination template-value δ , while the remaining template parameters coincide with the signal's phase parameters. One can see that $|\mathcal{X}|$ decreases much more rapidly compared to $|X_{\text{spin}}|$. Therefore $|\mathcal{X}|$ dominantly determines the global maximum structure of the detection statistic.

5.8 Conclusions

The family of global-correlation hypersurfaces derived here provides an approximate analytical description of the global large-value structure of the coherent detection statistic \mathcal{F} in the phase-parameter space of continuous gravitational-wave searches.

For observation times longer than one sidereal day, but still much smaller compared to one year, it is the orbital motion of the Earth which generates a family of global-correlation equations. The solution to each of these equations is a different hypersurface in parameter space. The detection statistic is expected to have large values at the intersection of these hypersurfaces. In this context, the Earth's spinning motion plays a minor role, because it only varies the detection statistic within the intersection regions determined by the global-correlation hypersurfaces.

While embedding previously published results [188] in the present theory, this work leads to a substantially improved understanding of the global correlations in the coherent detection statistic.

In a comparison study with results of the \mathcal{F} -statistic from numerically simulated as well as from hardware-simulated signals in the presence of noise, the analytical predictions by the global-correlation equations have been qualitatively well recovered.

The improved understanding of the global correlations in the coherent detection statistic presented here leads to a number of applications for CW searches. In this Chapter, one direct application has been described: The global large-value structure of the detection statistic produced by stationary instrumental-noise lines mimicking astrophysical sources is also well described by the global-correlation equations. This permitted the construction of a veto method, where such false candidate events are excluded.

Moreover, reparameterization of the original phase parameters by the parameters u_m from the global-correlation equations offers evident advantages in solving further problems related to CW searches. For example using the u_m -parameters can help in placing templates more efficiently. As these parameters “absorb” the global correlations leading to a linear phase model, the metric in these parameters will be explicitly *flat*, which means independent of the parameters (cf. [185, 4]).

Furthermore, exploiting the global parameter-space correlations, an enhanced hier-

archical search scheme is obtained via reparameterizing the phase parameters of the candidate events based on u_m -parameters. In fact, this gives rise to a novel type of hierarchical semi-coherent search technique for CW sources: the Global-Correlation Transform (GCT) method [4]. Typically, in such a multistage scheme [164, 165] one breaks up the data set into a sequence of short data segments, of which each segment is analyzed coherently in a first stage. This is followed by an incoherent combination of the coherent results from each segment. The GCT technique, which is described in the next Chapter, achieves significantly improved sensitivity compared to conventional semi-coherent methods at even lower computational cost.

New method for CW detection exploiting global correlations

Appeared in Physical Review Letters 103, 181102, (2009)

6.1 Overview and context

As mentioned in the introductory Chapter 2, direct detection of gravitational waves is the most significant remaining test of Einstein's General Theory of Relativity, and will become an important new astronomical tool.

Section 2.3.4 described various possible generation mechanisms [133, 127, 128, 131, 130] of continuous gravitational-wave (CW) signals from rapidly rotating neutron stars. Most such stars are electromagnetically invisible, but might be detected and studied via gravitational waves. Recent simulations of neutron star populations [191, 151, 136] suggest that CW sources might eventually be detected with new instruments such as LIGO [58, 54]. World-wide efforts are underway to search for CW signals [158, 1, 12] and observational upper limits already place some constraints on neutron star physics [155, 159].

Fully coherent searches (over realistic ranges of parameter space and year-long ob-

ervation times) for unknown sources of continuous gravitational waves are computationally prohibitive. Less expensive hierarchical searches divide the data into shorter segments which are analyzed coherently, then detection statistics from different segments are combined incoherently. This Chapter presents an improved method for the incoherent combination scheme, the Global Correlation Transform (GCT), which exploits global parameter-space correlations in the coherent detection statistic. Application to simulated data shows significant sensitivity improvements compared with previously available methods, increasing the spatial volume probed by more than two orders of magnitude at lower computational cost.

6.2 Fully coherent CW matched filtering: \mathcal{F} -statistic

Because the expected CW signals are weak, sensitive data analysis methods are needed to extract these signals from detector noise. A powerful method is derived in Ref. [55]. This scheme is based on the principle of maximum likelihood detection, which leads to coherent matched filtering. Rotating neutron stars emit monochromatic CW signals, apart from a slowly changing intrinsic frequency. But the terrestrial detector location Doppler-modulates the amplitude and phase of the waveform, as the Earth moves relative to the solar system barycenter (SSB). The parameters describing the signal's amplitude variation may be analytically eliminated by maximizing the coherent matched-filtering statistic [55]. The remaining search parameters describing the signal's phase are the source's sky location, frequency and frequency derivatives, and the resulting coherent detection statistic is called the \mathcal{F} -statistic (cf. Section 5.2).

This work considers isolated CW sources whose frequency varies linearly with time in the SSB frame. The corresponding phase parameter-space \mathcal{P} is four-dimensional. Standard “physical” coordinates on \mathcal{P} are the frequency $f(t_0)$ at some fiducial time t_0 , the frequency's first time derivative \dot{f} , and a unit vector $\mathbf{n} = (\cos \delta \cos \alpha, \cos \delta \sin \alpha, \sin \delta)$ on the two-sphere S^2 , pointing from the SSB to the source. Here α and δ are right ascension and declination. Thus, a point in parameter space $p \in \mathcal{P}$ may be labeled by $p = \{f(t_0), \dot{f}, \mathbf{n}\}$. The \mathcal{F} -statistic $\mathcal{F}_p[h]$ is a functional of the detector data set h , and is

a function of the point in parameter space $p \in \mathcal{P}$.

All-sky searches for unknown CW sources using the \mathcal{F} -statistic are computationally expensive. For maximum sensitivity, one must convolve the full data set with signal waveforms (templates) corresponding to all possible sources. But the number of templates required for a fully coherent search increases as a high power of the observation time. For one year of data, the computational cost to search a realistic range of parameter space exceeds the total computing power on Earth [160, 55]. Thus a fully-coherent search is limited to much shorter observation times. The problem is addressed by using hierarchical semi-coherent search methods as follows.

6.3 Hierarchical semi-coherent search strategies

In hierarchical semi-coherent search methods the data is broken into segments of duration T , where T is much smaller than one year. Each segment is analyzed coherently, computing the \mathcal{F} -statistic on a *coarse* grid of templates. Then the \mathcal{F} values from all segments (or statistics derived from \mathcal{F}) are incoherently combined using a common *fine* grid of templates. Such a strategy is referred to as “semi-coherent”, because phase information is discarded between segments.

Originally, hierarchical semi-coherent search methods were designed to combine the simple Fourier power of successive short Fourier-transformed segments (typically with $T = 30$ min). In this case, the maximum possible segment length is short, because of the requirement that the signal power should not be spread over more than one Fourier frequency bin by the signal’s Doppler shift [192].

The Stack-Slide method [162] adds Fourier power along paths of frequency bins corresponding to the signal frequency, in close analogy to the Radon transform. The Powerflux method [158, 159] is another variant thereof, summing weighted power taking into account non-stationarities of the noise and the direction-dependent detector antenna patterns.

The Hough transform method [161, 163, 164, 157, 158], on the other hand, sums bi-

nary number counts instead of power. Number counts are obtained by setting a threshold on power, and adding 1 if the threshold is exceeded and 0 otherwise. The final number count is the total number of threshold crossings along a time-frequency path of a putative signal.

6.3.1 \mathcal{F} -statistic based hierarchical searches

In recent years, the availability of increased computational resources make it possible to use substantially longer coherent integration times T up to a day or longer.

However, the same semi-coherent techniques have still been continued to use while employing the \mathcal{F} -statistic rather than Fourier power. Thereby, the Stack-Slide method [165] sums \mathcal{F} values along putative signal tracks in the time-frequency plane. The Hough transform method [164] sums $H(\mathcal{F} - \mathcal{F}_{\text{th}})$ where \mathcal{F}_{th} is a constant predefined threshold. The Heavyside function $H(x)$ is unity for positive x and vanishes elsewhere. This latter technique is currently used by Einstein@Home [12], a public distributed computing project carrying out the most sensitive blind CW searches.

A central long-standing problem in these semi-coherent methods is the design of, and link between, the coarse and fine grids. Current methods, while creative and clever, are arbitrary and ad hoc constructions. This work removes all arbitrariness by finding the optimal solution for the incoherent step through rigorous mathematical derivation. The key quantity is the fractional loss, called *mismatch* \mathcal{M} , in expected \mathcal{F} -statistic (or sum of \mathcal{F} -statistics in the incoherent step) for a given signal p at a nearby grid point p' . Locally Taylor-expanding \mathcal{M} (to quadratic order) in the differences of the coordinates $\{f(t_0), \dot{f}, \mathbf{n}\}$ of p and p' defines a signature $(+, +, +, +)$ metric ds^2 [173, 174, 160, 187]. Current methods consider parameter correlations in \mathcal{F} to *linear* order in T and discard higher orders in T from the metric.

The \mathcal{F} -statistic has strong *global* correlations [188, 3] in the physical coordinates $\{f(t_0), \dot{f}, \mathbf{n}\}$, that extend outside the region in which the mismatch is well-approximated by the local metric given above. Recent work [3] has shown that (for a given signal) the region where the expected \mathcal{F} -statistic has maximal value may be described by a separate equation for each order of T , when T is small compared to one year. The solutions to

each equations is a hypersurface, whose intersections describe the global correlations in \mathcal{F} -statistic.

For currently used values of T (a day or longer) it is also crucial to consider the fractional loss and global structure of \mathcal{F} to *second-order* in T [3]. For source frequencies above 1 kHz and for values of T longer than about 60 h, additional orders in T would be needed.

6.4 The GCT method

This work exploits the global correlations in the coherent detection statistic \mathcal{F} to construct a significantly improved semi-coherent search technique for continuous gravitational waves. We call the new method “Global Correlation Transform” (GCT). The GCT technique leads to the optimal solution for the incoherent combination step and makes four important improvements.

First, the advanced understanding of the global correlations yields new coordinates which enable to obtain the first analytical solution for the incoherent-step metric.

Second, previous approaches obtain the fine grid in an ad hoc manner, while refining in three dimensions, \dot{f} and \mathbf{n} . Here, the derivation of the incoherent-step metric gives rise to refine fine grid in only one dimension, \dot{f} . This greatly reduces the computational cost at *equal detection sensitivity*, although it also reduces the accuracy with which the parameters of a source are estimated. But this is a very profitable trade, because in a hierarchical search the primary goal of the first stages is to discard the uninteresting regions of parameter space. Later follow-up stages use longer coherent integrations to more accurately determine the source parameters.

Third, existing techniques combine the coherent results less effectively than the GCT, because they do not use metric information beyond linear order in T . This gives the GCT higher sensitivity at equal computational cost.

Fourth, the GCT can simultaneously do a Stack-Slide-like summing of \mathcal{F} values and a Hough-like summing of $H(\mathcal{F} - \mathcal{F}_{\text{th}})$, with a lower total computational cost than either

one of these methods individually.

For a given CW source with realistic phase parameter values ($f \leq 1$ kHz, $|\dot{f}| \leq f/50$ yr) and coherent data segment lengths $T \leq 60$ h, the global-correlation structure of the \mathcal{F} -statistic is well described by the first- and second-order global-correlation equations [3]:

$$\begin{aligned}\nu(t) &= f(t) + f(t)\dot{\boldsymbol{\xi}}(t) \cdot \mathbf{n} + \dot{f} \boldsymbol{\xi}(t) \cdot \mathbf{n}, \\ \dot{\nu}(t) &= \dot{f} + f(t)\ddot{\boldsymbol{\xi}}(t) \cdot \mathbf{n} + 2\dot{f}\dot{\boldsymbol{\xi}}(t) \cdot \mathbf{n}, \\ \text{where } f(t) &\equiv f(t_0) + (t - t_0)\dot{f}.\end{aligned}\tag{6.1}$$

Here $\boldsymbol{\xi}(t) \equiv \mathbf{r}_{\text{orb}}(t)/c$, with $\mathbf{r}_{\text{orb}}(t)$ denoting the vector from the Earth's barycenter to the SSB, and c the speed of light. Apart from an overall factor, the quantities $\nu(t)$ and $\dot{\nu}(t)$ are called the ‘‘global-correlation parameters’’. They can be interpreted as the source's instantaneous frequency and frequency derivative at the detector, at detector time t .

The global-correlation parameters provide new coordinates (ν and $\dot{\nu}$) on \mathcal{P} . It is useful to also introduce new (real-valued) sky coordinates n_x and n_y (as in [185]):

$$n_x(t) + i n_y(t) = f(t) \tau_E \cos \delta_D \cos \delta e^{i[\alpha - \alpha_D(t)]}.\tag{6.2}$$

Here $\tau_E = R_E/c \approx 21$ ms is the light travel time from the Earth center to the detector, and $\alpha_D(t)$, δ_D are the detector position at time t . The metric separation ds^2 is

$$\begin{aligned}ds^2/(2\pi)^2 &= d\nu^2 T^2/12 + \gamma^2 d\dot{\nu}^2 T^4/720 + dn_x^2/2 \\ &+ dn_y^2/2 - d\nu dn_y T/(\pi\ell) + d\dot{\nu} dn_x T^2/(\pi\ell)^2.\end{aligned}\tag{6.3}$$

In defining differences in coordinates $\{\nu, \dot{\nu}, n_x, n_y\}$, the time t in Equations (6.1) and (6.2) is the midpoint of the data segment spanning times $[t - T/2, t + T/2]$, and $\gamma = 1$. To simplify the form of the metric, T is taken to be a positive integer number ℓ of sidereal days.

The new coordinates $\{\nu, \dot{\nu}, n_x, n_y\}$ have important advantages over the original coordinates $\{f, \dot{f}, \mathbf{n}\}$. The metric is explicitly coordinate-independent (showing that \mathcal{P} is flat). In fact, the region around a point p in which the mismatch \mathcal{M} is well-approximated by ds^2 is *much* larger. Using $\{\nu, \dot{\nu}, n_x, n_y\}$ coordinates the metric ds^2 remains accurate up to $\mathcal{M} = 0.3$. In contrast, in the $\{f, \dot{f}, \mathbf{n}\}$ coordinates ds^2 can yield errors greater than

10% for mismatches as small as 0.001. In part, this is because the metric in $\{f, \dot{f}, \mathbf{n}\}$ varies significantly over the $\mathcal{M} = 0.3$ region.

Consider a segment of data h_p which contains a strong CW source with phase parameters p . If the sky separation patch is small enough to neglect the dn_x and dn_y terms in Equation (6.3), then $\mathcal{F}_{p'}[h_p]$ is extremized for all p' that have the *same global-correlation parameters* ν and $\dot{\nu}$ as p . This set of points in \mathcal{P} forms a two-dimensional surface $d\nu = d\dot{\nu} = 0$. Thus, for all sources within the sky patch, there exists a different (f, \dot{f}) pair with those same values of ν and $\dot{\nu}$. This property is exploited by the GCT algorithm.

6.5 An implementation of the GCT method

6.5.1 The coherent stage

To start, the data set is divided into N segments of length T (potentially including short gaps in operation) labeled by the integer $j = 1, \dots, N$. The segments span time intervals $[t_j - T/2, t_j + T/2]$. The detector-time midpoint of segment j is t_j and

$$t_0 = \frac{1}{N} \sum_{j=1}^N t_j \quad (6.4)$$

is the fiducial time.

Every segment is analyzed *coherently* on a coarse grid in phase parameter space \mathcal{P} . This grid is constructed so that no point in \mathcal{P} is farther than a specified distance from some coarse-grid point, where the distance measure is defined by the metric above. To simplify the grid construction, large frequency bands are analyzed by breaking them into many narrow sub-bands. For each data segment j , and at each coarse grid point, the \mathcal{F} -statistic is evaluated, and “stats” are obtained. Here, the word “stat” denotes the two-tuple $(\mathcal{F}_j, H(\mathcal{F}_j - \mathcal{F}_{th}))$.

For simplicity, the same coarse grid is used for all data segments, being the Cartesian product of a rectangular grid in f, \dot{f} and a grid on the sky-sphere $\mathbf{n} \in S^2$. The spacings

in f and \dot{f} are

$$\Delta f = \frac{\sqrt{12m}}{\pi T}, \quad (6.5)$$

$$\Delta \dot{f} = \frac{\sqrt{720m}}{\pi T^2}, \quad (6.6)$$

where m is the one-dimensional metric mismatch parameter [cf. Equations (3.1) and (3.2)]. The spacing of the coarse sky grid is chosen so that the dn_x and dn_y terms in Equation (6.3) may be neglected. When orthogonally projected onto the equatorial unit disk, the sky grid is uniform, and contains $\approx 2\pi/(\Delta\varphi)^2$ points, with

$$\Delta\varphi = \frac{\sqrt{2m}}{\pi f \tau_E \cos \delta_D}. \quad (6.7)$$

6.5.2 The incoherent combination stage

The *incoherent* step combines the “stats” obtained by the coherent analysis, using a fine grid in \mathcal{P} . At each point in the fine grid, a “stat” value is obtained by summing one stat value from each of the N coarse grids. The coarse grid point is the one with the same sky position as the fine grid point, which has the smallest separation in the global correlation parameters, calculated using the metric Equation (6.3) above. The final result is a “stat” value at each point on the fine grid. The first element of the stat is the sum of the \mathcal{F} -statistic values from the coarse grid points. The second element is a number count, reflecting the number of data segments in which \mathcal{F}_{th} was exceeded. A detectable CW signal leads to a fine-grid point with a high number count and a large sum of \mathcal{F} -statistics.

The spacing of the fine grid is determined from the metric for the fractional loss of the expected $\sum_{j=1}^N \mathcal{F}_j$ due to parameter offsets between a putative signal location and a fine grid point at the fiducial time t_0 . This may be calculated as in [162], by averaging the coarse-grid metric over the N different segments. Since each coarse-grid metric is no longer calculated at the data-segment midpoints (but at t_0), the coefficients change between segments because of the time-dependence of the parameter-space coordinates. For our choice of t_0 and T , the only additional term in the metric Equation (6.3) that does not average to zero is $(t_j - t_0)^2 T^2 d\dot{\nu}^2/12$, and the averaged metric takes a diagonal form

with diagonal elements identical to Equation (6.3) but with

$$\gamma^2 = 1 + \frac{60}{T^2 N} \sum_{j=1}^N (t_j - t_0)^2, \quad (6.8)$$

where the parameter offsets in Equation (6.3) are calculated at the fiducial time t_0 . Thus, the fine grid may be identical to the coarse grid except that the spacing $\Delta \dot{f}$ is smaller by a factor γ , which is of order N when the number of data segments is large. No further refinement in frequency or sky position is needed. Coherent integration over the total observation time would require refining both $\Delta \dot{f}$ and Δf (increasing points $\propto N^3$), plus similar sky refinements.

6.6 GCT versus Hough performance

6.6.1 Application to simulated data

Monte-Carlo simulations are used to illustrate the improved performance of the GCT compared with the conventional Hough transform method. The software tools used are part of LALApps [8] and employ accurate barycentering routines with timing errors below $3\mu\text{s}$.

To provide a realistic comparison, simulated data sets covered the same time intervals as the input data used for the current (S5R5) Einstein@Home search [12]. Those data, from LIGO Hanford (H1, 4km) and LIGO Livingston (L1, 4km), are not contiguous, but contain gaps when the detectors are not operating. The total time interval spanned is about 264 days, containing 121 data segments of duration 25 h (so approximately $\ell = 1$).

The false alarm probabilities are obtained using 5 000 simulated data sets with different realizations of stationary Gaussian white noise, with one-sided strain spectral density $\sqrt{S_h} = 3.25 \times 10^{-22} \text{ Hz}^{-1/2}$. To find the detection probabilities, different CW signals with fixed strain amplitude h_0 are added. The remaining simulated-source parameters (as defined in [55]) are randomly drawn from a population uniformly distributed in $\cos(\text{inclination angle } \iota)$, polarization angle ψ , initial phase ϕ_0 , the entire sky, in the

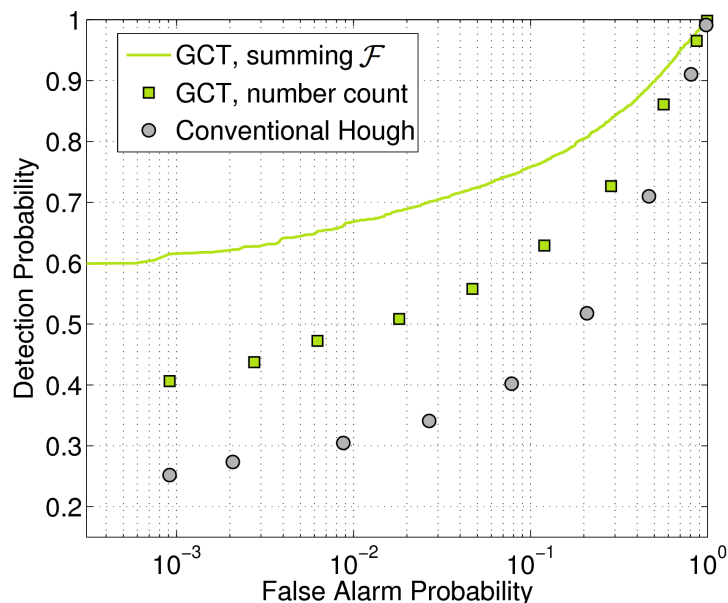


Figure 6.1: Comparison of receiver operating characteristic curves. The curve labeled “GCT, summing \mathcal{F} ” refers to the GCT method using the summing- \mathcal{F} -statistics mode of operation, “GCT, number count” denotes the results from the GCT method using the number-count mode of operation, and “Conventional Hough” indicates the results for the conventional Hough transform method currently is use. Because the number count (using $\mathcal{F}_{\text{th}} = 2.6$) is discrete, the latter two curves consist of discrete points. In both modes of operation, the GCT performs significantly better than the conventional Hough method.

frequency range of $f(t_0) \in [100.1, 100.3]$ Hz, and over a range in frequency derivative of $\dot{f} \in [-1.29, -0.711]$ nHz/s.

6.6.2 Results

Figure 6.1 compares the performance of the two methods. The receiver operating characteristic is the detection probability as a function of false alarm probability, at fixed source strain amplitude $h_0 = 6 \times 10^{-24}$. Because the number count (using $\mathcal{F}_{\text{th}} = 2.6$) is discrete, the two “curves” in Figure 6.1 consist of discrete points. The GCT (using *either* number counts *or* summed \mathcal{F} as a detection statistic) is superior to the conventional Hough method.

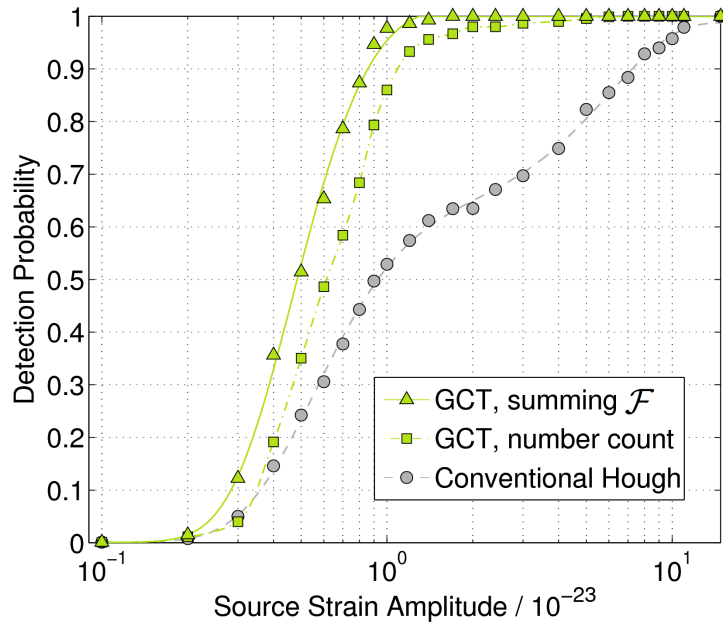


Figure 6.2: Probability of detection as a function of source strain amplitude h_0 , at a fixed false alarm probability of 1%. The curve labeled “GCT, summing \mathcal{F} ” refers to the GCT method using the summing- \mathcal{F} -statistics mode of operation, “GCT, number count” denotes the results from the GCT method using the number-count mode of operation, and “Conventional Hough” indicates the results for the conventional Hough transform method currently is use. For each of the three sets of points, the continuous curve in the background represents a polynomial fit to the discrete data points. In both modes of operation, the GCT performs significantly better than the conventional Hough method.

In addition, the GCT is computationally faster. This comparison used *identical* coherent stages ($m = 0.3$, with 2981 coarse-grid points) for the GCT and conventional Hough method. But in the incoherent combination stage, the GCT and the conventional Hough method used *different* fine grids. The GCT fine grid had 506 times as many points as the coarse grid, but the Hough fine grid had 7056 times as many points. In spite of using 14 times fewer fine-grid points, the GCT gave *substantially higher* sensitivity.

Figure 6.2 shows another comparison of the GCT and Hough method. It compares the detection efficiencies for *different* values of source strain amplitude h_0 , at a fixed 1% false alarm probability. As above, each point in Figure 6.2 is obtained by analyzing 2000 simulated data sets. Again, the GCT in both modes of operation performs substantially better than the Hough method. For example, compare the source strain am-

plitude h_0 needed to obtain 90% detection probability. The strain required by the GCT in number-count operation mode is smaller by a factor of about six than the strain needed by the Hough method, making the “distance reach” [55] of the GCT six times larger. This increases the number of potentially detectable sources by more than two orders of magnitude, since the “visible” spatial volume increases as the cube of the distance. In fact the lower computational cost of the GCT would also allow increases in N or T , even further improving the sensitivity.

These results are qualitatively independent of frequency, as confirmed in additional comparisons.

6.7 Conclusions

A new semi-coherent technique for detecting continuous gravitational-wave sources has been described. In contrast to previous approaches, the GCT exploits global parameter-space correlations in the coherent detection statistic \mathcal{F} to optimally solve the subsequent incoherent combination step. For coherent integration times $T \leq 60$ h, the global correlations are well-described by the second-order (in T) formulae presented here. The method should also be extendible to longer coherent integration times by including higher orders in T . It could also be extended to search for CW signals from non-isolated sources (i.e. in binary systems) as well as to space-based detectors. The method also has applicability in radio, X- and γ -ray astronomy, such as in searches for weak radio or γ -ray pulsars, or pulsations from low-mass X-ray binaries.

Realistic Monte-Carlo simulations show that the GCT is much more sensitive than the Hough transform method (currently the most sensitive CW search technique). The GCT is also computationally simpler, and more efficient.

The LIGO Scientific Collaboration is currently working to deploy the GCT on the Einstein@Home project [12], starting with LIGO S6 data. The combination of new and more sensitive search techniques, plus new and more sensitive data, greatly increases the chance of making the first gravitational wave detection of a CW source. The detection

of CW signals will provide new means to discover and locate neutron stars, and will eventually provide unique insights into the nature of matter at high densities.

Summary and outlook

Gravitational waves as predicted by Einstein's General Theory of Relativity have so far eluded direct observation. In recent years, substantial advances in the field have enabled to construct a new generation of gravitational-wave observatories that offer the first realistic promise of a direct detection.

The long-lasting type of signals from continuous gravitational-wave (CW) sources, such as rapidly spinning neutron stars, are expected to be relatively weak and thus may be the hardest to detect, while also requiring the largest computational demand due to the great number of wave cycles. But given the possibility of year-long observations, CW signals could also yield the most precise information about their source and their emission mechanism is likely to be determined.

A CW detection could also mark the beginning of a survey for an electromagnetically invisible neutron-star population, which could well be much larger than conventional pulsars. Besides, the gravitational-wave window may also reveal CW sources not anticipated in our current thinking, which is so far largely based on electromagnetic observations of the universe.

The work presented in this dissertation is streamlined towards the goal of detecting CW signals from previously unknown sources through the development, study and application of enhanced data-analysis techniques.

An all-sky search for CW sources has been presented using 510 h of LIGO S4 data. The main computational work of the search has been distributed over hundreds of thousands of computers via the volunteer computing project Einstein@Home. This enormous computing capacity has allowed the exploration of a wide parameter space,

despite of using comparably long coherent integration times of 30 h, subdividing the 510 h of data into 17 segments. To enhance the sensitivity of the search by combining the coherent-analysis results from the 17 data segments, a highly efficient coincidence scheme has been developed and applied in a post-processing stage. Moreover, the sensitivity of the search has been estimated through Monte-Carlo methods. In addition, a veto method has been implemented to discriminate parts of parameter space contaminated by instrumental artifacts. While no credible CW source has been found, in the 100 to 200 Hz band, more than 90% of sources uniformly populated with dimensionless strain amplitude greater than 10^{-23} would have been detected.

Using 840 h of early S5 LIGO data, a further broadband all-sky CW search with Einstein@Home has been presented. The 840 h have been analyzed coherently over 30 h in each of 28 data segments. The subsequent post-processing has efficiently combined these 28 coherently-analyzed segments. Despite probing a slightly larger parameter space, this analysis has achieved 3 times better sensitivity over the antecedent S4 search. Over large parts of parameter space these are the most sensitive CW search results to date. In the 125 to 225 Hz band, more than 90% of sources with strain amplitude greater than 3×10^{-24} would have been detected.

Furthermore, a comprehensive study of the global parameter-space correlations in the coherent statistic for CW detection has been carried out. The novel insights obtained have proven to be the key to further important improvements of crucial aspects for CW data analysis, which include the following:

- The better understanding of the global correlations has allowed the construction of a veto method for coherent searches which excludes false candidate events from stationary instrumental-noise artifacts (“lines”).
- The global correlations give rise to new coordinates on the parameter space which in turn lead to a flat parameter-space metric (being explicitly coordinate-independent) for coherent searches. This enormously simplifies the template-grid construction.
- Additionally, the region around a point in parameter space where the fractional loss in coherent detection statistic is well-approximated by the metric is much larger using these new coordinates based on the global correlations. In fact, there

is indication that in these coordinates the number of templates required to cover the parameter space scales with coherent observation time like T^3 , for T values of practical interest (1 day up to a few days). In contrast, employing conventional coordinates a scaling of T^5 applies, which has been used so far. Thus, this is a critical improvement, because the number computations is what ultimately limits the search sensitivity.

- The new coordinates derived from the global correlations have also allowed to calculate a metric for the incoherent combination step in hierarchical searches for the first time. This has been long-standing problem in CW data analysis.
- In consequence, a new hierarchical semi-coherent search technique has been developed (referred to as GCT method), exploiting the improved understanding of the global correlations. The GCT method has shown substantially increased search sensitivity (by factor of about 6) in comparison to previously available methods at even lower computational cost. It is therefore a significant advance for deep all-sky broadband CW surveys.

These novel aspects require further study and investigation, which is subject to ongoing and future work.

Comparing the different search techniques presented in this dissertation, significant advances in terms of increasing sensitivity have been made. This progress is shown in an artistic illustration in Figure 7.1a. Assuming a population of CW sources uniformly distributed, the volume of space probed, growing with the cube of distance reached, is shown for the different types of searches. The Einstein@Home LIGO S4 search presented in Chapter 3 is labeled by “E@H S4” in Figure 7.1a. As described in Chapter 4, this search has been extended to about 3 times better sensitivity using early S5 LIGO data, in addition to using a refined search setup [labeled “E@H S5R1” in Figure 7.1a]. The analysis currently underway on the Einstein@Home project employs an implementation of the Hough transform method as given in [164] and uses 121 S5 data segments of 25 h from both 4-km LIGO detectors. This search improves upon the first S5 analysis by a factor of about 4 [labeled “E@H S5R5 (Hough method)” in Figure 7.1a]. Using this same data set, the GCT technique introduced in Chapter 6 is expected to yield a drastic improvement over the conventional Hough method by factor of about 6 [labeled “E@H

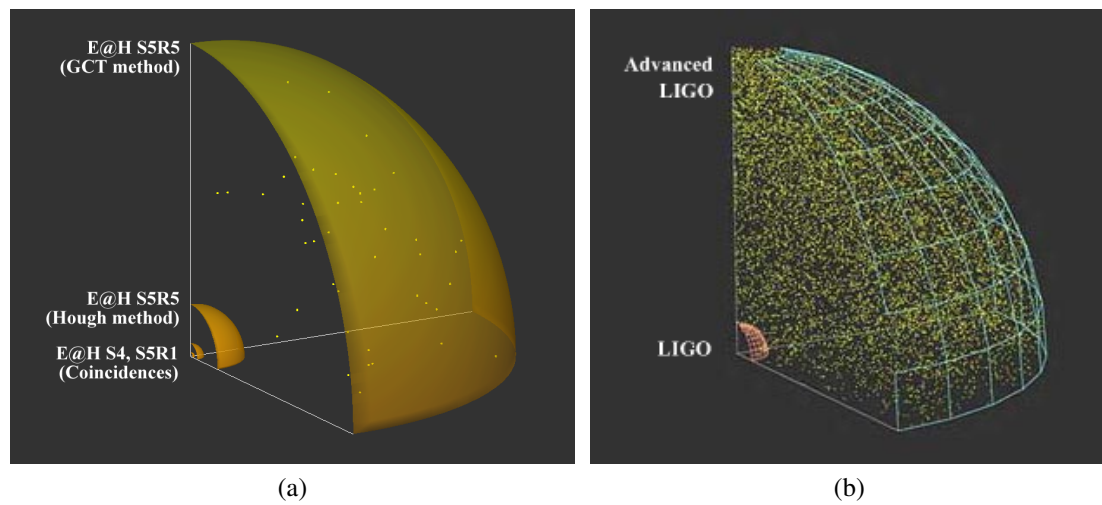


Figure 7.1: Artistic illustration of the relative increase in spatial volume probed for a uniform population of sources. In (a), the sensitivity increase associated with the different CW search techniques presented in this dissertation is shown. The label “E@H S4” refers to the S4 Einstein@Home search (cf. Chapter 3), “E@H S5R1” references the first S5 Einstein@Home search (cf. Chapter 4), “E@H S5R5 (Hough method)” indicates the currently ongoing Einstein@Home search based on the conventional Hough transform method, and “E@H S5R5 (GCT method)” relates to GCT technique (cf. Chapter 6) assuming the same data set. For comparison, in (b), taken from [193], the enhancement in instrument sensitivity of the planned Advanced LIGO detector over initial LIGO is indicated.

S5R5 (GCT method)” in Figure 7.1a]. In fact, the lower computational cost of the GCT method could also be reinvested to even further improve the sensitivity.

In Figure 7.1a the detector instrument performance has been assumed not to change substantially, while the sensitivity enhancements shown arise primarily from advances in data analysis. For comparison, Figure 7.1b illustrates the increase in volume of space captured resulting from improving the detector instruments, while using the same data analysis method. As visualized in Figure 7.1b, the planned Advanced LIGO detector improves the sensitivity (and so the distance reach) by more than a factor of 10 beyond initial LIGO.

Thus Figure 7.1 clearly demonstrates the significance of the GCT method for all-sky broadband CW data analyses with Earth-based detectors. Therefore, further work is currently in progress to use the GCT method on the Einstein@Home project to ana-

lyze the future LIGO S6 data, replacing the currently used implementation of the Hough transform technique. The combination of new and more sensitive search techniques, plus new and more sensitive data, greatly increases the chance of the first detection of a CW source. Given the current progress and the encouraging prospects of future developments, there is reason to be optimistic that listening to the tones of an astrophysical continuous gravitational-wave source will finally become reality within the next decade.

Appendix

Search for CW sources in NAUTILUS data

Appeared in Classical Quantum Gravity 25, 184012, (2008)

A.1 Overview and context

This Chapter presents results from analyzing data from the NAUTILUS resonant bar detector [41] for continuous gravitational-wave (CW) signals. Over the frequency band of [922.2; 923.2] Hz and the spin-down range of $[-1.463 \times 10^{-8}; 0]$ Hz/s and over the entire sky, this search analyzes about half a year of NAUTILUS data collected in the year 2001. The data is divided into segments of 2 sidereal days. Each segment of data is analyzed coherently using matched filtering in the form of the \mathcal{F} -statistic [55, 117].

In this analysis, a low threshold has been set on the \mathcal{F} -statistic to obtain a set of candidates that are further examined for coincidences among various data segments. For some candidates the change of the signal-to-noise ratio has also been investigated when increasing the coherent observation time from 2 to 4 days. No evidence of gravitational-wave signals was found. Therefore, upper limits have been placed on the dimensionless gravitational-wave amplitude over the parameter space searched. Depending on frequency, the upper limits range from 3.4×10^{-23} to 1.3×10^{-22} .

Previous analyses of bar detector data for CW signals include the search of the galactic center and the globular cluster 47 Tucanae with the ALLEGRO detector [194], the search of the galactic center using the EXPLORER detector data [195], and an all-sky search using the EXPLORER data [196, 197].

Section A.2 presents the data analysis methods used in this search. Section A.3 outlines the search procedure. In Section A.4, the analysis of the candidates is discussed. This analysis consists of two parts: the first part is the search for coincidences among the candidates obtained from a different data segments and the second part is an investigation of the increase in signal-to-noise ratio of candidates when increasing the observation time. In Section A.5, upper limits are imposed on the gravitational-wave amplitude over the parameter space that has been searched.

A.2 Data analysis methods

In order to search for gravitational waves from long lived periodic sources here the maximum likelihood (ML) method is used. For the case of Gaussian noise the ML method consists of linearly filtering the data with a template matched to the signal that one is searching for. The main complication of the matched filtering is that the signal depends on several unknown parameters. This requires evaluation of the likelihood function over a large parameter space. In order to minimize the computation time we use several data analysis tools. *Firstly*, we find the maximum likelihood estimators of some parameters (4 in the case of a CW signal from a rotating neutron star) in a closed analytic form, thereby reducing the dimensionality of the parameter space to be searched. This likelihood function over the reduced parameter space is the \mathcal{F} -statistic, which is derived in [55]. *Secondly*, data of length equal to an integer multiple of a sidereal day is analyzed. This leads to a considerable simplification of the \mathcal{F} -statistic and consequently reduces the number of numerical operations to evaluate it. The \mathcal{F} -statistic for an observation time equal to an integer number of sidereal days is given in Section III. of [185]. *Thirdly*, optimal numerical algorithms are used, in particular the Fast Fourier Transform (FFT) [170, 171] in order to calculate the \mathcal{F} -statistic efficiently. *Fourthly* the number

of \mathcal{F} -statistic calculations is minimized over the parameter space by solving a covering problem for this space [198, 199]. Below, the latter two data analysis tools are explained in more detail. The response function of a resonant bar detector to a gravitational-wave signal from a spinning neutron star is summarized in Section 2.1 of [197].

Fast Fourier Transform. Estimates have shown [160, 172] that for the bandwidth and the spin-down range presently searched, only one frequency-derivative (spin-down) parameter is needed to be taken into account in order to reasonably match the signal. Consequently, the phase modulation function $\phi(t)$ of the waveform is given by

$$\phi(t) = \omega_0 t + \omega_1 t^2 + (\omega_0 + 2\omega_1 t) \frac{\mathbf{n}_0 \cdot \mathbf{r}_d(t)}{c}, \quad (\text{A.1})$$

where ω_0 is angular frequency and ω_1 is the spin-down parameter, \mathbf{n}_0 is the constant unit vector in the direction of the star in the Solar System Barycenter (SSB) reference frame (it depends on the right ascension α and the declination δ of the source), and \mathbf{r}_d is the vector joining the SSB with the detector and c is the speed of light. The detection statistic \mathcal{F} involves two integrals of the form

$$F = \int_0^{T_0} x(t) a(t) e^{-i\phi(t)} dt, \quad (\text{A.2})$$

where $x(t)$ is the data stream, $a(t)$ is the amplitude modulation function that depends on δ and α . The above integral is not a Fourier transform because the frequency ω_0 in the phase multiplies the term $\mathbf{n}_0 \cdot \mathbf{r}_d(t)$ which is a non linear function of time. In order to convert the integral into a Fourier transform we introduce the following interpolation procedure. The phase $\phi(t)$ [Equation (A.1)] can be written as

$$\phi(t) = \omega_0 [t + \phi_m(t)] + \phi_s(t), \quad (\text{A.3})$$

where

$$\phi_m(t) \equiv \frac{\mathbf{n}_0 \cdot \mathbf{r}_d(t)}{c}, \quad (\text{A.4})$$

$$\phi_s(t) \equiv \omega_1 t^2 + 2 \frac{\mathbf{n}_0 \cdot \mathbf{r}_d(t)}{c} \omega_1 t. \quad (\text{A.5})$$

The functions $\phi_m(t)$ and $\phi_s(t)$ do not depend on the angular frequency ω_0 . One may write the integral (A.2) as

$$F = \int_0^{T_0} x(t) a(t) e^{-i\phi_s(t)} \exp \{ -i\omega_0 [t + \phi_m(t)] \} dt. \quad (\text{A.6})$$

The integral (A.6) can be interpreted as a Fourier transform (and computed efficiently with an FFT), if $\phi_m = 0$. In order to convert equation (A.6) to a Fourier transform we introduce a new time variable t_b , so called *barycentric time* [200, 55],

$$t_b \equiv t + \phi_m(t). \quad (\text{A.7})$$

In the new time coordinate the integral (A.6) is approximately given by (see Section III. D of [55])

$$F \cong \int_0^{T_0} x[t(t_b)]a[t(t_b)]e^{-i\phi_s[t(t_b)]}e^{-i\omega_0 t_b} dt_b. \quad (\text{A.8})$$

Thus in order to compute the integral (A.6), we first multiply the data $x(t)$ by the function $a(t) \exp[-i\phi_s(t)]$ for each set of the parameters ω_1, δ, α and then resample the resulting function according to equation (A.7). At the end the FFT is performed.

The covering problem. The covering problem is related to finding the minimum number of templates in the parameter space [199], so that the fractional loss in signal to ratio is not less than $1 - MM$ (MM is the minimal match parameter introduced by Owen [174]). In order to solve the covering problem we introduce a useful approximate model of the gravitational-wave signal from a rotating neutron star. The model relies on (i) neglecting all spin-downs in the phase modulation due to motion of the detector with respect to the SSB; and (ii) discarding the component of the vector \mathbf{r}_d (connecting the SSB and the detector) which is perpendicular to the ecliptic plane. These approximations lead to the following phase model of the signal:

$$\phi_{\text{lin}}(t) = \omega_0 t + \omega_1 t^2 + \alpha_1 \mu_1(t) + \alpha_2 \mu_2(t), \quad (\text{A.9})$$

where α_1 and α_2 are new constant parameters,

$$\alpha_1 \equiv \omega_0 (\sin \alpha \cos \delta \cos \varepsilon + \sin \delta \sin \varepsilon), \quad (\text{A.10})$$

$$\alpha_2 \equiv \omega_0 \cos \alpha \cos \delta, \quad (\text{A.11})$$

where ε is the obliquity of the ecliptic and where $\mu_1(t)$ and $\mu_2(t)$ are known functions of time,

$$\mu_1(t) \equiv R_{\text{ES}}^y(t) + R_{\text{E}}^y(t) \cos \varepsilon, \quad (\text{A.12})$$

$$\mu_2(t) \equiv R_{\text{ES}}^x(t) + R_{\text{E}}^x(t). \quad (\text{A.13})$$

R_{ES}^x is the x -component of the vector joining the center of Earth and the SSB, and R_{E}^x is the x -component of the vector joining the center of Earth and the detector. $R_{\text{ES}}^y(t)$ and $R_{\text{E}}^y(t)$ are the corresponding y -components. We also neglect the slowly varying modulation of the signal's amplitude, so finally we approximate the whole signal $h(t)$ by

$$h(t) = A_0 \cos(\phi_{\text{lin}}(t) + \phi_0), \quad (\text{A.14})$$

where A_0 and ϕ_0 are the constant amplitude and initial phase, respectively. The above signal model is called *linear* because it has the property that its phase given by Equation (A.9) is a linear function of the parameters. It is shown in [189] that the above model is a good approximation to the accurate response of the detector to the GW signal in the sense that the Fisher matrix for the linear model reproduces well the Fisher matrix for the accurate model. Thus whenever a Fisher matrix is needed, the Fisher matrix for the linear model can be used as an approximation to the Fisher matrix for the accurate model. The great advantage of the linear model is that components of its Fisher matrix are constant, independent of the values of the parameters. In order to solve the covering problem for the parameter space we use the Fisher matrix as a metric on the parameter space. Because the components of the Fisher matrix are constant the grid is uniform what greatly simplifies its construction. In our search, as a grid we use the hypercubic lattice [198]. However we have an additional constraint. In order to apply the FFT algorithm the nodes of the grid must coincide with the Fourier frequencies. We have constructed a suitable grid by performing rotations and dilatations of the original hypercubic lattice. The grid is constructed in the parameters $\omega_0, \omega_1, \alpha_1, \alpha_2$ and then transformed to parameters $\omega_0, \omega_1, \delta, \alpha$ for which the \mathcal{F} -statistic is calculated.

The linear parametrization has one more application. We use it in order to calculate the threshold for the \mathcal{F} -statistic corresponding to a certain false alarm probability. Namely, using the linear parametrization the parameter space is divided into cells as explained in [55, 172]. All the cells are exactly the same and their number N_c is easily calculated using the Fisher matrix (see Section III. B of [172]). The false alarm probability α is the probability that \mathcal{F} exceeds threshold \mathcal{F}_o in *one or more* cells and is given by

$$\alpha = 1 - [1 - P_F(\mathcal{F}_o)]^{N_c}, \quad (\text{A.15})$$

where P_F is the false alarm probability for a single cell.

A.3 Search procedure

We have searched the data collected by the NAUTILUS detector in the year 2001. The bandwidth of $[922.2; 923.2]$ Hz, where the detector is most sensitive, has been analyzed. We have divided the data into segments which span two sidereal days. We have assumed a minimum pulsar spin-down age τ_{min} equal to 1000 yrs and so we have searched the negative frequency time derivatives in the range of $[-1.463 \times 10^{-8}; 0]$ Hz/s. For this τ_{min} and two days of the observation time it is sufficient to include only one spin-down in the phase $[160, 172]$. Each two day sequence was analyzed coherently using the \mathcal{F} -statistic. We have used the constrained hypercubic grid as explained in the previous section. For the grid construction we have assumed the minimal match parameter $MM = \sqrt{3}/2$ [174]. Using this minimal-match value our grid consists of around 3.1×10^{13} grid points (2^{19} frequency bins, $\sim 10^3$ spin-down parameters, $\sim 6 \times 10^4$ sky positions). The threshold on $2\mathcal{F}$ corresponding to 1% false alarm probability has been calculated using Equation (A.15) and is around 72. In order to compensate the loss of signal-to-noise ratio (SNR) due to the discreteness of the grid, imperfect templates and numerical approximation in evaluation of the \mathcal{F} -statistic (resampling procedure) we have adopted two lower thresholds on $2\mathcal{F}$ equal to 40 and 50. We have registered parameters of all templates which crossed the threshold of 40. For threshold crossings of 50 we have performed a verification procedure. The verification procedure consisted of calculating the \mathcal{F} -statistic for the template parameters of the candidate using a 4-day segment of data involving the original 2-day segment. For a true gravitational-wave signal by this procedure one would expect an increase of signal-to-noise ratio by $\sqrt{2}$. In total, 93 data segments of 2-day duration have been analyzed. In Figure A.1 we have presented the two-sided amplitude spectrum of the NAUTILUS detector data that we have analyzed. The spectrum was obtained in the following way. We have estimated the power spectrum density in each of the 93 2-day data sequences and then we have taken the square root of the average of the 93 power spectra. The best sensitivity is around $5 \times 10^{-22} \text{ Hz}^{-1/2}$. Moreover we have obtained the rms error of our power spectrum estimate by calculating the variance from the estimates of the spectra of in each of the 93 data segments. The relative 1σ error in the amplitude power spectrum is around 18%.

During the search we have obtained 537 665 380 candidates above the $2\mathcal{F}$ -threshold

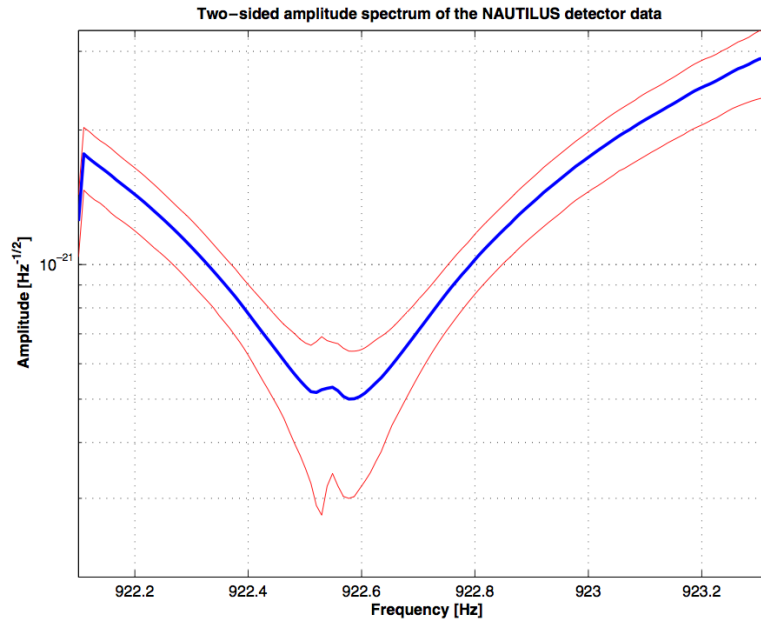


Figure A.1: Estimation of the two-sided amplitude spectrum of the NAUTILUS data in the year 2001 and the rms error of the estimate. The thick line shows the estimate and the two thin lines correspond to the 1σ error.

of 40 and 9 038 817 above the $2\mathcal{F}$ -threshold of 50.

A.4 Analysis of candidates

A.4.1 Signal-to-noise ratio of the candidates

In Figure A.2, a histogram of the frequencies of all the candidates above the $2\mathcal{F}$ -threshold of 50 is plotted. The histogram shows an excess of candidates in the frequency band of $[922.4; 922.6]$ Hz. This excess is a result of the presence of an instrumental noise interference in the data that appears as a series of harmonics in the bandwidth of the detector. One of the harmonics is located in the subband $[922.2; 923.2]$ Hz. The effect of the harmonic is visible in our estimate of the spectrum (Figure A.1) and appears

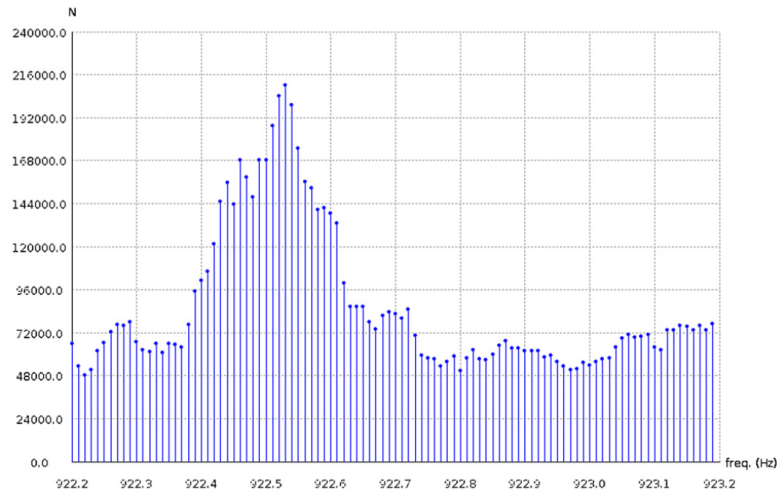


Figure A.2: Histogram of the frequencies of candidates obtained in the search of all 93 2-day data segments above a $2\mathcal{F}$ -threshold of 50.

as a bump in the band $[922.5; 922.6]$ Hz.

As a first step in the candidate analysis, the increase in signal-to-noise ratio has been calculated when increasing the observation time from 2 to 4 days. This has been carried out for all the candidates above the threshold of $2\mathcal{F} = 50$. Figure A.3 shows the highest increase in SNR for candidates when going from a 2-day data segment to the 4-day one. The maximum is calculated for each of the 93 data segments analyzed. Typically, the highest gain in the signal-to-noise found is 1.2. This should be compared with the theoretical gain of $\sqrt{2}$ of SNR when we increase the observation time by a factor of 2. The instrumental noise interference present in the data to which we attribute these maximum SNR increases does not give a higher increase of the SNR because its frequency changes erratically over the observation time of days and it cannot reproduce the Doppler shift of a real CW signal modulated by detector motion with respect to the SSB. Assuming that the 2-day sequence is independent of the 4-day sequence we could perform the F -test that consists of calculation of the ratio F of the \mathcal{F} -statistic for 4 days observation time and the \mathcal{F} -statistic for 2 days observation time. Taking as the null hypothesis for the test that data is only Gaussian noise the $2\mathcal{F}$ -statistic has the central χ^2 distribution with 4-degrees of freedom and the ratio F has Fisher-Snedecor distribution $F(4, 4)$. The typical highest value of F for a given data segment is around 1.5 The probability of F

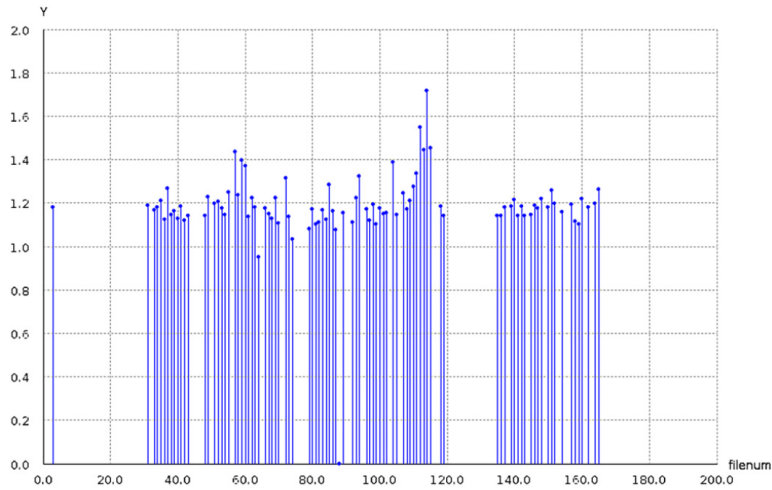


Figure A.3: Highest increase (vertical axis) in signal-to-noise ratio for candidates in each of the 93 data segments analyzed. The 2-day segments of Nautilus 2001 data are numbered from 1 to 182. The missing lines in the plot indicate that the corresponding data segment has not been analyzed.

crossing the threshold 1.5 is around 37%. This would give a high confidence that data is noise only. Unfortunately this is only a crude approximation because the 2-day sequence is contained in the 4-day one and the assumption of independence of the two \mathcal{F} -statistic is not fulfilled.

A.4.2 Coincidences among the candidates from different data segments

Candidates from different data segments are considered *coincident* if they cluster closely together in the four-dimensional parameter space $(\omega_0, \omega_1, \delta, \alpha)$. We employ the clustering method described in Chapter 3, which uses a grid of “coincidence cells”. This method will reliably detect strong signals which would produce candidates with closely-matched parameters in many of the different data segments.

In a first step, the frequency value of each candidate above the threshold of $2\mathcal{F} = 40$ is shifted to the same fiducial time: the GPS start time of the earliest ($j = 1$) segment, $t_{\text{fiducial}} = t_1 = 662\,547\,735.9988098$ s. Defining T_0 to be the time span of two sidereal

days, the frequencies of the candidates are shifted to t_{fiducial} via

$$\omega_0(t_{\text{fiducial}}) = \omega_0(t_j) + (j - 1) 2\omega_1 T_0, \quad (\text{A.16})$$

where t_j is the starting time of the j 'th data segment, given by $t_j = t_{\text{fiducial}} + (j - 1) T_0$.

To find coincidences, a grid of cells is constructed such that the cells are rectangular in the coordinates $(\omega_0, \omega_1, \delta, \alpha \cos \delta)$. The dimensions of the cells are adapted to the parameter space search. Thus, the cells are constructed to be as small as possible to reduce the probability of coincidences due to false alarms. However, since each of the 93 different data segments uses a slightly different parameter space grid, the coincidence cells must be chosen to be large enough that the candidates from a source (which would appear at slightly different points in parameter space in each of the 93 data segments) would still lie in the same coincidence cell. As a conservative choice we use cell sizes in ω_0 of 5.8×10^{-4} Hz, in ω_1 of 2.08×10^{-11} Hz s $^{-1}$, and an isotropic cell grid in the sky with equatorial spacing of 0.028 rad. Each candidate event is assigned to a particular cell. In cases where 2 or more candidate events from the same data segment j fall into the same cell, only the candidate having the largest value of $2\mathcal{F}$ is retained in the cell. Then the number of candidate events per cell coming from distinct data segments is counted.

From the 93 different data segments, this coincidence method found that we get candidates which appear consistently in no more than 4 data segments uniformly over the search bandwidth, where there are no instrumental interferences. This is the background of the number of coincidences. We would like to test the null hypothesis that the coincidences are result of the noise only. Let us assume that the parameter space is divided into N_{cell} independent coincidence cells, the candidate events are independent and the probability for a candidate event to fall into any given coincidence cell is $1 = 1/N_{\text{cell}}$. Thus probability ϵ that a given coincidence cell is populated with one or more candidate event is given by

$$\epsilon = 1 - \left(1 - \frac{1}{N_{\text{cell}}}\right)^{\varepsilon_{\text{seg}}}, \quad (\text{A.17})$$

where ε_{seg} is the number of candidate events per data segment. The probability p_F that any given coincidence cell contains candidate events from \mathcal{C}_{max} or more distinct data segments is given by a binomial distribution

$$p_F = \sum_{n=\mathcal{C}_{\text{max}}}^{N_{\text{seg}}} \binom{N_{\text{seg}}}{n} \epsilon^n (1 - \epsilon)^{N_{\text{seg}} - n}. \quad (\text{A.18})$$

Finally the probability P_F that there is \mathcal{C}_{max} or more coincidences in one or more of the N_{cell} cells is

$$P_F = 1 - (1 - p_F)^{N_{cell}} . \quad (\text{A.19})$$

The expected number of cells with \mathcal{C}_{max} or more coincidences is given by

$$N_F = N_{cell} p_F . \quad (\text{A.20})$$

In our case the number of cells is given by $N_{cell} = 5.9 \times 10^{10}$, the number of data segments is $N_{seg} = 93$, and the number of candidates per data segment is $\varepsilon_{seg} = 5.8 \times 10^6$. From Equation (A.19) we find that the probability of finding $\mathcal{C}_{max} = 4$ or more coincident candidates is almost one. Thus for the background coincidences we can accept the null hypothesis that they are from noise only with a high confidence.

As shown in Figure A.4, over the bandwidth [922.4; 922.6] Hz we find an excess of coincidences with the maximum of 8 coincidences. By Equation (A.19), the false alarm probability associated with 8 or more coincidences is of the order of 10^{-11} and thus they cannot be attributed to noise. We consider these coincidences to be due to the instrumental interference present in the data.

A.5 Upper limits

The verification procedure consisting of coincidences among the candidates from distinct data segments and an analysis of the increase of signal-to-noise ratio presented in Section A.4 did not produce convincing evidence of a gravitational-wave signal. Therefore, we proceed to estimate the upper limits for the amplitudes of the gravitational-wave signals in the parameter space that we have searched. Detection of a signal is signified by a large value of the \mathcal{F} -statistic that is unlikely to arise from the noise-only distribution. If instead the value of \mathcal{F} is consistent with pure noise with high probability we can place an upper limit on the strength of the signal. One way of doing this is to take the loudest event obtained in the search and solve the equation

$$\mathcal{P} = P_D(\rho_{ul}, \mathcal{F}_{loudest}) , \quad (\text{A.21})$$

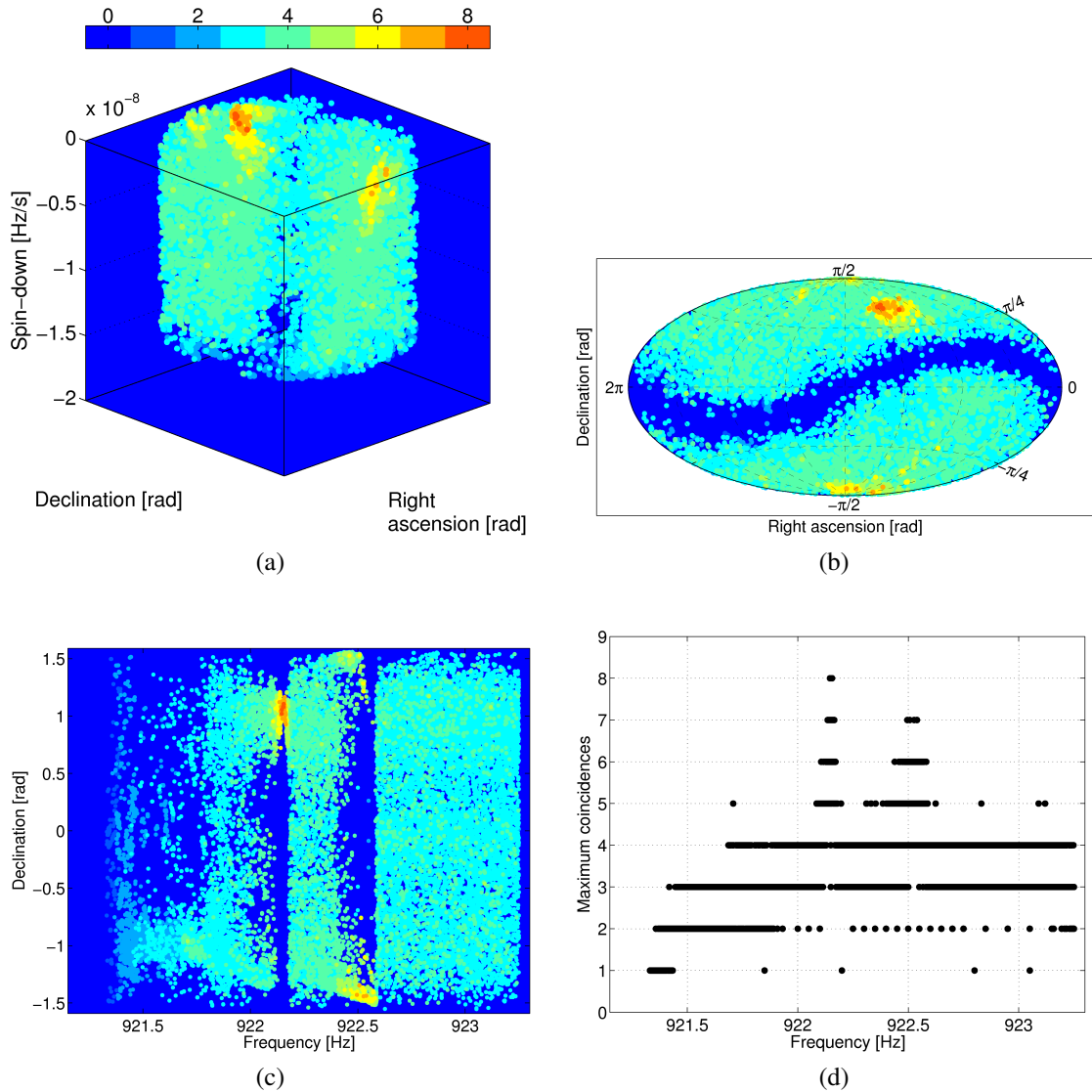


Figure A.4: Results of the coincidence search among the candidates from different data segments. The different plots show the numbers of coincidences (color-coded) in a 3D map of sky and spin-down (a), in a 2D Hammer-Aitoff projection of the sky (b), in a 2D plot of declination over frequency (c), and in a histogram as a function of frequency (d).

for signal-to-noise ratio ρ_{ul} , where P_D is the detection probability, $\mathcal{F}_{\text{loudest}}$ is the value of the \mathcal{F} -statistic corresponding to the loudest event, and \mathcal{P} is a chosen confidence. Then ρ_{ul} is the desired upper limit with confidence \mathcal{P} . We can also obtain an upper limit ρ_{ul} with confidence \mathcal{P} for several independent searches from

$$\mathcal{P} = 1 - \prod_{s=1}^L [1 - P_D(\rho_{\text{ul}}, \mathcal{F}_{\text{loudest } s})], \quad (\text{A.22})$$

where $\mathcal{F}_{\text{loudest } s}$ is the threshold corresponding to the loudest event in s 'th search and L is the number of searches. Here \mathcal{P} is the probability that a signal with signal-to-noise ratio ρ_{ul} crosses the threshold $\mathcal{F}_{\text{loudest } s}$ in at least one of the L independent searches. To calculate ρ_{ul} we assume that the data have a Gaussian distribution and consequently the probability of detection P_D has a non-central χ^2 distribution with 4 degrees of freedom and the noncentrality parameter equal to ρ_{ul}^2 . We have investigated this assumption by obtaining histograms of the $2\mathcal{F}$ -statistic values of the candidates and comparing them to the central χ^2 distribution with 4 degrees of freedom. The result is shown in Figure A.5. There is an overall qualitative agreement of candidates distributions with the theoretical one. However, the candidates distributions do not pass a goodness-of-fit test for a χ^2 distribution at the significance level of 5%.

In order to translate the upper limit on the SNR into an upper limit on the gravitational-wave amplitude, Equation (93) of [55] is used for the SNR of a CW signal averaged over the source position and orientation. Thus h_{ul} and ρ_{ul} are related by the following formula:

$$h_{\text{ul}}(f) = \frac{5}{2} \sqrt{\frac{S(f)}{T_o}} \rho_{\text{ul}}, \quad (\text{A.23})$$

where $S(f)$ is one-sided spectral density at frequency f . We have used Equations (A.22) and (A.23) to obtain upper limits in 0.1 Hz bands over the bandwidth [922.2; 923.2] Hz that we have searched. The upper limit results are presented in Figure A.6. Assumed Gaussian noise, we have chosen the confidence $\mathcal{P} = 90\%$ and the upper limits is denoted by $h_o^{90\%}$. The best upper limit obtained is equal to 3.4×10^{-23} at a frequency of 922.55 Hz. Using a 1σ rms error of the amplitude power spectrum estimate, we reckon that this upper limit has likewise an error of 18%.

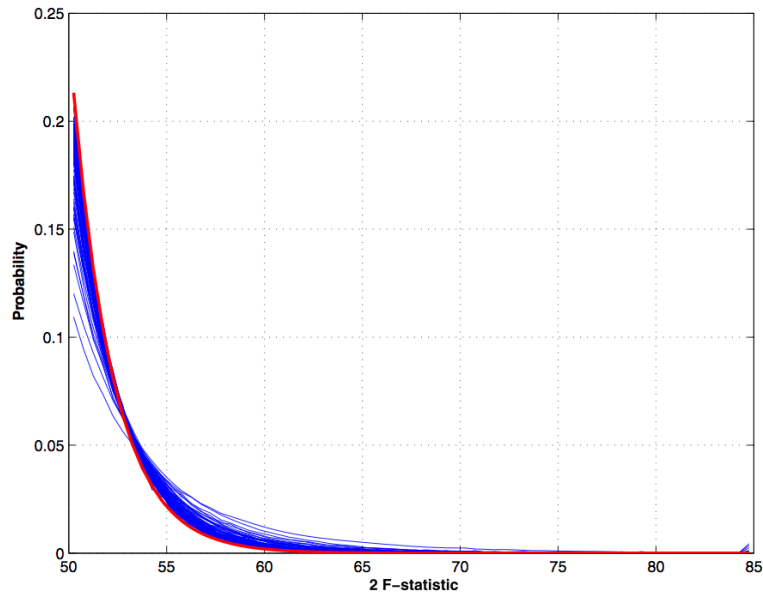


Figure A.5: Probability distribution of $2\mathcal{F}$ -statistic values of the candidates. The light lines are obtained from histograms of the $2\mathcal{F}$ values of each data segment. The thick line represents the theoretical central χ^2 distribution with 4 degrees of freedom.

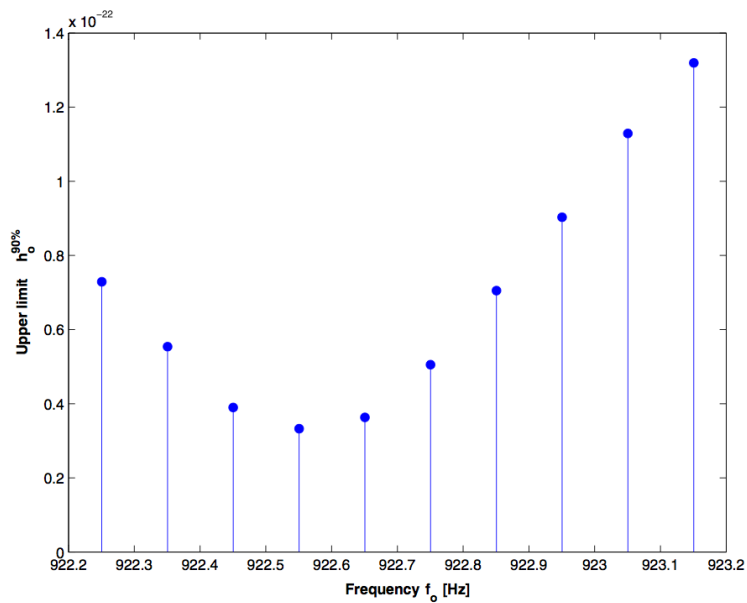


Figure A.6: Upper limits based on the loudest candidate for 0.1 Hz frequency bands over the 1 Hz bandwidth searched.

Search for tight binary radio pulsars in Arecibo radio data

B.1 Overview and context

Radio pulsars are neutron stars with an immensely strong magnetic field. They rotate and accelerate electrons in their vicinity to close to the speed of light. These electrons emit polarized light in a narrow cone. When this cone sweeps across the line of sight to Earth, the radio emission may be observed regularly, just like a lighthouse. Some radio pulsars are also seen in visible light, X- and gamma rays.

So far, pulsars have been the primary way that neutron stars can be observed. About 1800 of them are known today [149]. Only a tiny fraction of pulsars is in binary systems where their masses can be determined. The known sample is not large enough to determine a firm upper mass limit, which would in turn give more detailed insight into the physics of such extremely dense forms of matter.

Radio pulsars in short-orbit binary systems form an interesting subclass of neutron stars. These provide an excellent laboratory for testing relativistic gravitational physics in the strong-field regime. They also lead to valuable information regarding the inspiral rates for Galactic binary neutron star systems, which particularly relevant to gravitational-wave searches.

The search for binary pulsars in very tight binary orbits on the order of minutes is

fundamentally limited by the computational resources available. In the past years, the concept of volunteer computing, such as the CW search project of Einstein@Home, has emerged for solving many such problems.

Using some fraction of the Einstein@Home power, the present project aims to search PALFA radio data from the Arecibo telescope for binary pulsars with orbital periods as short as 11 minutes. Mostly based on [6, 201, 202], a brief summary of this search project will be given in the following.

B.2 Pulsars in circular orbits

Since the search targets are pulsars with short orbital periods, the orbits of the system are assumed to be circularized. The phase model $\phi(t)$ for signal with spinning frequency f is given by

$$\phi(t) = 2\pi f [t + \tau \sin(\Omega_{\text{orb}}t + \psi_0)] , \quad (\text{B.1})$$

where $\tau = r_{\text{orb}} \sin(\iota)$ denotes the projected orbital radius with inclination angle ι , $\Omega_{\text{orb}} = 2\pi/P_{\text{orb}}$ is the orbital angular velocity and ψ_0 is the initial orbital phase. Summarizing the search parameters in vectorial form of $\Lambda = (f, \Omega_{\text{orb}}, \tau, \psi_0)$, one may rewrite Equation (B.1) in terms of the resampled time $t'(t, \Lambda)$ as

$$\phi(t', \Lambda) = 2\pi f t'(t, \Lambda) + \phi_0 . \quad (\text{B.2})$$

Thus, proper resampling of the time series allows to remove the Doppler modulation due to the binary motion from the signal. In a next step, the resampled time series is simply Fast Fourier transformed (FFT) searching for many different values of f in parallel.

Because the signals of radio pulsars are not sinusoidal but pulsed, the frequency analysis will show frequency components at the fundamental frequency f and at higher harmonics (integer multiples of f). Summing these components is a well-known trick to improve sensitivity. The radio intensity waveform of the pulsed signal can be written as a weighted sum of trigonometric functions of integer multiples of the phase,

$$\mathcal{S}(t', \Lambda) = \sum_{n=1}^{N_{\text{harmonics}}} \omega_n \sin(n \phi(t', \Lambda) + \phi_{0,n}) . \quad (\text{B.3})$$

B.3 Search methodology

Searches for new binary radio pulsars so far were either so-called “acceleration searches” [203] or “sideband searches” [204]. The former correct for the varying time-delays by using an approximation of the binary orbit which is valid only if the observation time is much less than the orbital period of the binary system. The latter is efficient only when many binary orbits are visible during the observation time. There is a gap between those methods where both experience a large loss in sensitivity. The present search uses data sets covering 5 minutes of observation. Thus, the acceleration search becomes significantly less sensitive for orbital periods shorter than 50minutes. The sideband search loses sensitivity for orbital periods longer than 3 minutes. Using the complete sinusoidal signal phase model (without any approximations) as done here will close the resulting gap and can correct for binary periods down to 11 minutes, meaning where one may “see” up to half an orbit of such a binary with its strong Doppler variations.

B.3.1 Detection statistic

The demodulated power \mathcal{P}_n represents the detection statistic, which has the expectation value

$$\mathcal{P}_n(\Lambda_0, \Lambda) = \frac{\omega_n}{4T} \left| \int_0^T \exp [i \Delta\phi_n(t', \Lambda_0, \Lambda)] dt \right|^2, \quad (\text{B.4})$$

with $\Delta\phi_n(t', \Lambda_0, \Lambda)$ defining the phase difference between the signal phase described by Λ_0 and the template phase characterized by Λ :

$$\Delta\phi_n(t', \Lambda_0, \Lambda) = n [\phi(t'(t, \Lambda_0)) - \phi(t'(t, \Lambda))] . \quad (\text{B.5})$$

The power from all harmonics will be incoherently combined by harmonic summing.

B.3.2 Mismatch

The so-called mismatch μ leading to a loss in signal power due to imperfectly matching the signal phase is defined by

$$\mu = 1 - \frac{\mathcal{P}(\Lambda_0, \Lambda)}{\mathcal{P}(\Lambda_0, \Lambda_0)}. \quad (\text{B.6})$$

Taylor-expanding the above right-hand side to quadratic order in the parameter offsets defines a metric g_{jk} on the signal manifold as

$$\mu = g_{jk}(\Lambda_0) \Delta\Lambda^j \Delta\Lambda^k + \mathcal{O}[(\Delta\Lambda)^3]. \quad (\text{B.7})$$

This metric can be used as a distance measure on the parameter space, which is a common approach used in gravitational-wave data analysis [173, 174, 160, 187] to address the template placement problem. The elements of the phase metric are obtained as

$$g_{jk}(\Lambda_0) = \langle \partial_j \phi \partial_k \phi \rangle - \langle \partial_j \phi \rangle \langle \partial_k \phi \rangle, \quad (\text{B.8})$$

where where $\partial_j \phi$ represents the partial derivative of ϕ with respect to the j th parameter and the time average is defined by

$$\langle q \rangle \equiv \frac{1}{T} \int_0^T q(t) dt. \quad (\text{B.9})$$

B.3.3 Template placement

Because this search is for previously unknown sources, a large number of possible signal templates have to be probed.

In doing the FFT, the frequency dimension has to be treated separately from the other parameters by constructing the frequency-projected metric

$$\gamma_{jk} = g_{jk} - \frac{g_{fj} g_{fk}}{g_{ff}}. \quad (\text{B.10})$$

Thus, templates have to be placed in the ‘‘orbital’’ parameters Ω_{orb} , τ and ψ_0 .

For each orbital template the time series is resampled and analyzed for periodicities using the FFT plus subsequent harmonic summing.

Traditionally, the template bank is based on a lattice using the underlying parameter-space metric of Equation (B.8), such that the maximum possible mismatch for any signal is less than some predefined value. If the metric components are not constant over the parameter space the construction of a lattice-based template bank can become fairly complicated.

One way out is given by the random template bank approach [205]. The idea behind is to relax the requirement of a complete coverage to a certain confidence $\eta < 1$, and templates are thrown randomly onto the parameter space. The required number of templates to throw is related to the square root of the metric determinant. Apart from the obvious simplicity of this approach, also surprisingly efficient results are achieved. In particular in higher dimensions, this approach becomes extremely efficient compared to full lattice coverings. As the metric in the present case is non-constant over the parameter space, this space is divided into smaller patches over which the metric is assumed not to vary and the proper number of templates is then randomly placed.

B.3.4 PALFA search

The PALFA search [206] uses the 7-beam ALFA receiver and the Wideband Arecibo Pulsar Processors (WAPPs) at the 305 m dish of the Arecibo radio observatory in Puerto Rico. In this survey, 256-channel radio spectra over a band of 100 MHz centered at 1.4 GHz are generated every $64 \mu\text{s}$ and 2 bytes per sample are stored.

The search covers regions of sky close to the Galactic plane ($|b| \lesssim 5^\circ$), in the inner Galaxy ($40^\circ \lesssim \ell \lesssim 70^\circ$) and in the anticenter direction ($170^\circ \lesssim \ell \lesssim 210^\circ$). Preliminary estimates indicate that this survey could potentially find hundreds of new pulsars and might be able for the first time to find pulsars in extreme binary systems. So far, other searches have discovered 48 new pulsars.

B.3.5 The search pipeline

The raw data of PALFA observations comes in stretches of 268 s at a sample rate of $64 \mu\text{s}$ over a 100-MHz-wide band of 256 channels. First, some data conditioning is

carried out. This involves removal of narrow- and wideband strong burst-like and weak radio frequency interferences in time and frequency domain.

The second step is called de-dispersion. Because the pulsar radio signals interact with the interstellar medium, dispersion of the pulse signal results [207]. As radio telescopes observe a wide band of radio frequencies, this dispersion effect has to be corrected for by adjusting the radio frequency dependent delay of the pulsar-signal arrival time. Since the exact amount of dispersion depends on the unknown distance to the pulsar and the number of electrons along this distance, a number of different trial values of dispersion is considered and each of the resulting data sets is searched independently. In this analysis 628 different dispersion measure (DM) trial values in the range of 0 to $1002.4 \text{ pc cm}^{-3}$ are used. This process is done on the Einstein@Home servers.

Third, the de-dispersed time series are sent out to the Einstein@Home volunteers. Their computers perform the demodulation step by resampling the de-dispersed time series according to each template of the random bank. This is followed by computing the FFT and harmonic summing of power to increase sensitivity to narrow pulses. Information about any statistically significant candidates is returned back to the Einstein@Home servers.

The final post-processing involves procedures as identifying multiple instances of the same candidate, folding of the time series for promising candidates, and inspection of further diagnostic figures.

B.3.6 Search parameter space scanned

Due to the finite computing resources available the fraction of parameter space analyzed is constraint to astrophysically interesting regions. The search is for a minimum neutron star mass of $1.2 M_{\odot}$ and a maximum companion mass of $1.6 M_{\odot}$. The minimum orbital period searched for is 11 minutes, up to spin frequencies of 400 Hz and summation of up to 16 harmonics. The random template is designed to cover $\eta = 90\%$ of the parameter space with mismatch $\mu \leq 0.2$. In addition, the time series is downsampled by a factor of 2, and single-byte precision is used.

B.4 Analysis of simulated signals

To shed some light on the search parameter-space structure, the loss in power at different parameter-space locations for a given signal is investigated in the absence of noise and dispersion. For this purpose, the obtained signal power is calculated on an extremely dense (“over-covering”) grid in parameter space. The result of one such example is shown in Figure B.1. The iso-mismatch contours (of constant power loss) are quite extended in parameter space, revealing the strong global correlations present among the search parameters $(f, \Omega_{\text{orb}}, \tau, \psi_0)$.

For testing purposes of the search pipeline, data sets containing simulated Gaussian noise in addition to binary pulsar signals have been prepared, including dispersion effects. These data sets are subsequently analyzed using the random template bank constructed with maximum 0.2 mismatch at $\eta = 90\%$ confidence. In addition, this search involves the same analysis for different DM trials values, because the simulated signals have been artificially dispersed. The results for two simulated signals are shown in Figure B.2. The search pipeline has well recovered the injected signals. However, the iso-mismatch contours are also quite extended in parameter space as already shown earlier in Figure B.1. The strong global correlations present among the search parameters cause offsets from the true signal parameters in Figure B.2, In particular for the low-spinning-frequency example. This is also part of the reason why the best-found projected orbital radius τ of the first simulated signals is offset from the signal’s true value.

B.5 Current status

The project is currently processing input data at a daily rate of about 20 minutes of survey observation time. The observations themselves are taken at a rate 70 minutes per day. So far, the total data processed comprises about 17 hours.

A number of improvements to different parts of the search pipeline are currently un-

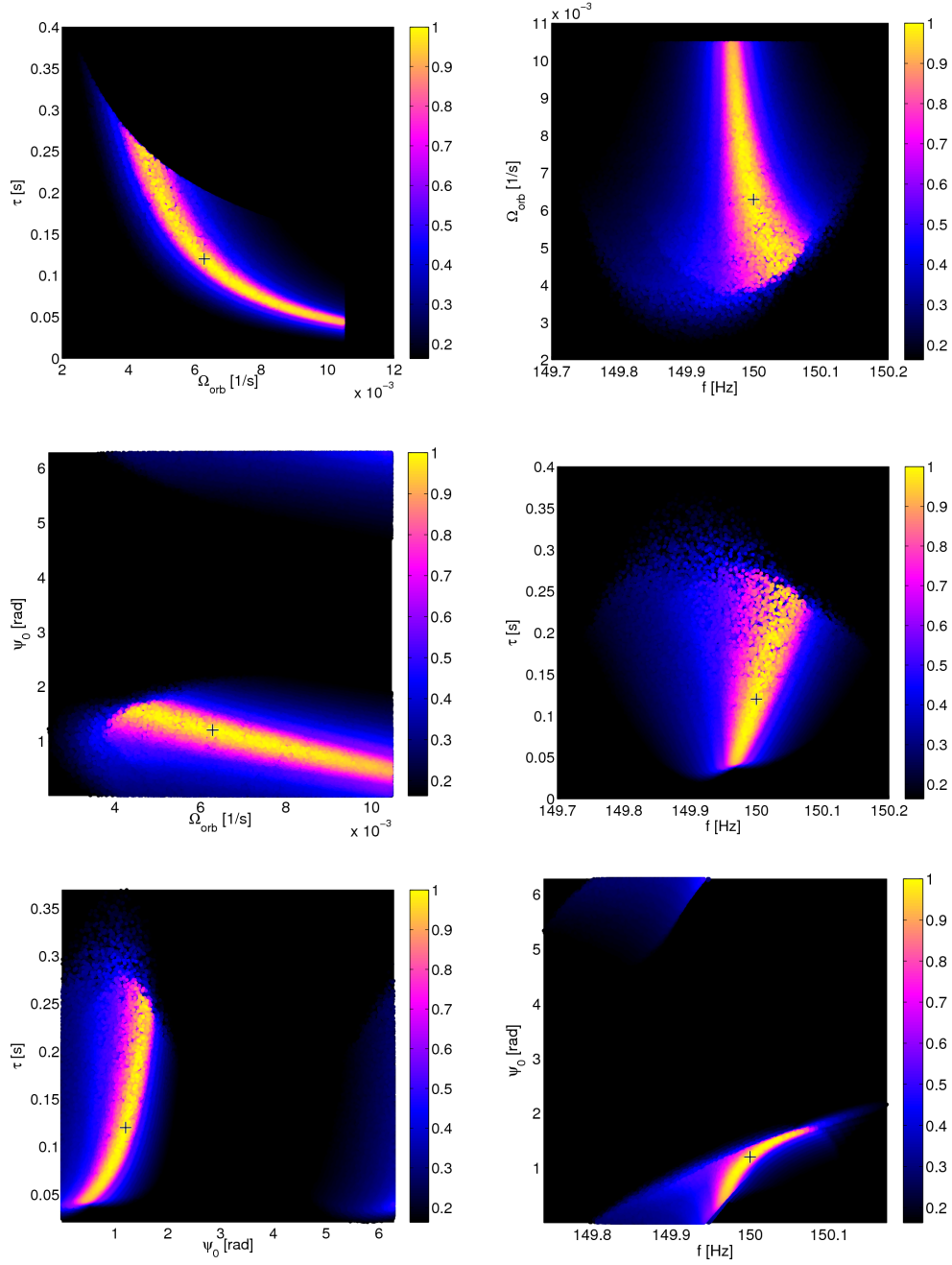


Figure B.1: Visualization of the global correlations among the physical signal parameters shown in different projections of the search parameter space, and in the absence of noise. The simulated signal shown has the parameters $f = 150$ Hz, $P_{\text{orb}} = 1000$ s, $\tau = 0.12$ s, $\psi_0 = 1.2$. In each plot the signal location is indicated by the black “+”. The color code corresponds to normalized power.

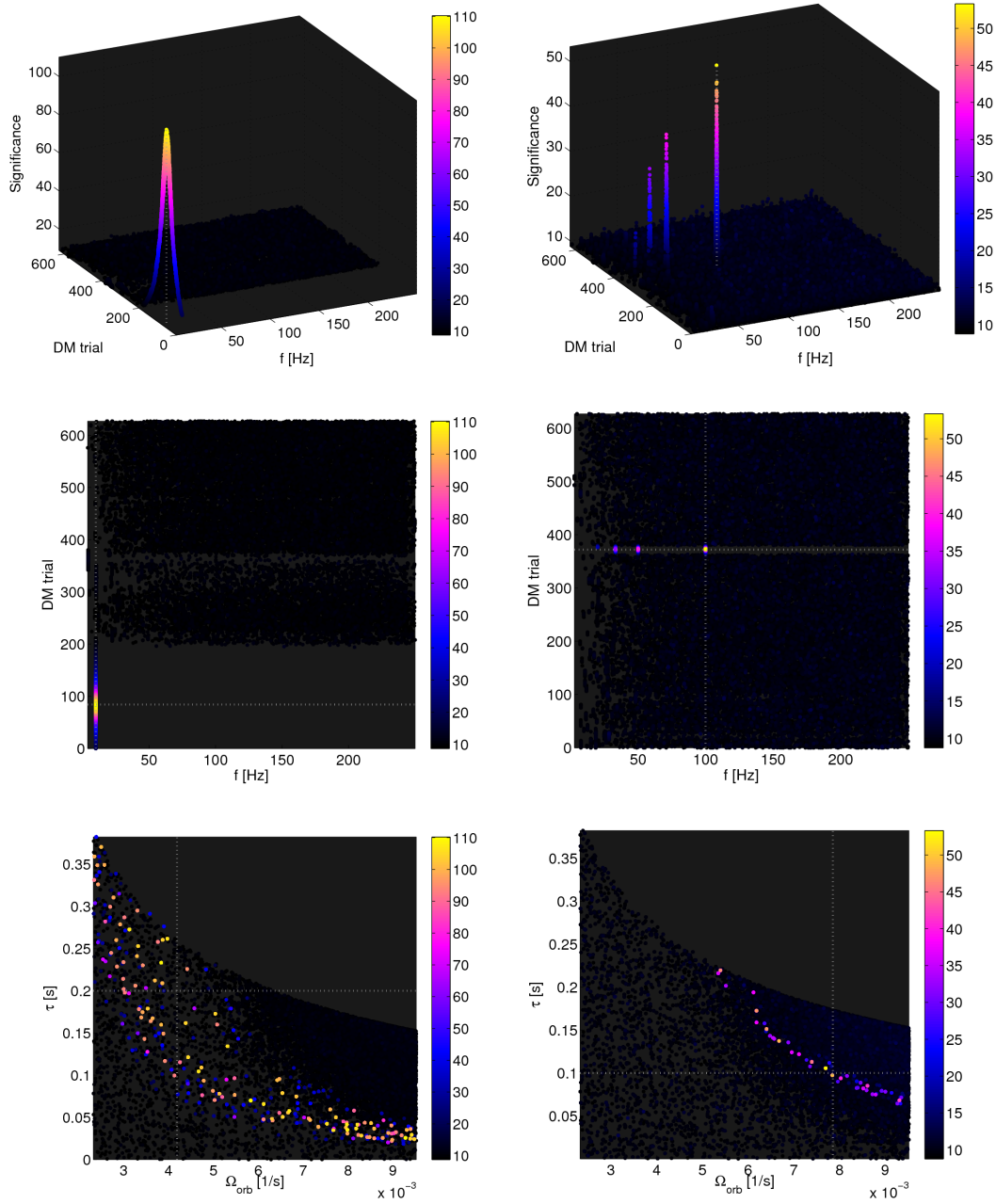


Figure B.2: Results of searching data sets containing simulated binary radio pulsar signals in different projections of the search parameter space. The color code corresponds to the statistical significance obtained for each template. The injected signal location is indicated by the white dotted lines. The left column refers to a simulated signal with parameters $f = 10$ Hz, $P_{\text{orb}} = 1500$ s, $\tau = 0.2$ s, $\psi_0 = 0$, and $\text{DM} = 50$ pc cm $^{-3}$. The right column refers to a simulated signal with parameters $f = 100$ Hz, $P_{\text{orb}} = 800$ s, $\tau = 0.1$ s, $\psi_0 = \pi$, and $\text{DM} = 230$ pc cm $^{-3}$. Both injected signals have 5% duty cycle and Gaussian pulse profile.

der development. Some of the improvements will result from using the enormous computing capabilities of GPUs (Graphics Processing Units). However, this requires some translation of the software code written for CPUs into GPU-suitable code. In addition, further code optimization is planned regarding the different platforms Einstein@Home volunteers use. Once these enhancements are in place, there is realistic promise that the project's data processing rate should surpass realtime processing speed.

References

- [1] B. Abbott et al. (LIGO Scientific Collaboration), “Einstein@Home search for periodic gravitational waves in LIGO S4 data”, *Physical Review D*, **79**, 022001, (2009).
- [2] B. Abbott et al. (LIGO Scientific Collaboration), “Einstein@Home search for periodic gravitational waves in early S5 LIGO data”, *Physical Review D*, **80**, 042003, (2009).
- [3] H. J. Pletsch, “Parameter-space correlations of the optimal statistic for continuous gravitational-wave detection”, *Physical Review D*, **78**, 102005, (2008).
- [4] H. J. Pletsch and B. Allen, “Exploiting global correlations to detect continuous gravitational waves”, *Physical Review Letters*, **103**, 181102, (2009).
- [5] P. Astone, M. Bassan, P. Bonifazi, K. M. Borkowski, R. J. Budzyński, A. Chincarini, E. Coccia, S. D’Antonio, M. D. P. Emilio, V. Fafone, S. Frasca, S. Foffa, G. Giordano, P. Jaranowski, W. Kondracki, A. Królak, M. Maggiore, A. Marini, Y. Minenkov, I. Modena, G. Modestino, A. Moleti, G. V. Pallottino, C. Palomba, R. Parodi, M. Pietka, G. Pizzella, H. J. Pletsch, L. Quintieri, F. Ricci, A. Rocchi, F. Ronga, R. Sturani, R. Terenzi, R. Vaccarone, and M. Visco, “All-sky search of NAUTILUS data”, *Classical Quantum Gravity*, **25**, 184012, (2008).
- [6] B. Knispel, B. Allen, O. Bock, J. M. Cordes, B. Machenschalk, C. Messenger, H. J. Pletsch, and R. Prix, “A new search for binary pulsars in Arecibo radio data with Einstein@Home”, *Poster presentation, 13th Gravitational Wave Data Analysis Workshop, San Juan, Puerto Rico*, (2009), <http://cgwa.phys.utb.edu/gwdaw13/>.
- [7] The the GNU General Public License version 2, <http://www.gnu.org/licenses/old-licenses/gpl-2.0.html>.

-
- [8] The LSC Algorithm Library (LAL) and the LSC Algorithm Library Applications (LALApps), <http://www.lsc-group.phys.uwm.edu/daswg/>.
- [9] The Einstein@Home CVS archive,
<http://www.gravity.phys.uwm.edu/cgi-bin/cvs/viewcvs.cgi/einsteinathome/?cvsroot=lscsoft>.
- [10] The LIGO Scientific Collaboration computational and data storage resources,
<https://www.lsc-group.phys.uwm.edu/lscdatagrid/>.
- [11] C. Aulbert and H. Fehrmann, “Gravitationswellensuche mit einem der weltweit größten Supercomputer”, *Tätigkeitsbericht 2008, Max-Planck-Gesellschaft*, (2008).
- [12] Einstein@Home was chosen as key project of the American Physical Society’s World Year of Physics 2005 activities, <http://einstein.phys.uwm.edu/>.
- [13] A. Einstein, “Die Feldgleichungen der Gravitation”, *Sitzungsberichte der Preussischen Akademie der Wissenschaften zu Berlin*, 844, (1915).
- [14] A. Einstein, “Näherungsweise Integration der Feldgleichungen der Gravitation”, *Sitzungsberichte der Preussischen Akademie der Wissenschaften zu Berlin*, 688, (1916).
- [15] A. Einstein, “Über Gravitationswellen”, *Sitzungsberichte der Preussischen Akademie der Wissenschaften zu Berlin*, 154, (1918).
- [16] R. A. Hulse and J. H. Taylor, “Discovery of a pulsar in a binary system”, *The Astrophysical Journal Letters*, **195**, L51, (1975).
- [17] J. H. Taylor and J. M. Weisberg, “A new test of general relativity - gravitational radiation and the binary pulsar PSR 1913+16”, *The Astrophysical Journal*, **253**, 908, (1982).
- [18] J. H. Taylor and J. M. Weisberg, “Further experimental tests of relativistic gravity using the binary pulsar PSR 1913+16”, *The Astrophysical Journal*, **345**, 434, (1989).

- [19] M. Burgay, N. D'Amico, A. Possenti, R. N. Manchester, A. G. Lyne, B. C. Joshi, M. A. McLaughlin, M. Kramer, J. M. Sarkissian, F. Camilo, V. Kalogera, C. Kim, and D. R. Lorimer, "An increased estimate of the merger rate of double neutron stars from observations of a highly relativistic system", *Nature*, **426**, 531, (2003).
- [20] M. Kramer, D. R. Lorimer, A. G. Lyne, M. McLaughlin, M. Burgay, N. D'Amico, A. Possenti, F. Camilo, P. C. C. Freire, B. C. Joshi, R. N. Manchester, J. Reynolds, J. Sarkissian, I. H. Stairs, and R. D. Ferdman, "Testing GR with the double pulsar: Recent results", in *Proceedings of 22nd Texas Symposium on Relativistic Astrophysics*, (Stanford University, Stanford, California, 2004).
- [21] S. Weinberg, *Gravitation and cosmology: Principles and applications of the general theory of relativity*, (Wiley, New York, 1972).
- [22] C. W. Misner, K. S. Thorne, and J. A. Wheeler, *Gravitation*, (W. H. Freeman and Company, San Francisco, 1973).
- [23] R. M. Wald, *General relativity*, (The University of Chicago Press, Chicago, 1984).
- [24] B. F. Schutz, *A first course in general relativity*, (Cambridge University Press, Cambridge, 1985).
- [25] K. S. Thorne, "Gravitational Radiation", in S. W. Hawking and W. Israel, eds., *300 Years of Gravitation*, Astronomical Society of the Pacific Conference Series, (Cambridge University Press, Cambridge, UK, 1987).
- [26] L. S. Finn, "Gravitational radiation sources and signatures", *XXVI SLAC Summer Institute on Particle Physics "Gravity: From the Hubble Length to the Planck Length"*, (1998).
- [27] É. É. Flanagan and S. A. Hughes, "The basics of gravitational wave theory", *New Journal of Physics*, **7**, 204, (2005).
- [28] K. D. Kokkotas, "Gravitational wave astronomy", *Reviews in Modern Astrophysics*, **20**, 140, (2008).

- [29] B. S. Sathyaprakash and B. F. Schutz, “Physics, astrophysics and cosmology with gravitational waves”, *Living Reviews in Relativity*, **12**(2), (2009), <http://www.livingreviews.org/lrr-2009-2/>.
- [30] D. Garfinkle, “Gauge invariance and the detection of gravitational radiation”, *American Journal of Physics*, **74**, 196, (2006).
- [31] P. R. Saulson, *Fundamentals of interferometric gravitational wave detectors*, (World Scientific Publishers, Singapore, 1994).
- [32] J. Hough and S. Rowan, “Laser interferometry for the detection of gravitational waves”, *Journal of Optics A: Pure and Applied Optics*, **7**, 257, (2005).
- [33] J. Hough and S. Rowan, “Gravitational wave detection by interferometry (ground and space)”, *Living Reviews in Relativity*, **3**(3), (2000), <http://www.livingreviews.org/lrr-2000-3/>.
- [34] W. E. Couch and E. T. Newman, “Generalized Lienard-Wiechert fields”, *Journal of Mathematical Physics*, **13**, 929, (1972).
- [35] J. Weber, “Detection and generation of gravitational waves”, *Physical Review*, **117**, 306, (1960).
- [36] J. Weber, “Evidence for Discovery of Gravitational Radiation”, *Physical Review Letters*, **22**, 1320, (1969).
- [37] J. Weber, “Anisotropy and Polarization in the Gravitational-Radiation Experiments”, *Physical Review Letters*, **25**, 180, (1970).
- [38] V. Fafone, “Resonant-mass detectors: status and perspectives”, *Classical Quantum Gravity*, **21**, 377, (2004).
- [39] M. E. et al. (ALLEGRO Collaboration), “The Allegro gravitational wave detector: data acquisition and analysis”, *Physical Review D*, **54**, 1264, (1996).
- [40] P. Astone et al., “Long-term operation of the Rome ”Explorer” cryogenic gravitational wave detector”, *Physical Review D*, **47**, 362, (1993).

- [41] A. P. et al. (ROG Collaboration), “The gravitational wave detector NAUTILUS operating at $T = 0.1$ K”, *Astroparticle Physics*, **7**, 231, (1997).
- [42] G. A. Prodi and Cothers, “Initial Operation of the Gravitational Wave Detector AURIGA”, in E. Coccia, G. Veneziano, and G. Pizzella, eds., *Second Edoardo Amaldi Conference on Gravitational Waves*, Edoardo Amaldi Foundation Series, vol. 4, p. 148, (World Scientific, Singapore; River Edge, U.S.A., 1998).
- [43] I. S. Heng, D. G. Blair, E. N. Ivanov, and M. E. Tobar, “Long term operation of a niobium resonant bar gravitational wave antenna”, *Phys. Lett. A*, **218**, 190, (1996).
- [44] A. de Waard, M. Bassan, Y. Benzaim, V. Fafone, J. Flokstra, G. Frossati, L. Gottardi, C. T. Herbschleb, A. Karbalai-Sadegh, K. Kuit, H. van der Mark, Y. Minenkov, J. B. R. Oonk, G. V. Pallottino, J. Pleikies, A. Rocchi, O. Usenko, and M. Visco, “Preparing for science run 1 of MiniGRAIL”, *Classical Quantum Gravity*, **23**, 79, (2006).
- [45] M. Bonaldi, M. Cerdonio, L. Conti, P. Falferi, P. Leaci, S. Odorizzi, G. Prodi, M. Saraceni, E. Serra, and J. Zendri, “Principles of wide bandwidth acoustic detectors and the single-mass dual detector”, *Physical Review D*, **74**, 022003, (2006).
- [46] F. A. E. Pirani, “On the Physical Significance of the Riemann Tensor”, *Acta Physica Polonica*, **15**, 389, (1956).
- [47] M. E. Gertsenshtein and V. I. Pustovoit, “On the Detection of Low-Frequency Gravitational Waves”, *Soviet Journal of Experimental and Theoretical Physics*, **16**, 433, (1963).
- [48] R. Weiss, “Electromagnetically Coupled Broadband Gravitational Antenna”, *Quarterly Progress Report of the Research Laboratory of Electronics of the MIT*, **105**, 54, (1972).
- [49] G. E. Moss, L. R. Miller, and R. L. Forward, “Photon-noise-limited laser transducer for gravitational antenna.”, *Applied Optics*, **10**, 2495, (1971).

- [50] R. L. Forward, “Wideband laser-interferometer gravitational-radiation experiment”, *Physical Review D*, **17**, 379, (1978).
- [51] B. F. Schutz and M. Tinto, “Antenna patterns of interferometric detectors of gravitational waves. I - Linearly polarized waves”, *Monthly Notices of the Royal Astronomical Society*, **224**, 131, (1987).
- [52] P. R. Saulson, “If light waves are stretched by gravitational waves, how can we use light as a ruler to detect gravitational waves?”, *American Journal of Physics*, **65**, 501, (1997).
- [53] L. S. Finn, “Response of interferometric gravitational wave detectors”, *Physical Review D*, **79**, 022002, (2009).
- [54] B. C. Barish and R. Weiss, “LIGO and the detection of gravitational waves”, *Physics Today*, **52**, 44, (1999).
- [55] P. Jaranowski, A. Królak, and B. F. Schutz, “Data analysis of gravitational-wave signals from spinning neutron stars. I. The signal and its detection”, *Physical Review D*, **58**, 063001, (1998).
- [56] M. Plissi, K. Strain, C. Torrie, N. Robertson, S. Killbourn, S. Rowan, S. Twyford, H. Ward, K. Skeldon, and J. Hough, “Aspects of the suspension system for GEO600”, *Rev. Sci. Instrum.*, **69**, 3055, (1998).
- [57] H. Vahlbruch, M. Mehmet, S. Chelkowski, B. Hage, A. Franzen, N. Lastzka, S. Gossler, K. Danzmann, and R. Schnabel, “Observation of squeezed light with 10-dB quantum-noise reduction”, *Physical Review Letters*, **100**, 033602, (2008).
- [58] A. Abramovici et al., “LIGO - The Laser Interferometer Gravitational-Wave Observatory”, *Science*, **256**, 325, (1992).
- [59] B. Caron et al., “The VIRGO Interferometer for Gravitational Wave Detection”, *Nuclear Physics B (Proc. Sup.)*, **54**, 167, (1997).
- [60] F. Acernese et al. (Virgo Collaboration), “Virgo status”, *Classical Quantum Gravity*, **25**, 184001, (2008).

-
- [61] B. Willke et al., “The GEO 600 gravitational wave detector”, *Classical Quantum Gravity*, **19**, 1377, (April 2002).
- [62] H. Grote et al. (LIGO Scientific Collaboration), “The status of GEO 600”, *Classical Quantum Gravity*, **25**, 114043, (2008).
- [63] M. Ando et al., “Stable Operation of a 300-m Laser Interferometer with Sufficient Sensitivity to Detect Gravitational-Wave Events within Our Galaxy”, *Physical Review Letters*, **86**(18), 3950, (2001).
- [64] R. W. P. Drever and Colleagues, “Gravitational wave detectors using laser interferometers and optical cavities”, in *Quantum optics, experimental gravity and measurement theory*, Proc. NATO ASI Quantum Optics and Experimental General Relativity, p. 503, (Plenum, New York, 1983).
- [65] B. J. Meers, “Recycling in laser-interferometric gravitational-wave detectors”, *Physical Review D*, **38**, 2317, (1988).
- [66] D. E. McClelland, “Status of the Australian consortium for interferometric gravitational astronomy”, in V. G. Gurzadyan, R. T. Jantzen, and R. Ruffini, eds., *The Ninth Marcel Grossmann Meeting*, p. 1864, (2002).
- [67] A. C. Searle, S. M. Scott, D. E. McClelland, and L. S. Finn, “Optimal location of a new interferometric gravitational wave observatory”, *Physical Review D*, **73**, 124014, (2006).
- [68] R. Adhikari, P. Fritschel, and S. Waldman, “Enhanced LIGO”, *LIGO Technical Note*, LIGO–T060156–01, (2006).
- [69] J. R. Smith (for the LIGO Scientific Collaboration), “The path to the enhanced and advanced LIGO gravitational-wave detectors”, *Classical Quantum Gravity*, **26**, 114013, (2009).
- [70] E. Gustafson, D. Shoemaker, K. Strain, and R. Weiss, “LSC White Paper on Detector Research and Development”, *LIGO Technical Note*, LIGO–T990080–00–D, (1999).

-
- [71] T. Creighton, “Advanced LIGO: sources and astrophysics”, *Classical Quantum Gravity*, **20**, 853, (2003).
- [72] R. Flaminio et al., “Advanced Virgo White Paper”, *Virgo Technical Document*, VIR–NOT–DIR–1390–304, (2005).
- [73] B. Willke et al., “The GEO-HF project”, *Classical Quantum Gravity*, **23**, S207, (2006).
- [74] K. Kuroda and the LCGT Collaboration, “The status of LCGT”, *Classical Quantum Gravity*, **23**, S215, (2006).
- [75] M. A. Papa, “Progress towards gravitational-wave astronomy”, *Classical Quantum Gravity*, **25**(11), 114009, (2008).
- [76] B. Abbott et al. (LIGO Scientific Collaboration), “Analysis of LIGO data for gravitational waves from binary neutron stars”, *Physical Review D*, **69**, 122001, (2004).
- [77] B. Abbott et al. (LIGO Scientific Collaboration), “Search for gravitational waves from galactic and extragalactic binary neutron stars”, *Physical Review D*, **72**, 082001, (2005).
- [78] B. Abbott et al. (LIGO Scientific Collaboration), “Search for gravitational waves from primordial black hole binary coalescences in the galactic halo”, *Physical Review D*, **72**, 082002, (2005).
- [79] B. Abbott et al. (LIGO Scientific Collaboration), “Joint LIGO and TAMA300 search for gravitational waves from inspiralling neutron star binaries”, *Physical Review D*, **73**, 102002, (2006).
- [80] B. Abbott et al. (LIGO Scientific Collaboration), “Search for gravitational waves from binary black hole inspirals in LIGO data”, *Physical Review D*, **73**, 062001, (2006).
- [81] B. Abbott et al. (LIGO Scientific Collaboration), “Search for gravitational waves from binary inspirals in S3 and S4 LIGO data”, *Physical Review D*, **77**, 062002, (2008).

- [82] B. Abbott et al. (LIGO Scientific Collaboration), “Search of S3 LIGO data for gravitational wave signals from spinning black hole and neutron star binary inspirals”, *Physical Review D*, **78**, 042002, (2008).
- [83] B. Abbott et al. (LIGO Scientific Collaboration), “Search for gravitational waves from low mass binary coalescences in the first year of LIGO’s S5 data”, *Physical Review D*, **79**, 122001, (2009).
- [84] C. Cutler, T. A. Apostolatos, L. Bildsten, L. S. Finn, E. E. Flanagan, D. Kennefick, D. M. Markovic, A. Ori, E. Poisson, and G. J. Sussman, “The last three minutes - Issues in gravitational-wave measurements of coalescing compact binaries”, *Physical Review Letters*, **70**, 2984, (1993).
- [85] M. Shibata, K. Taniguchi, and K. Uryū, “Merger of binary neutron stars with realistic equations of state in full general relativity”, *Physical Review D*, **71**, 084021, (2005).
- [86] B. F. Schutz, “Determining the Hubble constant from gravitational wave observations”, *Nature*, **323**, 310, (1986).
- [87] D. E. Holz and S. A. Hughes, “Using gravitational-wave standard sirens”, *The Astrophysical Journal*, **629**, 15, (2005).
- [88] N. Dalal, D. E. Holz, S. A. Hughes, and B. Jain, “Short GRB and binary black hole standard sirens as a probe of dark energy”, *Physical Review D*, **74**, 063006, (2006).
- [89] C. L. Fryer and K. C. New, “Gravitational waves from gravitational collapse”, *Living Reviews in Relativity*, **6**(2), (2003), <http://www.livingreviews.org/lrr-2003-2/>.
- [90] T. Zwerger and E. Mueller, “Dynamics and gravitational wave signature of axisymmetric rotational core collapse.”, *Astronomy and Astrophysics*, **320**, 209, (1997).
- [91] H. Dimmelmeier, J. A. Font, and E. Müller, “Relativistic simulations of rotational core collapse II. Collapse dynamics and gravitational radiation”, *Astronomy and Astrophysics*, **393**, 523, (2002).

- [92] C. D. Ott, A. Burrows, E. Livne, and R. Walder, “Gravitational waves from axisymmetric, rotating stellar core collapse”, *The Astrophysical Journal*, **600**, 834, (2004).
- [93] C. D. Ott, A. Burrows, L. Dessart, and E. Livne, “A new mechanism for gravitational-wave emission in core-collapse supernovae”, *Physical Review Letters*, **96**, 201102, (2006).
- [94] B. Abbott et al. (“LIGO Scientific Collaboration”), “First upper limits from LIGO on gravitational wave bursts”, *Physical Review D*, **69**, 102001, (2004).
- [95] B. Abbott et al. (LIGO Scientific Collaboration), “Search for gravitational waves associated with the gamma ray burst GRB030329 using the LIGO detectors”, *Physical Review D*, **72**, 042002, (2005).
- [96] B. Abbott et al. (LIGO Scientific Collaboration), “Upper limits on gravitational wave bursts in LIGO’s second science run”, *Physical Review D*, **72**, 062001, (2005).
- [97] B. Abbott et al. (LIGO Scientific Collaboration), “Upper limits from the LIGO and TAMA detectors on the rate of gravitational-wave bursts”, *Physical Review D*, **72**, 122004, (2005).
- [98] B. Abbott et al. (LIGO Scientific Collaboration), “Search for gravitational-wave bursts in LIGO’s third science run”, *Classical Quantum Gravity*, **23**, S29, (2006).
- [99] L. Baggio et al. (LIGO Scientific Collaboration), “A joint search for gravitational wave bursts with AURIGA and LIGO”, *Classical Quantum Gravity*, **25**, 095004, (2008).
- [100] B. Abbott et al. (LIGO Scientific Collaboration), “Search for gravitational wave radiation associated with the pulsating tail of the SGR 1806-20 hyperflare of 27 December 2004 using LIGO”, *Physical Review D*, **76**, 062003, (2007).
- [101] B. Abbott et al. (LIGO Scientific Collaboration), “Search for gravitational wave radiation associated with the pulsating tail of the SGR 1806-20 hyperflare of 27 December 2004 using LIGO”, *Physical Review D*, **76**, 062003, (2007).

- [102] B. Abbott et al. (LIGO Scientific Collaboration), “Search for gravitational-wave bursts in LIGO data from the fourth LSC science run”, *Classical Quantum Gravity*, **24**, 5343, (2007).
- [103] B. Abbott et al. (LIGO Scientific Collaboration), “Search for gravitational waves associated with 39 gamma-ray bursts using data from the second, third, and fourth LIGO runs”, *Physical Review D*, **77**, 062004, (2008).
- [104] B. Abbott et al. (LIGO Scientific Collaboration), “First joint search for gravitational-wave bursts in LIGO and GEO 600 data”, *Classical Quantum Gravity*, **25**, 245008, (2008).
- [105] B. Abbott et al. (LIGO Scientific Collaboration), “Search for gravitational-wave bursts from soft gamma repeaters”, *Physical Review Letters*, **101**, 211102, (2008).
- [106] B. Allen, “The stochastic gravity-wave background: Sources and detection”, in J. A. Miralles, J. A. Morales, and D. Saez, eds., *Some Topics on General Relativity and Gravitational Radiation*, p. 3, (1997).
- [107] R. A. Battye and E. P. S. Shellard, “Primordial gravitational waves : a probe of the early universe”, *Submitted to the Gravity Research Foundation essay competition 1996*, arXiv:astro-ph/9604059, (1996).
- [108] T. Regimbau and J. A. de Freitas Pacheco, “Cosmic background of gravitational waves from rotating neutron stars”, *Astronomy and Astrophysics*, **376**, 381, (2001).
- [109] T. Regimbau and B. Chauvineau, “A stochastic background from extra-galactic double neutron stars”, *Classical Quantum Gravity*, **24**, 627, (2007).
- [110] D. M. Coward, R. R. Burman, and D. G. Blair, “Simulating a stochastic background of gravitational waves from neutron star formation at cosmological distances”, *Monthly Notices of the Royal Astronomical Society*, **329**, 411, (2002).
- [111] A. Cooray, “Gravitational-wave background of neutron star-white dwarf binaries”, *Monthly Notices of the Royal Astronomical Society*, **354**, 25, (2004).

- [112] B. Abbott et al. (LIGO Scientific Collaboration), “Upper limits on a stochastic background of gravitational waves”, *Physical Review Letters*, **95**, 211101, (2005).
- [113] B. Abbott et al. (LIGO Scientific Collaboration and ALLEGRO Collaboration), “First cross-correlation analysis of interferometric and resonant-bar gravitational-wave data for stochastic backgrounds”, *Physical Review D*, **76**, 022001, (2007).
- [114] B. Abbott et al. (LIGO Scientific Collaboration), “Upper limit map of a background of gravitational waves”, *Physical Review D*, **76**, 082003, (2007).
- [115] B. Abbott et al. (LIGO Scientific Collaboration), “Searching for stochastic background of gravitational waves with LIGO”, *The Astrophysical Journal*, **77**, 062002, (2008).
- [116] C. W. Helstrom, *Statistical Theory of Signal Detection*, International Series of Monographs in Electronics and Instrumentation, vol. 9, (Pergamon Press, Oxford; New York, 1968), 2nd edition.
- [117] P. Jaranowski and A. Królak, “Gravitational-Wave Data Analysis. Formalism and Sample Applications: The Gaussian Case”, *Living Reviews in Relativity*, **8**(3), (2005), <http://www.livingreviews.org/lrr-2005-3/>.
- [118] K. Danzmann and A. Rüdiger, “LISA technology; concept, status, prospects”, *Classical Quantum Gravity*, **20**(10), S1, (2003).
- [119] T. Prince, “LISA: The Laser Interferometer Space Antenna”, in *Bulletin of the American Astronomical Society*, vol. 35, p. 751, (2003).
- [120] S. A. Hughes, “A brief survey of LISA sources and science”, in S. M. Merkowitz and J. C. Livas, eds., *Laser Interferometer Space Antenna: 6th International LISA Symposium*, American Institute of Physics Conference Series, vol. 873, p. 13, (2006).
- [121] C. Cutler and K. S. Thorne, “An overview of gravitational-wave sources”, in *Proceedings of the 16th International Conference on General Relativity and Gravitation*, p. 72, (World Scientific, New Jersey, USA, 2002).

- [122] B. Abbott et al. (LIGO Scientific Collaboration), “Setting upper limits on the strength of periodic gravitational waves from PSR J1939+2134 using the first science data from the GEO 600 and LIGO detectors”, *Physical Review D*, **69**, 082004, (2004).
- [123] B. J. Owen, “Detectability of periodic gravitational waves by initial interferometers”, *Classical Quantum Gravity*, **23**, S1, (2006).
- [124] B. Abbott et al. (LIGO Scientific Collaboration), “Coherent searches for periodic gravitational waves from unknown isolated sources and Scorpius X-1: results from the second LIGO science run”, *Physical Review D*, **76**, 082001, (2007).
- [125] R. Prix, “Gravitational Waves from Spinning Neutron Stars”, in W. Becker, ed., *Neutron stars and pulsars*, Astrophysics and Space Science Library, vol. 357, p. 651, (Springer Berlin Heidelberg, Germany, 2009).
- [126] L. Bildsten, “Gravitational radiation and rotation of accreting neutron stars”, *The Astrophysical Journal*, **501**, L89, (1998).
- [127] G. Ushomirsky, C. Cutler, and L. Bildsten, “Deformations of accreting neutron star crusts and gravitational wave emission”, *Monthly Notices of the Royal Astronomical Society*, **319**, 902, (2000).
- [128] C. Cutler, “Gravitational waves from neutron stars with large toroidal B-fields”, *Physical Review D*, **66**, 084025, (2002).
- [129] A. Melatos and D. J. B. Payne, “Gravitational radiation from an accreting millisecond pulsar with a magnetically confined mountain”, *The Astrophysical Journal*, **623**, 1044, (2005).
- [130] B. J. Owen, “Maximum elastic deformations of compact stars with exotic equations of state”, *Physical Review Letters*, **95**, 211101, (2005).
- [131] D. I. Jones and N. Andersson, “Gravitational waves from freely precessing neutron stars”, *Monthly Notices of the Royal Astronomical Society*, **331**, 203, (2002).
- [132] C. V. D. Broeck, “The gravitational wave spectrum of non-axisymmetric, freely precessing neutron stars”, *Classical Quantum Gravity*, **22**, 1825, (2005).

- [133] B. J. Owen, L. Lindblom, C. Cutler, B. F. Schutz, A. Vecchio, and N. Andersson, “Gravitational waves from hot young rapidly rotating neutron stars”, *Physical Review D*, **58**, 084020, (1998).
- [134] N. Andersson, K. D. Kokkotas, and N. Stergioulas, “On the relevance of the r-mode instability for accreting neutron stars and white dwarfs”, *The Astrophysical Journal*, **516**, 307, (1999).
- [135] C. Cutler, G. Ushomirsky, and B. Link, “The crustal rigidity of a neutron star and implications for PSR B1828-11 and other precession candidates”, *The Astrophysical Journal*, **588**, 975, (2003).
- [136] C. J. Horowitz and K. Kadau, “Breaking strain of neutron star crust and gravitational waves”, *Physical Review Letters*, **102**, 191102, (2009).
- [137] D. J. B. Payne and A. Melatos, “Frequency Spectrum of Gravitational Radiation from Global Hydromagnetic Oscillations of a Magnetically Confined Mountain on an Accreting Neutron Star”, *The Astrophysical Journal*, **641**, 471, (2006).
- [138] M. Zimmermann and E. Szedenits, Jr., “Gravitational waves from rotating and precessing rigid bodies - Simple models and applications to pulsars”, *Physical Review D*, **20**, 351, (1979).
- [139] C. Cutler and D. I. Jones, “Gravitational wave damping of neutron star wobble”, *Physical Review D*, **63**, 024002, (2001).
- [140] N. Andersson, “Gravitational waves from instabilities in relativistic stars”, *Classical Quantum Gravity*, **20**, 105, (2003).
- [141] N. Stergioulas, “Rotating Stars in Relativity”, *Living Reviews in Relativity*, **6**(3), (2003), <http://www.livingreviews.org/lrr-2003-3/>.
- [142] N. Andersson, “A New Class of Unstable Modes of Rotating Relativistic Stars”, *The Astrophysical Journal*, **502**, 708, (1998).
- [143] J. L. Friedman and S. M. Morsink, “Axial Instability of Rotating Relativistic Stars”, *The Astrophysical Journal*, **502**, 714, (1998).

- [144] B. J. Owen, L. Lindblom, C. Cutler, B. F. Schutz, A. Vecchio, and N. Andersson, “Gravitational waves from hot young rapidly rotating neutron stars”, *Physical Review D*, **58**, 084020, (1998).
- [145] N. Andersson, K. D. Kokkotas, and N. Stergioulas, “On the Relevance of the R-Mode Instability for Accreting Neutron Stars and White Dwarfs”, *The Astrophysical Journal*, **516**, 307, (1999).
- [146] R. V. Wagoner, “Conditions for Steady Gravitational Radiation from Accreting Neutron Stars”, *The Astrophysical Journal Letters*, **578**, L63, (2002).
- [147] N. Andersson, D. I. Jones, and K. D. Kokkotas, “Strange stars as persistent sources of gravitational waves”, *Monthly Notices of the Royal Astronomical Society*, **337**, 1224, (2002).
- [148] N. Andersson, K. D. Kokkotas, and V. Ferrari, “The R-Mode Instability in Rotating Neutron Stars”, *International Journal of Modern Physics D*, **10**, 381, (2001).
- [149] R. N. Manchester, G. B. Hobbs, A. Teoh, and M. Hobbs, “The Australia Telescope National Facility Pulsar Catalogue”, *The Astrophysical Journal*, **129**, 1993, (2005), <http://www.atnf.csiro.au/research/pulsar/psrcat/>.
- [150] B. J. Owen, “Probing neutron stars with gravitational waves”, *LIGO Technical Document*, T0900053–v1, (2009).
- [151] B. Knispel and B. Allen, “Blandford’s argument: The strongest continuous gravitational wave signal”, *Physical Review D*, **78**, 044031, (2008).
- [152] B. Abbott et al. (LIGO Scientific Collaboration), “Limits on Gravitational-Wave Emission from Selected Pulsars Using LIGO Data”, *Physical Review Letters*, **94**, 181103, (2005).
- [153] R. J. Dupuis and G. Woan, “Bayesian estimation of pulsar parameters from gravitational wave data”, *Physical Review D*, **72**, 102002, (2005).
- [154] B. Abbott et al. (LIGO Scientific Collaboration), “Upper limits on gravitational wave emission from 78 radio pulsars”, *Physical Review D*, **76**, 042001, (2007).

- [155] B. Abbott et al. (LIGO Scientific Collaboration), “Beating the spin-down limit on gravitational wave emission from the Crab pulsar”, *The Astrophysical Journal Letters*, **683**, L45–L49, (2008).
- [156] K. Wette, B. J. Owen, B. Allen, M. Ashley, J. Betzwieser, N. Christensen, T. D. Creighton, V. Dergachev, I. Gholami, E. Goetz, R. Gustafson, D. Hammer, D. I. Jones, B. Krishnan, M. Landry, B. Machenschalk, D. E. McClelland, G. Mendell, C. J. Messenger, M. A. Papa, P. Patel, M. Pitkin, H. J. Pletsch, R. Prix, K. Riles, L. Sancho de la Jordana, S. M. Scott, A. M. Sintes, M. Trias, J. T. Whelan, and G. Woan, “Searching for gravitational waves from Cassiopeia A with LIGO”, *Classical Quantum Gravity*, **25**, 235011, (2008).
- [157] B. Abbott et al. (LIGO Scientific Collaboration), “First all-sky upper limits from LIGO on the strength of periodic gravitational waves using the Hough transform”, *Physical Review D*, **72**, 102004, (2005).
- [158] B. Abbott et al. (LIGO Scientific Collaboration), “All-sky search for periodic gravitational waves in LIGO S4 data”, *Physical Review D*, **77**, 022001, (2008).
- [159] B. Abbott et al. (LIGO Scientific Collaboration), “All-sky LIGO Search for Periodic Gravitational Waves in the Early S5 Data”, *Physical Review Letters*, **102**, 111102, (2009).
- [160] P. R. Brady, T. Creighton, C. Cutler, and B. F. Schutz, “Searching for periodic sources with LIGO”, *Physical Review D*, **57**, 2101, (1998).
- [161] B. F. Schutz and M. Alessandra Papa, “End-to-end algorithm for hierarchical area searches for long-duration GW sources for GEO 600”, in *Proceedings of Moriond meeting “Gravitational Waves and Experimental Gravity”*, p. 199, (Savoie, France, 1999).
- [162] P. R. Brady and T. Creighton, “Searching for periodic sources with LIGO. II. Hierarchical searches”, *Physical Review D*, **61**, 082001, (2000).
- [163] M. A. Papa, B. F. Schutz, and A. M. Sintes, “Searching for continuous gravitational wave signals: The hierarchical Hough transform algorithm”, in V. Ferrari,

- J. C. Miller, and L. Rezzolla, eds., *ICTP Lecture Notes Series Vol. III*, p. 431, (Trieste, Italy, 2000).
- [164] B. Krishnan, A. M. Sintes, M. A. Papa, B. F. Schutz, S. Frasca, and C. Palomba, “Hough transform search”, *Physical Review D*, **70**, 082001, (2004).
- [165] C. Cutler, I. Gholami, and B. Krishnan, “Improved stack-slide searches for gravitational-wave pulsars”, *Physical Review D*, **72**, 042004, (2005).
- [166] N. Seto, “Gravitational wave astrometry for rapidly rotating neutron stars and estimation of their distances”, *Physical Review D*, **71**, 123002, (2005).
- [167] D. Sigg et al. (for the LIGO Scientific Collaboration), “Status of the LIGO detectors”, *Classical Quantum Gravity*, **23**, S51, (2006).
- [168] B. Abbott et al. (LIGO Scientific Collaboration), “Search for gravitational waves associated with 39 gamma-ray bursts Using data from the second, third, and fourth LIGO runs”, *Physical Review D*, **77**, 062004, (2008).
- [169] B. Abbott et al. (LIGO Scientific Collaboration), “Search for gravitational waves from binary inspirals in S3 and S4 LIGO data”, *Physical Review D*, **77**, 062002, (2008).
- [170] J. W. Cooley and J. W. Tukey, “An Algorithm for the Machine Calculation of Complex Fourier Series”, *Mathematics of Computation*, **19**, 297, (1965).
- [171] C. Rader and N. Brenner, “A new principle for fast Fourier transformation”, *Acoustics, Speech and Signal Processing, IEEE Transactions on*, **24**, 264, (1976).
- [172] P. Jaranowski and A. Królak, “Data analysis of gravitational-wave signals from spinning neutron stars. III. Detection statistics and computational requirements”, *Physical Review D*, **61**, 062001, (2000).
- [173] R. Balasubramanian, B. S. Sathyaprakash, and S. V. Dhurandhar, “Gravitational waves from coalescing binaries: Detection strategies and Monte Carlo estimation of parameters”, *Physical Review D*, **53**, 3033, (1996).
- [174] B. J. Owen, “Search templates for gravitational waves from inspiraling binaries: Choice of template spacing”, *Physical Review D*, **53**, 6749, (1996).

- [175] D. P. Anderson, J. Cobb, E. Korpela, M. Lebofsky, and D. Werthimer, “SETI@home: An experiment in public-resource computing”, *Commun. ACM*, **45**, 56, (2002).
- [176] S. M. Larson, C. D. Snow, M. Shirts, and V. S. Pande, “Folding@Home and Genome@Home: Using distributed computing to tackle previously intractable problems in computational biology”, in R. Grant, ed., *Computational Genomics*. Horizon Press, (2002).
- [177] G. Mendell, “Short-Time Fourier Transform Specification”, *LIGO Technical Document*, T020043–00–W, (2002).
- [178] X. Siemens, B. Allen, J. Creighton, M. Hewitson, and M. Landry, “Making $h(t)$ for LIGO”, *Classical Quantum Gravity*, **21**, S1723, (2004).
- [179] A. Dietz et al. (for the LIGO Scientific Collaboration), “Calibration of the LIGO Detectors for S4”, *LIGO Technical Document*, T050262, (2005).
- [180] Einstein@Home is built upon the BOINC (Berkeley Open Infrastructure for Network Computing) architecture, <http://boinc.berkeley.edu/>.
- [181] D. P. Anderson, “BOINC: A System for Public-Resource Computing and Storage”, in *GRID '04: Proceedings of the Fifth IEEE/ACM International Workshop on Grid Computing*, p. 4, (IEEE Computer Society, Washington DC, USA, 2004).
- [182] D. P. Anderson, C. Christensen, and B. Allen, “Grid resource management - Designing a runtime system for volunteer computing”, in *SC '06: Proceedings of the 2006 ACM/IEEE conference on Supercomputing*, p. 126, (Association for Computing Machinery, New York, NY, USA, 2006).
- [183] B. Krishnan, B. J. Owen, R. Prix, and A. M. Sintes, “Searching for isolated pulsars using Einstein@Home”, *LIGO Technical Document*, T080340, (2008).
- [184] J. P. Snyder, *Flattening the earth: Two thousand years of map projections*, (University of Chicago Press, Chicago, 1993).

- [185] P. Astone, K. M. Borkowski, P. Jaranowski, and A. Królak, “Data analysis of gravitational-wave signals from spinning neutron stars. IV. An all-sky search”, *Physical Review D*, **65**, 042003, (2002).
- [186] S. J. Waldman et al. (LIGO Science Collaboration), “Status of LIGO at the start of the fifth science run”, *Classical Quantum Gravity*, **23**, S653, (2006).
- [187] R. Prix, “Search for continuous gravitational waves: Metric of the multidetector \mathcal{F} -statistic”, *Physical Review D*, **75**, 023004, (2007).
- [188] R. Prix and Y. Itoh, “Global parameter-space correlations of coherent searches for continuous gravitational waves”, *Classical Quantum Gravity*, **22**, S1003, (2005).
- [189] P. Jaranowski and A. Królak, “Data analysis of gravitational-wave signals from spinning neutron stars. II. Accuracy of estimation of parameters”, *Physical Review D*, **59**, 063003, (1999).
- [190] K. Jotania, S. R. Valluri, and S. V. Dhurandhar, “A study of the gravitational wave form from pulsars”, *Astronomy and Astrophysics*, **306**, 317, (1996).
- [191] C. Palomba, “Simulation of a population of isolated neutron stars evolving through the emission of gravitational waves”, *Monthly Notices of the Royal Astronomical Society*, **359**, 1150, (2005).
- [192] P. Astone, S. Frasca, and M. A. Papa, in S. Meshkov, ed., *Proceedings of the Aspen Winter Conference on Gravitational Waves and their Detection*, (1997).
- [193] Advanced LIGO, <http://www.ligo.caltech.edu/advLIGO/>.
- [194] E. Mauceli, M. P. McHugh, W. O. Hamilton, W. W. Johnson, and A. Morse, “Search for periodic gravitational radiation with the ALLEGRO gravitational wave detector”, arXiv:gr-qc/0007023, (2000).
- [195] P. Astone et al., “Search for periodic gravitational wave sources with the Explorer detector”, *Physical Review D*, **65**, 022001, (2001).
- [196] P. Astone et al., “All-sky upper limit for gravitational radiation from spinning neutron stars”, *Classical Quantum Gravity*, **20**, 665, (2003).

- [197] P. Astone et al., “An all-sky search of EXPLORER data”, *Classical Quantum Gravity*, **22**, 1243, (2005).
- [198] J. H. Conway and N. J. A. Sloane, *Sphere Packings, Lattices and Groups*, (Springer-Verlag, New York, USA, 1993).
- [199] R. Prix, “Template-based searches for gravitational waves: efficient lattice covering of flat parameter spaces”, *Class. Quant. Grav.*, **24**, S481, (2007).
- [200] B. F. Schutz, “Data Processing Analysis and Storage for Interferometric Antennas”, in D. G. Blair, ed., *The Detection of Gravitational Waves*, p. 406, (1991).
- [201] B. Knispel, B. Allen, O. Bock, J. M. Cordes, B. Machenschalk, C. Messenger, H. J. Pletsch, and R. Prix, “The search for tight binary radio pulsars in Arecibo radio data with Einstein@Home”, *Poster presentation, 8th Edoardo Amaldi Conference on Gravitational Waves, New York City, USA*, (2009), <http://www.amaldi8.org/>.
- [202] “The Einstein@Home Arecibo Radio Pulsar search, Project Background”, (2009), <http://einstein.phys.uwm.edu/radiopulsar/html/>.
- [203] H. M. Johnston and S. R. Kulkarni, “On the detectability of pulsars in close binary systems”, *The Astrophysical Journal*, **368**, 504, (1991).
- [204] S. M. Ransom, J. M. Cordes, and S. S. Eikenberry, “A new search technique for short orbital period binary pulsars”, *The Astrophysical Journal*, **589**, 911, (2003).
- [205] C. Messenger, R. Prix, and M. A. Papa, “Random template banks and relaxed lattice coverings”, *Physical Review D*, **79**, 104017, (2009).
- [206] J. M. Cordes et al., “Arecibo Pulsar Survey Using ALFA. I. Survey Strategy and First Discoveries”, *The Astrophysical Journal*, **637**, 446, (2006).
- [207] A. Hewish, S. J. Bell, J. D. H. Pilkington, P. F. Scott, and R. A. Collins, “Observation of a Rapidly Pulsating Radio Source”, *Nature*, **217**, 709, (1968).

Acknowledgments

Gravitational-wave science has never before been at a point so close to the first direct observation. I have enjoyed being part of and contributing to this exciting and rapidly developing field in a world-leading research group at the AEI.

Therefore, I am most indebted to my supervisor, Bruce Allen. His constant encouragement, support, and advice have stimulated my work and helped me to move forward, as well as his genuine concern for my development as a scientist, which I am particularly grateful for. I also appreciate the great deal of freedom I enjoyed in pursuing my research and the very creative and positive atmosphere of our scientific discussions.

I also would like to thank Maria Alessandra Papa for her valuable support and many scientifically beneficial conversations, which led to improve my work.

I am also grateful to Reinhard Prix for providing critical insights into my work, immensely helpful suggestions and the numerous enlightening discussions.

I also thank Chris Messenger for sharing his valuable advice and many helpful suggestions, which were of great benefit for this work.

Thanks should also be extended to the members of the LSC Continuous Waves Working Group, including the chairs Keith Riles and Graham Woan, for the help and advice given to me. For their efforts of carefully reviewing the work of the Einstein@Home analyses, Peter Shawhan and Teviet Creighton earn great appreciation. I also extend my gratitude to Bernard Schutz for co-refereeing this dissertation.

Many thanks are due to the great support and care of the ATLAS cluster administration duo, Carsten Aulbert and Henning Fehrmann.

For support, inspiration and friendship, I also thank Benjamin Knispel, Stefanos Giampanis, Christian Röver, Bernd Machenschalk, Oliver Bock, Andrzej Królak, Badri Krishnan, Alicia Sintés, Ajith Parameswaran, and many others.

I am deeply grateful to my parents Gertrud and Karl-Heinz, my brother Stephan and my grandmother Elisabeth for their constant support and encouragement, and especially to Christina for her love. I am proud to share this with you all.

Curriculum Vitae

Holger Johannes Pletsch

Date of Birth	August 16, 1982
Place of Birth	Saarburg, Germany
2007 – 2009	International Max Planck Research School on Gravitational Wave Astronomy (doctoral studies), Max-Planck-Institut für Gravitationsphysik (Albert-Einstein-Institut) and Gottfried Wilhelm Leibniz Universität Hannover, Germany
2005 – 2006	Master of Science in Physics, University of Wisconsin – Milwaukee, United States of America
2003 – 2005	Diploma studies of Physics, Technische Universität Kaiserslautern, Germany
2002 – 2003	Distance studies of Physics and Mathematics (FiPS and FiMS), Technische Universität Kaiserslautern, Germany
2002 – 2003	Civilian Service
2002	Abitur, Gymnasium Saarburg

Publications

H. J. Pletsch and B. Allen, “Exploiting global correlations to detect continuous gravitational waves”, *Physical Review Letters*, **103**, 181102, (2009).

<http://arxiv.org/abs/0906.0023/>

B. Abbott, ... , H. J. Pletsch, ... , J. Zweizig (The LIGO Scientific Collaboration), “Einstein@Home search for periodic gravitational waves in early S5 LIGO data”, *Physical Review D*, **80**, 042003, (2009).

<http://arxiv.org/abs/0905.1705/>

B. Abbott, ... , H. J. Pletsch, ... , J. Zweizig (The LIGO Scientific Collaboration and the Virgo Collaboration), “An upper limit on the stochastic gravitational-wave background of cosmological origin”, *Nature*, **460**, 990, (2009).

B. Abbott, ... , H. J. Pletsch, ... , J. Zweizig (The LIGO Scientific Collaboration), “Stacked search for gravitational waves from the 2006 SGR 1900+14 storm”, *Astrophysical Journal Letters*, **701**, L68, (2009).

<http://arxiv.org/abs/0905.0005/>

B. Abbott, ... , H. J. Pletsch, ... , J. Zweizig (The LIGO Scientific Collaboration), “Search for gravitational waves from low mass binary coalescences in the first year of LIGO’s S5 data”, *Physical Review D*, **79**, 122001, (2009).

<http://arxiv.org/abs/0901.0302/>

B. Abbott, ... , H. J. Pletsch, ... , J. Zweizig (The LIGO Scientific Collaboration), “All-Sky LIGO Search for Periodic Gravitational Waves in the Early Fifth-Science-Run Data”, *Physical Review Letters*, **102**, 111102, (2009).

<http://arxiv.org/abs/0810.0283/>

P. Astone, M. Bassan, P. Bonifazi, K. M. Borkowski, R. J. Budzynski, A. Chincarini, E. Coccia, S. D'Antonio, M. Di Paolo Emilio, V. Fafone, S. Frasca, S. Foffa, G. Giordano, P. Jaranowski, W. Kondracki, A. Krolak, M. Maggiore, A. Marini, Y. Minenkov, I. Modena, G. Modestino, A. Moleti, G. V. Pallottino, C. Palomba, R. Parodi, M. Pietka, G. Pizzella, H. J. Pletsch, L. Quintieri, F. Ricci, A. Rocchi, F. Ronga, R. Sturani, R. Terenzi, R. Vaccarone, and M. Visco, "All-sky search of NAUTILUS data", *Classical Quantum Gravity*, **25**, 184012, (2008).

<http://arxiv.org/abs/arXiv:0809.0273/>

B. Abbott, ... , H. J. Pletsch, ... , J. Zweizig (The LIGO Scientific Collaboration), ... , D. Palmer, "Search for Gravitational-Wave Bursts from Soft Gamma Repeaters", *Physical Review Letters*, **101**, 211102, (2008).

<http://arxiv.org/abs/0808.2050/>

B. Abbott, ... , H. J. Pletsch, ... , J. Zweizig (The LIGO Scientific Collaboration), "First joint search for gravitational-wave bursts in LIGO and GEO 600 data", *Classical Quantum Gravity*, **25**, 245008, (2008).

<http://arxiv.org/abs/0807.2834/>

H. J. Pletsch, "Parameter-space correlations of the optimal statistic for continuous gravitational-wave detection", *Physical Review D*, **78**, 102005, (2008).

<http://arxiv.org/abs/0807.1324/>

B. Abbott, ... , H. J. Pletsch, ... , J. Zweizig (The LIGO Scientific Collaboration), "Beating the spin-down limit on gravitational wave emission from the Crab pulsar", *The Astrophysical Journal Letters*, **683**, L45, (2008).

<http://arxiv.org/abs/0805.4758/>

B. Abbott, ... , H. J. Pletsch, ... , J. Zweizig (The LIGO Scientific Collaboration), "Einstein@Home search for periodic gravitational waves in LIGO S4 data", *Physical Review D*, **79**, 022001, (2009).

<http://arxiv.org/abs/0804.1747/>

B. Abbott, ... , H. J. Pletsch, ... , J. Zweizig (The LIGO Scientific Collaboration and the Virgo Collaboration), “Astrophysically triggered searches for gravitational waves: status and prospects”, *Classical Quantum Gravity*, **25**, 114051, (2008).

<http://arxiv.org/abs/0802.4320/>

K. Wette, B. J. Owen, B. Allen, M. Ashley, J. Betzwieser, N. Christensen, T. D. Creighton, V. Dergachev, I. Gholami, E. Goetz, R. Gustafson, D. Hammer, D. I. Jones, B. Krishnan, M. Landry, B. Machenschalk, D. E. McClelland, G. Mendell, C. J. Messenger, M. A. Papa, P. Patel, M. Pitkin, H. J. Pletsch, R. Prix, K. Riles, L. Sancho de la Jordana, S. M. Scott, A. M. Sintes, M. Trias, J. T. Whelan, G. Woan, “Searching for gravitational waves from Cassiopeia A with LIGO”, *Classical Quantum Gravity*, **25**, 235011, (2008).

<http://arxiv.org/abs/0802.3332/>

B. Abbott, ... , H. J. Pletsch, ... , J. Zweizig (The LIGO Scientific Collaboration), “Search of S3 LIGO data for gravitational wave signals from spinning black hole and neutron star binary inspirals”, *Physical Review D*, **77**, 062002, (2008).

<http://arxiv.org/abs/0712.2050/>

B. Abbott, ... , H. J. Pletsch, ... , J. Zweizig (The LIGO Scientific Collaboration), “LIGO: the Laser Interferometer Gravitational-Wave Observatory”, *Reports on Progress in Physics*, **72**, 076901, (2009).

<http://arxiv.org/abs/0711.3041/>

B. Abbott, ... , H. J. Pletsch, ... , J. Zweizig (The LIGO Scientific Collaboration), K. Hurley, “Implications for the Origin of GRB 070201 from LIGO Observations”, *The Astrophysical Journal*, **681**, 1419, (2008).

<http://arxiv.org/abs/0711.1163/>

B. Abbott, ... , H. J. Pletsch, ... , J. Zweizig (The LIGO Scientific Collaboration and AURIGA Collaboration), “A Joint Search for Gravitational Wave Bursts with AURIGA and LIGO”, *Classical Quantum Gravity*, **25**, 095004, (2008).

<http://arxiv.org/abs/0710.0497>

B. Abbott, ... , H. J. Pletsch, ... , J. Zweizig (The LIGO Scientific Collaboration), “Search for Gravitational Waves Associated with 39 Gamma-Ray Bursts Using data from the Second, Third, and Fourth LIGO Runs”, *Physical Review D*, **77**, 062004, (2008).

<http://arxiv.org/abs/0709.0766/>

B. Abbott, ... , H. J. Pletsch, ... , J. Zweizig (The LIGO Scientific Collaboration), “All-sky search for periodic gravitational waves in LIGO S4 data”, *Physical Review D*, **77**, 022001, (2008).

<http://arxiv.org/abs/0708.3818/>

B. Abbott, ... , H. J. Pletsch, ... , J. Zweizig (The LIGO Scientific Collaboration), “Search for gravitational waves from binary inspirals in S3 and S4 LIGO data”, *Physical Review D*, **77**, 062002, (2008).

<http://arxiv.org/abs/0704.3368/>

B. Abbott, ... , H. J. Pletsch, ... , J. Zweizig (The LIGO Scientific Collaboration), “Search for gravitational-wave bursts in LIGO data from the fourth science run”, *Classical Quantum Gravity*, **24**, 5343, (2007).

<http://arxiv.org/abs/0704.0943/>

B. Abbott, ... , H. J. Pletsch, ... , J. Zweizig (The LIGO Scientific Collaboration), “Search for gravitational wave radiation associated with the pulsating tail of the SGR 1806-20 hyperflare of 27 December 2004 using LIGO”, *Physical Review D*, **76**, 062003, (2007).

<http://arxiv.org/abs/astro-ph/0703419/>

B. Abbott, ... , H. J. Pletsch, ... , J. Zweizig (The LIGO Scientific Collaboration), ALLEGRO Collaboration, “First cross-correlation analysis of interferometric and resonant-bar gravitational-wave data for stochastic backgrounds”, *Physical Review D*, **76**, 022001, (2007).

<http://arxiv.org/abs/gr-qc/0703068/>

B. Abbott, ... , H. J. Pletsch, ... , J. Zweizig (The LIGO Scientific Collaboration),
“Upper limit map of a background of gravitational waves”, *Physical Review D*, **76**,
082003, (2007).

<http://arxiv.org/abs/astro-ph/0703234/>

B. Abbott, ... , H. J. Pletsch, ... , J. Zweizig (The LIGO Scientific Collaboration),
“Upper limits on gravitational wave emission from 78 radio pulsars”, *Physical
Review D*, **76**, 042001, (2007).

<http://arxiv.org/abs/gr-qc/0702039/>

B. Abbott, ... , H. J. Pletsch, ... , J. Zweizig (The LIGO Scientific Collaboration),
“Searches for periodic gravitational waves from unknown isolated sources and
Scorpius X-1: Results from the second LIGO science run”, *Physical Review D*, **76**,
082001, (2007).

<http://arxiv.org/abs/gr-qc/0605028/>

